ALMA MATER STUDIORUM
UNIVERSITÀ DI BOLOGNA

Dipartimento di Fisica e Astronomia

DOTTORATO DI RICERCA IN
ASTROFISICA

Ciclo XXXIII

Tesi di Dottorato

Scalar-tensor theories in light of cosmological tensions

Presentata da: Matteo Braglia

Supervisore:
Dr. Fabio Finelli

Coordinatore di Dottorato:
Prof. Francesco Rosario Ferraro

Esame finale anno 2021

Settore Concorsuale: 02/C1 – Astronomia, Astrofisica, Fisica della Terra e dei Pianeti
Settore Scientifico Disciplinare: FIS/05 – Astronomia e Astrofisica

Dedicated to my family

ACKNOWLEDGMENTS

E' un grande piacere per me esprimere il mio rispetto e la mia gratitudine verso il mio supervisore Fabio Finelli, che ha creduto in me ancora prima dell'inizio del mio dottorato, partendo dalla mia tesi di laurea magistrale. Nonostante il mio carattere alle volte testardo, le nostre discussioni sono sempre state costruttive e hanno prodotto risultati scientifici che, senza di esse, non avrebbero visto la luce. A Fabio sono particolarmente riconoscente per avermi insegnato l'importanza della chiarezza nell'esporre i propri risultati e l'attitudine ad analizzare un problema scientifico a 360 gradi, senza prenderlo direttamente di petto. Nondimeno, lo ringrazio per la sua amicizia e per aver reso l'IASF (ora OAS) un ambiente famigliare dove uno studente può sentirsi subito a casa.

Grazie all'IASF ho conosciuto persone squisite. Tra tutte vorrei ringraziare Mario Ballardini, Jose Ramon Bermejo, Angelo Ferrari, Enrico Franceschi, Matteo Galaverni, Dhiraj Kumar Hazra e Daniela Paoletti. In particolare vorrei ringraziare Mario per il continuo sostegno e scambio di idee, per la sua amicizia, le risate e per le sue lezioni di surf grazie alle quali non ho imparato assolutamente nulla. Dhiraj mi ha insegnato l'importanza di essere sempre fieri della propria produzione scientifica e di non sentirsi secondi a nessuno, perchè tanto lo si è di sicuro, e grazie alla nostra amicizia siamo riusciti a divertirci e a mettere una grande passione nella notra ricerca. Inoltre, ringrazio Daniela per avermi fatto muovere i primi passi nella ricerca a partire dal mio Master.

Durante il dottorato ho avuto l'immenso piacere e onore di collaborare con ricercatori che hanno illuminato la mia visione della cosmologia, ma soprattutto mi hanno stupito per la loro professionalità e gentilezza, che mai mi sarei aspettato da persone che prima del mio dottorato conoscevo come nomi ricorrenti nei libri di testo. Uno su tutti, Kazuya Koyama. Kazuya mi ha accolto durante il mio periodo in visita all'ICG a Portsmouth e grazie ad una pacatezza a cui non ero abituato è stato da subito semplice e piacevole tenere il passo con le sue mille idee. I suoi consigli sono sempre stati di valore. Alexei A. Starobinsky è stato una guida per la mia ricerca e ascoltando le sue parole ho sempre trovato nuova ispirazione. Durante gli ultimi mesi del mio dottorato ho avuto anche il piacere di lavorare con Xingang Chen e di apprezzarne il turbine di nuove idee che in ogni nostra discussione ha tirato fuori dal cappello. La lista, tuttavia, è molto lunga ed è doveroso un ringraziamento a tutti i miei collaboratori: Mario Ballardini, Xingang Chen, Will T. Emond, Fabio Finelli, A. Emir Gümrükçüoğlu, Dhiraj Kumar Hazra, Kazuya Koyama, Sachiko Kuroyanagi, Giovanni Marozzi, Daniela Paoletti, Massimo Rossi, George F. Smoot, L. Sriramkumar, Alexei A. Starobinsky, Caterina Umiltà. Ringrazio anche i miei referee, Nicola Bartolo e Julien Lesgourgues per il tempo speso nella lettura della mia tesi.

Grazie al dottorato, ho conosciuto tante persone con cui ho condiviso momenti che non hanno avuto niente a che vedere con la ricerca. Oltre a tutte le persone all'IASF, all'Università di Bologna e agli amici dell'ICG di Portsmouth, voglio ringraziare Laura e Rory per avermi ospitato nella loro accogliente casetta di Southsea e Andrea, Caterina, Margherita e Umberto per le tante risate, molto spesso molto fuori luogo.

La ricerca porta spesso ad allontanarsi dai propri affetti e amicizie. Io, invece, sono stato decisamente fortunato a passare questi 3 anni vicino alla mia città natale e ho potuto continuare la mia vita con gli amici di sempre e con la mia famiglia. Questo è stato un privilegio di cui farò sempre tesoro. Questo momento storico, unito alle vicissitudini della sorte, ha confermato quanto sia cruciale avere una famiglia forte e che si sostiene in ogni momento a prescindere dalle difficoltà.

Per concludere, la più bella sorpresa è stata incotrare Alice, che mi ha sempre dato tutto il suo supporto, rendendo ogni passo naturale e, senza che io me ne rendessi conto, portando il peso delle mie scelte sulle sua spalle invece che sulle mie. A lei va il mio ultimo e più grande grazie.

Matteo Braglia

ABSTRACT

In this PhD thesis, I study cosmologies within the simplest scalar-tensor theories of gravity consisting in a scalar field σ non-minimally coupled to the Ricci scalar through a function $F(\sigma)$ that induces a time-variation in the Newton constant and a potential $V(\sigma)$. I explore the new physics in these cosmologies and use publicly available data to constrain them.

Depending on the functional form of the non-minimal coupling and the potential, the cosmological dynamics changes significantly. For some of the models, the specific dynamics helps recover the consistency with very stringent tests of General Relativity from Solar System and laboratory experiments without the need of any screening mechanisms.

When compared to publicly available data, all these models feature a value of the Hubble constant H_0 larger than the standard ΛCDM cosmology. This makes scalar-tensor theories one of the most interesting candidates to solve the H_0 tension which is becoming one of the most pressing questions in the post-Planck cosmology.

In order to better characterize the phenomenology of scalar-tensor theories, I also investigate their degeneracy with parameters describing the physics of neutrinos. I show that bounds on the effective number of active neutrinos and their masses are slightly relaxed in this context, although they are only a very weakly degenerate with the modification to gravity studied in this thesis and the full inclusion of CMB and LSS data used here.

Finally, I address the issue of initial conditions within these theories and present a new regular isocurvature mode connected with the variation of the Newton constant which is absent in Einstein gravity. Although the observational imprints are different, the allowed fraction of this mode, relative to the adiabatic one, is constrained by Cosmic Microwave Background data at a similar level to other known isocurvature modes.

SINTESI

In questa tesi di Dottorato studio la cosmologia delle più semplici teorie scalari-tensoriali della gravità che consistono in un campo scalare σ accoppiato non-minimalmente al tensore di Ricci per mezzo di una funzione $F(\sigma)$ che induce una variazione nel tempo della costante di Newton e un potenziale $V(\sigma)$. Esploro la nuova fisica in queste cosmologie e uso dati pubblici per vincolarle.

A seconda della forma funzionale dell'accoppiamento non-minimale e del potenziale di σ, la dinamica della cosmologia cambia significativamente. Per alcuni modelli, la particolare dinamica aiuta a ritrovare la consistenza con gli stringenti test sulla Relatività Generale da esperimenti nel Sistema Solare e in laboratorio, senza il bisogno di nessun meccanismo di screening.

Inoltre, quando testati con dati pubblici, tutti questi modelli sono caratterizzati da un valore della costante di Hubble H_0 più alto che nel modello standard ΛCDM. Questo rende le teorie scalar-tensoriali uno dei migliori candidati a risolvere la tensione su H_0, la quale sta diventando una delle questioni più pressanti della cosmologia post-Planck.

Per caratterizzare ancora meglio la fenomenologia di queste teorie, investigo anche la loro degenerazione con i parametri che descrivono la fisica dei neutrini. Mostro come i vincoli sul numero effettivo di neutrini e sulla loro massa vengano rilassati in questo contesto, nonostante siano solo debolmente degeneri con la modifica della gravità.

Per concludere, esploro anche la possibilità di usare perturbazioni di isocurvatura come condizioni iniziali per l'evoluzione delle perturbazioni lineari in queste teorie e presento un nuovo modo regolare che è assente in Relatività Generale. Nonostante i diversi effetti sulle osservabili cosmologiche, la frazione di questo modo, relativa al modo adiabatico, permessa dai dati sulla Radiazione Cosmica di Fondo è simile a quella di altri modi di isocurvature già conosciuti.

List of Publications

Publications discussed in this thesis:

- D. Paoletti, **M. Braglia**, F. Finelli, M. Ballardini and C. Umiltà, *Isocurvature fluctuations in the effective Newton's constant*, Phys. Dark Univ. **25**, 100307 (2019), doi:10.1016/j.dark.2019.100307, [arXiv:1809.03201].

- M. Rossi, M. Ballardini, **M. Braglia**, F. Finelli, D. Paoletti, A. A. Starobinsky and C. Umiltà, *Cosmological constraints on post-Newtonian parameters in effectively massless scalar-tensor theories of gravity*, Phys. Rev. D **100**, no. 10, 103524 (2019), doi:10.1103/PhysRevD.100.103524, [arXiv:1906.10218].

- **M. Braglia**, M. Ballardini, W. T. Emond, F. Finelli, A. E. Gümrükçüoğlu, K. Koyama, D. Paoletti, *Larger value for H_0 by an evolving gravitational constant*, Phys. Rev. D **102**, no. 2, 023529 (2020), doi:10.1103/PhysRevD.102.023529, [arXiv:2004.11161].

- **M. Braglia**, W. T. Emond, F. Finelli, A. E. Gümrükçüoğlu, K. Koyama, *Unified framework for Early Dark Energy from α-attractors*, Phys. Rev. D **102**, no. 2, 083513 (2020), doi:10.1103/PhysRevD.102.083513,[arXiv:2005.14053].

- M. Ballardini, **M. Braglia**, F. Finelli, D. Paoletti, A. A. Starobinsky, C. Umiltà, *Scalar-tensor theories of gravity, neutrino physics, and the H_0 tension*, JCAP 10 (2020) 044, doi:10.1088/1475-7516/2020/10/044, [arXiv:2004.14349].

- **M. Braglia**, M. Ballardini, F. Finelli, K. Koyama, *Early modified gravity in light of the H_0 tension and LSS data*, Phys. Rev. D **103**, no. 4, 043528 (2021), doi:10.1103/PhysRevD.103.043528, [arXiv:2011.12934].

- D. Paoletti, **M. Braglia**, F. Finelli, M. Ballardini and C. Umiltà, *Planck 2018 constraints on isocurvature fluctuations in extended Jordan-Brans-Dicke gravity*, In preparation (2021).

Publications not discussed in this thesis:

- M. Ballardini, **M. Braglia**, F. Finelli, G. Marozzi and A. A. Starobinsky, *Energy-momentum tensor and helicity for gauge fields coupled to a pseudoscalar inflaton*, Phys. Rev. D **100**, no. 12, 123542 (2019), doi:10.1103/PhysRevD.100.123542, [arXiv:1910.13448].

- **M. Braglia**, D. K. Hazra, L. Sriramkumar, F. Finelli, *Generating primordial features at large scales in two field models of inflation*, JCAP 08 (2020) 025, doi:10.1088/1475-7516/2020/08/025, [arXiv:2004.00672].

- **M. Braglia**, D. K. Hazra, F. Finelli, G. F. Smoot, L. Sriramkumar, A. A. Starobinsky, *Generating PBHs and small-scale GWs in two-field models of inflation*, JCAP 08 (2020) 001, doi: 10.1088/1475-7516/2020/08/001,[arXiv:2005.02895].

- **M. Braglia**, X. Chen, D. K. Hazra, *Probing Primordial Features with the Stochastic Gravitational Wave Background*, [arXiv:2012.05821].

Contents

Introduction

Chapter 1 I review the cosmology of the ΛCDM standard concordance model and the equations governing both the background (homogeneous and isotropic) and perturbed dynamics of the Friedmann-Lemaitre-Robertson-Walker (FLRW) cosmology. This chapter does not original work and the main purpose is to present equations and mathematical concepts that the following chapters rely on.

Chapter 2 I present a short review on Scalar-Tensor theories of gravity and show how the non-minimally coupled theories that are considered in this thesis fits into the broader context of (beyond) Horndeski theories. I derive all the equations relevant for non-minimally coupled theories, that I will use in the subsequent Chapters, and discuss the main constraints on these theories from a variety of tests of gravity.

Chapter 3 I review the the state of the art of the H_0 tension. I contextualize the problem and provide the reader with an updated list of indirect (model dependent) and local (model independent) measurements of the Hubble constant.

The standpoint that I adopt in this thesis is that such a discrepancy between early and local measurements of H_0 calls for some new physics. In this spirit, I discuss how the H_0 tension can be recast in a tension on the comoving sound horizon at baryon drag r_s and explain why solutions that modify the ΛCDM model prior to recombination seem to be favored over the ones that modify it at small redshifts. To corroborate this conclusion, I discuss three popular early time solutions to the H_0 tension: dark radiation, Early Dark Energy (EDE) and Modified Gravity (MG).

This Chapter is mainly a review the H_0 tension to set the stage for the following Chapters, but it also contains results from my original work in Ref. [1].

Chapter 4 I present cosmological constraints on ST theories in which the scalar degree of freedom (σ) is nearly massless and coupled to the Ricci scalar through a function of the form $F(\sigma) = N_{\rm pl}^2 + \xi\sigma^{2n}$ and discuss the complementarity of cosmological observations to laboratory and solar system ones in constraining deviations from General Relativity.

Furthermore, I analyze in depth the implications of these theories for the H_0 tension. I show that, although the tension cannot be completely solved, it is naturally eased within ST theories, featuring a considerably reduced fine tuning with respect to other solutions to the H_0 tension such as EDE.

This Chapter contains original work from Refs. [2–4].

Chapter 5 I build on the results on the previous Chapter and extend the model by endowing it with a quartic potential $V(\sigma) = \lambda\sigma^4/4$ that induces a small effective mass. I show that the potential modifies the motion of the scalar field which at late times settles in its minimum at $\sigma = 0$, thus evading any constraint on the deviation from GR.

I present cosmological constraints on the model using several combinations of Cosmic Microwave Background (CMB) and Large Scale Structure datasets and show that the extended parameter space relaxes the constraints on the coupling ξ and allows for a larger H_0 than the massless case. In particular, the $\xi \geq 0$ branch of the coupling, which is ruled out by data in the massless case, is now perfectly allowed.

This Chapter contains original work from Ref. [3].

Chapter 6 I discuss joint constraints on the physics of neutrinos and ST models. The results of this Chapter are constraints on the parameters describing the effective number of relativistic species in the form of neutrinos, i.e. $N_{\rm eff}$ and their total masses $\sum m_\nu$, in the ST context.

Contrary to the expectations (neutrino physics is degenerate with many models of MG, e.g. $f(R)$ theories), I find that there is only a small degeneracy between ST theories so that $N_{\rm eff}$ and m_ν do not vary sensibly with respect to their ΛCDM value, although, as expected, the constraints are a bit relaxed.

This Chapter contains original work from Ref. [4].

Chapter 7 I present a new set of isocurvature initial conditions for the cosmological perturbations in ST models. I analytically derive the most general set of initial conditions as solutions to the full set differential equations in a power series of $k\tau$, where k is the wavevector of the mode and τ the conformal time and explore its imprint on cosmological observables. I focus on the new isocurvature mode due to the presence of the scalar field σ and present the theoretical CMB spectra.

I close the Chapter by presenting bounds on the allowed fraction of such an isocurvature initial conditions obtained with Planck 2015 and 2018 data.

This Chapter contains original work from Ref. [5] and preliminary results from Ref. [6].

Chapter 8 Finally, I critically discuss and summarize the results of the previous Chapter and discuss open directions and the future perspectives for new research that may follow this Thesis work.

Chapter 1

Basics of Cosmology and the ΛCDM model

With the beginning of the 21st century, Cosmology has undergone significant progresses on both the theoretical and observational sides. Ever since the discovery of the accelerated expansion of the Universe [7], several astrophysical and cosmological data, which span a large range of scales and describe processes occurred during different cosmological epochs, have confirmed evidence of a *dark* nature of our Universe. The latter is indeed now known to be composed of about 68% of Dark Energy and 27% of Dark Matter, with the ordinary baryonic matter only accounting for the remaining 5%. Although the nature of Dark Energy (DE) and Dark Matter (DM) is still unknown, this has not stopped cosmologist from settling to a standard cosmological model, in which DE is in the simplest form of a cosmological constant Λ and the majority of DM is non-relativistic (cold). At the current time, despite facing its own theoretical problems, some of which I will describe later in this Chapter, the standard ΛCDM model is the most economic model, which is in remarkable agreement with the largest number of observations. Besides the former assumptions on the dark components, the other pillars of the ΛCDM model are:

- the validity of the laws of General Relativity (GR);
- the isotropy and homogeneity of the Universe, also known as the cosmological principle;
- the Hot Big Bang model history agreeing perfectly with the observed abundance of light elements and the thermal nature of the relic blackbody radiation permeating the Universe;
- an accelerated period of inflation to explain the non-observation of magnetic monopoles, the flatness of the Universe, the correlation of apparently causally disconnected patches in the CMB sky and to provide the adiabatic and Gaussian spectrum of initial conditions needed to seed structure formation;

- the current stage of accelerated expansion consistent with a cosmological constant Λ.

The power of the ΛCDM model is that all these assumptions can be described by a minimal number of 6 parameters (see Section 1.13), which are exquisitely constrained by the outstanding measurement of the Cosmic Microwave Background (CMB) anisotropies by WMAP [8] and Planck [9] and by large scale structure measurements.

In this Chapter, I will briefly describe the formalism, based on GR, needed to head out on the rest of the thesis. I then go on to describe the ΛCDM, its predictions and the main observables that are used to test them. As understood, this Chapter only gives an incomplete overview of these subjects and I refer to popular textbooks [10–20] for more detailed information.

1.1 General Relativity and the Friedmann-Lemaitre-Robertson-Waker

The formalism used to describe the expansion of the Universe and relate it to the its energetic budget is the one of GR. In this framework, an event is a point of the 4-dimensional spacetime manifold and, once chosen a coordinate system, it can be described by its coordinates $x^\mu = (x^0, x^1 x^2, x^3) = (t, x, y, z)$. All the information of interest is encoded in the 2-rank symmetric metric tensor $g_{\mu\nu}(x)$, used to define distances and lengths of vectors on the manifold. Considering two events x^μ and $x^\mu + dx^\mu$ separated by an infinitesimal increment dx^μ, the spacetime interval

$$ds^2 = g_{\mu\nu}(x) dx^\mu dx^\nu \tag{1.1.1}$$

gives the squared distance between the two events.

Given a metric, test particles move along the trajectories that extremize their actions. Such trajectories $x^\mu(\lambda)$, where λ is an affine parameter, are called geodesics and satisfy the following equation

$$\frac{d^2 x^\mu}{d\lambda^2} + \Gamma^\mu_{\rho\sigma} \frac{dx^\rho}{d\lambda} \frac{dx^\sigma}{d\lambda} = 0, \tag{1.1.2}$$

where the Christoffel symbols are given in terms of the metric $g_{\mu\nu}$ as

$$\Gamma^\sigma_{\mu\nu} = \frac{1}{2} g^{\sigma\rho} \left(\frac{\partial g_{\nu\rho}}{\partial x^\mu} + \frac{\partial g_{\mu\rho}}{\partial x^\nu} - \frac{\partial g_{\mu\nu}}{\partial x^\rho} \right). \tag{1.1.3}$$

In order to derive the field equations for the metric $g_{\mu\nu}$ it is useful to introduce the Einstein-Hilbert action:

$$S = \int d^4x\sqrt{-g}\left[\frac{R}{16\pi G} + \mathcal{L}_m\right], \tag{1.1.4}$$

where g is the determinant of the metric and R is the so-called Ricci scalar, obtained by contracting the first and third indices of the tensor defined as

$$R_{\mu\nu} \equiv R^{\alpha}_{\mu\alpha\nu} = \Gamma^{\alpha}_{\mu\nu,\alpha} - \Gamma^{\alpha}_{\mu\alpha,\nu} + \Gamma^{\alpha}_{\beta\alpha}\Gamma^{\beta}_{\mu\nu} - \Gamma^{\alpha}_{\beta\nu}\Gamma^{\beta}_{\mu\alpha}. \tag{1.1.5}$$

Starting from Eq. (1.1.4) and computing the Euler-Lagrange equations for the metric, one can derive the Einstein field equations

$$G_{\mu\nu} \equiv R_{\mu\nu} - \frac{1}{2}g_{\mu\nu}R = 8\pi G T_{\mu\nu} \tag{1.1.6}$$

which relate the total energy-momentum tensor describing the constituents of the Universe, on the right hand side, to the geometry of the Universe on the left hand side. An important consequence, crucial for cosmology, of the form of $R_{\mu\nu}$ in Eq. (1.1.5) is that the Einstein tensor $G_{\mu\nu}$ satisfies a set of equations called Bianchi identities $\nabla_\nu G^{\mu\nu} = 0$ that lead to the conservation of the total energy-momentum tensor

$$\nabla_\nu T^{\mu\nu} = 0. \tag{1.1.7}$$

Note that ∇_μ is the covariant derivative associated to the metric $g_{\mu\nu}$ that acts on a tensor A^{σ}_{ρ} as $\nabla_\mu A^{\sigma}_{\rho} = \partial_\mu A^{\sigma}_{\rho} - \Gamma^{\nu}_{\rho\mu}A^{\sigma}_{\nu} + \Gamma^{\sigma}_{\mu\nu}A^{\nu}_{\rho}$.

In principle, in order to determine the metric of the Universe, one should solve the Einstein equations (1.1.6). In cosmology, the isotropy and homogeneity of the Universe imply that the 4-dimensional spacetime has a maximally symmetric 3-dimensional subspace, so that its metric assumes the general form:

$$ds^2 = -dt^2 + a^2(t)\gamma_{ij}dx^i dx^j \tag{1.1.8}$$

where the t is the physical time coordinate and the metric on hypersurfaces of equal time γ_{ij} is given by

$$\gamma_{ij} = \delta_{ij} + k\frac{x_i x_j}{1 - k(x_k x^k)}, \tag{1.1.9}$$

where $k = -1, 0, +1$ for a spatially hyperbolic, flat or spherical Universe respectively. Hereafter, I will restrict to $k = 0$ since CMB and other cosmological observations agree very well with a flat geometry [21–23] (see however Refs. [24–26] for recent papers claiming that the Universe can instead be closed).

The metric (1.1.8) is called Friedmann-Lemaitre-Robertson-Walker (FLRW) metric and can also be written in spherical coordinates as:

$$ds^2 = -dt^2 + a^2(t)(dr^2 + r^2 d\Omega^2). \tag{1.1.10}$$

The quantity $a(t)$ is the scale factor and together with its time derivative $H(t) = d \log a(t)/dt$ describes the expansion of the Universe. Sometimes, another time variable called conformal time τ, which is related to the physical time by $d\tau = dt/a(t)$, is useful.

With the symmetries of the FLRW metric, the form of the energy-momentum tensor $T_{\mu\nu}$ is greatly simplified. Indeed, symmetries connected with space translations and rotations require its components to transform in a particular way. Specifically, T^{00} has to transform as a scalar, T^{0i} as a vector and T^{ij} as a tensor with respect to these transformations. Isotropy and homogeneity imply that T^{0i} has to vanish and T^{ij} has to be proportional to the 3-metric g_{ij}. These requirements restrict the energy-momentum tensor to take the perfect fluid form as follows:

$$T^{\mu\nu} = P g^{\mu\nu} + (\rho + P) U^\mu U^\nu, \tag{1.1.11}$$

where $U^\mu = dx^\mu/\sqrt{-ds^2}$ is the 4-velocity vector, P is the total pressure and ρ the total density of the fluid.

1.1.1 Redshift, distances and horizons in a FLRW Universe

Starting from the FLRW metric in Eq. (1.1.8) useful concepts can be introduced. Perhaps the most important one is redshift. The wavelength of light emitted from an object receding from us is stretched out by the expansion of the Universe. Therefore, we observe a wavelength which is longer than the one emitted. The redshift z, defined as

$$1 + z \equiv \frac{\lambda_{\text{obs}}}{\lambda_{\text{emit}}} = \frac{a(t_0)}{a(t)} \tag{1.1.12}$$

quantifies this effect. For nearby sources, it is convenient to expand $a(t)$ in a power series around t_0 to get

$$a(t) = a(t_0)[1 + (t - t_0)H_0 + \dots], \tag{1.1.13}$$

where I have introduced the Hubble constant

$$H_0 \equiv \left(\frac{\dot{a}(t)}{a(t)} \right)_{t=t_0} = 100h \, \mathrm{km\ s^{-1} Mpc^{-1}}. \tag{1.1.14}$$

For close objects $t_0 - t$ is just the physical distance d and the redshift increases linearly with distance $z \simeq H_0 d$. Historically, the Hubble constant was first introduced by Hubble [27] to explain the redshift of the spectrum of galaxies with the famous Hubble law

$$v_{\mathrm{gal}} = Hd \tag{1.1.15}$$

that was the first observational proof that the Universe is expanding. Contrary to far galaxies, nearby ones show a blueshift instead of a redshift, because their motion is dominated by their peculiar velocity with respect to the comoving grid which is determined by local gravity.

The parameter h is established to be around $h \sim 0.7$, but its exact value is currently under debate. In fact, some direct measurements of H_0 are in tension with its inference from CMB, Baryonic Oscillations measurements from galaxy surveys and other early time experiments. This so-called H_0 tension, will be explained in details in Chapter 3 and will be discussed extensively in the rest of this thesis.

Another important concept is that of distances. Indeed, in a FLRW Universe this can assume different meanings and one has to be careful in defining distances. First of all, it is very useful to redefine the radial coordinate $d\chi \equiv dr/\sqrt{1-kr^2}$. In order to investigate the propagation of light we note that photons follow null geodesics, i.e. $ds^2 = 0$. For a radial trajectory $\theta, \varphi = 0$ are geodesics and, using the metric (1.1.8), null geodesics become simply $d\tau^2 - dr^2 = 0$ and are therefore described by straight lines in the $\tau - \chi$ plane, that is $\chi(\tau) = \pm\tau + \mathrm{const.}$ The comoving distance $\chi(\tau)$, however, is not observable and to get the physical distance, it has to be multiplied by the scale factor $d_{\mathrm{phys}}(t) = a(t)\chi(t)$.

The luminosity distance d_L and the angular diameter distance d_A are also extensively used in cosmology. The former relates the observed flux F of a source with intrinsic luminosity L at comoving distance χ and redshift z as

$$F = \frac{L}{4\pi\chi^2(1+z)} \equiv \frac{L}{4\pi d_L^2}, \tag{1.1.16}$$

where we have identified

$$d_L = \chi(1+z). \tag{1.1.17}$$

The latter instead measures the distance between the observer and the object when light was emitted. To measure it one has to know the object physical and angular sizes D and $\delta\theta$ respectively as $d_A = D/\delta\theta$, so that $d_A = \frac{\chi}{1+z}$ and the following relation between angular diameter and luminosity distances holds

$$d_A = \frac{d_L}{(1+z)^2}. \tag{1.1.18}$$

The last concept that I wish to introduce is that of cosmological horizon. If the Universe has a finite age, as for instance in the FLRW metric (see following Section), light can only travel a finite distance from its beginning and, at any given moment, an observer can receive information coming only from a finite volume of the Universe. The boundary of this volume is the so-called particle horizon and its comoving size is given by[1]

$$\chi_{\rm ph}(\tau) = \tau - \tau_i = \int\limits_{\tau_i}^{\tau} d\tau = \int\limits_{\ln a_i}^{\ln a} (aH)^{-1} d\,\ln\,a. \tag{1.1.19}$$

Note that, sometimes the same name is used for both the *particle horizon* and the so-called *Hubble radius* defined as H^{-1}. When the dominating component of the Universe satisfies the strong energy condition $\rho + 3P > 0$, however they are indeed of the same magnitude. Nevertheless there are situations, as for the case of inflation, in which the two are different, so it is important to keep in mind their different meaning: the particle horizon is the maximum distance a photon can travel from the time of the Big-Bang, whereas the Hubble radius is the distance over which photon can travel with a Hubble time H^{-1}. In fact, the comoving Hubble radius, i.e. $(aH)^{-1}$, is related to the particle horizon by Eq. (1.1.19).

For completeness, there exists also another kind of horizon, called event horizon which is complementary to the particle horizon and defined as

$$\chi_e(\tau) = \int\limits_{\tau}^{\tau_f} d\tau = \tau_f - \tau \tag{1.1.20}$$

in which τ_f is the final moment of life of the Universe, equal to $\tau_f = +\infty$ if it expands forever. The meaning of χ_e is that an observer will never receive signals sent at a given moment τ from points with $\chi > \chi_e$.

---

[1] Here τ_i is taken to be the initial Big-Bang singularity (see again next Section).

1.1.2 The Friedmann Equations

With the FLRW metric and the perfect fluid form of $T_{\mu\nu}$ in hand, one can simply plug them into the Einstein equations (1.1.6) to derive the so-called Friedmann equations, that, once solved, allow us to determine the time evolution of the scale factor $a(t)$. They are given by:

$$H^2 = \frac{8\pi G}{3}\sum_i \rho_i - \frac{k}{a^2} \tag{1.1.21}$$

$$\dot{H} = -4\pi G \sum_i (\rho_i + P_i) + \frac{k}{a^2}, \tag{1.1.22}$$

where the index i runs over the energetic components of the Universe, which in the ΛCDM model are simply the matter and radiation contribution and the cosmological constant one. Combining these equations together, it is possible to derive an equation for the second derivative of the scale factor as

$$\ddot{a} = -\frac{4\pi G}{3} a(\rho + 3P). \tag{1.1.23}$$

From Eq. (1.1.23), it is understood that the Universe decelerates, i.e. $\ddot{a} < 0$, when a fluid satisfies the so-called strong energy condition $w > -\frac{1}{3}$, where I have defined the equation of state w as $w \equiv P/\rho$. Since ordinary matter pressure is always positive, the current acceleration of the Universe has to be explained by an exotic component that violates the strong energy condition. In the ΛCDM model, this is achieved by the cosmological constant which, as the name says, has a constant equation of state $w = -1$ over all the cosmological evolution.

Note that $H > 0$ for an expanding Universe, so the scale factor is a growing function of time. This means that there exists a time, say $t = 0$, at which $a(t = 0) = 0$. This is the known Big-Bang singularity [28]. At that time the particle horizon defined in the previous Section vanishes and pressure and density are predicted to be infinite by classical physics.

In order to compare theoretical predictions of a model to observations, it is useful to define the density parameter Ω_i for each component as

$$\Omega_i \equiv \frac{\rho_i}{\rho_{\mathrm{crit}}} = \frac{8\pi G}{H^2}\rho_i \tag{1.1.24}$$

where ρ_{crit} is the density value corresponding to a flat Universe, as can be seen substituting $\rho = \rho_{\mathrm{crit}}$ in the first of Eqs.(1.1.21). If the sum of the density parameters of each component $\Omega_{\mathrm{tot}} = \sum_i \Omega_i$ is $>$, $<$ or $= 1$ the Universe is closed, open or flat

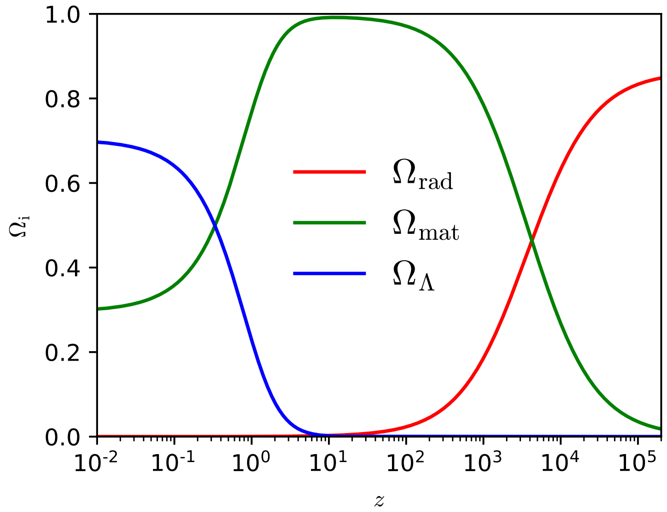

Figure 1.1: Evolution of the density contrasts Ω_i for matter, radiation and cosmological constant.

respectively.

To close the system of equations describing the Universe and its content, the conservation equations for the energy-momentum tensor are used. Indeed, the 0 component of $\nabla^\mu T_{\mu\nu} = 0$, together with the perfect fluid form of the energy-momentum tensor leads to the continuity equation:

$$\dot{\rho} = -3H(\rho + P). \tag{1.1.25}$$

If the different components of the Universe follow an hydrodynamic equation of state Eq. (1.1.25) can be integrated to obtain the evolution of density with respect to the scale factor

$$\rho_i(t) = \rho_{0i} \left(\frac{a(t)}{a_0} \right)^{-3(1+w_i)}. \tag{1.1.26}$$

Note that $w_i = 0,\ 1/3,\ -1$, for non-relativistic matter, radiation and a cosmological constant respectively. Therefore for these components Eq. (1.1.25) leads to the simple scaling laws $\rho_m \propto a^{-3}$ whereas $\rho_r \propto a^{-4}$ and $\rho_\Lambda = \text{const}$. Since the scale factor increases with time, radiation first dominates the Universe. However, since it is diluted along the expansion faster than the matter component, the latter overtakes radiation at the so-called equivalence redshift defined by $\rho_r(z_{\rm eq}) \equiv \rho_m(z_{\rm eq})$. Eventually, also the matter contribution redshits away and the Universe starts to accelerate because of the cosmological constant domination at the redshift of matter-cosmological constant equivalence z_Λ. This is depicted in Fig. 1.1.

1.2 The Hot Big-Bang model

Of the three cosmological eras shown in Fig. 1.1, the last moments of the radiation era are very well understood because they rely on our good understanding of quantum field theory and nuclear physics at the energy scales that can be reached in laboratories and accelerators. The radiation era can be divided into the following stages:

- *Quark era* $T > T_{\rm QH} \simeq 200 - 300$ MeV: at very high temperatures matter exists in the form of the quark-gluon plasma. At $T = T_{\rm QH}$ the Universe undergoes a phase transitions and pairs of quarks and antiquarks join together to form hadrons, including pions and nucleons.

- *Hadron era* $T_{\rm QH} > T > T_\pi \simeq 130$ MeV: pion-pion interactions are very important and the perfect fluid approximation cannot be applied until pions and antipions annihilate at $T = T_\pi$.

- *Lepton era* $T_\pi > T > T_e \simeq 0.5$ MeV: leptons dominate the Universe until positrons and electrons annihilate at $T = T_e$. It is during this era that the primordial nucleosynthesis occurs.

- *Plasma era* $T_e > T > T_{\rm eq} \simeq 1$ eV: the Universe is filled with photons, matter (protons, electrons and helium nuclei) and neutrinos, which have already decoupled from the background fluid of tightly coupled photons and baryons since the Lepton era.

After $z_{\rm eq}$, the matter-radiation equivalence, the baryons-photons fluid is still tightly coupled because of Thompson scattering between photons and electrons and can be considered as a single fluid in statistical equilibrium. As the temperature T decreases in the so-called recombination era electrons start to recombine in nuclei. Then, as the Universe expands, Thompson scattering becomes more inefficient photons decouple from the cosmological fluid. However, note that both decoupling and recombination are not exactly instantaneous processes. Rather, they are characterized by a small, but finite duration.

The Hot Big Bang model therefore leads to the following predictions:

- it predicts light-element abundances in perfect agreement with observations [29];

- it naturally accounts naturally for the expansion of the Universe;

- it explains the presence of the CMB (see below) as a relic of the hot thermal phase [30].

1.3 Problems of the Standard Big-Bang Model and Inflation

Despite its many successes, the standard Big-Bang model faces some serious problems, which are ultimately related to each other:

- **The magnetic monopole problem**. Great Unified Theories (GUT) that aim at explaining the fundamental physics at very high energies predict the production of topological defects like magnetic monopoles, cosmic strings or domain walls. The predicted density of these defects at present days is much higher than that of the matter [16], but no such objects have ever been observed in the Universe.

- **The flatness problem**. An intuitive way to formulate this problem is as follows. The Friedmann equations (1.1.21) in the presence of a non-zero spatial curvature become:

  $$\Omega(t) - 1 = \frac{k}{(aH)^2} = -\Omega_k. \tag{1.3.1}$$

  From this equation it is clear that, in order to explain cosmological observations that are compatible with a flat Universe, the initial density parameter has to be very close to 1 [16]:

  $$\Omega_i - 1 = (\Omega_0 - 1)\frac{(H_0 a_0)^2}{(H_i a_i)^2} = (\Omega_0 - 1)\left(\frac{\dot{a}_0}{\dot{a}_i}\right)^2 \leq 10^{-56} \tag{1.3.2}$$

  therefore the Universe has to be very close to flat near the Big-Bang singularity.

- **The horizon problem**. The finiteness of the conformal time elapsed between the initial Big-Bang singularity implies that regions we observe in the sky were never in causal contact. As can be seen from Fig. 1.2, if two CMB photons, emitted close to the Big-Bang singularity at t_i, were separated by a sufficient comoving distance, their past light cones will never overlap. In particular, being the angle subtended by the comoving horizon at recombination $\theta_{\rm hor} = 1.16°$, regions separated by an angle $\theta > 2\theta_{\rm hor}$ would never come in causal contact in the standard Hot Big-Bang scenario. This is in stark contrast with the observed spectrum of the CMB which is essentially homogeneous and isotropic over the whole sky, if one does not consider its tiny anisotropies of the order of 10^{-5}.

It can be shown that all these problems are related to each other [31] so I will focus on the horizon one in the following. In order to find a solution to this problem, it is

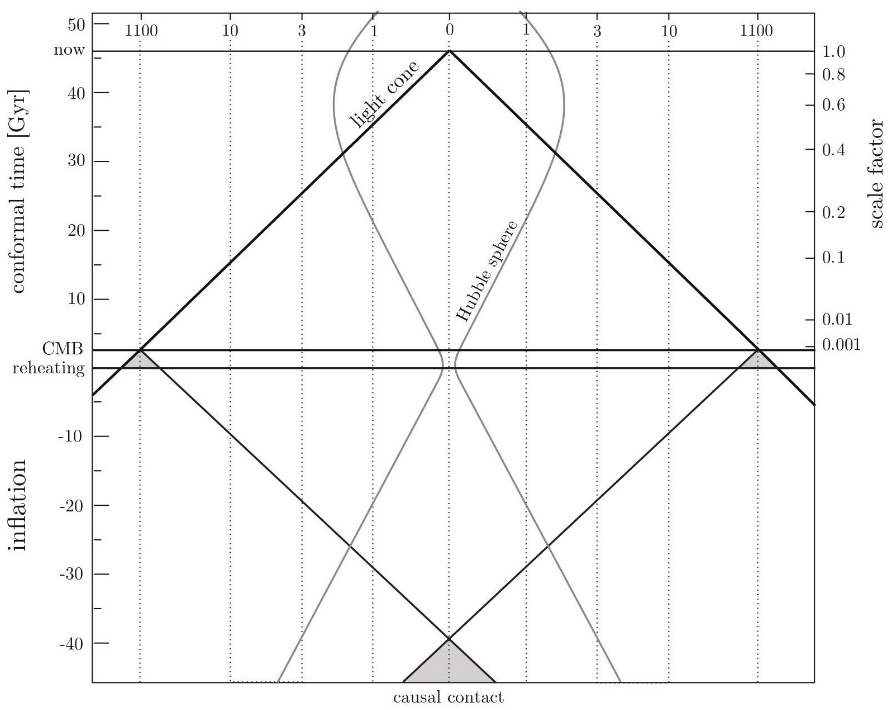

Figure 1.2: Representation of the horizon problem [top] and of its solution [bottom]. Figure taken from [31].

useful to realize where the problem comes from. The Hubble radius for a Universe dominated by a fluid with $P = w\rho$ is given by

$$(aH)^{-1} = H_0^{-1} a^{\frac{1}{2}(1+3w)} \tag{1.3.3}$$

so that it grows with the expansion of the Universe for ordinary matter satisfying the strong energy condition. Therefore, in this case, the integral in Eq. (1.1.19) is dominated by the its upper limit of integration.

The solution is then at hand. Postulating a non-growing comoving Hubble radius in the early Universe, the integral in Eq. (1.1.19) becomes instead dominated by its lower integration limit and the particle horizon becomes much larger than the Hubble one. This is the paradigm of *inflation*. Thanks to a shrinking Hubble radius, large scales λ become smaller than the comoving particle horizon and they could have been in causal contact in the past, as can be seen from Fig. 1.2, from which it is also seen that the initial singularity is now pushed to negative conformal times $\tau_i \to -\infty$.

Eq. (1.3.3) suggests that a shrinking Hubble radius can be obtained by considering a fluid with negative pressure. The simplest physical model of inflation where this can be obtained is the one of single field inflation in which an homogeneous scalar field $\phi(t)$, as required by the symmetries of the FLRW spacetime, slowly roll down its potential.

The action of such a scalar field in a curved spacetime is

$$S = \int d^4x \sqrt{-g}\Big[-\frac{1}{2}g^{\mu\nu}\partial_\mu\phi\partial_\nu\phi - V(\phi)\Big] \tag{1.3.4}$$

and its energy-momentum tensor can be recast in the form of a perfect fluid defining the scalar field density and pressure as

$$\rho_\phi = \frac{1}{2}\dot{\phi}^2 + V(\phi) \tag{1.3.5}$$

$$P_\phi = \frac{1}{2}\dot{\phi}^2 - V(\phi). \tag{1.3.6}$$

Substituting ρ_ϕ and P_ϕ in Eqs. (1.1.21) gives the Friedmann equations

$$H^2 = \frac{1}{3M_{\rm pl}^2}\left[\frac{1}{2}\dot{\phi}^2 + V(\phi)\right] \tag{1.3.7}$$

$$\dot{H} = -\frac{1}{2}\frac{\dot{\phi}^2}{M_{\rm pl}^2}, \tag{1.3.8}$$

while the Euler-Lagrange equations of motion lead to the Klein-Gordon equation

$$\ddot{\phi} + 3H\dot{\phi} + \frac{\partial V}{\partial\phi} = 0. \tag{1.3.9}$$

Using these equations, the violation of the strong energy condition is violated if the potential energy dominates over the kinetic one. This condition can also be satisfied if the so-called Hubble slow-roll parameters

$$\epsilon \equiv -\frac{\dot{H}}{H^2} \tag{1.3.10}$$

$$\eta \equiv \frac{\dot{\epsilon}}{H\epsilon} \tag{1.3.11}$$

$$\delta \equiv -\frac{\ddot{\phi}}{H\dot{\phi}} \tag{1.3.12}$$

are small, that is $\epsilon, |\delta| \ll 1$, that implies $|\eta| \ll 1$. When these conditions are satisfied, inflation is said to be in the slow-roll regime and the Friedmann and Klein-Gordon simplify to

$$H^2 \approx \frac{V}{M_{\rm pl}^2} \tag{1.3.13}$$

and

$$3H\dot{\phi} \approx -V_{,\phi}\,. \tag{1.3.14}$$

The Hubble slow-roll parameters ϵ and η become

$$\epsilon \approx \epsilon_V \equiv \frac{M_{\rm pl}^2}{2}\left(\frac{V_{,\phi}}{V}\right)^2 \tag{1.3.15}$$

$$|\eta| \approx |\eta_V| \equiv M_{\rm pl}^2 \frac{V_{,\phi\phi}}{V}, \tag{1.3.16}$$

where ϵ_V and η_V are called potential slow-roll parameter and slow-roll inflation occurs for $\epsilon_V, \eta_V \ll 1$. These parameters are useful to determine if inflation can occur just considering the shape of the potential.

The existence of Universe as observed today implies that inflation needs to end. The important question is therefore how long inflation has to be in order to solve the horizon problem and how it can end. Defining the number of e-folds as

$$N \equiv \int_{a_I}^{a_E} d\,\ln\,a = \int_{t_I}^{t_E} dt\,H, \tag{1.3.17}$$

where t_I and t_E are the initial and ending time of inflation, defined as $\epsilon(t_E) = 1$. The high degree of homogeneity in the CMB can be explained, in the simplest slow roll models, if inflation last more than $50 - 60$ e-folds.

In a completely homogeneous and isotropic Universe, however, structures cannot form. Indeed inflation, besides solving the aforementioned problems of the Hot Big-Bang cosmology, also predicts an adiabatic spectrum of tiny fluctuations on top of the homogeneous background. These are the quantum vacuum fluctuations of the inflaton field that get stretched during inflation, cross the Hubble radius and get frozen. Once the fluctuations cross the Hubble radius, they classicalize and behave as a Gaussian stochastic field. Eventually, they re-enter the Hubble radius after inflation and they seed for the large-scale structure observed today in galaxies and clusters. Most importantly, the primordial fluctuation are imprinted in the CMB anisotropies, that is small temperature (and polarization) fluctuations of the order $\delta T/T \sim 10^{-5}$ around its $T_0 = 2.72548 \pm 0.00057\,K$ [32]. In the standard picture, inflation is followed by a period of reheating during which the inflaton decays into Standard Model particles.

1.4 Cosmological Perturbations Theory

In this Chapter, I briefly review the theory of cosmological perturbations on top of the homogeneous and isotropic Universe. It is because of such tiny inhomogeneities and anisotropies that we observe the CMB anisotropies and structure formation ultimately started out. For reviews see Refs. [33, 34].

A quantity that can be used to roughly estimate whether a perturbation of a given wavelength λ can collapse to start structure formation is the Jeans length λ_J. This is computed, by simply comparing the attractive and repulsive forces of pressure and gravity respectively. Given a spherical inhomogeneity of radius λ and mass M, in a background fluid of density ρ, it will grow if the self-gravitational force per unit mass, $F_g \simeq GM/\lambda^2$ exceeds the opposing force per unit mass arising from pressure $F_P = P/(\rho\lambda^)$, leading to the condition

$$\lambda > \lambda_J \equiv c_s^2 (G\rho)^{-1/2}, \tag{1.4.1}$$

where c_s^2 is the speed of sound of the fluid, given in Eq. (1.8.14) below. If this condition is not satisfied, the perturbation freely propagates as an oscillating wave. The Jeans length, however, is a concept that makes only sense within Newtonian gravity, which is an adequate description only for perturbations with scales smaller than the Hubble radius. For larger scales, a General Relativistic approach, that I introduce in the next Section, is needed.

I will follow the notation of Ref. [35]. In particular, since I will have to deal with perturbations at linear order, it is useful to work in their Fourier space rather than in real space. Indeed, since inflation predicts an initial distribution of density perturbations which is Gaussian at leading order, Fourier modes are decoupled, gratly simplifying their treatment. My notation for the Fourier transform of a Gaussian field $A(\mathbf{x})$ is:

$$A(\mathbf{x}, \tau) = \int \frac{d\mathbf{k}}{(2\pi)^3} \, A(\mathbf{k}, \tau) \, e^{i\mathbf{k}\cdot\mathbf{x}}. \tag{1.4.2}$$

With these conventions, the power spectrum of the function A is then defined as

$$\langle A(k) A(k') \rangle = (2\pi)^3 \mathcal{P}(k) \delta^{(3)}(k - k'), \tag{1.4.3}$$

where $\delta^{(3)}(k - k')$ is the Dirac delta distribution function. Also, I will rise and lower spatial indices, denoted with latin letters i, j, $k, \ldots$ with the Kronecker delta δ_{ij}.

1.5 Perturbations to the Metric

The idea is to consider small perturbations $\delta g_{\mu\nu}$ around the background FLRW metric $\bar{g}_{\mu\nu}$, so that the full metric can be written as

$$ds^2 = a^2(\tau)[-(1+2A)d\tau^2 + 2B_i dx^i d\tau + (\delta_{ij} + h_{ij})dx^i dx^j]. \tag{1.5.1}$$

The metric perturbations can be divided into scalar, vector and tensor according to their transformation properties under the group of 3-rotations and 3-translations. In particular, δg_{00} is a scalar perturbation, δg_{0i} can be composed as

$$B_i = \partial_i B + \hat{B}_i, \tag{1.5.2}$$

where $\hat{B}_i$ is the vector traceless ($\partial_i \hat{B}^i = 0$) part of B_i and B its scalar one. δg_{ij} can be instead decomposed as follows

$$h_{ij} = 2C\delta_{ij} + 2\partial_{\langle i}\partial_{j\rangle}E + 2\partial_{(i}\hat{E}_{j)} + 2\hat{E}_{ij}, \tag{1.5.3}$$

where I denote divergenceless quantities with an overhat and I have defined

$$\partial_{\langle i}\partial_{j\rangle}E \equiv \left(\partial_i\partial_j + \frac{1}{3}\nabla^2\right)E, \tag{1.5.4}$$

$$\partial_{(i}\hat{E}_{j)} \equiv \frac{1}{2}(\partial_i\hat{E}_j + \partial_j\hat{E}_i). \tag{1.5.5}$$

The first two terms on the right hand side of Eq. (1.5.3) are the scalar part of h_{ij} and the third is the vector one. The fourth term, i.e. $\hat{E}_{ij}$ encodes the transverse and traceless tensorial degrees of freedom of the FLRW metric and physically represents Gravitational Waves propagating on the background FLRW metric. Therefore, 10 degrees of freedom are encoded in the FLRW metric, but only 4 of them are scalar perturbations. Note that scalar, vector and tensor perturbations evolve independently on each other because of the so-called decomposition theorem [14]. Physically, scalar perturbations are the ones induced by inhomogeneities in the energy density of matter and radiation and are the ones that exhibit gravitational instability and eventually lead to the formation of the large scale structure in the Universe, therefore these will be the focus of the next Sections. Vector perturbations are instead related to the rotational motion of the fluid and very quickly decay with the expansion of the Universe. Tensor perturbations, as mentioned above, describe Gravitational Waves propagating in the FLRW metric.

1.5.1 Gauge Transformations

In order to simplify the equations above, it is often convenient to exploit the so-called gauge invariance of GR and choose a particular coordinate system, or gauge. An infinitesimal coordinate transformation is

$$x^\mu \to \tilde{x}^\mu = x^\mu + d^\mu(x^\nu) \tag{1.5.6}$$

where

$$d^0 = \alpha(x^\nu), \tag{1.5.7}$$

$$d^i = \partial^i \beta(x^\nu) + \epsilon^i(x^\nu); \tag{1.5.8}$$

$\partial^i \beta$ is longitudinal, i.e. irrotational ($\varepsilon_{ijk}\partial^j \partial^k \beta = 0$), and ϵ_i is transverse, i.e. divergenceless.

Under the transformation (1.5.6) the metric transforms as

$$\tilde{g}_{\alpha\beta}(\tilde{x}^\rho) = \frac{\partial x^\gamma}{\partial \tilde{x}^\alpha} \frac{\partial x^\delta}{\partial \tilde{x}^\beta} g_{\gamma\delta}(x^\rho). \tag{1.5.9}$$

Assuming that d^μ is of the same order of the perturbations, the equation above can be easily linearized and the metric $\tilde{g}_{\alpha\beta}$ rewritten as

$$\tilde{g}_{\alpha\beta}(\tilde{x}^\rho) = \bar{g}_{\alpha\beta}(\tilde{x}^\rho) + \delta\tilde{g}_{\alpha\beta}. \tag{1.5.10}$$

The relation between the old and new metric is readily found to be

$$\delta g_{\alpha\beta} \to \delta\tilde{g}_{\alpha\beta} = \delta g_{\alpha\beta} - \bar{g}_{\alpha\beta,\gamma} d^\gamma - \bar{g}_{\beta\delta} d^\delta{}_{,\alpha} - \bar{g}_{\alpha\delta} d^\delta{}_{,\beta} \,, \tag{1.5.11}$$

where both the right and left hand side are computed at the point $\tilde{x}^\rho$.

From Eq. (1.5.11), it is easy to find the transformation laws of scalar perturbations, that is:

$$A \to \quad A - \alpha' - \mathcal{H}\alpha \tag{1.5.12}$$

$$B \to \quad B + \alpha - \beta' \tag{1.5.13}$$

$$C \to \quad C - \mathcal{H}T - \tfrac{1}{3}\nabla^2\beta \tag{1.5.14}$$

$$E \to \quad E - \beta. \tag{1.5.15}$$

Therefore metric perturbations are not uniquely defined and depend on the specific time slicing of the space time and on the specific choice of spatial coordinates on these time slices.

A possible way to avoid this ambiguity is to define so-called gauge invariant variables that do not change under the gauge transformation (1.5.6), as for example the so-called Bardeen variables [36]:

$$\Psi_B \equiv \quad A + \mathcal{H}(B - E') + (B - E')', \tag{1.5.16}$$

$$\Phi_B \equiv \quad -C - \mathcal{H}(B - E') + \tfrac{1}{3}\nabla^2 E. \tag{1.5.17}$$

Note that an infinite number of gauge invariant variables can be constructed as a linear combination of Ψ_B and Φ_B.

1.5.2 Gauge Fixing

Another possibility is instead to use the gauge freedom to impose conditions on the scalar and vector perturbations. This procedure is known as gauge fixing and can be very useful as, depending on the problem considered, there could be gauges where the physical interpretation and/or computations is easier. Furthermore, the choice of the gauge is sometimes crucial when it comes to numerically integrating the equations governing the evolution of the cosmological perturbations.

Among the several possible choices of gauge, two of them are particularly relevant.

- *Newtonian (or longitudinal) gauge.* It is defined by the conditions

  $$B_l = E_l = 0. \tag{1.5.18}$$

  Defining $A \equiv \Psi$ and $C \equiv \Phi$. The metric then becomes

  $$ds^2 = a^2(\tau)[-(1 + 2\Psi)d\tau^2 + (1 - 2\Phi)\delta_{ij}dx^i dx^j]. \tag{1.5.19}$$

  This gauge is fixed uniquely as any transformation with $\beta \neq 0$ ($\alpha \neq 0$) spoils the condition E_l ($B_l = 0$). The function Ψ plays the role of the gravitational potential in the weak field limit of the Einstein equations and thus the Newtonian gauge has a clear physical interpretation.

- *Synchronous gauge.* It is defined by

  $$A_s = B_s = 0, \tag{1.5.20}$$

so that the metric becomes

$$ds^2 = a^2(\tau)[-d\tau^2 + (\delta_{ij} + h_{ij})dx^i dx^j]. \tag{1.5.21}$$

In order to be consistent with the notation of Ref. [35], I define $2C \equiv h/3$ and $2E \equiv \mu$. It is useful to write h_{ij} as a Fourier integral

$$h_{ij}(\mathbf{x}, \tau) = \int \frac{d\mathbf{k}}{(2\pi)^3} e^{i\mathbf{k}\cdot\mathbf{x}} \left[\hat{k}_i \hat{k}_j h(\mathbf{k}, \tau) + \left(\hat{k}_i \hat{k}_j - \frac{1}{3}\delta_{ij}\right) 6\eta(\mathbf{k}, \tau)\right], \ \mathbf{k} = \hat{k}k. \tag{1.5.22}$$

It then becomes clear that the gauge is specified by the two functions h and μ in real space and by h and η in Fourier space. Unlike the Newtonian one, the synchronous gauge is not uniquely fixed, since the choice of the initial time-slicing is arbitrary [18]. This can result in fictitious gauge modes in the solutions to the Einstein equations, so usually the gauge freedom is used to fix the CDM velocity to zero $\theta_c = 0$. The synchronous gauge is particularly useful for the integration of the perturbed Einstein equations (see below) because of its numerical stability.

Other possible choices of gauge include the so-called *spatially flat* and *comoving* gauge, that are useful to perform calculations in the inflationary context.

1.6 Perturbed Einstein Equations

Splitting the Einstein tensor into a background part and a perturbed one as $G\mu\nu = G^{(0)}_{\mu\nu} + \delta G_{\mu\nu}$, and analogously for the energy-momentum tensor, the perturbed Einstein equations are simply given by:

$$\delta G^\mu_\nu = 8\pi G \delta T^\mu_\nu, \tag{1.6.1}$$

where all the quantities are intended to be computed in a specific gauge.

In order to explicitly write down each of the components of the equation above, the energy-momentum tensor can be written as

$$\begin{aligned} T^0_0 &= -(\bar{\rho} + \delta\rho), & (1.6.2)\\ T^0_i &= (\bar{\rho} + \bar{P})v_i = -T^i_0, & (1.6.3)\\ T^i_j &= (\bar{P} + \delta P)\delta^i_j + \Sigma^i_j, & (1.6.4) \end{aligned}$$

where $\delta\rho$ and δP are the perturbations to the denisty and pressure of the perfect fluid, $v^i \equiv dx^i/d\tau$ its coordinate velocity and where $\Sigma^i_j \equiv T^i_j - \delta^i_j T^k_k/3$ is the traceless anisotropic shear perturbation to T^i_j. Following Ref. [35], it is also useful to define the variables θ and σ as

$$\begin{aligned} \theta &\equiv ik^j v_j, & (1.6.5) \\ (\bar{\rho}+\bar{P})\sigma &\equiv -(\hat{k}_i\hat{k}_j - \frac{1}{3}\delta_{ij})\Sigma^i_j & (1.6.6) \\ \delta &\equiv \delta\rho/\rho. & (1.6.7) \end{aligned}$$

Also, the relations between the quantities in the synchronous and in the Newtonian gauge under the gauge transformation (1.5.6) are given by [35]:

$$\begin{aligned} \delta^{(S)} &= \delta^{(N)} - \alpha\frac{\bar{\rho}'}{\bar{\rho}}, & (1.6.8) \\ \theta^{(S)} &= \theta^{(N)} - \alpha k^2, & (1.6.9) \\ \delta P^{(S)} &= \delta P^{(N)} - \alpha\bar{P}', & (1.6.10) \\ \sigma^{(S)} &= \sigma^{(N)}, & (1.6.11) \end{aligned}$$

and

$$\Psi = \frac{1}{2k^2}\left[h'' + 6\eta'' + \mathcal{H}(h' + 6\eta')\right], \qquad (1.6.12)$$

$$\Phi = \eta - \frac{1}{2k^2}\mathcal{H}(h' + 6\eta'), \qquad (1.6.13)$$

where again all the quantities are evaluated at the same space-time coordinate.

Then, the Einstein equations take the following form [35, 37]

$$\begin{aligned} k^2\eta - \frac{1}{2}\mathcal{H}h' &= -8\pi G a^2 \sum_i \frac{\delta\rho_i^{(S)}}{2}, & (1.6.14) \\ k^2\eta' &= 8\pi G a^2 \sum_i (\bar{\rho}_i + \bar{P}_i)\frac{\theta_i^{(S)}}{2}, & (1.6.15) \\ h'' + 2\mathcal{H}h' - 2k^2\eta &= -24\pi G a^2 \sum_i \delta P_i^{(S)}, & (1.6.16) \\ (h+6\eta)'' + 2\mathcal{H}(h+6\eta)' - 2k^2\eta &= -24\pi G a^2 \sum_i (\bar{\rho}_i + \bar{P}_i)\sigma_i^{(S)}, & (1.6.17) \end{aligned}$$

in *synchronous gauge* and the following one

$$k^2\Phi + 3\mathcal{H}(\Phi' + \mathcal{H}\Psi) = -8\pi G a^2 \sum_i \frac{\delta\rho_i^{(N)}}{2}, \tag{1.6.18}$$

$$k^2(\Phi' + \mathcal{H}\Psi) = 8\pi G a^2 \sum_i (\bar{\rho}_i + \bar{P}_i)\frac{\theta_i^{(N)}}{2}, \tag{1.6.19}$$

$$\Phi'' + \mathcal{H}(\Psi + 2\Phi)' + \left(2\frac{a''}{a} - \mathcal{H}^2\right) + \frac{k^2}{3}(\Phi - \Psi) = 4\pi G a^2 \sum_i \delta P_i^{(N)}, \tag{1.6.20}$$

$$k^2(\Phi - \Psi) = 12\pi G a^2 \sum_i (\bar{\rho}_i + \bar{P}_i)\sigma_i^{(N)}, \tag{1.6.21}$$

in the *Newtonian gauge*, where the index i runs over all species contributing to the content of the Universe.

1.7 Boltzmann Equations for Matter and Radiation

In the previous Section, I derived the perturbed Einstein equations describing the evolution of metric perturbations. In order to close the system of differential equations, they have to be supplemented by those governing the time evolution of the density and velocity perturbations. The latter equations should include the interactions between the different matter components and therefore are more complicated than the ones obtained by simply perturbing the conservation equations of the energy-momentum tensor, which describe uncoupled fluids. The systematic way to deal with such interactions is to write down and solve the Boltzmann equations for each species [14].

In the following, I will derive the Boltzmann equations only in the synchronous gauge and refer to Ref. [35] for those in the Newtonian gauge. I work in the phase space described by spatial coordinates x^i and their conjugate momenta P_i. The latter is just the spatial part of the energy-momentum 4-vector P_i, given by

$$P_i = a(\delta_{ij} + \frac{1}{2}h_{ij})p^j, \tag{1.7.1}$$

where $p^j = \delta^{ji}p_i$ is the proper momentum measured by an observer at fixed spatial coordinates. The phase space infinitesimal volume is $dV = dx^1dx^2dx^3dP_1dP_2dP_3$ and its zeroth-order is proportional to a^3. At the zeroth-order p_i scales as a^{-1}, so it is useful to define the quantity $q_j = ap_j$ and its modulus q and direction n_j as $q_j = qn_j$, with $n^in_i = 1$ [38]. Another useful quantity is $\epsilon = (q^2 + a^2m^2)^{1/2} = a(p^2 + m^2)^{1/2}$, where $(p^2 + m^2)^{1/2}$ is the proper energy measured by a comoving observer which can be related to the 0 component of the energy-momentum 4-vector as $P_0 = -\epsilon$.

All this conventions set up, the Boltzmann equations can now be derived starting from the equations for the phase space distribution f_j for the j-th species

$$\frac{df_j}{d\tau} = C[f_j], \tag{1.7.2}$$

that gives the number of particles in dV

$$f(x^i, P_j, \tau) dV = dN. \tag{1.7.3}$$

The term $C[f_i]$ is the collision term describing the interaction between different particle species. The zeroth-order phase space distribution is simply the Fermi-Dirac (for fermions, − sign) or the Bose-Einstein (for bosons, + sign) distribution function and depends only on ϵ (or q)

$$f_0 = f_0(\epsilon) = g_s \left[e^{\epsilon/aT} \pm 1\right]^{-1} \tag{1.7.4}$$

where the factor g_s is the number of spin degrees of freedom.

The perturbed phase-space distribution can be expanded around its zeroth-order as

$$f(x^i, P_j, \tau) = f_0(q)(1 + \Upsilon(x^i, q, n_j, \tau)), \tag{1.7.5}$$

and using that

$$T_{\mu\nu} = \int \sqrt{-g} dP_1 dP_2 dP_3 \frac{P_\mu P_\nu}{P^0} f(x^i, P_j, \tau), \tag{1.7.6}$$

the components of the energy-momentum tensor can be written in terms of Υ as

$$T^0_0 = -\int q^2 dq d\Omega \, \frac{\sqrt{q^2 + m^2 a^2}}{a^4} f_0(1 + \Upsilon), \tag{1.7.7}$$

$$T^0_i = -\int q^3 dq d\Omega \, \frac{n_i f_0 \Upsilon}{a^4}, \tag{1.7.8}$$

$$T^i_j = -\int q^4 dq d\Omega \, \frac{n^i n_j}{a^4 \sqrt{q^2 + m^2 a^2}} f_0(1 + \Upsilon), \tag{1.7.9}$$

where $d\Omega$ is the solid angle associated with n^i.

Turning the total derivative with respect to τ in Eq. (1.7.2) into partial derivatives

$$\frac{df}{d\tau} = \frac{\partial f}{\partial \tau} + \frac{dx^i}{d\tau}\frac{\partial f}{\partial x^i} + \frac{dq}{d\tau}\frac{\partial f}{\partial q} + \frac{dn_i}{d\tau}\frac{\partial f}{\partial n_i} \tag{1.7.10}$$

and use the geodesic equations to find the appropriate expression for $dq/d\tau$, the unintegrated Boltzmann equation in Fourier space in the synchronous gauge becomes

$$\frac{\partial \Upsilon}{\partial \tau} + i\frac{q}{\epsilon}(\mathbf{k}\cdot\hat{n})\Upsilon + \frac{d\ln f_0}{d\ln q}\left(\eta' - \frac{h'+6\eta'}{2}\mu^2\right) = \frac{1}{f_0}C[f], \qquad (1.7.11)$$

where $\mu \equiv \hat{k}\cdot\hat{n}$. Eq. (1.7.11) is valid for any species, regardless of its nature. I now consider separately each species to give an appropriate expression for the collision factor and integrate the Boltzmann equation (1.7.11).

1.7.1 Neutrinos

For simplicity, I focus here on massless neutrinos for which $\epsilon = q$. Their energy density, pressure and anisotropic stress are given by Eq. (1.7.7). The procedure is then to integrate out the q-dependence from Eq. (1.7.11) by taking its moments, and to expand the angular dependence of the perturbation Υ in Legendre polynomials $P_l(\mu)$ as:

$$F_\nu(\mathbf{k},\hat{n},\tau) \equiv \frac{\int q^3 dq\, f_0 \Upsilon}{\int q^3 dq\, f_0} \equiv \sum_{l=0}^{\infty}(-i)^l(2l+1)F_{\nu l}(\mathbf{k},\tau)P_l(\mu). \qquad (1.7.12)$$

The density, velocity and stress perturbations of neutrino are given by

$$\delta_\nu = \frac{1}{4\pi}\int d\Omega\, P_0(\mu)F_\nu = F_{\nu 0}, \qquad (1.7.13)$$

$$\theta_\nu = \frac{3i}{16\pi}\int d\Omega\, P_1(\mu)F_\nu = \frac{3}{4}kF_{\nu 1}, \qquad (1.7.14)$$

$$\sigma_\nu = -\frac{1}{8\pi}\int d\Omega\, P_0(\mu)F_\nu = \frac{1}{2}F_{\nu 2}, + \qquad (1.7.15)$$

so that, in order to find the equations respectively for the neutrino density, velocity and stress, the unintegrated collisionless (neutrinos are weakly interacting with other particles) Boltzmann equation (1.7.11) has to be multiplied by the Legendre polynomials and integrated over $d\mathbf{q}$. Therefore, one is left with an infinite hierarchy of equations for the multipole moments of the distribution function. The usual way to deal with such an hierarchy is to truncate it at some $l_{\max}$. In the case of neutrinos the multipole $F_{\nu l}$ becomes negligible for $l \geq 3$ and it is safe to truncate neglect multipoles with to $l \geq 3$. One is thus left with the following set of equations

$$\begin{aligned}
\delta'_\nu &= -\frac{4}{3}\theta_\nu - \frac{2}{3}h', && (1.7.16)\\
\theta'_\nu &= k^2\left(\frac{1}{4}\delta_\nu - \sigma_\nu\right), && (1.7.17)\\
2\sigma'_\nu &= \frac{8}{15}\theta_\nu - \frac{3}{5}kF_{\nu 3} + \frac{4}{15}(h' + 6\eta'), && (1.7.18)\\
F'_{\nu l} &= \frac{k}{2l+1}[lF_{\nu(l-1)} - (l+1)F_{\nu(l+1)}],\ \ l \geq 3. && (1.7.19)
\end{aligned}$$

1.7.2 Photons

The evolution of the photon distribution can be treated similarly to the one for massless neutrinos, but now the collision term is not negligible. Indeed, before the time of recombination, photons are tightly coupled to baryons because of Thomson scattering and some energy transfer between baryons and photons is also present afterwards during freestreaming. In both cases, the contribution of the Thomson scattering to the collision term has to be considered.

Due to scattering of electron density perturbation with wavevector $\mathbf{k}$, photons are polarized in a plane orthogonal to their propagation $\hat{n}$. It is useful to introduce the Stokes parameters $F_\gamma(\mathbf{k}, \hat{\mathbf{n}}, \tau)$ and $G_\gamma(\mathbf{k}, \hat{\mathbf{n}}, \tau)$, as the sum of the phase space densities in the two polarization states for $\mathbf{k}$ and $\hat{n}$, and their difference respectively. Their explicit expressions can be found in Ref. [35, 39].

The Boltzmann equations take the form [35]:

$$\begin{aligned}
\delta'_\gamma &= -\frac{4}{3}\theta_\gamma - \frac{2}{3}h', && (1.7.20)\\
\theta'_\gamma &= k^2\left(\frac{1}{4}\delta_\gamma - \sigma_\gamma\right) + an_e\sigma_T(\theta_b - \theta_\gamma), && (1.7.21)\\
\sigma'_\gamma &= \frac{4}{15}\theta_\gamma - \frac{3k}{10}F_{\gamma 3} + \frac{2}{15}(h' + 6\eta') - \frac{an_e}{20}\sigma_T(18\sigma_\gamma - G_{\gamma 0} - G_{\gamma 2}), && (1.7.22)\\
F'_{\gamma l} &= \frac{k}{2l+1}[lF_{\gamma(l-1)} - (l+1)F_{\gamma(l+1)}] - an_e\sigma_T F_{\gamma l},\ \ l \geq 3, && (1.7.23)
\end{aligned}$$

where n_e is the proper mean density of the electrons and $\sigma_T = 0.6652 \times 10^{-24}\text{cm}^{-2}$ the Thomson cross section. Here the hierarchy is truncated at $l = 2$ as higher multipoles are suppressed [35].

1.7.3 Cold Dark Matter

The simplest case, however, is that of cold dark matter, since it can be treated as a pressureless perfect fluid interacting with other particles only through gravity. As mentioned above, CDM can be used to define the synchronous coordinates setting by setting $\theta_c = 0$. Therefore the only equation for CDM is:

$$\delta_c' = -\frac{1}{2}h', \tag{1.7.24}$$

that could have also been derived from perturbing the continuity equation (1.1.25) with $P = 0$, since the collision term for CDM is negligible.

1.7.4 Baryons

As discussed above, baryons are tightly coupled to photons, causing an energy-momentum transfer represented by the term $an_e\sigma_T(\theta_b - \theta_\gamma)$ in Eq. (1.7.21). The Boltzmann equations for baryons then become [35]:

$$\begin{aligned} \delta_b' &= -\theta_b - \frac{1}{2}h', & (1.7.25)\\ \theta_b' &= -\mathcal{H}\theta_b + c_s^2 k^2 \delta_b - \frac{4\rho_{\gamma 0}}{3\rho_{b0}} an_e\sigma_T(\theta_b - \theta_\gamma). & (1.7.26) \end{aligned}$$

Tight-Coupling Approximation

At early times the Hubble time $t_H \approx a\tau$ is larger than the characteristic baryon-photons interaction time scale $t_{b\gamma} \approx 1/(n_e\sigma_T)$. Combining Eqs. (1.7.21) and (1.7.26) with $\mathcal{H}\theta_b + \frac{1}{3}k^2\delta_\gamma$ as a forcing term, it is easy to see that $\theta_\gamma = \theta_b$ in the $\sigma_T \to \infty$ limit. Therefore it is safe to set $\theta_\gamma = \theta_b$ at very early times deep in the radiation era. The equation governing the evolution of θ_γ is obtained by combining Eqs. (1.7.21) and (1.7.26) so to cancel the scattering terms as [40]:

$$\left(\frac{4}{3}\Omega_\gamma + \Omega_b\right)\theta_\gamma' = -\Omega_b\mathcal{H}\theta_\gamma + \frac{1}{3}\Omega_\gamma k^2\delta_\gamma. \tag{1.7.27}$$

The scattering terms can also be neglected in the equations for the density contrast of photons and baryons leading to:

$$\begin{aligned} \delta_b' &= -\theta_\gamma - \frac{1}{2}h', & (1.7.28)\\ \delta_\gamma' &= -\frac{4}{3}\theta_\gamma - \frac{2}{3}h'. & (1.7.29) \end{aligned}$$

1.8 Initial Conditions for Cosmological Perturbations

The coupled set of the Einstein-Boltzmann equations is usually solved numerically using Einstein-Boltzmann codes such as `CLASS`[1] [41, 42] or `CAMB`[2]. In order to solve them, however, a set of initial conditions for the metric and density perturbations has to be chosen. To this purpose, it is customary to define the initial conditions for cosmological perturbations deep in the radiation era after neutrino decoupling, when all the modes of observational interest are well outside the Hubble radius.

As mentioned in Section 1.3, these initial conditions are connected to the spectra of primordial perturbations produced during inflation. In the simplest single field inflationary models, initial conditions are adiabatic, in contrast to isocurvature perturbations spectrum that can be produced only if more than a single scalar field is active during inflation. In the following, I explain what is meant by adiabatic and isocurvature perturbations.

1.8.1 Adiabatic and Isocurvature Perturbations

Consider, for example, the matter-radiation plasma in the early Universe. From the entropy per matter particle is given by $\Gamma = T^3/n_m$, where n_m is the number density of matter particles, it is possible to define the entropy perturbation as:

$$\mathcal{S} \equiv \frac{\delta\Gamma}{\Gamma} = 3\frac{\delta T}{T} - \delta_m = \frac{3}{4}\delta_r - \delta_m, \tag{1.8.1}$$

where I have used the fact that $\rho_r \propto T^4$. In order for the entropy perturbation to vanish, the following condition must hold:

$$\delta_\gamma \simeq \delta_\nu \simeq \frac{4}{3}\delta_c \simeq \frac{4}{3}\delta_b. \tag{1.8.2}$$

From Eq. (1.8.1), it is possible to construct a gauge-invariant entropy perturbations:

$$\mathcal{S} = H\left(\frac{\delta P}{\dot{p}} - \frac{\delta\rho}{\dot{\rho}}\right). \tag{1.8.3}$$

---

[1] https://github.com/lesgourg/class_public

[2] https://camb.info/

Furthermore, Eq. (1.8.1) can be generalized to two barotropic fluids, each with a constant equation of state $w_i = P_i/\rho_i$, as follows [43]:

$$\mathcal{S}_{ij} = \frac{\delta_i}{1+w_i} - \frac{\delta_j}{1+w_j}. \tag{1.8.4}$$

Perturbations that satisfy the condition Eq. (1.8.2) are referred to as *adiabatic* perturbations. In fact, in the literature, they are also-called *curvature* perturbations, since they are associated to perturbations to the local geometry of the Universe (see also next subsection), or *isentropic* perturbations, since the relative entropy perturbation in Eq. (1.8.4) vanishes when Eq. (1.8.2) holds.

If instead the matter components are perturbed without a correspondent perturbation to the local geometry of the Universe, i.e. without a curvature perturbation, the perturbations are said to be *entropy* or *isocurvature* ones. Initial conditions that belong to one category or to the other lead to very distinct predictions and I can anticipate that isocurvature perturbations are very constrained by current cosmological data, see next Section.

For the reasons above, it is customary to set adiabatic initial conditions on the cosmological perturbations that read as follows (in the synchronous gauge) [35]:

$$\begin{aligned}
h &= Ck^2\tau^2, && (1.8.5)\\
\eta &= 2C - C\frac{5+4R_\nu}{6(15+4R_\nu)}k^2\tau^2, && (1.8.6)\\
\delta_c &= \delta_b = \frac{3}{4}\delta_\gamma = \frac{3}{4}\delta_\nu = -\frac{C}{2}k^2\tau^2, && (1.8.7)\\
\theta_c &= 0, && (1.8.8)\\
\theta_b &= \theta_\gamma \equiv \theta_{\gamma b} = -\frac{C}{18}k^4\tau^3, && (1.8.9)\\
\theta_\nu &= -\frac{C}{18}\frac{23+4R_\nu}{15+4R_\nu}k^4\tau^3, && (1.8.10)\\
\sigma_\nu &= \frac{4C}{3(12+R_\nu)}k^2\tau^2, && (1.8.11)\\
& && (1.8.12)
\end{aligned}$$

where C is an overall normalization constant that has to be matched to the so-called COBE normalization of the CMB power spectrum and R_ν is the neutrinos fraction $\rho_{\nu 0}/(\rho_{\nu 0} + \rho_{\gamma 0})$. However, in addition to the adiabatic mode, also four non-singular isocurvature modes exist [40]. They are called baryon isocurvature mode, CDM isocurvature mode, neutrino density isocurvature mode and neutrino velocity isocurvature mode and are not excited in single-field inflationary models, but rather require more sophisticated mechanisms involving additional fields for their generation

[43].

1.8.2 The Curvature Perturbation

As mentioned above, the names *adiabatic* and *curvature* perturbations are used interchangeably in the literature. It is the purpose of this Subsection to explicitly show why.

First of all, it is useful to relate the pressure perturbation to the density fluctuations as follows:

$$\delta P = c_s^2 \delta\rho + \delta P_{\rm nad}, \tag{1.8.13}$$

where

$$c_s^2 = \left(\frac{\delta P}{\delta\rho}\right)_\Gamma \tag{1.8.14}$$

is the adiabatic speed of sound and

$$\delta P_{\rm nad} = \left(\frac{\delta P}{\delta\Gamma}\right)_\rho \delta\Gamma \tag{1.8.15}$$

is the so-called non-adiabatic contribution to the total pressure, which, as the name says, vanishes for adiabatic perturbations. Note that when multiple fluids coexist at the same time, which is the situation needed to have non-vanishing isocurvature perturbations, the relation $c_i^2 = w_i$ no longer holds. The reason the non-adiabatic pressure is so important will become clear in a bit.

A key quantity is the so-called gauge invariant comoving curvature perturbation, defined as [44]:

$$\mathcal{R} = \Phi + \mathcal{H}\frac{\theta}{k^2} \tag{1.8.16}$$

in the Newtonian gauge and I have defined $\mathcal{H} \equiv a'/a$. Upon using the background and the perturbed Einstein equation given in the previous Sections, $\mathcal{R}$ can be also expressed as:

$$\mathcal{R} = \Phi + \frac{\mathcal{H}}{\mathcal{H}^2 - \mathcal{H}'}(\Phi' + \mathcal{H}\Psi) = \Phi + \frac{2\mathcal{H}}{a^2(\rho + P)}(\Phi' + \mathcal{H}\Psi). \tag{1.8.17}$$

$$\mathcal{R} = \Phi + \frac{\mathcal{H}}{\mathcal{H}^2 - \mathcal{H}'}(\Phi' + \mathcal{H}\Psi) = \Phi + \frac{2}{3\mathcal{H}(1 + w)}(\Phi' + \mathcal{H}\Psi). \tag{1.8.18}$$

Finally, combining the perturbed Einstein equations (1.6.18), an useful equation for the Newtonian potential Φ can be derived:

$$\Phi'' + \mathcal{H}[\Psi' + (2+3c_s^2)\Phi'] + [\mathcal{H}^2(1+2c_s^2) + 2\mathcal{H}']\Psi + k^2 c_s^2 \Psi - \frac{1}{3}(\Psi - \Phi) = 4\pi G a^2 \delta P_{\rm nad}. \tag{1.8.19}$$

and used to write the following equation governing the evolution of $\mathcal{R}$

$$\mathcal{R}' = \frac{\mathcal{H}}{P+\rho}\delta P_{\rm nad} + k^2 \frac{\mathcal{H}}{4\pi G a^2(\rho + P)}\left[\left(c_s^2 - \frac{1}{3}\right)\Psi + \frac{1}{3}\Phi\right]. \tag{1.8.20}$$

This equation clearly shows that, for adiabatic perturbations with $\delta P_{\rm nad}$, the comoving curvature perturbation $\mathcal{R}$ is conserved and its time derivative vanishes for scales outside the Hubble radius $k \ll aH$.

The latter is the reason why adiabatic perturbations are also-called curvature perturbations. Indeed they can be characterized by the comoving curvature perturbation $\mathcal{R}$, whose spectrum deep in the horizon era has to be matched to the one produced during inflation, since it is constant on super-Hubble scales.

On the other hand, since the entropy perturbation is related to the non-adiabatic pressure by $\mathcal{S} = H\delta P_{\rm nad}/\dot{P}$, if any mechanism in the primordial Universe also lays down an initial isocurvature perturbation, the situation is more complicated as it sources a time evolution for $\mathcal{R}$, even in the super-Hubble limit, as can be seen by Eq. (1.8.20).

1.9 Cosmic Microwave Background Anisotropies

During its expansion the Universe cooled down. Around $z_{\rm rec} \approx 1100$, the temperature became sufficiently low that the scattering between protons and photons in the primordial plasma stopped being efficient and the atoms started to recombine eventually leading to the decoupling of matter and radiation. The CMB that is observed in the Universe today consists in the relic photons that decoupled from the primordial plasma at that time.

As expected by the prediction of the Hot Big Bang model [30], CMB has an almost perfect blackbody thermal spectrum, with a temperature $T_{\rm CMB} = 2.7255 \pm 0.0006\,{\rm K}$ isotropic in all directions in the sky [45, 46]. As mentioned above, though, the propagation of primordial the CMB photons through the small inhomogeneities of the Universe manifest itself in temperature anisotropies over the sky, of the order $\delta T/T \equiv \Theta \sim 10^{-5}$ [47]. These anisotropies are the fingerprint of the primordial fluctuation produced in the early Universe. The CMB anisotropies were mapped with a very high precision with the WMAP experiment [48], but their most accurate

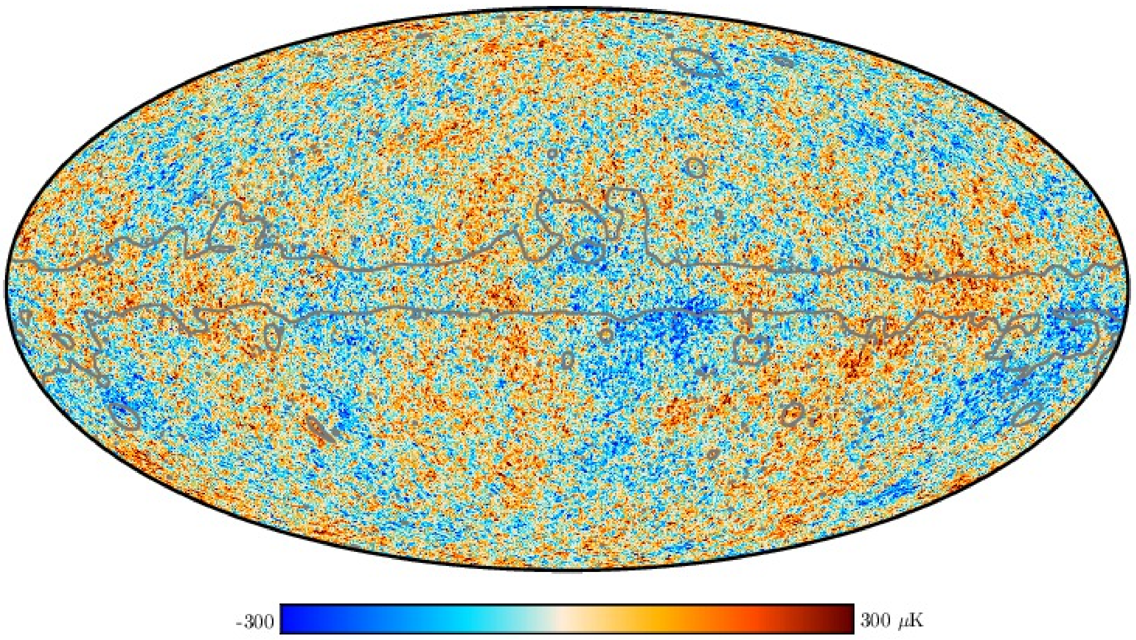

Figure 1.3: Planck 2018 SMICA temperature map. Figure taken from Ref. [9].

mapping to date is the one shown in Fig. 1.3 from the third data release (DR3) of the Planck mission in 2018 [9].

In addition to temperature fluctuations, CMB anisotropies are also polarized [14], due mainly to the Thomson scattering between baryons and photons before decoupling. However, the polarization signal is much weaker than the temperature one. This can be seen from Fig. 1.4, which shows the polarization signal is about 10% of the total temperature fluctuations for small angular scales and only 1% for large angular scales. Contrary to the usual treatment in terms of the Stoke parameters Q and U ($V = 0$ at a very good accuracy for the CMB), when it comes to CMB analysis it is more useful to consider combinations of them that are invariant under the rotation of the observation frame. These are the so-called E and B modes [39,49,50]. The former modes are scalar functions describing the part of the polarization signal which is even under parity transformations and has a non-zero correlation with temperature fluctuations, also even under parity transformations. The B-modes instead are instead odd and have a zero correlation with temperature and E modes in absence of parity violating interactions, see however [51]. The E mode polarization has been successfully measured by Planck and other CMB experiments (see below). Only upper limits exist for primordial B mode polarization, which is a unique signature of primordial gravitational waves generated during inflation or exotic models with vector modes, only foreground contributions have been measured so far.

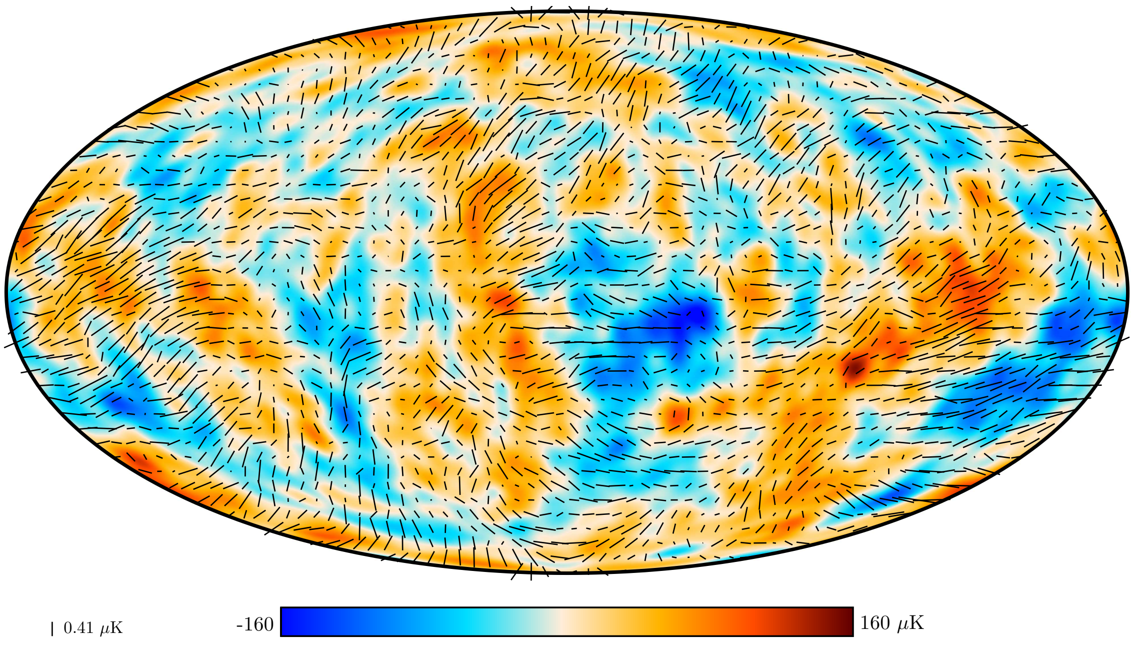

Figure 1.4: Planck 2018 polarization map. Figure taken from Ref. [9].

The information contained in maps of CMB anisotropies can be compressed in the angular power spectrum. For example, the temperature anisotropy field $\Theta(\theta, \phi) \equiv \frac{\delta T(\theta,\phi)}{T}$ of the CMB can be expanded in terms of its multipole moments [52]:

$$\Theta(\theta, \phi) = \sum_{l=1}^{\infty} \sum_{m=-l}^{l} a_{lm} Y_{lm}(\theta\phi), \tag{1.9.1}$$

where Y_{lm} are the spherical harmonic functions and the index l is related to the angular scale $\theta \sim \frac{2\pi}{l}$. If the distribution of δT is Gaussian, the multipole moments a_{lm} are fully characterized by their angular power spectrum:

$$\langle a^*_{l'm'} a_{lm} \rangle = \delta_{ll'} \delta_{mm'} C_l^{\mathrm{TT}}, \tag{1.9.2}$$

where the average is performed over an ensemble of different angular power realizations. In practice, a real observer is limited to one Universe and the spectra are computed averaging over the different $2l + 1$ independent modes:

$$C_l = \frac{1}{2l+1} \sum_{m=-l}^{m=l} |a_{lm}|^2. \tag{1.9.3}$$

The fundamental limitation to the accuracy with which the CMB angular power spectra are measured is the cosmic variance, i.e. the fact that there are only $2l + 1$

independent modes for each l, that leads to an intrinsic error on each C_l given by:

$$\Delta C_l = \sqrt{\frac{2}{2l+1}} C_l. \tag{1.9.4}$$

Similarly, also the E and B modes can be expanded in spherical harmonics and their spectra computed as:

$$C_l^{EE} \equiv \langle E_{lm}^* E_{lm} \rangle, \tag{1.9.5}$$

$$C_l^{TE} \equiv \langle a_{lm}^* E_{lm} \rangle, \tag{1.9.6}$$

$$C_l^{BB} \equiv \langle B_{lm}^* B_{lm} \rangle. \tag{1.9.7}$$

Finally, CMB photons are deflected by the large scale structure in the Universe, described by a spectrum $C_\ell^{\phi\phi}$, see Ref. [53].

The temperature and E-mode polarization spectra from the Planck DR3 are shown in Fig. 1.5 and a summary of the current measurements of all the CMB spectra by several CMB experiments is shown in Fig. 1.6.

As can be seen from Fig. 1.7, the shape of the spectrum strongly depends on the initial conditions on the cosmological perturbations discussed in Section 1.8. Comparing to the left panel of Fig. 1.5, it is possible to see by eye that the initial conditions that agree with observations are the adiabatic ones, as predicted by the simplest inflationary models. In fact, a very small fraction isocurvature perturbations, eventually correlated with adiabatic ones, is still allowed by Planck DR3 [54]. I will come back to this point in Chapter 7.

In order to qualitatively discuss the physics that lead to the shape of the angular power spectrum in Fig. 1.5 (I will focus on the temperature spectrum for simplicity), it is useful to divide the anisotropies in the CMB in primary, that were originated at the time of decoupling, and secondary ones [55], generated by the interactions of the CMB photons with the LSS in the Universe during their journey from the last scattering surface to today.

Depending on the angular scale of interest in the power spectrum, different physical effects dominate the primary anisotropies. At large angular scales the dominant effect is the Sachs-Wolfe term [56], that consists in a variation in the CMB temperature caused by photons climbing out of the gravitational potential wells and rolling down potential hills due to dark matter perturbations. In this way, hot spots in the CMB sky correspond to underdense regions and cold spots to overdense ones.

At intermediate scales, it is possible to observe the fingerprint of the acoustic oscillations of the density and velocity fluctuations of the photon-baryons coupled fluid when they are inside the Hubble radius. For adiabatic perturbations, the cosine mode of the oscillations is excited [57] and, being the angular power spectrum proportional to the the perturbations squared, its peaks correspond to the scales that were in the extrema of their oscillations at the time of recombination. These are the so-called baryon acoustic oscillations (BAO) and their imprint in the matter power spectrum [58] is an important cosmological probe, complementary to the CMB anisotropy pattern. Note that the first CMB peak, located at $l \approx 220$, corresponds to the angular scale of the Hubble radius at recombination ($\theta \sim 1^\circ$) and can be used to estimate the total density parameter.

At small scales ($\ell \geq 1000$) the amplitude of the spectrum drops because of the so-called Silk damping [59]. Indeed, the tight coupling between baryons and photons is only an approximation valid if the scattering rate of photons off electrons is infinite. This condition is not always met, because in reality photons travel a finite distance in between scatters. After a Hubble time, a photon, with a mean free path $\lambda_{\rm mfp}$, has moved a distance of order λ_D. Any perturbation on scales smaller than λ_D is expected to be washed out resulting in the damping of small angular scales in Figs. 1.5 and 1.6.

The effects of secondary anisotropies, that may also provide information on structure formation, instead manifest as follows:

- Gravitational lensing: photons are observed as coming from a slightly different direction than the original one since they are deflected by the gravitational potentials due to the large-scale distribution of matter [53].

- Sunayev-Zel'dovich effect: in passing through the cluster of galaxies, photons may interact with free electrons of the hot inter-cluster medium by Inverse Compton scattering generating a spectral distortion [60, 61].

- Integrated Sachs-Wolfe effect (ISW): the gravitational potentials vary with time, shifting the energy of the photons travelling through them [62–64]. This effect can be divided into Early ISW, often considered as part of the primary anisotropies, that happens right after decoupling when radiation density still has non-negligible effect, and Late ISW due to the late time effect of dark energy on gravitational potentials. The latter is crucial in order to investigate the nature of dark energy with large scale structure (LSS) data .

.

In the following Chapters, I will use data from the Planck DR3 to constrain parameters for different cosmologies. Unless stated otherwise, I will always use the combination of temperature, polarization, and weak lensing CMB anisotropies angular power spectra [66, 67]. The high-multipoles likelihood $\ell \geq 30$ is based on `Plik`

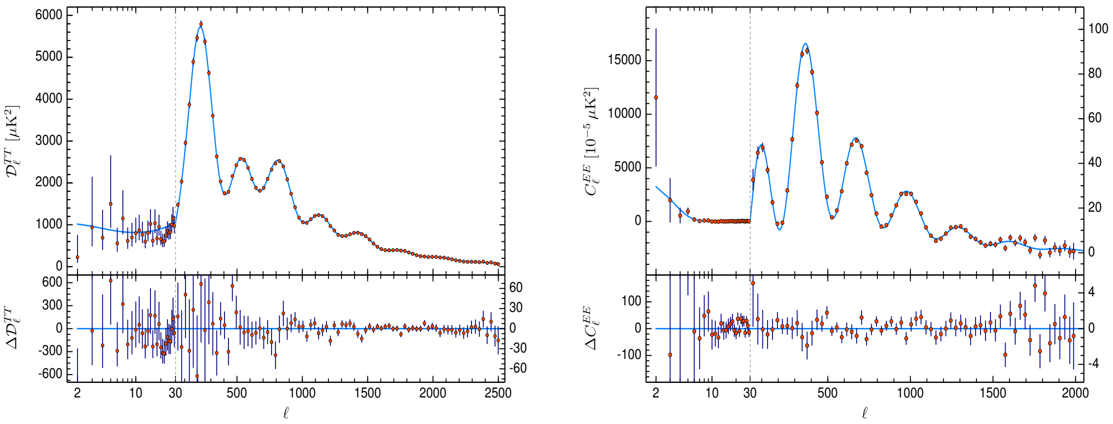

Figure 1.5: [Left] Temperature and [right] E-mode polarization normalized angular power spectrum, as measured by Planck 2018. The theoretical spectrum for the ΛCDM bestfit is plotted using a blue solid line in the bottom panels and the residuals with respect to this model are shown in the lower panels. Figure taken from Ref. [21].

likelihood. I will use the low-ℓ likelihood combination at $2 \leq \ell < 30$: temperature-only `Commander` likelihood plus the `SimAll` EE-only likelihood. For the *Planck* CMB lensing likelihood, and consider the *conservative* multipoles range, i.e. $8 \leq \ell \leq 400$. Throughout this thesis, I will refer to this dataset as P18.

1.10 The Matter Power Spectrum

As described in Section 1.4, the same linear perturbations that generate the CMB anisotropies pattern undergo gravitational instability leading to the distribution of galaxies and large scale structure in the Universe. The latter is best studied by mapping the distribution of the inhomogeneities in the Universe

In this context, one of the main observables is the matter power spectrum $P(k,\, z)$ defined as

$$\langle \delta_M(z,\, \mathbf{k})\, \delta_M^*(z,\, \mathbf{k}') \rangle \delta^3(\mathbf{k} - \mathbf{k}') P(z,\, k), \tag{1.10.1}$$

where I have defined the total matter density contrast as $\delta_M = (\delta\rho_c + \delta\rho_b)/(\rho_c + \rho_b)$.

Assuming an initial spectrum of adiabatic and Gaussian perturbations, as suggested in the previous Section, the power spectrum can be factorized into a power-law primordial contribution, describing the quantum the quantum fluctuations produced during inflation, and a transfer function describing its evolution in redshift, as

$$P(z,\, k) = \frac{2\pi^2}{k^3} A_s \left(\frac{k}{k_*}\right)^{n_s - 1} \delta_M^2(z,\, k), \tag{1.10.2}$$

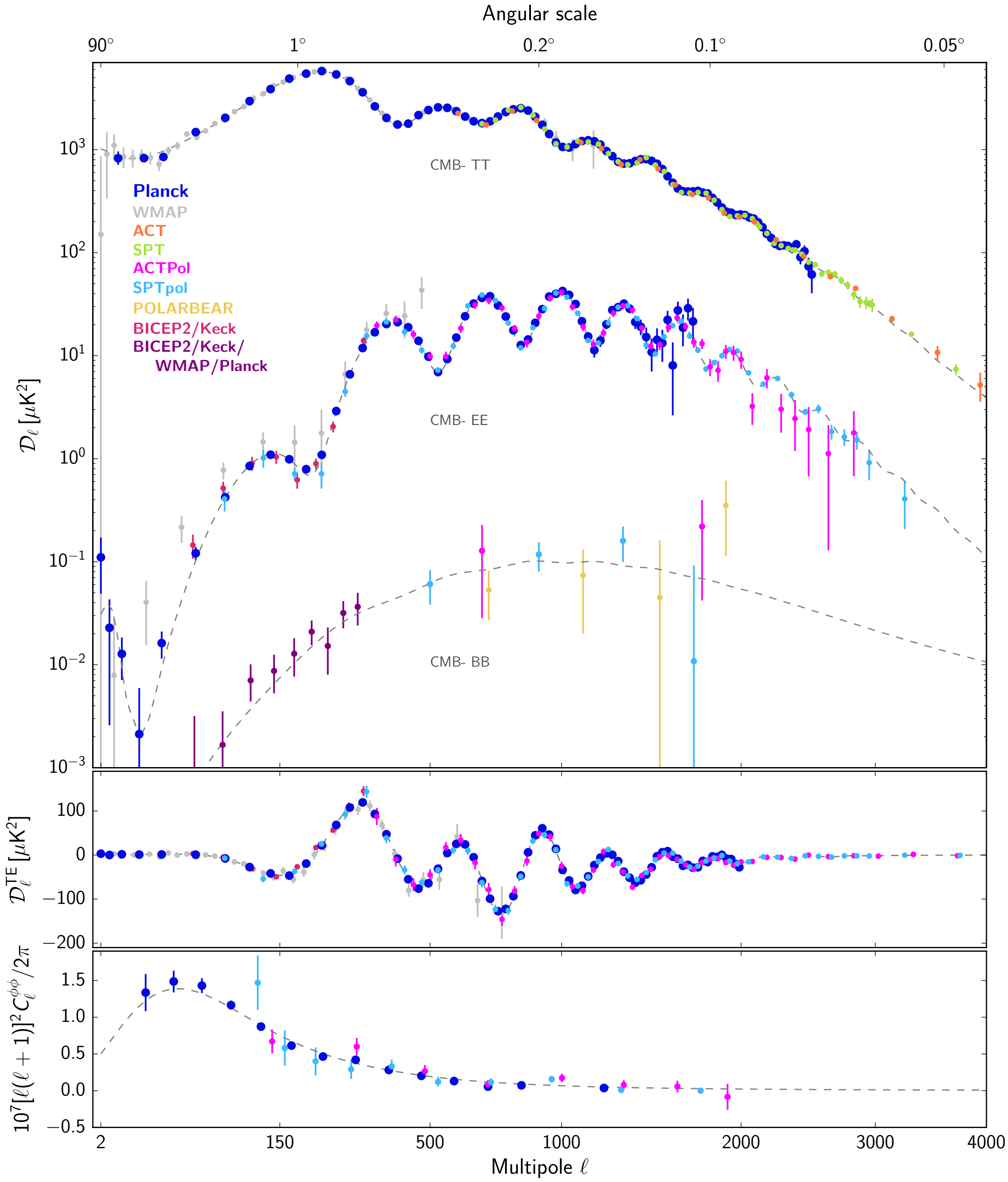

Figure 1.6: Compilation of recent CMB angular power spectrum measurements from which most cosmological inferences are drawn. The upper panel shows the power spectra of the temperature and E-mode and B-mode polarization signals, the next panel the cross-correlation spectrum between T and E, while the lower panel shows the lensing deflection power spectrum. Different colours correspond to different experiments, each retaining its original binning. For Planck, ACTPol, and SPTpol, the EE points with large error bars are not plotted (to avoid clutter). The dashed line shows the best-fit ΛCDM model to the Planck temperature, polarization and lensing data. Figure taken from Ref. [9].

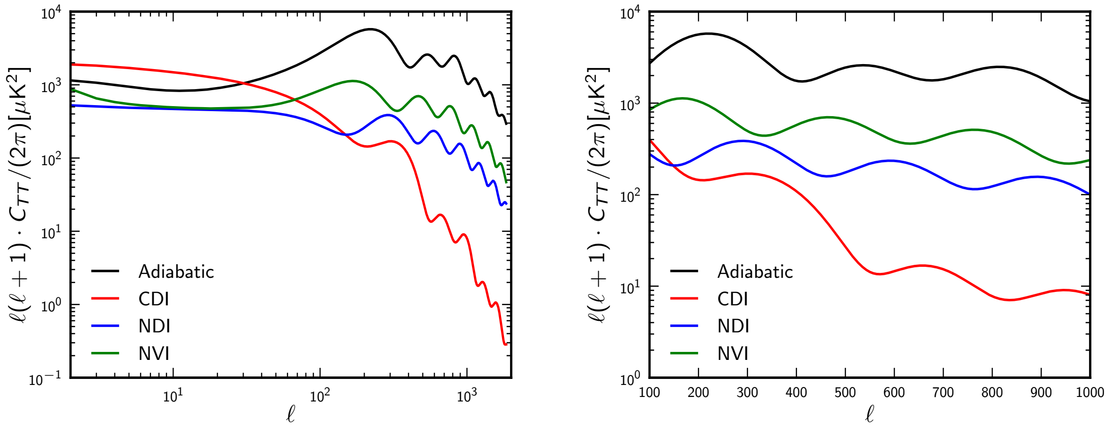

Figure 1.7: Temperature anisotropy shapes for the three isocurvature modes. [Left] The shapes of the CDM isocurvature modes, neutrino density isocurvature mode, and neutrino velocity isocurvature mode are shown together with the adiabatic mode. The modes have the same amplitude parameters ($\mathcal{P}_{\mathcal{RR}}$ for the adiabatic mode and $\mathcal{P}_{\mathcal{II}}$ for each isocurvature mode). [Right] The narrower multipole range illustrates the relative phases of the acoustic oscillations for these modes. Figure taken from Ref. [65].

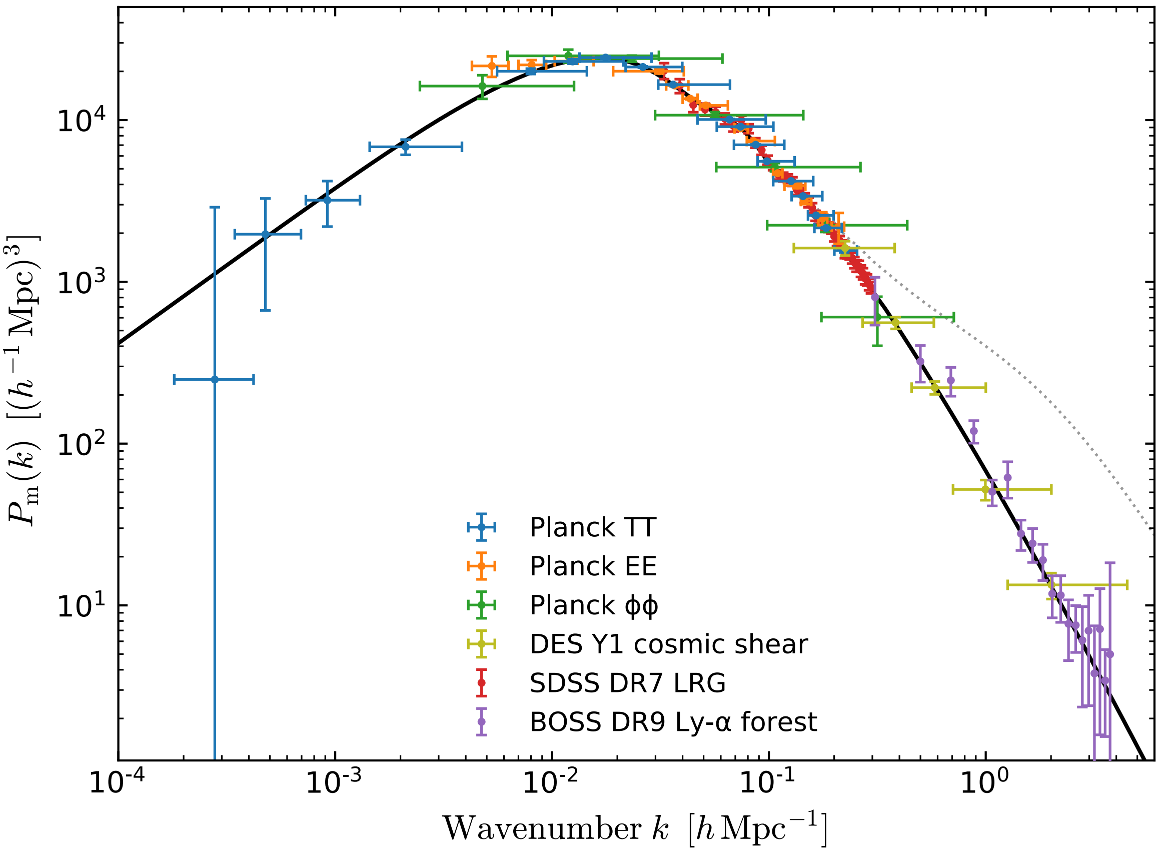

Figure 1.8: Linear-theory matter power spectrum $P(k)$ at $z = 0$ inferred from different cosmological probes (the dotted line shows the impact of non-linear clustering at $z = 0$) and ΛCDM model prediction (solid lines). Figure taken from Ref. [9].

where the pivot scale is typically $k = 0.05\text{Mpc}^{-1}$. The equation before shows how the power spectrum is sensitive to the parameters describing inflation that govern its amplitude and tilt.

In Fig. 1.8, I show the power spectrum inferred from different cosmological probes and the prediction of the ΛCDM model, which, as can be seen, fits all the data extraordinarily well. Note that the main feature of the matter power spectrum is a turnover in the growth of structure at $k \sim 2 \times 10^{-2} h\text{Mpc}^{-1}$, for scales that re-enter the horizon around the transition from radiation dominance to that of matter dominance, which makes the power spectrum sensitive to both ω_m and Ω_Λ. Another interesting feature is the small oscillatory pattern of the Baryonic Acoustic Oscillations to be discussed in the next section.

In the following Chapters, I will use the full shape of the BOSS DR12 pre-reconstructed power spectrum measurements [68]. In particular, I will consider the combination of the monopole and quadrupole of the power spectra of the three different sky-cuts CMASS NGC and CMASS SGC at effective redshift $z_{\text{eff}} = 0.57$ and LOWZ NGC at $z_{\text{eff}} = 0.32$ and follow the conventions of Refs. [69–71], where the data were analyzed with the Effective Field Theory of Large Scale Structure (EFTofLSS), for the maximum wavenumber considered ($k_{\text{max}} = 0.23\, h/\text{Mpc}$ for CMASS and $k_{\text{max}} = 0.20\, h/\text{Mpc}$ for NGC). Throughout this thesis, I will refer to this dataset as FS.

1.11 Baryon acoustic oscillations

Another observable commonly exploited to constrain cosmological parameter consists in the pattern of Baryon Acoustic Oscillations (BAO) which arises from the acoustic oscillations in the baryon-photon fluid driven by the gravitational potentials prior to recombination [72–74], see Refs. [75, 76] for reviews. These oscillations are at the origin of the acoustic peaks and troughs observed in the CMB spectra in Fig. 1.6, but the name BAO usually refers to their measurements in galaxy surveys. Their pattern in the galaxy surveys was first detected by Refs. [58, 77] is visible in Fig. 1.8 around $k \sim 0.1\, h/\text{Mpc}$ and has also been found in galaxy clusters surveys.

BAO are the archetypal example of statistical standard rule and exploit the idea that the clustering of structures may have a preferred scale that can be used to constrain the expansion history of the Universe. In practice, BAO constrain the acoustic scale ratio $D_V(z)/r_d$. In this expression r_d is the comoving size of the sound horizon at the time of baryon drag. Since its scale is around 147 Mpc, much larger than the one of virialized structures, BAO measurements are unaffected by nonlinear

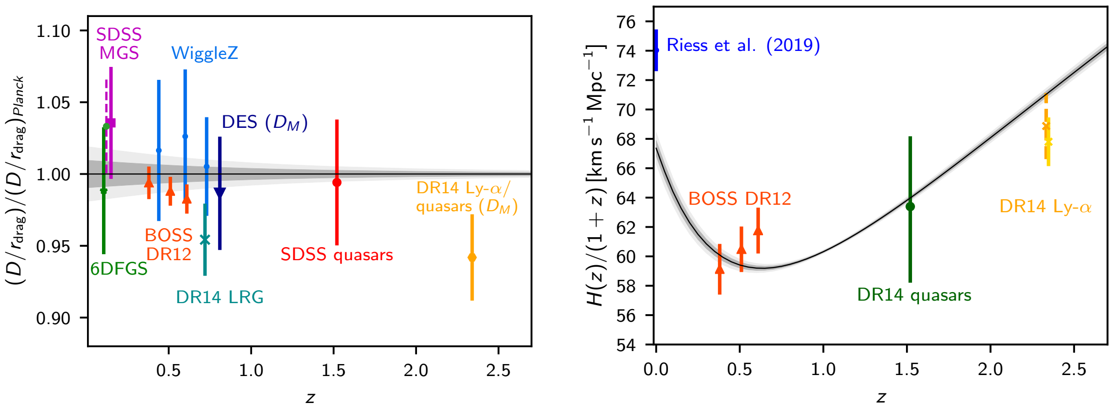

Figure 1.9: [Left] Acoustic-scale distance measurements divided by the corresponding mean distance ratio from Planck TT, TE, EE + lowE + lowT + lensing in the base-ΛCDM model. The grey bands show the 68 % and 95 % confidence ranges allowed for the ratio $D_V(z)/r_d$ by Planck TT, TE, EE + lowE + lowT + lensing (bands for D_m/r_d are very similar). [Right] Comoving Hubble parameter as a function of redshift. The grey bands show the 68 % and 95 % confidence ranges allowed by Planck TT, TE, EE + lowE + lowT + lensing in the base-ΛCDM model, clearly showing the onset of acceleration around $z = 0.6$. Figure taken from Ref. [21].

physics. The quantity $D_V(z)$ is instead given by

$$D_V(z) = \left[D_A^2(z)\frac{cz}{H(z)}\right]^{\frac{1}{3}} \tag{1.11.1}$$

and is a combination of the Hubble parameter and the comoving angular distance. I summarize the latest BAO results in the left panel of Fig. 1.9, taken from Ref. [9].

In the same way, BAO measurements along the line of sight constrain the combination $H(z)r_d$ as well. Since Planck constrains r_d to a great precision for the ΛCDM model, this can be converted to a measurement of $H(z)$, as can be seen from the right panel of Fig. 1.9.

In the following Chapters I will use BAO of the Baryon Spectroscopic Survey (BOSS) DR12 [78] post-reconstructed power spectrum measurements in three redshift slices with effective redshifts $z_{\rm eff} = 0.38, 0.51, 0.61$ [79–81], in combination with the 'small-z' measurements from 6dF [82] at $z_{\rm eff} = 0.106$ and the one from SDSS DR7 [83] at $z_{\rm eff} = 0.15$. Throughout this thesis, I will refer to this combination of BAO data as BAO. When combining these post-reconstructed this dataset with the FS data mentioned in the previous paragraph, I will only consider 'small-z' BAO and refer to the dataset as FS-BAO.

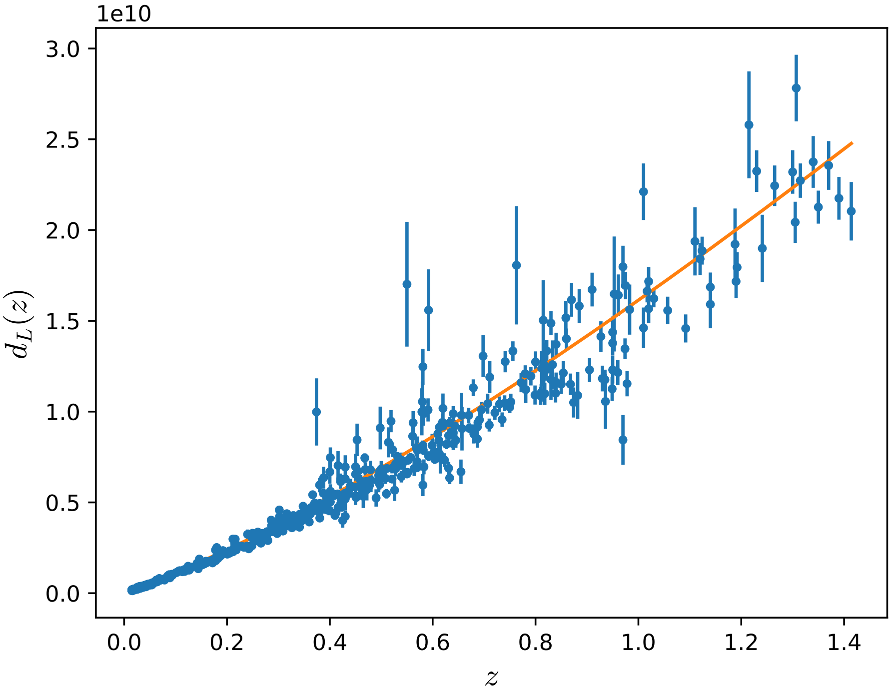

Figure 1.10: Luminosity distance of the Supernovae in the Pantheon sample of Ref. [84].

1.12 Supernovae

Although type Ia supernovae as standard candles played a central role and led to the discovery of the accelerated expansion of the Universe, they only have a little constraining power on (some of) the ΛCDM parameters compared to current CMB data. The use of Supernovae data is still important to fix the low-redshift background cosmology in theories beyond ΛCDM where dark energy is not in the form of a cosmological constant. However, the theories considered in the next Chapter show an evolution very similar to ΛCDM at late times and therefore are only slightly constrained by SN data.

In the following Chapters, I will use Pantheon supernovae dataset [84], which includes measurements of the luminosity distances of 1048 SNe Ia in the redshift range $0.01 < z < 2.3$, shown in Fig. 1.10. Throughout this thesis, I will refer to this dataset simply SN.

1.13 Summary of the ΛCDM Model

To summarize, the ΛCDM explains successfully many cosmological observations. Because of that, and because of its simplicity, it has now become the standard model of cosmology. Within this model, the Dark Matter permeating the Universe is assumed to be Cold and pressureless, and only a very small amount of Hot (or Warm) Dark Matter is allowed, and the current accelerated phase of the Universe is driven by the negative pressure of a cosmological constant Λ.

Under the assumptions of a primordial power spectrum described by a power-law, a CMB temperature of $T_\gamma = 2.7225$, an effective number of neutrinos of $N_{\rm eff} = 3.046$ and a He primordial abundance consistent with the BBN current measurement constrain the relative abundances of the ΛCDM components to be [21]

$$\begin{aligned} \Omega_M &= 0.31110 \pm 0.00561, \\ \Omega_c &= 0.2607 \pm 0.0035, \\ \Omega_b &= 0.04897 \pm 0.00064, \\ \Omega_\nu &< 0.016, \end{aligned} \tag{1.13.1}$$

at 68% CL and the curvature of the Universe is constrained to be

$$\Omega_k \leq 0.0026 \tag{1.13.2}$$

showing consistence with a flat Universe [21], that needs to be explained with an initial period of inflation before the onset of the standard Hot Big Bang history.

The quantum fluctuations produced during inflation act as seeds for CMB anisotropies and structure formation. While these quantum fluctuations can show non-Gaussian features or contain isocurvature components, in the ΛCDM model an adiabatic and Gaussian distribution of primordial fluctuations is assumed, which is easily produced by the simplest single field inflationary models. In this framework, the primordial power spectrum of the metric perturbations is described by a power-law, that can be parameterized by an amplitude A_s and a spectral index n_s computed at a reference scale, usually taken to be $k = 0.05$ Mpc^{-1} or $k = 0.002$ Mpc^{-1}.

The power of the ΛCDM model is thus that it can fit cosmological data with only an handful of parameters. These parameters are the energy densities of the baryons and CDM $\omega_b \equiv \Omega_b h^2$ and $\omega_c \equiv \Omega_c h^2$, the angular scale of the comoving sound horizon at the last scattering surface θ_*, the optical depth at reionization τ and the parameters describing the primordial power spectrum A_s and n_s.

Chapter 2

Modified Gravity and Scalar-Tensor theories

2.1 Modified gravity

The theory of General Relativity (GR), on which the ΛCDM model is based, is not only the most elegant scientific theory of gravity ever proposed, but also one of the most tested ones. More than a hundred years after Einstein first proposed his famous field equations, it is probably still the best description of cosmological and astrophysical phenomena to date. Besides governing the laws of the expanding Universe and several astrophysical observations, the recent detection of gravitational waves from coalescing confirms GR at a very precise level.

Despite its incredible success, however, there are various motivations to look at extensions or modifications to GR. For example, the nature of the dark components that are blind to electromagnetic interactions and constitute almost the totality of the energy budget of the Universe in the ΛCDM model is still unknown, and it is a natural question to ask ourselves whether it could be or not explained by a modification to the laws of GR on galactic or cosmological scales. Also, corrections to GR in the regime of strong gravity and the development of a quantum theory of gravity could resolve the Big Bang singularity or the ones associated with black holes. On one hand, all these problems have stimulated the research community to propose a wealth of theories to extend or modify GR, on the other they have triggered the search for optimal parameterizations to test such deviations from the laws of GR [85, 86].

From the historical point of view, one of the first steps in this direction was the idea of Dirac that fundamental constants might vary with time, which was later formalized by Jordan [87] and Brans and Dicke [88] in the Jordan-Brans-Dicke theory in which the Newton constant is promoted to a dynamical variable that depends on a new time-dependent scalar degree of freedom. The JBD is the prototypical version of the modern scalar-tensor (ST) theories of gravity [89], that are the focus of this thesis.

Note, however, that the addition of a new scalar degree of freedom is only one way to modify gravity, and many other possibilities like adding new vector or tensor degrees of freedom instead or breaking some of the GR assumptions as for example allowing for Lorentz-violating or Non-Local interactions, see e.g. Ref. [90] for a review.

2.2 Scalar-tensor theories

Since the JBD proposal, there has been a significant development in the scalar tensor theory of gravitation (see Ref. [91] for a recent review). In particular, it has been understood that the JBD is only the archetypal model of a much broader class of theories that involve a new scalar degree of freedom.

Indeed, from a theoretical point of view, the requirement for a theory to be classically viable is that the new scalar field, say σ, does not induce a so called Ostrogradsky instability [92]. A very simple way to avoid such instability is too require time derivatives in the Euler-Lagrange, or Klein-Gordon (KG), equation for the scalar field to be only up to second order so that only a single scalar degree of freedom is propagated. To this purpose, the Horndeski theory was constructed out [93] (see Ref. [94] for a recent review). The Horndeski Lagrangian easily satisfies the criterium above as it contains only second-order derivatives of σ. The importance of this class of ST theories for cosmology, however, has been understood only relatively recently in connection with the generalization of the Galileon symmetry [95] in curved space [96–98].

A further step towards the classification of healthy theories containing an additional scalar field was to understand that, having only up to second order time derivatives in the KG equation in not a necessary condition, albeit a sufficient one. By performing invertible disformal transformations starting from the Einstein-Hilbert action [99] (and therefore conserving the number of degrees of freedom [100]) or adding specific combinations of functions in the Lagrangian [101, 102], it is possible to propagate a single scalar degree of freedom even if the KG equation contains third order time derivatives. Theories belonging to this class, sometimes referred to as *beyond Horndeski* or *GLPV* theories [101], then paved the way to the so called Degenerate Higher Order Scalar Tensor (DHOST) theories [103–107]. Such theories are based on the idea that the absence of an extra scalar degree of freedom can also be ensured by the degeneracy of the mass matrix of the field ϕ, which leads to less restricting criterium than the ones mentioned above.

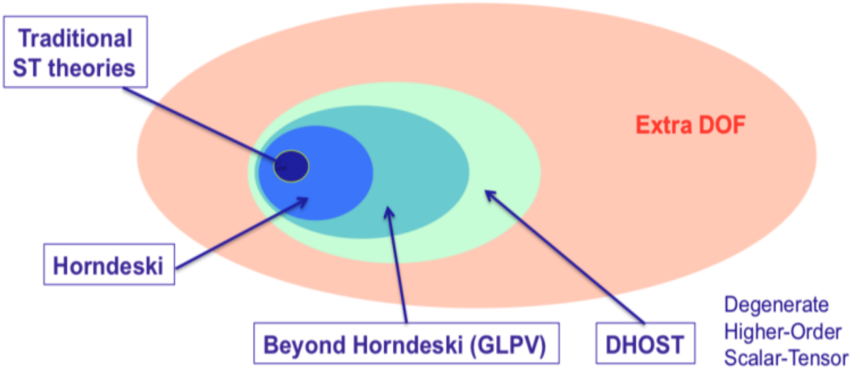

Figure 2.1: The landscape of Scalar Tensor theories. Figure taken from Ref. [108].

The corresponding Lagrangians can be written in the form

$$\begin{aligned} S[g,\sigma] \;=\; & \int d^4x\,\sqrt{-g}\,\Bigg[F_{(2)}(X,\sigma)\,{}^{(4)}R + P(X,\sigma) + Q(X,\sigma)\Box\sigma + \sum_{I=1}^{5} A_I(X,\sigma)L_a^{(2)} \\ & +F_{(3)}(X,\sigma)\,G_{\mu\nu}\sigma^{\mu\nu} + \sum_{I=1}^{10} B_I(X,\sigma)L_a^{(3)} + \mathcal{L}_m\Bigg]\;, \end{aligned} \tag{2.2.1}$$

where $X = \nabla^\mu\sigma\nabla_\mu\sigma$ and the functions $L_i^{(2)}$ and $L_i^{(3)}$ are quadratic and cubic in $\sigma_{\mu\nu}$ respectively and represent all the possible contractions of the second-order derivatives $\sigma_{\mu\nu}$ with the metric $g_{\mu\nu}$ and the scalar field gradient σ_μ. Note that these functions are not arbitrary functions of σ and X and, in order to represent a viable theory, they have to satisfy specific degeneracy conditions [108]. The landscape of viable ST theories is summarized in Fig. 2.1.

2.2.1 *Traditional* Scalar-Tensor theories

The class of *traditional* ST theories, to which the models studied in this thesis belong, is the smallest subset of DHOST theories and their Lagrangian can be obtained by setting all the functions in Eq. (2.2.1) to zero except for:

$$F_{(2)}(X,\,\sigma) = \frac{F(\sigma)}{2} \qquad \text{and} \qquad P(X,\,\sigma) = X - V(\sigma) \tag{2.2.2}$$

leading to the following action

$$S = \int \mathrm{d}^4x\sqrt{-g}\left[\frac{F(\sigma)}{2}R - \frac{g^{\mu\nu}}{2}\partial_\mu\sigma\partial_\nu\sigma - V(\sigma) + \mathcal{L}_m\right]\,. \tag{2.2.3}$$

The metric $g_{\mu\nu}$ is the physical metric to which the matter fields in $\mathcal{L}_m$ are minimally coupled and the conformal frame in which the action takes the form above, is the so called Jordan frame. By performing a conformal transformation of the form $\hat{g}_{\mu\nu} \propto F g_{\mu\nu}$ it is possible to switch to the corresponding Einstein frame in which the canonically rescaled scalar field is universally coupled to the trace of the matter energy-momentum tensor.

In principle, also the possibility of a non-canonical kinetic term is allowed, but usually that can be remapped into a canonical one by performing a field redefinition [109]. It is therefore seen that a model is completely specified by choosing a functional form for the non-minimal coupling $F(\sigma)$ and the potential $V(\sigma)$. The form of $F(\sigma)$, however, is not arbitrary since it induces some conditions that the theory needs to satisfy in order to have a stable FLRW evolution. For the action (2.2.3), indeed, there are in total three physical degrees of freedom associated with the gravity sector (that is, the metric and the σ field) [110]. In order to avoid negative kinetic energy states in the tensor sector the following equation has to be satisfied

$$F > 0\,, \tag{2.2.4}$$

and the positivity of the kinetic term in the reduced quadratic action of the scalar field perturbations leads to the second condition

$$F\,(2\,F + 3\,F_\sigma^2) > 0\,. \tag{2.2.5}$$

For the matter sector, any fluid that satisfies the null energy condition and has real sound speed will be stable. Note that the conditions (2.2.4) and (2.2.5) also ensure the positivity of the effective gravitational and cosmological Newton constants (see Eq. (2.2.19) below).

The field equations are obtained by varying the action with respect to the metric:

$$G_{\mu\nu} = \frac{1}{F(\sigma)}\left[T_{\mu\nu} + \partial_\mu\sigma\partial_\nu\sigma - \frac{1}{2}g_{\mu\nu}\partial^\rho\sigma\partial_\rho\sigma \quad - g_{\mu\nu}V(\sigma) + (\nabla_\mu\nabla_\nu - g_{\mu\nu}\Box)F(\sigma)\right]. \tag{2.2.6}$$

The Einstein trace equation results:

$$R = \frac{1}{F}\left[-T + \partial_\mu\sigma\partial^\mu\sigma + 4V + 3\Box F\right], \tag{2.2.7}$$

where T is the trace of the energy-momentum tensor. The Klein-Gordon (KG) equation can be obtained varying the action with respect to the scalar field:

$$-\Box\sigma - \frac{1}{2}F_{,\sigma}R + V_{,\sigma} = 0, \tag{2.2.8}$$

and substituting the Einstein trace equation one obtains:

$$-\Box\sigma\left(1 + \frac{3}{2}\frac{F_{,\sigma}^2}{F}\right) + V_{,\sigma} - 2\frac{VF_{,\sigma}}{F} + \frac{F_{,\sigma}}{2F}\left[T - \partial_\mu\sigma\partial^\mu\sigma\left(1 + 3F_{,\sigma\sigma}\right)\right] = 0\,. \tag{2.2.9}$$

If I specify instead to a flat FLRW metric, as in Eq. (1.1.8), the Friedmann and the KG equations reduce to:

$$3H^2F = \rho + \frac{\dot\sigma^2}{2} + V(\sigma) - 3H\dot F \tag{2.2.10}$$

$$= \rho + \rho_\sigma, \tag{2.2.11}$$

$$-2\dot H F = \rho + p + \dot\sigma^2 + \ddot F - H\dot F \tag{2.2.12}$$

$$= (\rho + p) + \rho_\sigma + p_\sigma. \tag{2.2.13}$$

$$\ddot\sigma + 3H\dot\sigma = \frac{F_\sigma}{2F + 3F_\sigma^2}\left[\rho - 3p + 4V - 2\frac{F\,V_\sigma}{F_\sigma} - \left(1 + 3F_{\sigma\sigma}\right)\dot\sigma^2\right]. \tag{2.2.14}$$

The above equations lead to the straightforward associations:

$$\rho_\sigma = \frac{\dot\sigma^2}{2} + V(\sigma) - 3H\dot F \tag{2.2.15}$$

and

$$p_\sigma = \frac{\dot\sigma^2}{2} + V(\sigma) + \ddot F + 2H\dot F \tag{2.2.16}$$

where in the equation for p_σ I have explicitly substituted the KG equation. It is possible to recover an expression for the dark energy (DE) density parameter dividing ρ_σ for the quantity $3H^2F$ which represents the critical density.

Alternatively, it is also convenient to define new density parameters in a framework which mimics Einstein gravity at present and satisfy the conservation law $\dot{\rho}_{\rm DE} + 3H(\rho_{\rm DE} + p_{\rm DE}) = 0$ [110, 111]:

$$\begin{aligned} \rho_{\rm DE} &= \frac{F_0}{F}\rho_\sigma + (\rho_m + \rho_r)\left(\frac{F_0}{F} - 1\right) , && (2.2.17) \\ p_{\rm DE} &= \frac{F_0}{F}p_\sigma + p_r\left(\frac{F_0}{F} - 1\right) . && (2.2.18) \end{aligned}$$

The effective parameter of state for DE can be defined as $w_{\rm DE} \equiv p_{\rm DE}/\rho_{\rm DE}$.

Because of the non-minimal coupling, the Newton constant in the Friedmann equations is replaced by $G_N := (8\pi F)^{-1}$ that now varies with time. This has not to be confused with the effective *gravitational constant* that regulates the attraction between two test masses and is measured in laboratory experiments, which is instead given by [111]:

$$G_{\rm eff} = \frac{1}{8\pi F}\left(\frac{2F + 4F_{,\sigma}^2}{2F + 3F_{,\sigma}^2}\right) . \qquad (2.2.19)$$

The deviations from general relativity (GR) can also be parameterized by means of the so-called Post-Newtonian (PN) parameters [85] where the metric is expanded in powers of the gravitational potential Φ. For the theories described by Eq. (2.2.3), only the parameters $\gamma_{\rm PN}$ and $\beta_{\rm PN}$ differ from GR predictions, for which they both equal unity. In terms of these parameters the line element can be expressed as:

$$\mathrm{d}s^2 = -(1 + 2\Phi - 2\beta_{\rm PN}\Phi^2)\mathrm{d}t^2 + (1 - 2\gamma_{\rm PN}\Phi)\mathrm{d}x_i \mathrm{d}x^i, \qquad (2.2.20)$$

where the only non-zero PN parameters are given by the following expressions [111]:

$$\begin{aligned} \gamma_{\rm PN} &= 1 - \frac{F_{,\sigma}^2}{F + 2F_{,\sigma}^2}, && (2.2.21) \\ \beta_{\rm PN} &= 1 + \frac{F F_{,\sigma}}{8F + 12F_{,\sigma}^2}\frac{\mathrm{d}\gamma_{\rm PN}}{\mathrm{d}\sigma}. && (2.2.22) \end{aligned}$$

Linear perturbations

ST theories also modify the equations governing the evolution of cosmological perturbations. As in Chapter 1, I study linear fluctuations around the FLRW metric in the synchronous gauge and follow the conventions of Ref. [35]. Here, however, I also have to consider the scalar field perturbation $\delta\sigma$:

$$h^S_{ij} = \int \mathrm{d}^3k\, e^{i\vec{k}\cdot\vec{x}} \Big[\hat{k}_i \hat{k}_j\, h(\vec{k},\tau) + \left(\hat{k}_i \hat{k}_j - \frac{1}{3}\delta_{ij} \right) \eta(\vec{k},\tau) \Big], \tag{2.2.23}$$

$$\delta\sigma = \int \mathrm{d}^3k\, e^{i\vec{k}\cdot\vec{x}} \delta\sigma(\vec{k},\tau). \tag{2.2.24}$$

The modified Einstein equations at first order for scalar perturbations are:

$$\begin{aligned}
&\frac{k^2}{a^2}\eta - \frac{1}{2}H\dot{h} = -\frac{1}{2F}\left[\delta\rho + \dot{\sigma}\delta\dot{\sigma} + V_{,\sigma}\delta\sigma - \frac{F_{,\sigma}}{F}\left(\rho + \frac{\dot{\sigma}^2}{2} + V - 3H\dot{F}\right)\delta\sigma - \frac{k^2}{a^2}\delta F + \frac{1}{6}\dot{h}\dot{F}\right], \\
&\frac{k^2}{a^2}\dot{\eta} = \frac{1}{2F}\left[\sum_i (\rho_i + p_i)\theta_i + k^2\left(\dot{\sigma}\delta\sigma + \delta\dot{F} - H\delta F\right)\right], \\
&\ddot{h} + 3H\dot{h} - 2\frac{k^2}{a^2}\eta = -\frac{3}{F}\left[p + \dot{\sigma}\delta\dot{\sigma} - V_{,\sigma}\delta\sigma - \frac{F_{,\sigma}}{F}\left(p + \frac{\dot{\sigma}^2}{2} - V + \ddot{F} + 2H\dot{F}\right)\delta\sigma \right. \\
&\qquad\qquad \left. + \frac{2}{3}\frac{k^2}{a^2}\delta F + \delta\ddot{F} + 2H\delta\dot{F} + \frac{1}{3}\dot{h}\dot{F}\right], \\
&\ddot{h} + 6\ddot{\eta} + 3H(\dot{h} + 6\dot{\eta}) - 2\frac{k^2}{a^2}\eta = -\frac{3}{F}\left[\sum_i (\rho_i + p_i)\sigma_i + \frac{2}{3}\frac{k^2}{a^2}\delta F + \frac{\dot{F}}{3}(\dot{h} + 6\dot{\eta})\right],
\end{aligned} \tag{2.2.25}$$

where all perturbations are considered in the Fourier configuration. The quantities θ_i and σ_i represent the velocity potential and the anisotropic stress, respectively[1]. It can be seen from the last of these equations that the coupling function acts also as a source for the anisotropic stress.

The perturbed Klein-Gordon equation is:

$$\begin{aligned}
\delta\ddot{\sigma} = &-\delta\dot{\sigma}\left[3H + \frac{2(1+6\xi)\xi\sigma\dot{\sigma}}{F + 6\xi^2\sigma^2}\right] - \delta\sigma\left\{\frac{k^2}{a^2} + \frac{FV_{,\sigma,\sigma}}{F + 6\xi^2\sigma^2} - \frac{2\xi\sigma V_{,\sigma}}{F + 6\xi^2\sigma^2}\left[1 + \frac{F(1+6\xi)}{F + 6\xi^2\sigma^2}\right] \right. \\
&\left. + \frac{\xi}{F + 6\xi^2\sigma^2}\left[1 - \frac{2(1+6\xi)\xi\sigma^2}{F + 6\xi^2\sigma^2}\right]\Big[(1+6\xi)\dot{\sigma}^2 - 4V + (3p - \rho)\Big]\right\} - \frac{(3\delta p - \delta\rho)\,\xi\sigma}{F + 6\xi^2\sigma^2} - \frac{1}{2}\dot{h}\dot{\sigma}.
\end{aligned} \tag{2.2.26}$$

---

[1] Note that here σ_i has nothing to do with the initial condition on the scalar field σ that I will use in the next Chapters

2.3 Observational constraints on Scalar-Tensor theories

A snapshot of the current observational is given in Fig. 2.2, which is reproduced from Ref. [112]. In the plots, the gravitational forces are parameterized by the gravitational potential $\varepsilon \equiv \Phi = GM/r$ and the space curvature $\xi \equiv GM/r^3$, where M and r are the mass and the radius of a spherical object respectively. The plots show that gravity has been currently tested mostly in the large curvature regime with solar system and binary pulsar experiments operate, but that there is still a lot to explore on lower curvature scales[1]. At those scales, the plot shows that the relevant observations are cosmological ones. The constraints on ST theories that can be derived using cosmological data will be discussed in the following chapter and, in the following, I discuss the very tight constraints on ST theories by a series of other observations. Specifically I consider constraints from the observation of a neutron star merger and its optical counterpart, from Solar System and laboratory experiments and from Big Bang Nucleosynthesis.

Before going ahead, note also that Fig. 2.2 clearly shows the importance of studying gravity in different regimes. Indeed, many MG theories develop so called screening mechanisms that hide the modification to gravity in dense environments or small scales [113–116], but are not active on large cosmological scales (see Ref. [117] for a review). Only testing gravity on as much scales as possible we can hope to constrain possible deviations from GR in the optimal way.

2.3.1 Constraints from the speed of gravitational waves

A major step forward in constraining ST theories of gravity has been made thanks to the observation of a neutron star merger GW170817 and of its optical counterpart GRB170817A, on August 17, 2017 [118–121]. Indeed, the follow up of the gravitational event, i.e. a short gamma ray burst, was seen only 1.74 ± 0.05 s later by Fermi and the International Gamma-Ray Astrophysics Laboratory, allowing to constrain the speed of gravitational waves c_g to be essentially the same as the speed of light, with a precision of [118]:

$$-3 \cdot 10^{-15} \leq c_g/c - 1 \leq 7 \cdot 10^{-16} \,. \tag{2.3.1}$$

The crucial point here is that ST theories described by Eq. (2.2.1) can modify the speed of the propagation of gravitational waves. The evolution of linear, transverse-

---

[1] Note that the definition of ε and ξ has to be changed on such scales for which speaking of spherical objects is meaningless [112].

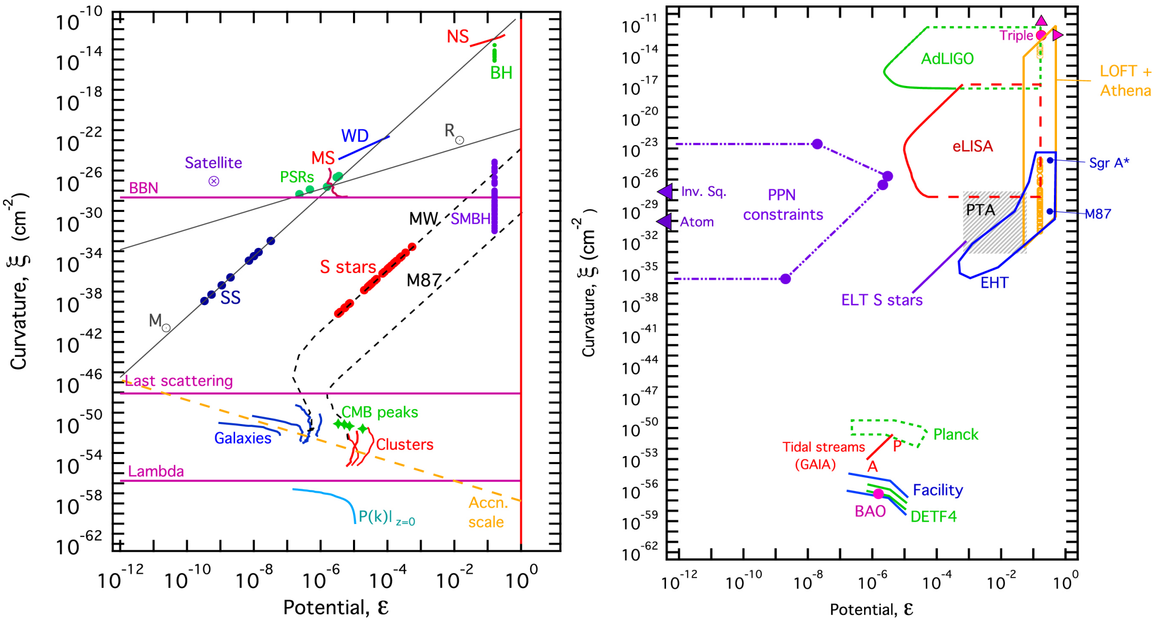

Figure 2.2: Left: A parameter space for gravitational fields. Right: The experimental version of the parameter space. See Ref. [112] for details. The horizontal lines in the left figure indicate the background curvature of the Universe at Big Bang Nucleosynthesis (BBN) and Last scattering, and the curvature associated with Λ. Some of the label abbreviations are: SS=planets of the Solar System MS=Main Sequence stars, WD=white dwarfs, PRSs=binary pulsars, NS=Neutron stars, BH= stellar mass black holes, MW=the Milky Way, SMBH=supermassive black holes. PPN= Parameterized Post-Newtonian regime, Inv.Sq.=laboratory tests of the inverse square law of the gravitational force, Atom=atom interferometry experiments, EHT=Event Horizon Telescope, ELT=the Extremely Large Telescope, DEFT4=a hypothetical stage 4 experiment of dark energy, Facility=a futuristic large radio telescope such as the Square Kilometer Array. Figure taken from Ref. [112].

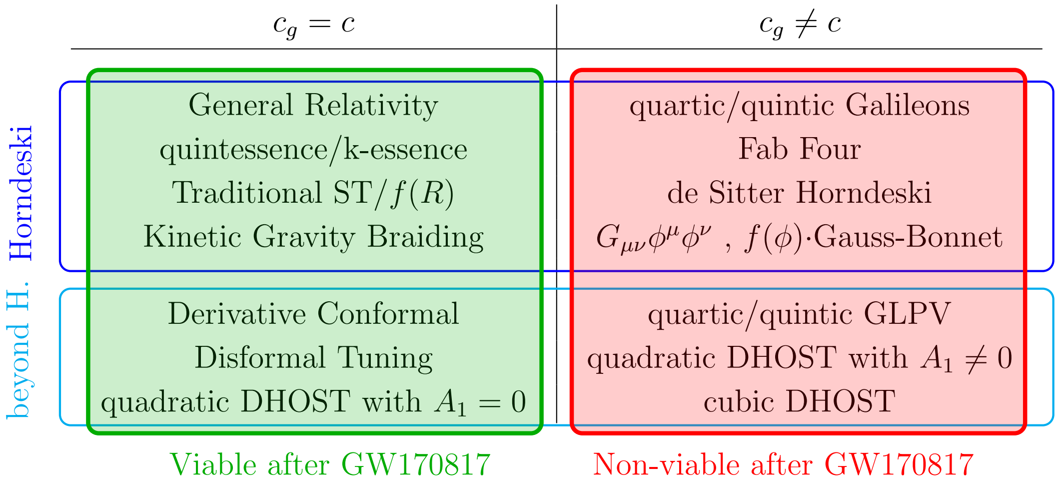

Figure 2.3: Summary of the viable (left) and non-viable (right) scalar-tensor theories after GW170817. Only simple Horndeski theories, $G_{4,X} \approx 0$ and $G_5 \approx$ constant, and specific beyond Horndeski models, conformally related to $c_g = 1$ Horndeski or disformally tuned, remain viable. Figure adapted from Ref. [122].

traceless tensor perturbations over a cosmological background is governed by the following equation [123]:

$$\ddot{h}_{+,\times} + (3 + \alpha_M)H\dot{h}_{+,\times} + (1 + \alpha_T)k^2 h_{+,\times} = 0\,, \tag{2.3.2}$$

where both $\alpha_M(\sigma)$ and $\alpha_T(\sigma)$ depend on the scalar field σ and their explicit expressions in terms of the Horndeski functions is given in the Appendix of Ref. [123]. Although the former term contributes to the damping of gravitational waves, the latter is a genuine modification to their speed of propagation which becomes $c_g^2 = 1 + \alpha_T$ and can therefore differ from the speed of light, which is equal to unity in our conventions.

As shown in Fig. 2.3, using Eq. (2.3.1) it is therefore possible to rule out a number of models that would otherwise be perfectly viable for other cosmological observations [122, 124–126] (see however Ref. [127] for a more critical take on this point). The importance of GW170817 is astounding, as it was the first case ever when it has been possible to rule out so many MG theories with a single event. Importantly, traditional ST theories, for which $\alpha_T = 0$ and $\alpha_M = \dot{F}/HF$, survive this constraint and are still viable after GW170817.

2.3.2 Constraints from Big Bang Nucleosynthesis

Theories where the Newton constant varies with time also modify the light elements production in BBN. The efficiency of the latter, which is the result of nuclear and weak reaction, is affected by the modification to the expansion rate of the Universe induced by a time-varying $G_N(t)$ (or equivalently $G_{\rm eff}(t)$).

Therefore, if at early times $G_N(t_{\mathrm{BBN}}) \neq G_N(t_0)$, there would be a variation of the light element abundances with respect to the standard BBN predictions. Using a parameterized form of ΔG_N, for which it depends on time through a monotonic power law $\propto t^{-\alpha}$, BBN data where used in Refs. [128, 129], to derive a constraint of $\Delta G_N/G_N = (G_N(t_{\mathrm{BBN}}) - G_N(t_0))/G_N(t_0) = 1.01^{0.20}_{-0.16}$ at a 68% CL level. A tighter constraint was also derived more recently in Ref. [130], which found $\Delta G_N = 0.02 \pm 0.06$.

2.3.3 Constraints from Solar System experiments

Among the most stringent constraints on the deviations from GR, belong the ones from Solar System tests [85]. Constraints on γ_{PN} can be derived from bounds on the deflection angle and on the time delay of light. Indeed, a light ray that grazes the surface of the sun is deflected by an angle

$$\delta\theta \simeq \frac{1+\gamma_{\mathrm{PN}}}{2} 1.7505'', \tag{2.3.3}$$

that makes it possible to constrain the quantity γ_{PN}. The tightest constraint on the deflection of light comes from the very long baseline interferometry (VLBI) observation of quasars and radio galaxies that are primary used to monitor the rotation of the Earth. Since they are sensitive to the deflection of light over almost the entire celestial sphere they lead to the optimal constraint $\gamma_{\mathrm{PN}} - 1 = (-2 \pm 3) \times 10^{-4}$ [131,132] as of 2010 (see also Ref. [133] for a slightly older constraint).

However, the tightest constrain on γ_{PN} comes from measurements of the time delay of light. A photon sent across the solar system past some object and returned to the Earth experiences a non-Newtonian time delay that depends again on the combination $(\gamma_{\mathrm{PN}} + 1)/2$ as (say it passes past the Sun, which is distant from us r, at the closest distance of d) [85]:

$$\delta t \simeq \frac{1+\gamma_{\mathrm{PN}}}{2} \left[240 - 20 \ln\left(\frac{d^2}{r}\right)\right] \mu s. \tag{2.3.4}$$

Using the Doppler tracking of the Cassini spacecraft that was on its way to Saturn, the bound $\gamma_{\mathrm{PN}} - 1 = (2.1 \pm 2.3) \times 10^{-5}$ was derived [134], almost an order of magnitude tighter than the ones from light deflection.

Constraints on β_{PN} are instead derived using the observation of the anomalous 43 arcseconds perihelion shit of Mercury's orbit. The advanced per orbit $\Delta\omega$ is given by [85]:

$$\Delta\omega_{\frac{6\pi m}{p}} \left[\frac{2 + 2\gamma_{\mathrm{PN}} - \beta_{\mathrm{PN}}}{3} \frac{\eta}{6} (2\alpha_1 - \alpha_2 + \alpha_3 + 2\zeta_2) + \frac{J_2 R^2}{2mp})\right] \tag{2.3.5}$$

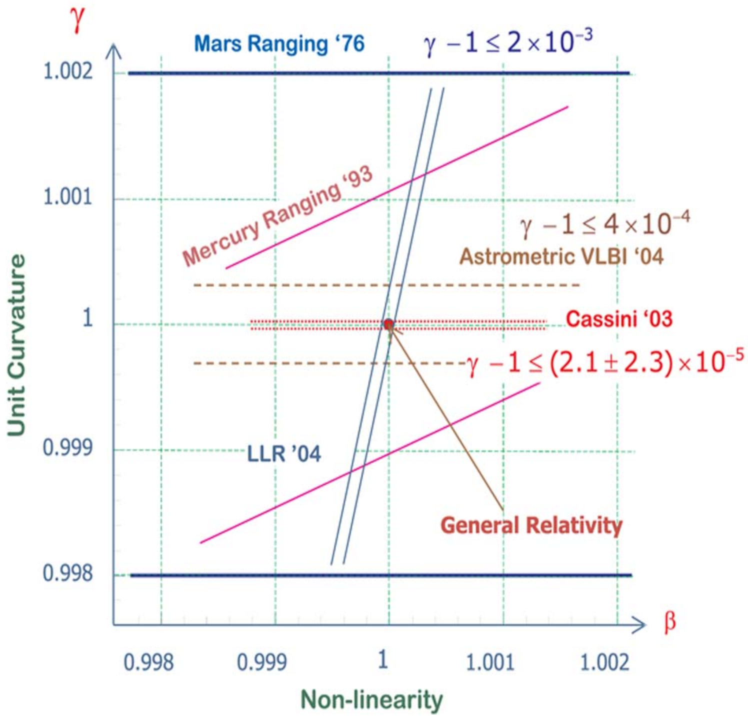

Figure 2.4: Constraints on the PN parameters $\gamma_{\rm PN}$ and $\beta_{\rm PN}$. Figure taken from Ref. [135].

but now it includes, in addition to relativistic PN contributions, also the ones from a possible Sun quadrupolar moment. In Eq. (2.3.5), m is the sum of the masses of the two bodies m_1 and m_2 and η is their reduced mass, p is the semi-latus rectum of the orbit, R is the mean radius of the oblate body and J_2 measures its quadrupole moment, whereas the αs and ζ_2 are additional PN parameters that are equal to zero in the ST theories under consideration. Therefore, unlike the deflection of light or its time-delay, here the measurement depends on the combination of $\gamma_{\rm PN}$ and $\beta_{\rm PN}$ so a bound on $\gamma_{\rm PN}$ has to be assumed. Adopting the one above from the Cassini spacecraft and using the latest inversions of helioseismology data that give $J_2 = (2.2 \pm 0.1) \times 10^{-7}$ [136, 137], it is possible to constrain $\beta_{\rm PN} - 1 = (4.1 \pm 7.8) \times 10^{-5}$ [85].

The limits in the plane $\gamma_{\rm PN} - \beta_{\rm PN}$ are shown in Fig. 2.4. As I will show in the next Chapters, and can be understood from Eqs. (2.2.21) and (2.2.22), these very tight bounds on the deviations from GR translate into bounds on the allowed parameters that describe the non-minimal coupling $F(\sigma)$.

2.3.4 Constraints from Laboratory experiments

Finally, another stringent constrain on ST theories comes from the very precise measurement of the Newton constant in laboratory constraints. Although it is not the

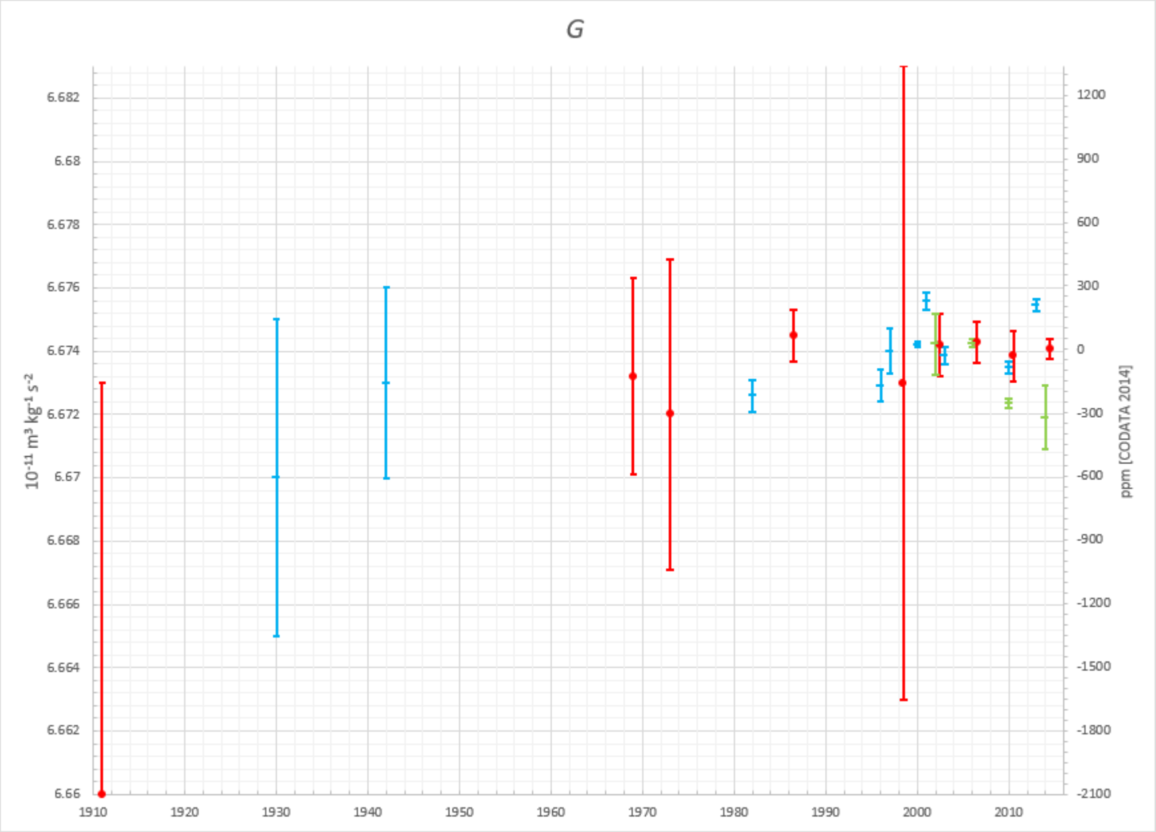

Figure 2.5: Timeline of measurements and recommended values for G since 1900: values recommended based on a literature review are shown in red, individual torsion balance experiments in blue, other types of experiments in green. Figure taken from Wikipedia.

main purpose of this thesis, note that laboratory constraints are also a powerful probe of screening mechanisms. [138]

The modern techniques used to measure are atom interferometry and very precise torsion balances. A timeline of measurements of G is shown in Fig. 2.5, where also the standard uncertainty is shown. The current value recommended by CODATA is $G = 6.67430(15) \times 10^{-11}$ m^3 kg^{-1} s$^{\cdot 2}$, with a standard uncertainty of 22 ppm. However, note that different experiments are in tension on the 4th figure after the comma, so there is currently an uncertainty (in units where $G = 1$) of 10^{-4}. This is the uncertainty that I would quote throughout this thesis. It is important to stress that, in the context of ST theories, the quantity that has to be confronted with laboratory tests is G_{eff} and not G_N, as it is the former that governs the interaction between test masses [110, 111].

Chapter 3

Cosmological tensions and new physics

3.1 The H_0 tension

As anticipated in the previous Chapter, one of the most challenging problems that Cosmology faces nowadays is to explain the so called H_0 tension.

The accurate measurement of the CMB anistropies has permitted the determination of the six ΛCDM parameters at a very precise level. In particular, the Hubble constant, or H_0, which is the normalization of the Hubble parameter measuring the rate of expansion of the Universe, is tightly constrained by the latest Planck CMB temperature, polarization and lensing data to $H_0 = 67.36 \pm 0.54$ km s^{-1}Mpc^{-1} [21]. However, this determination is not strictly speaking a measurement of the aforementioned quantity. Indeed, it is inferred from the CMB data assuming the underlying cosmological model to be the ΛCDM one.

Since the CMB photons started to travel freely in the Universe after recombination at redshift of the order $z_r \sim 1100$, CMB measurements are usually referred to as *Early* time measurements, as opposed to local measurements at very recent redshifts that are referred to as *Late* time ones. Contrary to early time measurements of H_0, late time ones are model independent. The most important example of the latter is the measurement obtained by calibrating the distance ladder using the luminosity of Cepheid variable stars performed by the SH0ES team [161].

With the first release by Planck, where a value for the Hubble constant of $H_0 = 67.3 \pm 1.2$ km s^{-1}Mpc^{-1} [162] was inferred, it was understood that it was in tension with the SH0ES measurement of $H_0 = 73.8 \pm 2.4$ km s^{-1}Mpc^{-1} [161]. At the time, however, the SH0ES measurement was not the only one in tension with Planck results, as another late time determination of H_0 by Carnegie Hubble Program based on the mid-infrared calibration of the Cepheid distance scale based on observations with the Spitzer Space Telescope, that is $H_0 = 74.3 \pm 2.5$ km s^{-1}Mpc^{-1} [154].

Ever since then, any CMB data used to calibrate the sound horizon and subsequently the BAO, like the new Planck releases or the ones from the Atacama Space

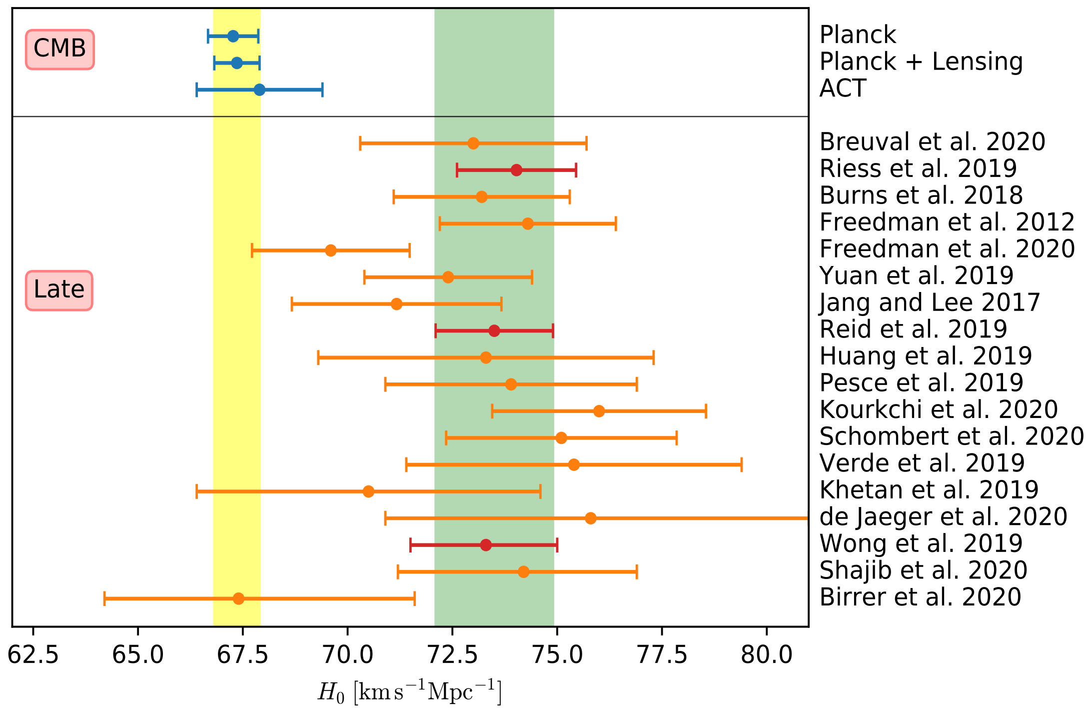

Figure 3.1: Values of H_0 together with their 68% CL errors from CMB and Late time measurements in Refs. [139–160].

Telescope or the South Space Telescope have lead to values of H_0 consistent that were consistent among each other, but in tension with SH0ES measurements. It is important to stress that, CMB measurements were not the only ones leading to such a discrepancy. Indeed, also results from the DES collaboration using also BAO and BBN data lead to $H_0 = 67.2^{+1.2}_{-1.0}$ km s^{-1}Mpc^{-1} [140] and at the same time other local measurements point to a value of H_0 closer to the one measured by the SH0ES team. As of the time I am writing this thesis, the situation is the one shown in Fig. 3.1, where I show a series of early and late time measurements of H_0 performed by different experiments using several and more refined techniques.

It is clear that, as the time passes, more measurements, many of which are independent on the others, accumulate casting doubts on the possibility that systematics is the cause of the tension. Indeed, although revisions of the determination of the Hubble rate based on the Cepheid calibration [163–165], from SNe Ia calibrated using the tip of the red giant branch method [153] point to values which are slightly smaller, i.e. 70 km s^{-1}Mpc^{-1}, it is unclear whether systematic errors alone can explain the tension [152, 166].

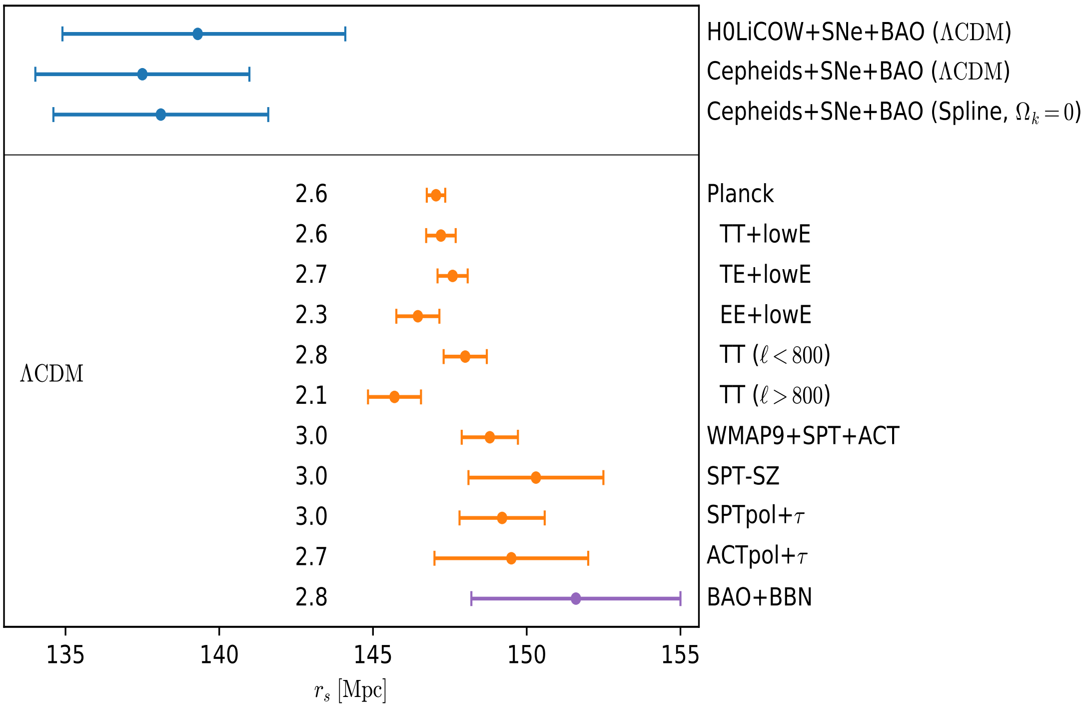

Figure 3.2: ΛCDM determination of the sound horizon from existing data (solid symbols) and forecasts (open symbols) from Ref. [177]. The plot is reproduced from the code in Ref. [177].

3.2 How to solve the H_0 tension

If the H_0 tension is taken at face value and under the assumption that there are no unaccounted systematic errors that can explain it, then it points to the need of new physics beyond the ΛCDM model. When it comes to build physical models that aim at a large H_0 there are mainly two possibilities. The first one is to introduce a late time modification to the expansion history of the Universe. Examples of such late time solutions are Refs. [167–176]. However, these models are tightly constrained by late-time observational data, especially those from BAO. Besides, some of the late time solutions lead to fast wiggles in the evolution of the Hubble parameter $H(z)$ in the region of the three BOSS BAO redshits, which might invalidate the reduction of BOSS data from a near-continuum range of redshifts to the constraints that are publicly available at three discrete redshifts.

A second solution is instead to introduce new physics around the redshift of recombination. This is probably the most followed route and the one I am going to discuss here in more details.

A quantity that is of crucial important is the comoving sound horizon, which is defined as:

$$r_s = \int_{z_d}^{\infty} dz' \, \frac{c_s}{H(z')} \tag{3.2.1}$$

where z_d is the end of the baryon drag epoch and $c_s(z)$ is the sound speed of baryons (1.8.14). This quantity represents the distance that the sound waves in the primordial plasma traveled from the Big-Bang at $z = \infty$ to z_d. Note that r_s is closely related to the same quantity evaluated at the time of the last scattering z_*, at which the optical depth becomes equal to one. The latter, which I denote as r_s^*, is about 2% smaller than r_s and is the one relevant for CMB power spectra, whereas r_s is relevant for BAO. However, their difference is nearly model independent and so both quantities can be used for the following arguments.

The reason r_s is so important is that the H_0 tension can be recast into a tension on r_s [177,178]. In fact, low redshift probes as BAO constrain the product $r_s H_0$ to be constant relating r_s and H_0 which are absolute scales for distance measurements at early and late times respectively. Although r_s is inferred from the CMB data, it can also be directly measured by only relying on the BAO giving a standard ruler and SNe being standard candles [179]. The result can be seen in Fig. 3.2 which shows the duality of the H_0 and r_s tension.

It is then clear that a lower r_s will reduce the H_0 tension, so, when introducing new early time physics, this is the direction that model builders should look at. In order to better understand why lowering the sound horizon results in a larger Hubble constant inferred from the CMB, it is useful to understand how H_0 is extracted by these data. This can be understood qualitatively as follows[1] [180].

The first step is to determine the two quantities ω_b and ω_m. ω_b can be determined from the effects that has on the damping scale of the CMB and, especially, from the effects on the boost and suppression of odd and even peaks of the CMB spectra. Indeed increasing ω_b, and thus the baryon to photon ratio η_b, alters the zero point of the acoustic oscillations in the primordial plasma. ω_m, on the other hand, can be precisely determined from the so called potential envelope effect [52]. Once ω_b and ω_m are known, since the radiation density can be determined from the temperature of the CMB which is precisely measured [46,181], it is possible to compute $c_s(z)$ and $H(z)$ in Eq. (3.2.1) for a given cosmological model and determine r_s (and consequently also r_s^*).

The second step is then to measure θ_s^*, which is the angular size of r_s^*. This quantity can be directly read off the spacing of the peaks of the temperature angular

---

[1] The only quantitative way to parameter estimation is by performing a full MCMC analysis, but the following argument helps get a taste of how a larger H_0 is obtained by lowering r_s with new physics.

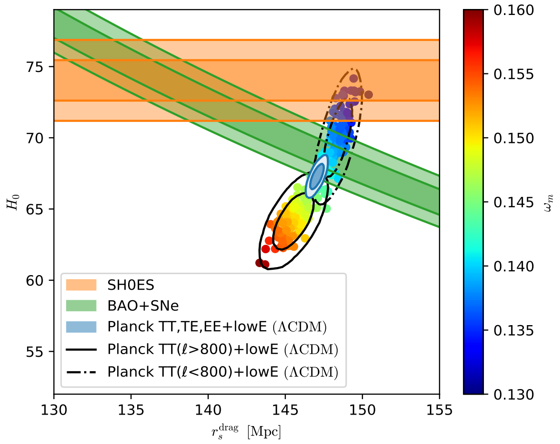

Figure 3.3: Orange and green bands show 68% and 95% CL contours from R19 and BOSS galaxy BAO + SN data respectively and are model independent. For P18, full results together with results for TT (limited to either $\ell > 800$ or $\ell < 800$) + lowE are shown. P18 results are obtained assuming the ΛCDM model. The plot is taken from Ref. [180].

power spectrum of the CMB as it is related to them by the relation $\theta_s^* = \pi/\Delta\ell$. Since $\Delta\ell$, and hence θ_s^*, is measured at the very precise level, any model that aims at solving the H_0 tension must preserve it. Note that the angular size of the comoving sound horizon is given by $\theta_s^* = r_s^*/D_A^*$, where the angular diameter distance is given by:

$$D_A^* = \int_0^{z_*} \frac{dz'}{H(z')}. \tag{3.2.2}$$

It is clear that, knowing r_s^*, the last step is to adjust D_A^*, and hence H_0, to keep θ_s^* fixed. In particular if r_s^* decreases, then a larger H_0 is needed for this. To make this more clear, in Fig. 3.3, I show the constraints in the $r_s - H_0$ plane from Ref. [180] for the ΛCDM model. As can be seen the value of r_s is too large and, although it can be lowered by enhancing the baryon density ω_b, this goes in the direction orthogonal to BAO and SN data so it spoils the fit to data sets other than CMB.

In the following, I introduce perhaps the three most important frameworks within which a lower r_s can be accommodated and explain how they ultimately leads to a larger H_0 by the introduction of extra relativistic degrees of freedom, an Early Dark Energy component or a modification to gravity.

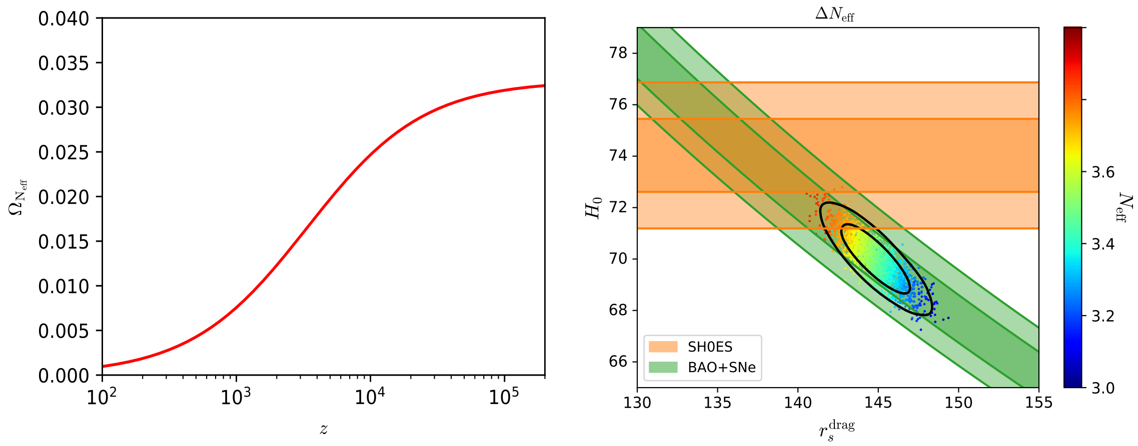

Figure 3.4: Evolution of the energy density fraction of extra relativistic species (left) and samples in the H_0-r_s plane for the analysis with the data set P18 + BAO + SN + R19. The plot is produced using the MCMC chains produced for the analysis in Ref. [3] and the code from Ref. [180].

3.3 Extra-Dark Radiation

Modifications to the expansion history of the early Universe are often enclosed in the parameter $N_{\rm eff}$, defined as

$$\rho_r = \left[1 + \frac{7}{8}\left(\frac{4}{11}\right)^{\frac{4}{3}} N_{\rm eff}\right]\rho_\gamma, \tag{3.3.1}$$

which parameterizes the effective number of relativistic species. For the Standard Model of particle physics, there are three species of active neutrinos corresponding to $N_{\rm eff} = 3.046$, where the small correction $N_{\rm eff} - 3 = 0.046$ accounts for the fact that neutrino decoupling is immediately followed by $e^+ e^-$ annihilation, see e.g. Ref. [182]. I refer to this as $\Delta N_{\rm eff}$ model in the following.

From the theoretical point of view, many Beyond Standard Model theories predict thermalized extra relativistic species making the parameterization above very useful to quickly test the model predictions in a very simple way, see e.g. Ref. [183] for a concrete example.

Concerning the H_0 tension, it is clear by looking at the definition in Eq. (3.3.1) that a positive $\Delta N_{\rm eff} \equiv N_{\rm eff} - 3.046$ increases the energy budget of the Universe and therefore its expansion history around recombination. This form of *dark radiation* only interacts gravitationally with the rest of the matter content of the Universe, being decoupled at the level of the Boltzmann equations, and, after recombination, it redshifts away with the radiation like behavior as $\propto a^{-4}$. This makes the $\Delta N_{\rm eff}$ a

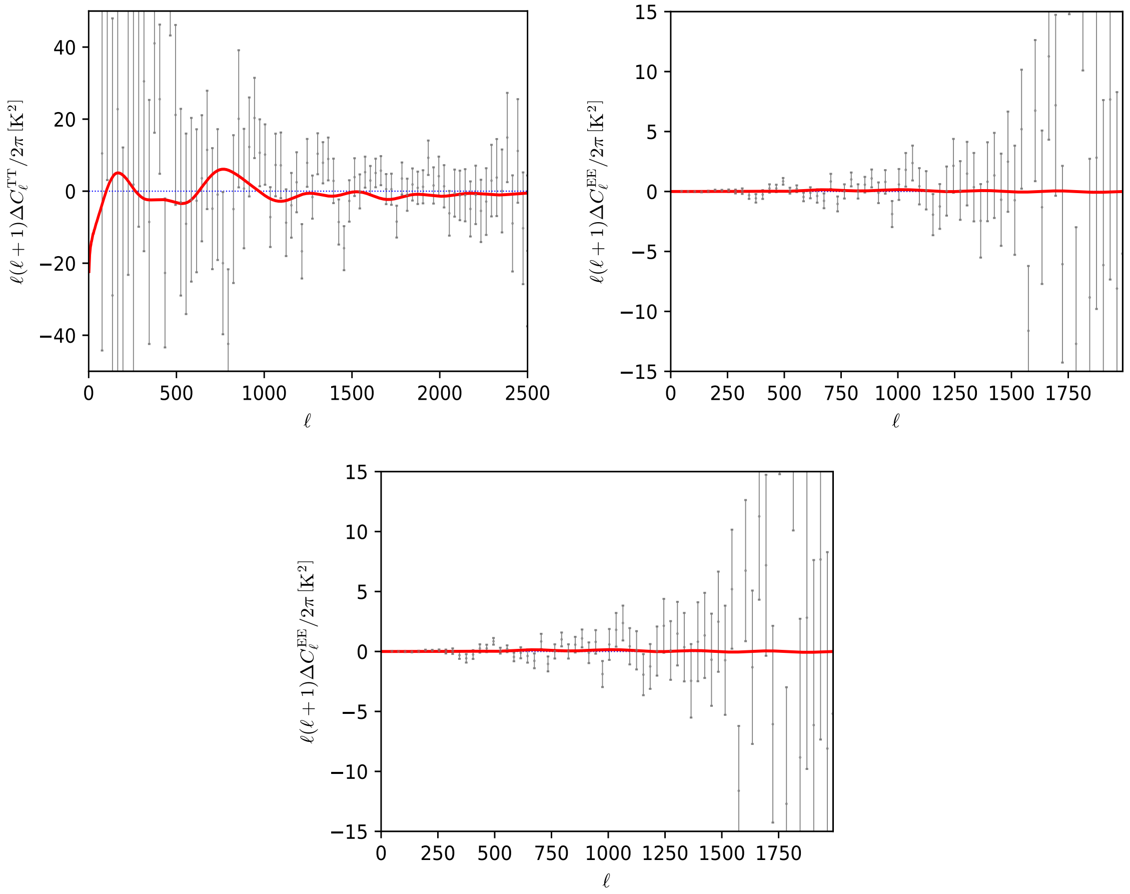

Figure 3.5: CMB TT (top left), EE (top right) and TE (bottom) residuals for the bestfit $\Delta N_{\rm eff}$ model. The plot is produced using the bestfit computed from the chains produced for the analysis in Ref. [3] and the code from Ref. [180].

perfect candidate to relieve the H_0 tension and indeed it is perhaps the one that was first considered in this context [161, 178, 184].

The evolution of the fraction of dark radiation corresponding to $\Delta N_{\rm eff} = 0.254$ is shown in the left panel of Fig. 3.4. Such value of $\Delta N_{\rm eff}$ is the mean value for obtained by performing an MCMC analysis with P18 + BAO + SN + R19 data, the results of which are presented in the right panel of Fig. 3.4. The positive (negative) correlation between $\Delta N_{\rm eff}$ and H_0 (r_s) can be appreciated by looking at the color bar. As can be seen the model successfully lowers r_s and therefore, as argued in the previous Section, leads to a larger $H_0 = 70.01 \pm 0.89$ km s^{-1}Mpc^{-1} reducing the tension with R19 at the 2.4σ level. The

It is interesting to note that the energy injected into the cosmic fluid from a variation of $\Delta N_{\rm eff} = 0.254$ is very small (of the order of $\Omega_{N_{\rm eff}} \simeq 0.032$, confirming that deviations from the ΛCDM model are tightly constrained by CMB data from P18. In fact, although it is clear from the color bar in Fig. 3.4 that a larger $\Delta N_{\rm eff}$ would completely solve the tension [169], the modification to the early Universe physics induced by this model already degrades the fit to CMB data.

Indeed, although there is an improvement in fitting the R19 data, I observe a degradation[1] of the total $\Delta\chi^2 = +3.9.$, overall fit to the total data set with respect to ΛCDM model, with a $\Delta\chi^2$, this improvement mostly comes from the reduction of the H_0 tension and to the better fit to R19, whereas the fit BAO and especially high-ℓ CMB data is worsened. I explicitly show this for the residuals ΔC_ℓ in Fig. 3.5 using The best-fit values for ΛCDM and the $\Delta N_{\rm eff}$ model for the data set P18 + BAO + SN + R19 are respectively:

$$\begin{aligned}&\theta_s = 1.0418, \quad 100\,\omega_b = 2.251, \quad \omega_c = 0.1189, \quad \tau_{\rm reio} = 0.057, \quad \ln 10^{10} A_s = 3.047,\\ &n_s = 0.9687,\end{aligned} \tag{3.3.2}$$

with a derived bestfit value of $H_0 = 68.42$ km s^{-1}Mpc^{-1}, and

$$\begin{aligned}&\theta_s = 1.0410, \quad 100\,\omega_b \;\; = 2.274, \quad \omega_c = 0.1246, \quad \tau_{\rm reio} = 0.058, \quad \ln 10^{10} A_s = 3.063,\\ &n_s = 0.9786, \quad N_{\rm eff} \quad = 3.41,\end{aligned} \tag{3.3.3}$$

leading to $H_0 = 70.53$ km s^{-1}Mpc^{-1}. As can be seen from Fig. 3.5 where the CMB TT, EE and TE residuals are plotted, the degradation is mainly due to the bad fit to Planck TTTEEE high-ℓ data of the $\Delta N_{\rm eff}$ model, with a partial $\Delta\chi^2$ of 9.07. The fit to other CMB BAO and SN data is not significantly different. For completeness, I also quote the best-fit parameters for the $\Delta N_{\rm eff}$ model obtained using only P18 data[2]:

$$\begin{aligned}&\theta_s = 1.041296, \quad 100\,\omega_b \;\; = 2.2195, \quad \omega_c = 0.11671, \quad \tau_{\rm reio} = 0.0533, \quad \ln 10^{10} A_s = 3.0339,\\ &n_s = 0.9577, \quad N_{\rm eff} \quad = 2.815,\end{aligned} \tag{3.3.4}$$

leading to $H_0 = 65.79$ km s^{-1}Mpc^{-1}, which is even smaller than the ΛCDM best-fit. In this case the fit to P18 worsens compared to the ΛCDM model one for the same dataset, with $\Delta\chi^2 = +0.17$.

Note, however, that the $\Delta N_{\rm eff}$ model is the simplest 1 parameter extension to ΛCDM to include extra relativistic species, but it does not take into account eventual interaction among such species or interactions between such species and other component of the Universe. In fact, the results presented here can be significantly improved if strong interactions between neutrinos, between neutrinos and additional

---

[1] Note the difference with the result of Ref. [3], where the bestfit values quoted are taken directly from the MCMC chains, whereas here I have extracted them using the PyMinuit minimizer, which a more accurate bestfit finder.

[2] See https://wiki.cosmos.esa.int/planck-legacy-archive/.

light relics or between dark matter and hidden gauge fields are introduced [185–188].

3.4 Early Dark Energy

Another popular model that has been proved to substantially ease, or even solve, the H_0 tension is the Early Dark Energy (EDE) model [189]. These models act to lower the comoving sound horizon introducing a new energetic component that is active only during a very narrow redshift window. From the phenomenological point of view, EDE is very economical solution to the H_0 tension, as it only modifies the prediction of the ΛCDM model for a very limited period of time.

In the original models, inspired by the string-axiverse scenario [190–192] the exotic energy density of a minimally coupled (e.g. with $F(\sigma) = 1$ in Eq. (2.2.3)) behaves like a cosmological constant at early times and eventually decays faster than radiation injecting energy into the cosmic fluid in a narrow redshift range. Since the scalar field is subdominant both during the early Universe and after its energy density has redshifted away as fast as, or even faster than, radiation.

Cosmological applications of very light axion-like particles were first studied in Ref. [193]. The action of these models is described by the Lagrangian in Eq. (2.2.3) with $F(\sigma) = 0$, where the shape of potential is not arbitrary as the latter is generated by non-perturbative effects, called instantons, that break the global U(1) symmetry to a discrete one, leading to [194]:

$$V(\sigma) = \sum_n c_n e^{-S_n} \cos\left(\frac{n\sigma}{f}\right). \tag{3.4.1}$$

Assuming the validity of the which is justified as long as $f > M_{\rm pl}$ [195, 196], since the instantons contributions scale as $S_n \simeq n M_{\rm pl}/f$ [194, 196], the leading order contribution scales as $\cos(\sigma/f)$. The potentials used in Ref. [189] take the form:

$$V(\sigma) = V_0 \left[1 - \cos\left(\frac{\sigma}{f}\right)\right]^n \tag{3.4.2}$$

where $V_0 \equiv m^2 f^2$, which corresponds to a fine-tuning of the instantons hierarchy in Eq. (3.4.2). S the averaged equation of state of the field σ during the oscillations around its minimum is given by [197]

$$w_n = \frac{n-1}{n+1}, \tag{3.4.3}$$

the scalar field contributes to the total dark matter of the Universe [193] for $n = 1$.

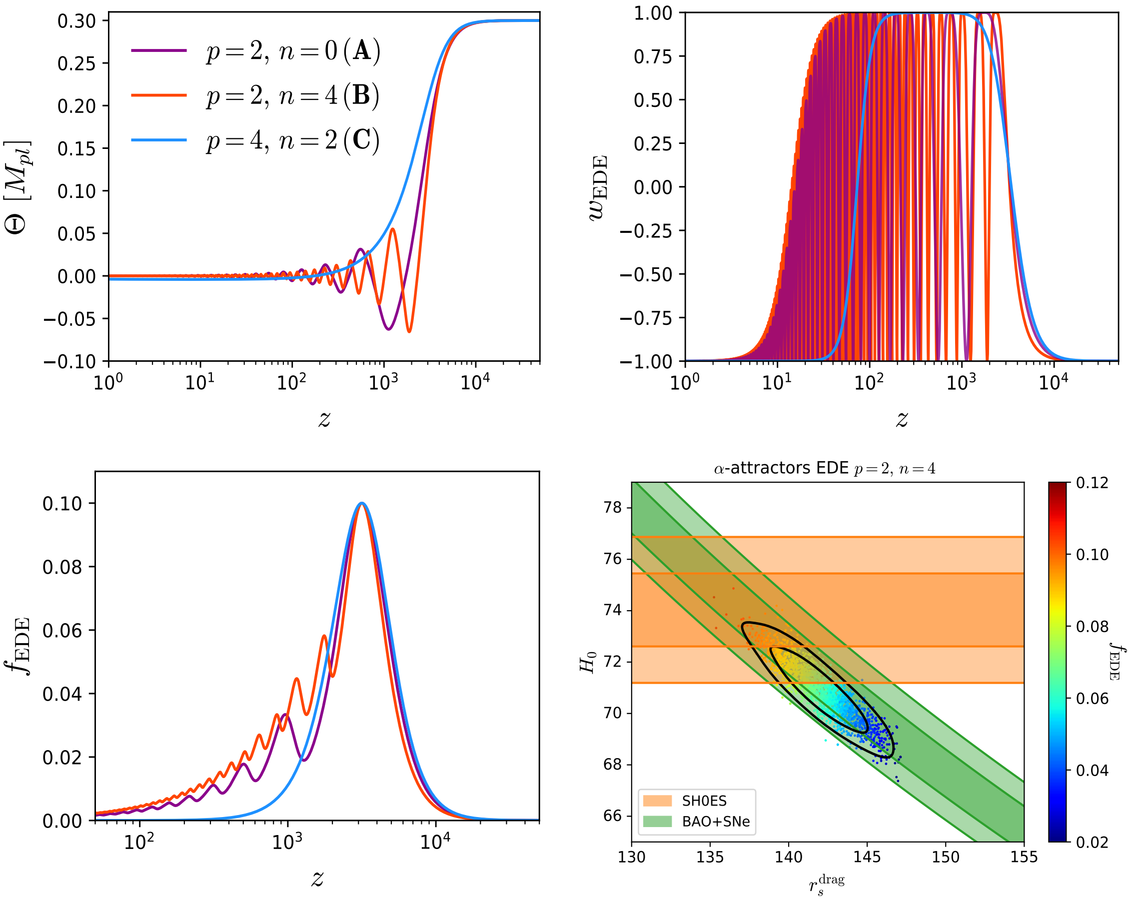

Figure 3.6: Evolution of the normalized scalar field Θ (top left), equation of state parameter $w_{\rm EDE}$ (top right) and the energy injection $f_{\rm EDE}$ (bottom left) for the three models with $(p,\ n) = \{(2,\ 0),\ (2,\ 4),\ (4,\ 2)\}$. For definiteness, I have chosen $f_{\rm EDE} = 0.1$, $\log_{10} z_c = 3.5$ and $\Theta_i = 0.4$. I also plot the samples in the H_0-r_s plane for the analysis with the data set P18 + BAO + SN + R19 (bottom right). The first three plots are taken from Ref. [1], and the fourth one is produced using the MCMC chains produced for the analysis in Ref. [1] and the code from Ref. [180].

Therefore, if a dilution of the field energy density as fast, or faster than radiation, is needed, $n \geq 2$ has to be considered. The best-fit integer value for n reported in Ref. [198] is $n = 3$.

An alternative can be to consider instead a potential which captures the feature of Eq. (3.4.2) around its minimum as proposed by Ref. [199], were a power law potential of the form

$$V(\sigma) = V_0 \left(\frac{\sigma}{M_{\rm pl}}\right)^{2n} \tag{3.4.4}$$

was studied. However, it has been shown in Ref. [198], that CMB polarization data are sensible enough to distinguish between the two model and prefer a large initial field displacement which can be supported by the potential in Eq. (3.4.2), but not by the one in Eq. (3.4.4).

Since the pioneering works in Refs. [189, 199, 200], a substantial effort has been made in building new models of EDE [198, 201–211]. In this Section, I consider the EDE model introduced in Ref. [1] in the context of the α-attractor framework. From the model building point of view, the only requirement to be consistent with the α-attractor construction is that the potential be of the form $V(\sigma) = f^2\left[\tanh\Theta\right]$ where I define $\Theta \equiv \phi/(\sqrt{6\alpha}M_{\rm pl})$ and α is a positive constant. Therefore, the α-attractor formulation makes the model free from some of theoretical inconsistencies that affect models inspired axion fields, as discussed above.

I therefore adopt a potential of the form [1, 212, 213]:

$$V(\Theta) = V_0 \frac{2^{2n}\tanh\left(\Theta\right)^{2p}}{\left[1+\tanh\left(\Theta\right)\right]^{2n}}\,, \tag{3.4.5}$$

where V_0, p and n are constants. The dynamics of the scalar field, that I show in Fig. 3.6, is similar to other models of EDE studied in the literature and is essentially that of an ultralight axion field [214]. The scalar field starts from its initial value Θ_i deep in the radiation era and remains frozen because of the Hubble friction. As mentioned above, the energy density of the scalar field is subdominant in this regime and its equation of state $w_{\rm EDE} \equiv P_{\rm EDE}/\rho_{\rm EDE}$ is equal to -1, hence the name "Early Dark Energy". Eventually, the effective mass of the scalar field becomes comparable to the Hubble rate H and ϕ starts to thaw. The redshift z_c at which this occurs can be implicitly defined from the relation $\frac{\partial^2 V(\phi_i)}{\partial\phi^2} \simeq 9H^2(z_c)$ [214]. After z_c, the Hubble friction is too weak to keep the scalar field up its potential and it rolls down in a very short time. When this happens, the potential energy of the scalar field is converted into a kinetic one and a certain amount of energy, parameterized by $f_{\rm EDE} \equiv \rho_{\rm EDE}(z_c)/3M_{\rm pl}^2H^2(z_c)$ is injected into the cosmic fluid. Depending on the slope of the potential and its structure around the minimum, the scalar field then starts to oscillate or simply freezes again once it has exhausted its inertia. The critical redshift z_c and the value of the energy injection $f_{\rm EDE}$ are the key parameters describing all EDE models [200]. As I am going to discuss, the shape of the energy injection and $w_{\rm EDE}$ crucially depend on the different possible dynamics of the scalar field after z_c. The scalar field energy density quickly redshifts away after z_c and its contribution becomes subdominant with respect to the other components of the Universe. The power of α-attractor EDE is exactly that it can consistently accommodate several distinct redshift shapes for the energy injection. This can be clearly seen from the three examples plotted in Fig. 3.6 (I refer to the caption for the parameters used).

In the cases **A** and **B** , the scalar field oscillates at the bottom of its poten-

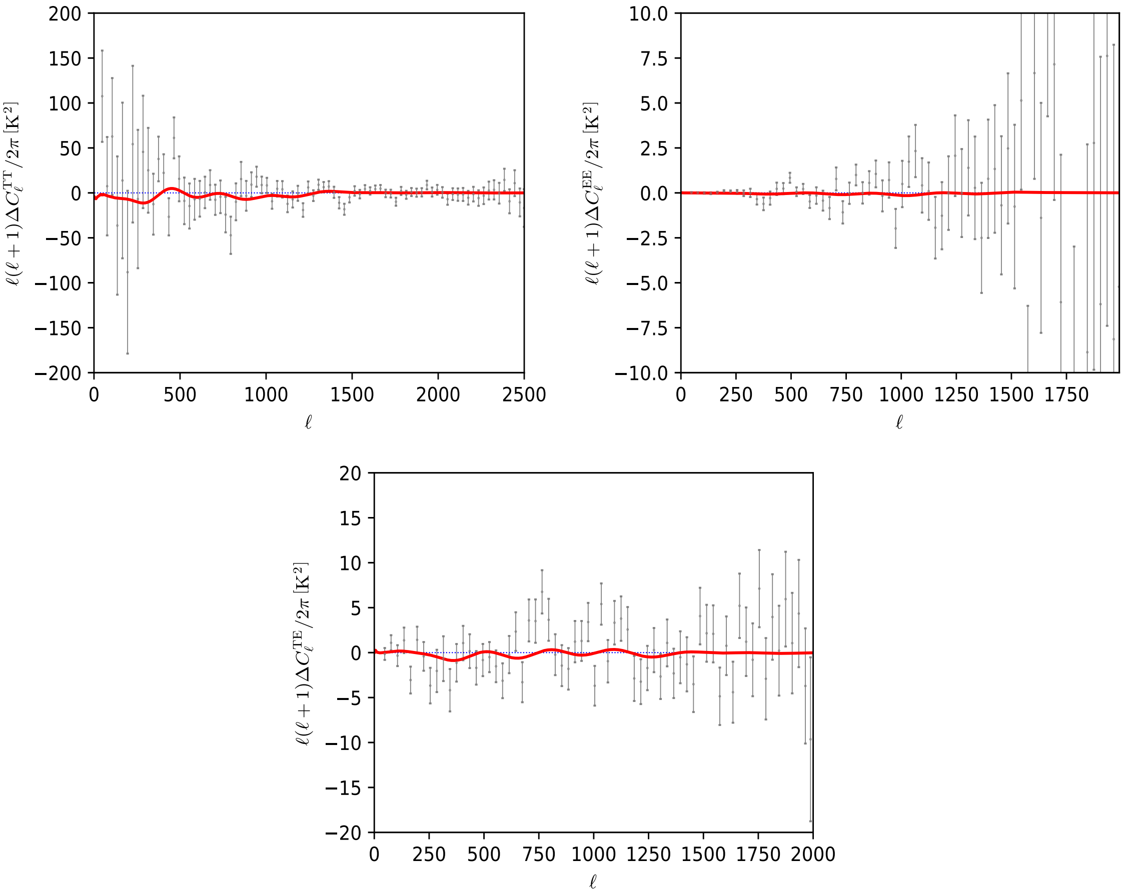

Figure 3.7: CMB TT (top left), EE (top right) and TE (bottom) residuals for the bestfit EDE **B** model. The plot is produced using the bestfit computed from the chains produced for the analysis in Ref. [1] and the code from Ref. [180].

tial leading to a highly oscillatory equation of state. In the **A** case, the potential is $\tanh^4\Theta \sim \Theta^4$ around $\Theta \simeq 0$ and therefore the shape for the energy injection closely resembles the one obtained in the so-called rock'n'roll model of Ref. [199] where $V(\phi) \propto \phi^4$. On the other hand, the **B** case looks more similar to the original EDE proposal of Ref. [189] (see e.g. Fig. 2 of Ref. [198]). However, given the asymmetry of our potential for the **B** case, the oscillatory pattern in the energy injection shows an asymmetric amplitude of odd and even peaks in the oscillations. Although this is barely visible in Fig. 3.6, this effect is more pronounced for larger Θ_i and might in principle lead to distinct results, as the CMB power spectrum is very sensitive to the shape of $f_{\rm EDE}(z)$ [180]. Indeed, because of such a sensitivity, the oscillatory patterns of the scalar field in models **A** and **B** leave different imprints on the CMB angular spectra as shown in Refs. [199] and [198]. Therefore, although at a first glance their background evolution might look similar, it is important to explore the phenomenology of both of them separately.

The case **C** is instead different. Unlike the first two oscillatory models, for this choice of p and n, the bottom of the potential is very close to flat and the scalar field shows no oscillations. This model looks similar to the canonical Acoustic Dark Energy (cADE) model proposed in Ref. [202]. As in cADE (see also Ref. [201]), the potential energy is suddenly converted to a kinetic one and the scalar field remains in a *kination* regime in which $w_{\rm EDE} = 1$, and its energy is kinetically dominant until it redshifts away. However, differently from cADE, where the potential was introduced by patching a quartic potential for positive values of ϕ to $V(\phi) = 0$ for negative ones, the potential **C** is consistently embedded in the α-attractor's construction. Some other possibilities can be obtained for other combinations of the potential parameters $(p,\, n)$.

The capability of these models to ease the H_0 tension is clear from the last panel in Fig. 3.6, where, for simplicity, I show the results for the model **B** obtained in Ref. [1] using the data set P18 + BAO + SN + R19. In fact, model **B** is the one that leads to the largest H_0 among the ones considered here, as expected from the fact that it resembles the one in Ref. [198] The positive (negative) correlation between $f_{\rm EDE}$ and H_0 (r_s) can be appreciated by looking at the color bar. Indeed, a mean value of $f_{\rm EDE} = 0.082 \pm 0.029$ leads to large $H_0 = H0 = 70.9 \pm 1.1$ km s^{-1}Mpc^{-1} reducing the tension with R19 at the level of 1.74σ, better than the $\Delta N_{\rm eff}$ model. Differently from the latter model, however, not only does the model improve the overall fit by a factor of $\Delta\chi^2 = -5.8$, but also it improves the fit to each separate data set, besides the obvious improvement in the fit to R19. The improvement in the fit to high-ℓ P18 data of $\Delta\chi^2 = -2$ can be appreciated by looking at Fig. 3.7, where the CMB residuals are plotted against P18 binned data. An exception is made for low-ℓ EE data for which the fit is worsen by the same factor. The best-fit values used in the plot for ΛCDM and the EDE model **B** for the data set P18 + BAO + SN + R19 are respectively[1]:

$$\begin{aligned}&\theta_s = 1.0419, \quad 100\,\omega_b = 2.252, \quad \omega_c = 0.1188, \quad \tau_{\rm reio} = 0.057, \quad \ln 10^{10} A_s = 3.049,\\ &n_s = 0.9690, \end{aligned} \tag{3.4.6}$$

with a derived bestfit value of $H_0 = 68.09$ km s^{-1}Mpc^{-1}, and

$$\begin{aligned}&\theta_s = 1.0416, \quad 100\,\omega_b \; = 2.261, \quad \omega_c = 0.1259, \qquad \tau_{\rm reio} = 0.063, \qquad \ln 10^{10} A_s = 3.071,\\ &n_s = 0.9765, \quad f_{\rm EDE} \quad = 0.061, \quad \log_{10},\, z_c = 3.49, \qquad \Theta_i = 0.104, \end{aligned} \tag{3.4.7}$$

---

[1] Here, I refer to the results of Ref. [1], where the choice of running with the Planck convention [67] of one massive neutrino with $m_\nu = 0.06$ eV. As can be seen by comparing the ΛCDM bestfit with the ones in Eq. (3.3.2), there is almost no difference.

leading to $H_0 = 70.17$ km s^{-1}Mpc^{-1}. The bestfit for P18 data was not calculated in Ref. [1]. In fact, this was not calculated even for other EDE models in other works in the literature, with the exception of Ref. [215], where the bestfit was computed without including CMB lensing in P18, but for a 1-parameter EDE model where Θ_i and $\log_{10} z_c$ were kept fixed. I will come back to this point in Section 5.5.

The results presented in this Section are for the α-attractor EDE model **B**. However, CMB data are very sensitive to the specific shape in redshift of the energy injection and therefore although all EDE models generically lead to a large H_0, quantitative arguments concerning the estimation of cosmological parameters, the H_0 tension and the fit to data set, may differ depending on the specific model under consideration [198, 202]. At the time I am writing this thesis, the EDE model which more efficiently reduces the is the axion-like original proposal of Refs. [189, 192, 198].

All in all, the capability to significantly reduce the H_0 tension has made EDE models very popular and they are now regarded as one of the most promising solution. However, they are not free from phenomenological and theoretical issues. Regarding the former, EDE has been recently claimed not to solve H_0 tension anymore when LSS data from weak lensing measurements and the full shape of the matter power spectrum are included [216–218]. Also, there is growing concern that EDE models may fail to alleviate the H_0 tension when no prior information on H_0 is included in the data set [216]. I will come back to these points in Chapter 5. Regarding the theoretical concerns, EDE models present a very high degree of fine tuning, as the parameters of the scalar field potential, which is not always theoretically sound itself, has to be tuned in such a way that the scalar field starts to roll precisely at the required redshift. The same holds for the initial conditions on the scalar field that regulates the amount of energy injection. The need to include EDE in a more theoretically sound framework has been addressed by α-attractor models presented here, models in which energy injection is produced by a phase transition [203, 208], or models in which the EDE field is coupled to gauge bosons [204, 207], whereas a concrete example of model in which the fine tuning is reduced by coupling the EDE field to massive neutrinos is the work of Ref. [205].

For the reasons explained above, it is clear the importance of testing the consistency of EDE with different data [219] and proposing new observations to further constrain these models [203, 207, 208, 220].

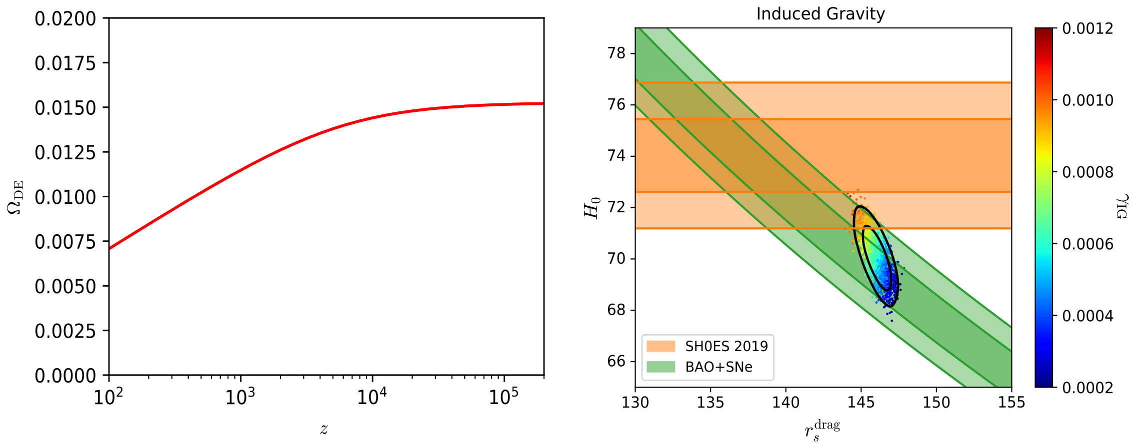

Figure 3.8: Evolution of the effective energy Dark Energy density fraction (left) and samples in the H_0-r_s plane for the analysis with the data set P18 + BAO + SN + R19. The plot is produced using the MCMC chains produced for the analysis in Ref. [4] and the code from Ref. [180].

3.5 Scalar-tensor theories

If the H_0 tension is taken at face value, it is also natural to ask ourselves if this can point towards theories of Modified Gravity that go beyond General Relativity. In fact, several modified gravity models have been proposed to solve the H_0 tension. Among them, some are strictly late time modifications to the dynamics of our Universe and some also change it at early time [2–4, 221–231]. In the spirit of this Chapter, the latter are the ones I am interested in.

As discussed in Chapter 1, Scalar-tensor (ST) theories are perhaps the simplest framework to test modifications to gravity that can also work as an alternative to the cosmological constant in explaining the observed acceleration of the Universe. The study of such theories is the subject of this Thesis and will be discussed in details in the next Chapters. Here, I only intend to give a general idea of why these theories are able to alleviate the H_0 tension. To do so, I consider the simplest example of ST theory, that is the extended Jordan-Brans-Dicke (JBD) theory [87, 88], that I recast in its Induced Gravity (IG) formulation [232]. The theory is described by Eq. (2.2.3) with $F(\sigma) = \gamma\sigma^2$, where γ is a positive constant, and I consider for simplicity a potential of the form $V(\sigma) = \lambda\, F(\sigma)^2/4$, for which the theory is effectively massless and discuss in details the choice of the potential in the following Chapters.

The degeneracy of the coupling γ, which regulates the strength of the modification to gravity, and H_0 was first noticed in Refs. [221] and [222] (see their Figures 7 and 8 respectively). The reason the modification to gravity helps ease the H_0 tension is easily understood. Indeed, in the IG theory, the effective contribution of the scalar field to the cosmic expansion is similar to the one from extra relativistic degrees of freedom, as can be seen from the left panel in Fig. 3.8. The scalar field, that has an effective equation of state, as computed from Eqs. (2.2.17), $w_{\rm DE} \simeq 1/3$, continuously injects energy during the early Universe before recombination reducing the comoving sound horizon r_s. Unlike in the $\Delta N_{\rm eff}$ model, however, its energy density redshifts away slower than a^{-4} and the scalar field contribution, although very small, is not completely negligible during the matter radiation era, as can be seen from Fig. 3.8 in which $\Omega_{\rm DE} \simeq 0.07$ at $z \simeq 100$, which can compared to Fig. 3.4 for the $\Delta N_{\rm eff}$ model. The compatibility of such models with laboratory experiments and Solar System observations will be discussed in details in the next Chapters.

To confirm the above argument, I plot samples from the chains used in Ref. [4] in Fig. 3.8. Note that the data set used is P18 + BAO + R19, whereas SN are not included because the modification to gravity changes the peak luminosity of SNe and this needs to be properly accounted in the analysis[1] [235–238].

As can be seen from Fig. 3.8, larger values for H_0 are indeed obtained for a larger value of γ. Indeed, a coupling as large as $\gamma = 0.00051^{+0.00043}_{-0.00046}$ (95% CL) leads to $H_0 = 70.06 \pm 0.81$ km s^{-1}Mpc^{-1} reducing the tension with R19 at the 2.4σ level, with a result which is similar to the one for the $\Delta N_{\rm eff}$ model. The best-fit values used in the plot for ΛCDM and the IG model for the data set P18 + BAO + R19 are respectively[2]:

$$\begin{aligned}
&\theta_s = 1.0418, \quad 100\,\omega_b = 2.251, \quad \omega_c = 0.1186, \quad \tau_{\rm reio} = 0.064, \quad \ln 10^{10} A_s = 3.062, \\
&n_s = 0.9704,
\end{aligned} \tag{3.5.1}$$

with a derived bestfit value of $H_0 = 68.50$ km s^{-1}Mpc^{-1}, and

$$\begin{aligned}
H_0 = 70.18, \quad 100\,\omega_b &= 2.253, \quad \omega_c = 0.1197, \quad \tau_{\rm reio} = 0.053, \quad \ln 10^{10} A_s = 3.044, \\
n_s = 0.9707, \quad \gamma_{\rm IG} &= 5 \times 10^{-4}.
\end{aligned} \tag{3.5.2}$$

The IG model leads to an improvement in the fit to data of $\Delta\chi^2 = -1.5$, which is better than the $\Delta N_{\rm eff}$ model. However, as can be seen from the plots in Fig. 3.9, the improvement comes mainly from the better fit to R19 and the fit to high-ℓ CMB data is worsened, although there is a gain in fitting low-ℓ EE polarization data. A similar

---

[1] Note also that the modification of the gravitational constant can also change the low-redshift distance ladder measurements of the Hubble constant [233, 234].

[2] Here, I refer to the results of Ref. [4], where the choice of running with the Planck convention [67] of one massive neutrino with $m_\nu = 0.06$ eV.

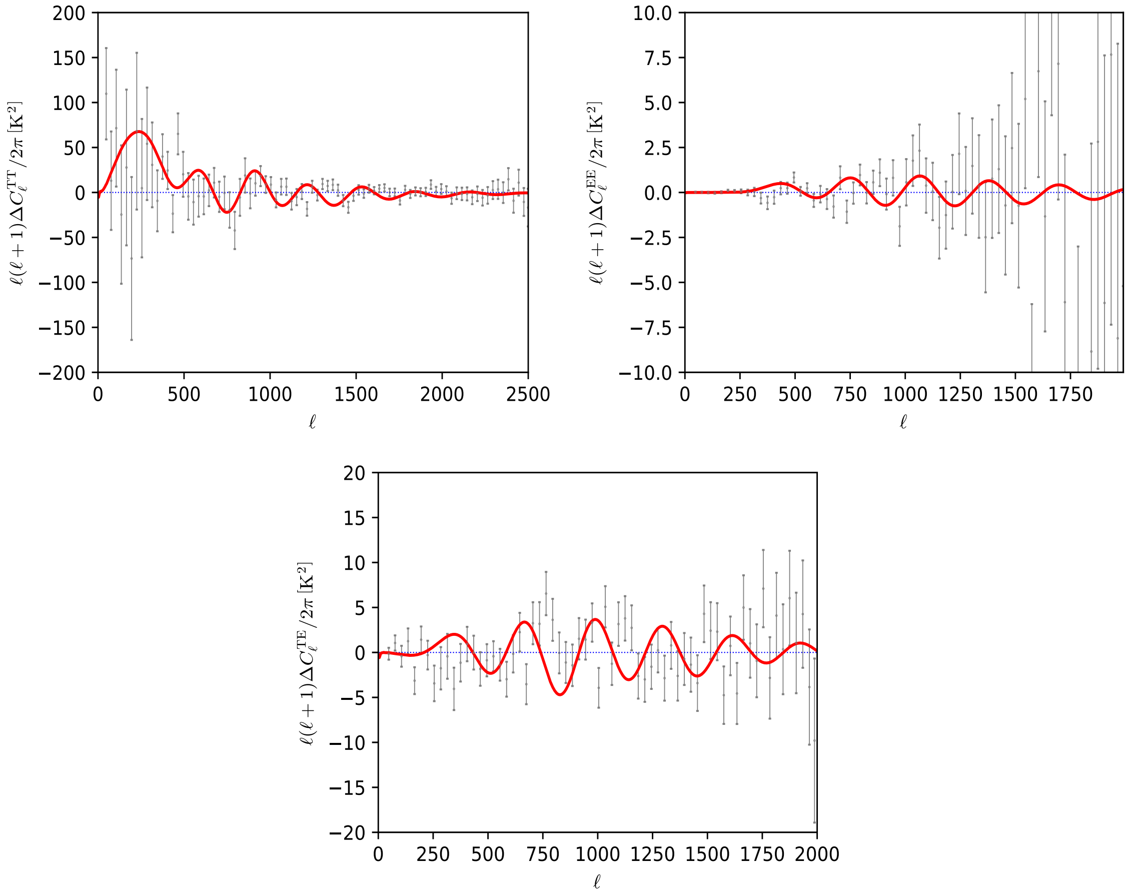

Figure 3.9: CMB TT (top left), EE (top right) and TE (bottom) residuals for the bestfit IG **B** model. The plot is produced using the bestfit computed from the chains produced for the analysis in Ref. [4] and the code from Ref. [180].

worsening of the fit is found for BAO data. For completeness, I also quote the best-fit parameters for the IG model obtained using only P18 data [4]:

$$\begin{aligned} H_0 = 67.73, \quad 100\,\omega_b &= 2.2398, \quad \omega_c = 0.12012, \quad \tau_{\rm reio} = 0.053, \quad \ln 10^{10} A_s = 3.0432, \\ n_s = 0.9673, \quad \gamma_{\rm IG} &= 1.005 \times 10^{-4}. \end{aligned} \tag{3.5.3}$$

Similarly to the $\Delta N_{\rm eff}$ model, the bestfit to P18 worsens compared to the ΛCDM model one for the same dataset, with $\Delta\chi^2 = +0.2$ (see Table 4.7 in the next Chapter).

Before concluding, it is worth to stress that the model presented here is perhaps the simplest and most studied model of modified gravity, and its relevance is also due to the fact that many Horndeski models can be very well approximated by the JBD one [239]. Furthermore, the most important feature of this model is that the scalar field naturally starts to move around the recombination driven by pressureless matter to which it is coupled at the level of the equations of motion. In this sense, the degree of fine tuning is much lower than models like EDE, that require the potential to acquire a specific value in order for the energy to be injected at a particular redshift, as discussed in the previous Section.

3.6 Summary

In this Chapter I have presented the status of the art of the so called H_0 tension and discussed the possibility to solve it using pre-recombination physics. As argued in Section 3.2, the most promising solution is to reduce the comoving sound horizon r_s, so that H_0 has to increase in order to keep the parameter θ_s, which is precisely measured from the spacing of the CMB peaked, fixed [177, 178, 180].

The three most popular frameworks, within which this goal is achieved are modifications to the radiation content of the Universe (which is active before recombination by definition), Early Dark Energy and models of Modified Gravity. For each class, I have therefore discussed a representative model, in order to capture the main features that lead to a larger H_0 inference. In particular, I have described how the H_0 tension is reduced within the $\Delta N_{\rm eff}$, the α-attractor EDE, and the extended JBD model. The results of the analysis are summarized in Fig. 3.10.

The tension with R19 is reduced at 2.4σ or $\Delta N_{\rm eff}$ and JBD models, and 1.74σ for EDE. This is not only due to a larger mean value for H_0, but also to a larger error, as can be seen from the normalized 1-dimensional posteriors in the right panel of Fig. 3.10. However, although very useful, Fig. 3.10 gives only rough information that has to be complemented by a detailed analysis of the fit of the models to the

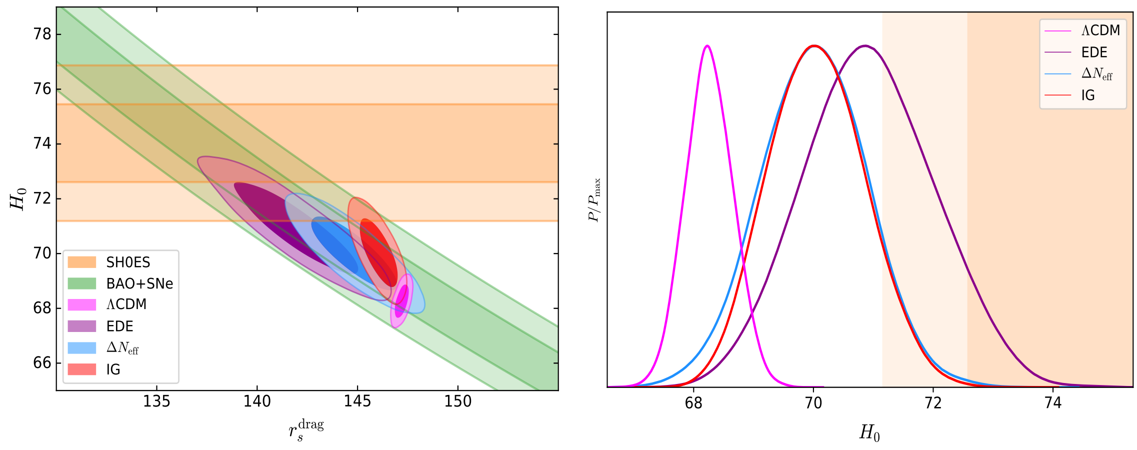

Figure 3.10: Two-dimensional plots in the $r_s - H_0$ plane (left) and marginalized posteriors for H_0 for the ΛCDM, ΔN_{eff}, α-attractor EDE and JBD model. The data set used is P18 + BAO + SN + R19, except for the JBD model for which SN data are not used. The plots are produced using the MCMC chains produced for the analysis in Ref. [1, 3, 4] and the code from Ref. [180].

data on one hand and by physical considerations on the other. Indeed, what cannot be appreciated by looking at Fig. 3.10 is that the three models fit the data in a different way and arrive at the posteriors in the right panel using different physics. In particular, the ΔN_{eff} model does not lead to an improvement in the fit compared to ΛCDM, and is only a parameterized model, whereas the EDE model, despite almost solving the H_0 tension, suffers from fine tuning issues and has been claimed to ruin the fit to LSS data.

The JBD model, on the other hand, is a model with solid physical foundations that addresses the tension without the need of fine tuning and improves the fit to data at the same time. This triggers the need of exploring in details the phenomenology of ST theories in relation to the H_0 tension, which is the subject of the next Chapters.

Chapter 4

Cosmological constraints on nearly massless Non-Minimally Coupled theories and consequences on the H_0 tension

4.1 Non-Minimally coupled theories

In this Chapter, I study the cosmological dynamics of Non-Minimally Coupled (NMC) theories described by the action (2.2.3) with $F(\sigma) = N_{\rm pl}^2 + \xi\sigma^2$, where $N_{\rm pl}$ and ξ are two constant that are arbitrary as long as they satisfy the stability conditions in Eqs. (2.2.4) and (2.2.5). Note that other theories, known as extended quintessence models [240–245], can be described by the same Lagrangian and a different choice of potential. I then use cosmological data to constrain this class of theories and discuss implications for the H_0 tension. Note that the NMC model reduces to General Relativity for $\xi = 0$ and to the eJBD model introduced in Section 3.5 for $N_{\rm pl} = 0$.

As discussed in Chapter 2, Solar System tests and laboratory experiments puts stringent constraints on ST theories. In order to satisfy these constraints one could follow several approaches when analyzing the theory on cosmological scales. The first one is to simply not care about those constraints at all. Indeed, as discussed in the previous Chapter, one is not guaranteed that the behavior of the theory is the same at cosmological and galactic or Solar System scales, so one could simply evoke a screening mechanism to hide gravitational effects at small scales [117]. This is in line with the philosophy of testing a gravitational theory on different scales to characterize it with complementary information. However, in its simplest formulation, the NMC theory described in the following Sections does not support any screening mechanism, since the scalar field σ is canonically coupled and the potential is not of the runaway form. Therefore if one wanted to implement a screening mechanism in the simplest model studied here, some additional assumptions would have to be adopted.

Another approach is instead to ensure by hand that the cosmological evolution of the scalar field is consistent with the value of the gravitational constant measured in laboratory. This can be done by setting suitable boundary conditions on the evolution of σ today, i.e. σ_0, so that the value of $G_{\rm eff}(\sigma_0)$ is *exactly* equal to its value measured in laboratory experiments and then see how the PN parameters deviate from GR (or viceversa one could fix the PN parameters and look at the deviation of $G_{\rm eff}(\sigma_0)$ from G). I will adopt the former approach in Section 4.2. Note that this additional condition on σ_0 reduces the number of free parameters in the theory.

However, as I will show in Section 4.3, this is not necessarily needed for the specific case of the NMC model. Indeed, for the negative branch of coupling $\xi < 0$, σ decreases and the modification of gravity at late times becomes smaller and smaller with redshift. As it turns out, cosmological data seem indeed to favour that branch and the resulting cosmological bounds on $G_{\rm eff}$ and the PN parameters are consistent with laboratory and Solar System ones. It is therefore important to explore the possibility of constraining σ_i itself with cosmological data.

An interesting feature of the NMC model is that it behaves very similarly to the $\Delta N_{\rm eff}$ model introduced in Sec. 3.3 of the previous Chapter at the background level. In this Chapter, I also discuss the consequences that this similarity has on the H_0 tension and show how it is naturally alleviated in this context.

Finally, for completeness, I also present the cosmological constraints on the IG (or eJBD) model introduced in Section 3.5. In this model, however, the scalar field grows and if the boundary conditions are not set on the scalar field, cosmological constraints are inevitably in tension with both laboratory and Solar System experiments.

This Chapter is based on the research work in Refs. [2–4] and the plots are produced using either `CLASSig` [2, 221], a modified version of the `CLASS`[1] [41, 42] for scalar-tensor theory of gravity, or with a modified version of `hiCLASS` [246, 247] which allows to study consistently oscillating scalar fields. The agreement of `CLASSig` and `hiCLASS` for the precision of current and future experiments has been demonstrated in [248].

4.2 Consistency condition on $G_{\rm eff}(t_0)$

I start by considering the NMC theory described above in which [2]. For later convenience I denote by a tilde the quantities normalized to $M_{pl} \equiv 1/\sqrt{8\pi G}$, where $G = 6.67 \times 10^{-8}$ cm^3 g^{-1} s^{-2} is the gravitational constant measured in a Cavendish-like experiment and I introduce the notation $\tilde{N}_{pl} \equiv 1 \mp \Delta\tilde{N}_{pl}$ for $\xi \gtrless 0$. Throughout this Section, I will restrict myself to a potential of the form $V \propto F^2$ in which the scalar field, as can be seen from Eq. (2.2.14) is effectively massless. This case generalizes the

---

[1] https://github.com/lesgourg/class_public

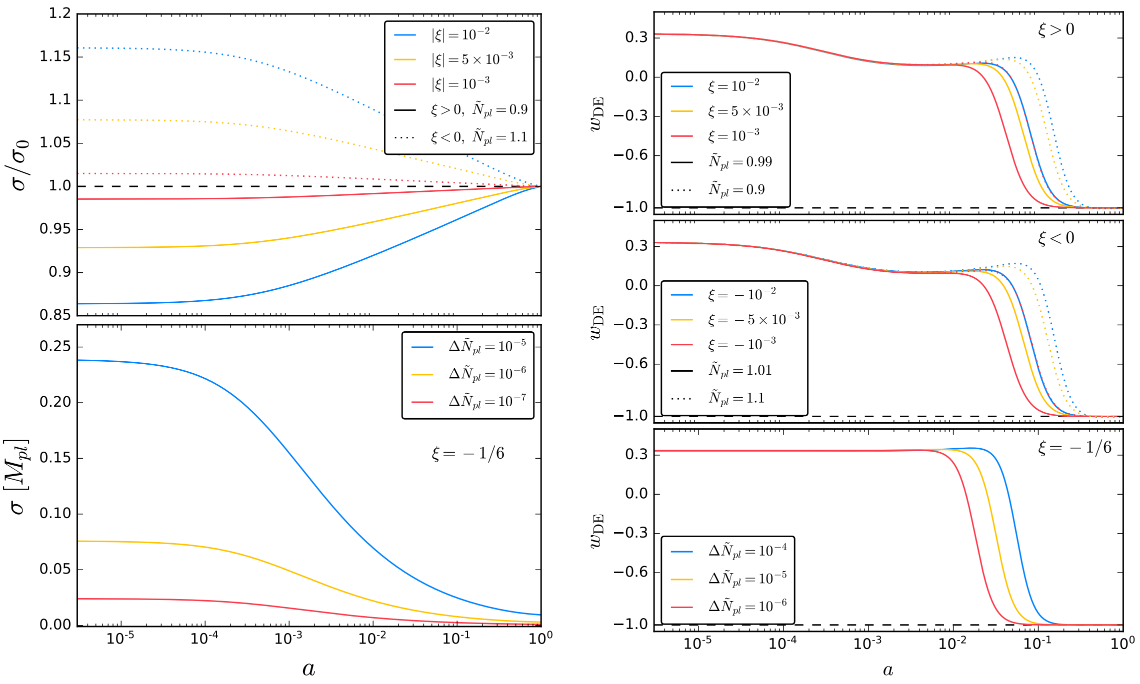

Figure 4.1: [Left] Top panel: relative evolution of σ for different values of ξ. Bottom panel: evolution of σ for different values of N_{pl} for the CC case, i.e. $\xi = -1/6$. [Right] Evolution of $w_{\rm DE}$ for different values of N_{pl} and ξ. I plot the effective parameter of state for DE for $\xi > 0$ in the upper panel, $\xi < 0$ in the central panel, and the CC case $\xi = -1/6$ in the bottom panel. Figure taken from Ref. [2].

broken scale invariant case [232, 249, 250] to NMC and is a particular case of the class of models with $V \propto F^M$ admitting scaling solutions [241]. Note that though for the form of $F(\sigma)$ used in the paper and for large values of σ, this potential looks similar to that in the Higgs inflationary model [251], in fact it is crucially different, since it is exactly flat in the Einstein frame[1] in the absence of other matter and cannot support a metastable inflationary stage in the early Universe. Contrary, this model may be used for description of dark energy in the present Universe.

The evolution of relevant background quantities is shown in Figs. 4.1 and 4.2. Depending on the sign of the non-minimal coupling, the scalar field σ grows or decreases for $\xi > 0$ or $\xi < 0$ respectively. In particular, as the magnitude of ξ increases, the field-excursion of σ and the growth or decay of σ is more pronounced. This can be best appreciated by looking at the plots for the Conformally Coupled case with $\xi = -1/6$, for which the scalar field decays very efficiently. This leads to an equation of state $w_{\rm DE}$ which is essentially equal to $1/3$, as for a relativistic fluid, till recent redshifts at which it becomes $w_{\rm DE} = -1$ so that the recent accelerated phase of the Universe is driven. This should be contrasted with smaller values of $|\xi|$ for which

---

[1] Although I always work in the physical Jordan frame, it is also useful to think about this class of theories in the dual Einstein frame where $\hat{g}_{\mu\nu} \propto F g_{\mu\nu}$, $\hat{V} = V/F^2$.

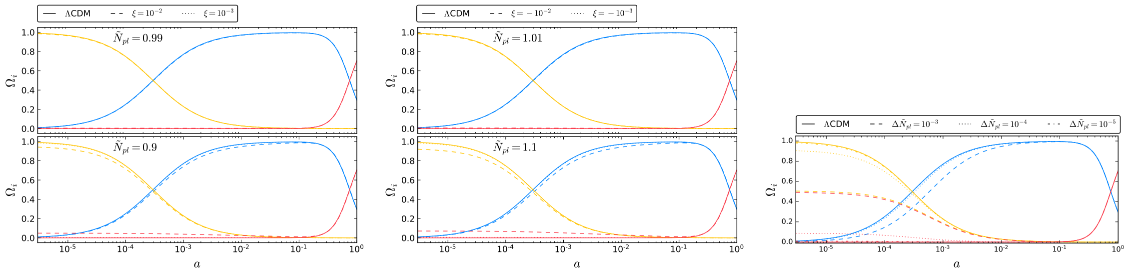

Figure 4.2: Evolution of the density parameters Ω_i: radiation in yellow, matter in blue, and effective DE in red. [Left] I plot $\tilde{N}_{pl} = 0.99$ ($\tilde{N}_{pl} = 0.9$) for $\xi = 10^{-2}$ (10^{-3}) in the top (bottom) panel. [Center] I plot $\tilde{N}_{pl} = 1.01$ ($\tilde{N}_{pl} = 1.1$) for $\xi = -10^{-2}$ (-10^{-3}) in the top (bottom) panel. [Right] Evolution of the density parameters Ω_i: radiation in yellow, matter in blue, and effective DE in red. [Right] I plot the CC case $\xi = -1/6$ for $\Delta\tilde{N}_{pl} = 10^{-3}$, 10^{-4}, 10^{-5}. Figure taken from Ref. [2].

the equation of state follows the one of the dominating component of the Universe, i.e. $w_{\rm EDE} \simeq 1/3$ during radiation dominated era and $w_{\rm EDE} \simeq 0$ during the matter dominated one. Note that the CC case is one of a particular theoretical relevance as the equations of motion for σ in a FLRW spacetime are conformally invariant in the absence of matter fields.

As mentioned above, the evolution displayed in Figs. 4.1 and 4.2 is obtained by imposing that the effective Newton's constant at present time, as given by Eq. (2.2.19), is compatible with Cavendish-like experiments. It is possible to distinguish three different cases beyond GR:

- $\tilde{N}_{pl} \to 0$ which is the IG case introduced in Section 3.5 and will be useful in the following. This leads to:
$$\tilde{\sigma}_0^2 = \frac{1}{\xi}\frac{1+8\xi}{1+6\xi}, \tag{4.2.1}$$
which is the same result as obtained in Ref. [221];

- $\xi \to -1/6$ which is the CC. In this particular case the polynomial equation (2.2.19) in σ_0 in quadratic and the solution is:
$$\tilde{\sigma}_0^2 = \frac{18\tilde{N}_{pl}^2(\tilde{N}_{pl}^2-1)}{1+3\tilde{N}_{pl}^2}; \tag{4.2.2}$$

- a general NMC case for $\xi \neq -1/6$:
$$\begin{aligned}\tilde{\sigma}_0^2 =& \frac{1-2\tilde{N}_{pl}^2+2\xi(4-3\tilde{N}_{pl}^2)}{2\xi(1+6\xi)}\\ &\pm\frac{\sqrt{1-4\xi(5\tilde{N}_{pl}^2-4)+4\xi^2(3\tilde{N}_{pl}^2-4)^2}}{2\xi(1+6\xi)}.\end{aligned} \tag{4.2.3}$$

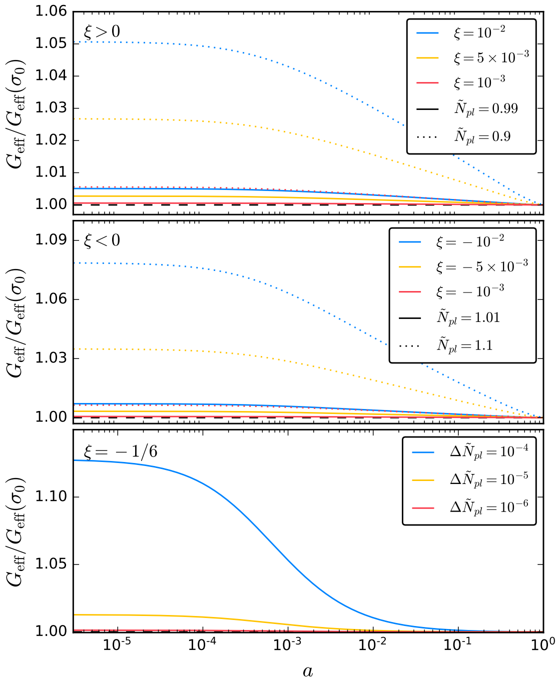

Figure 4.3: Evolution of the effective gravitational constant $G_{\rm eff}$ relative to its value today for different values of N_{pl} and ξ. From top to bottom, the cases with $\xi > 0$, $\xi < 0$, and $\xi = -1/6$ are displayed, respectively. Figure taken from Ref. [2].

By requiring $\tilde{\sigma}^2 \geq 0$ and $F \geq 0$, I obtain conditions on the two parameters $\tilde{N}_{pl}$ and ξ for the physical solution:

$$\tilde{N}_{pl} \quad < \quad 1 \ \text{ for } \ \xi > 0\,, \tag{4.2.4}$$

$$\tilde{N}_{pl} \quad > \quad 1 \ \text{ for } \ \xi < 0\,. \tag{4.2.5}$$

In Fig. 4.3 I show the evolution of the relative effective gravitational constant (2.2.19). It is interesting to see that the effective gravitational constant decreases in time for all the choices of both N_{pl} and ξ, regardless on the sign and the magnitude of the latter, which, however, affects the relative decrease of $G_{\rm eff}$ from early times to today. The PN parameters in Fig. 4.4 shows how the sign of ξ determines the departure of $\beta_{\rm PN}$ from 1.

4.2.1 CMB anisotropies and matter power spectra

The footprints of these scalar-tensor theories into the CMB anisotropies angular power spectra can be understood as follows. The redshift of matter-radiation equality is modified in ST theories by the motion of the scalar field driven by pressureless matter and this results in a shift of the CMB acoustic peaks for values $\xi \neq 0$, as for the IG case, see e.g. Figs. 3.9. In addition, a departure from $\tilde{N}_{pl} = 1$ induces a further change

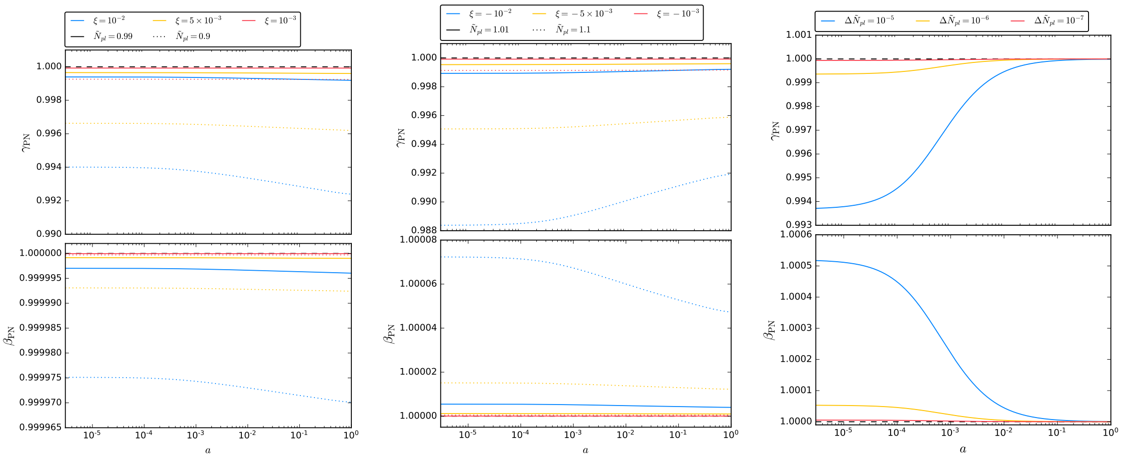

Figure 4.4: Evolution of the post-Newtonian parameters $\gamma_{\rm PN}$ and $\beta_{\rm PN}$ for different values of N_{pl} and ξ. I plot the cases with $\xi > 0$, $\xi < 0$ and $\xi = -\frac{1}{6}$ in the left, center and right panels respectively. Figure taken from Ref. [2].

both in the amplitude of the peaks and their positions. Note that by decreasing the value of $\Delta\tilde{N}_{pl}$ it is possible to suppress the deviations with respect to the ΛCDM model allowing for larger values of the coupling ξ compared to the IG case.

To explicitly see this effect, I show the relative differences with respect to the ΛCDM model for the lensed CMB angular power spectra anisotropies in temperature and E-mode polarization and the CMB lensing angular power spectra for different values of N_{pl} for $\xi > 0$ and $\xi < 0$ in Fig. 4.5. In addition, in the same plots I also the absolute difference of the TE cross-correlation weighted by the square root of the product of the two auto-correlators. Note that in the CC case, where $\xi = -1/6$ is larger than the values of the coupling shown in Fig. 4.5, a smaller $\Delta\tilde{N}_{pl}$ is needed to generate effects of the same order of magnitude.

Another important signature of the NMC model is in the matter power spectra, that I plot in Fig. 4.6 where I show the relative differences for the matter power spectrum at $z = 0$ with respect to the ΛCDM model for different values of the parameters. In all the cases the $P(k)$ is enhanced at small scales, i.e. $k \gtrsim 0.01$ h Mpc^{-1}, compared to the ΛCDM model. This is a generic feature of these theories and can be traced back $G_{\rm eff}$ decreasing with time. A larger gravitational strength at early time indeed enhances structure formation. An explicit example of ST theories in which a weaker gravitational strength at early time helps suppress structure formation is given in the next Chapter.

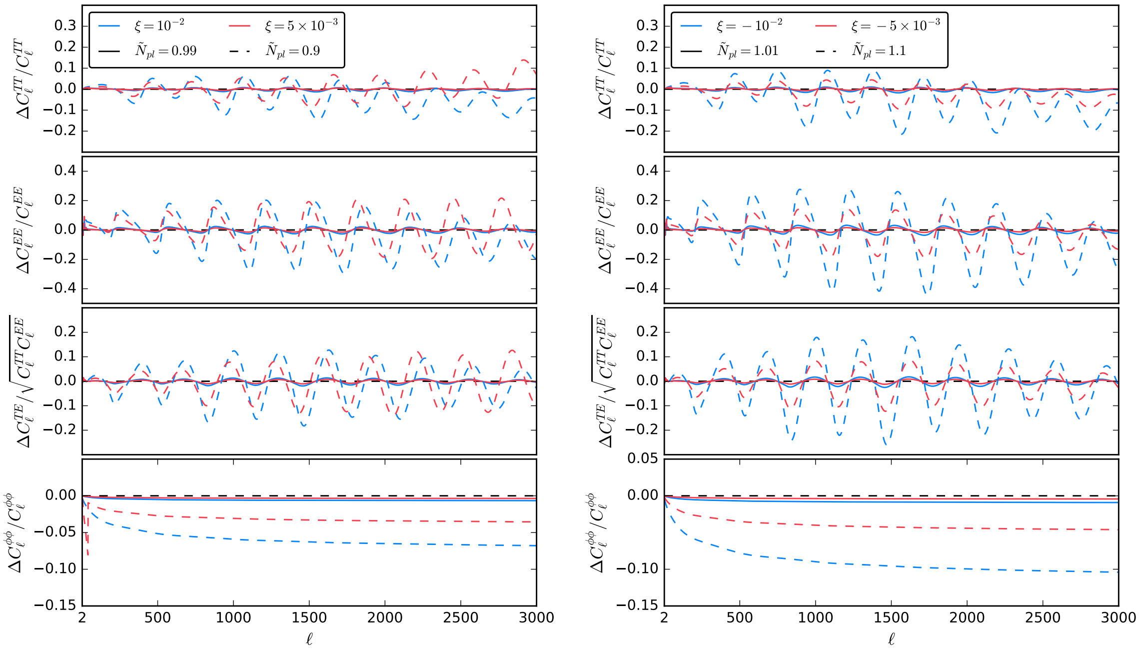

Figure 4.5: From top to bottom: relative differences of the TT-EE-TE-$\phi\phi$ power spectra with respect to the ΛCDM model for $\tilde{N}_{pl} = 1, 0.9$ ($\tilde{N}_{pl} = 1.01, 1.1$) and different values of $\xi = 10^{-2}$, 5×10^{-3} ($\xi = -10^{-2}$, -5×10^{-3}) in the left and right panel respectively. Figure taken from Ref. [2].

4.2.2 Cosmological constraints from Planck DR2

I now present the results of the of Ref. [2]. Note that the CMB and BAO data are not the most recent one. All the data sets are described in Chapter 1. Separate MCMCs for each of the two branches of negative and positive ξ were performed in Ref. [2]. Although this is not strictly necessary, it greatly simplifies the given that different boundary conditions have to be imposed in each branch.

The results from the MCMC exploration are summarized in Table 4.1. A lower bound is found for the positive branch of the coupling at 95% CL:

$$N_{pl} > 0.81\ [\mathrm{M}_{pl}], \tag{4.2.6}$$

$$\xi < 0.064. \tag{4.2.7}$$

I show in the left panel o Fig. 4.7 a zoom of the 2D parameter space (H_0, ξ) and compare the result of NMC to the ones for IG for the same data set obtained in Ref. [222], i.e. $N_{pl} = 0$. The constraint on ξ is degraded by almost two order of magnitude ($\xi < 0.0075$ at 95% CL for IG [222]) due to a degeneracy between N_{pl} and ξ, see right panel.

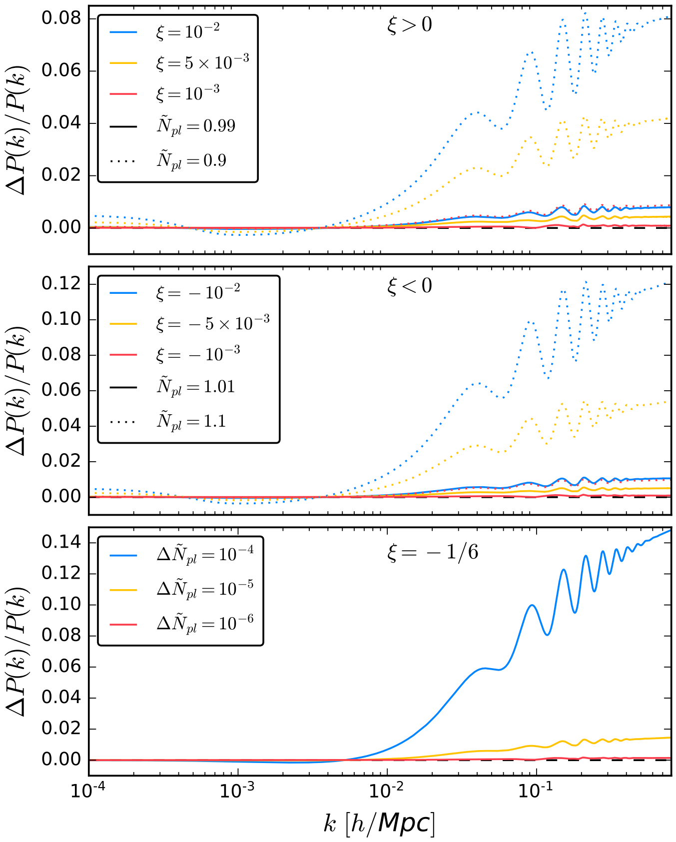

Figure 4.6: From top to bottom: relative differences of the matter power spectra at $z = 0$ with respect to the ΛCDM model for $\xi > 0$, $\xi < 0$ and $\xi = -1/6$. Figure taken from Ref. [2].

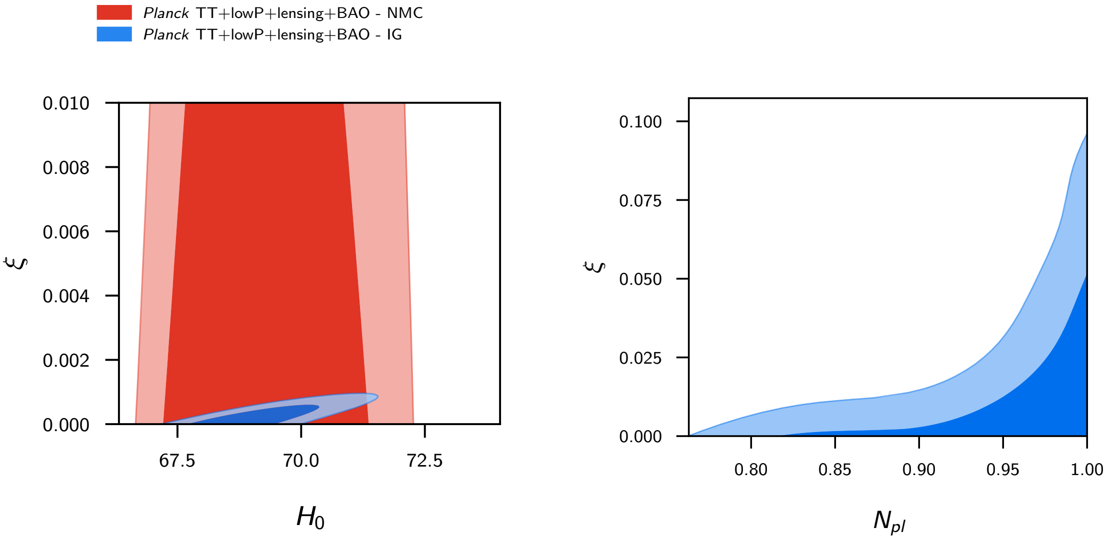

Figure 4.7: [Left] 2D marginalized confidence levels at 68% and 95% for (H_0, ξ) for NMC $\xi > 0$ (red) and IG (blue) with P15 + BAO11. [Right] 2D marginalized confidence levels at 68% and 95% for (N_{pl}, ξ) for NMC $\xi > 0$ with the same data set.

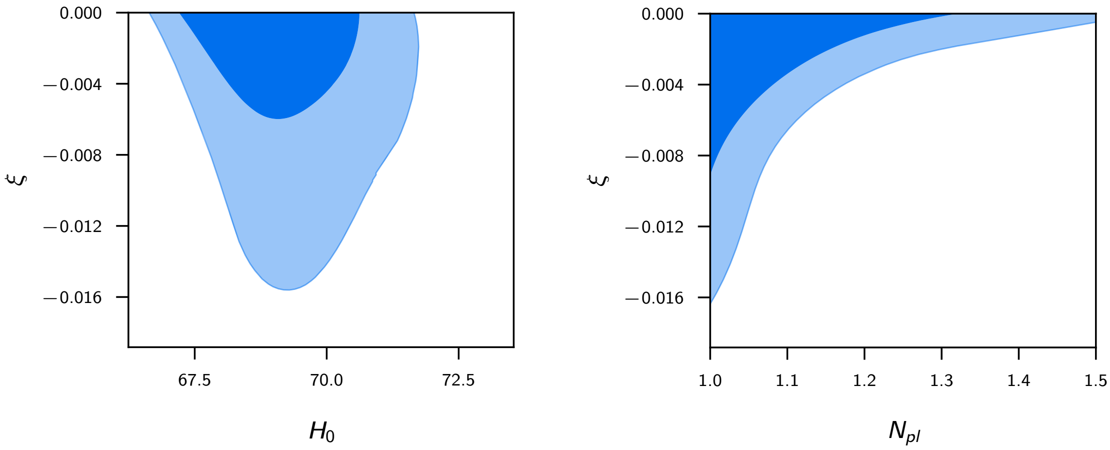

Figure 4.8: [Left] 2D marginalized confidence levels at 68% and 95% for (H_0, ξ) for NMC $\xi < 0$ with P15 + BAO11. [Right] 2D marginalized confidence levels at 68% and 95% for (N_{pl}, ξ) for NMC $\xi < 0$ with P15 + BAO11. Figure taken from Ref. [2].

The constraints for the negative branch are (see Fig. 4.8):

$$N_{pl} < 1.39 \ [\mathrm{M}_{pl}], \tag{4.2.8}$$

$$\xi > -0.11. \tag{4.2.9}$$

at the 95% CL for P15 + BAO11.

I also quote the derived constraints on the change of the effective Newton's constant (2.2.19) evaluated between the radiation era and the present time, and also its derivative at present time at 95% CL:

$$\frac{\delta G_{\rm eff}}{G} > -0.027\,, \tag{4.2.10}$$

$$\frac{\dot{G}_{\rm eff}}{G}(z=0) > -1.4\left[\times 10^{-13}\,\mathrm{yr}^{-1}\right]\,, \tag{4.2.11}$$

for $\xi > 0$, and:

$$\frac{\delta G_{\rm eff}}{G} > -0.027\,, \tag{4.2.12}$$

$$\frac{\dot{G}_{\rm eff}}{G}(z=0) > -0.97\left[\times 10^{-13}\,\mathrm{yr}^{-1}\right]\,, \tag{4.2.13}$$

for $\xi < 0$.

For the CC case, i.e. fixing $\xi = -1/6$, results are listed in Tab. 4.4. This model is severely constrained by data leading to tight upper bound on N_{pl} at 95% CL:

$$1 < N_{pl} < 1.000038 \ [\mathrm{M}_{pl}], \tag{4.2.14}$$

	P15 + BAO11 ΛCDM	P15 + BAO11 IG	P15 + BAO11 ($\xi > 0$)	P15 + BAO11 ($\xi < 0$)
$\omega_{\rm b}$	0.02225 ± 0.00020	$0.02224^{+0.00020}_{-0.00021}$	0.02226 ± 0.00019	0.02226 ± 0.00021
$\omega_{\rm c}$	0.1186 ± 0.0012	0.1191 ± -0.0014	0.1190 ± 0.0015	0.1189 ± 0.0015
H_0 [km s^{-1} Mpc^{-1}]	67.78 ± 0.57	$69.4^{+0.7}_{-0.9}$	$69.2^{+0.8}_{-1.1}$	$69.2^{+0.7}_{-1.0}$
$\tau_{\rm re}$	0.066 ± 0.012	$0.063^{+0.012}_{-0.014}$	0.068 ± 0.014	0.069 ± 0.013
$\ln\left(10^{10}A_{\rm s}\right)$	3.062 ± 0.024	$3.059^{+0.022}_{-0.026}$	$3.069^{+0.023}_{-0.027}$	3.071 ± 0.024
$n_{\rm s}$	0.9675 ± 0.0045	$0.9669^{+0.0042}_{-0.0047}$	0.9674 ± 0.0046	0.9728 ± 0.0043
ξ	...	< 0.00075 (95% CL)	< 0.064 (95% CL)	> -0.011 (95% CL)
N_{pl} [M$_{pl}$]	...	0	> 0.81 (95% CL)	< 1.39 (95% CL)
$\gamma_{\rm PN}$	1	> 0.9970 (95% CL)	> 0.995 (95% CL)	> 0.997 (95% CL)
$\beta_{\rm PN}$	1	1	> 0.99987 (95% CL)	< 1.000011 (95% CL)
$\delta G_{\rm N}/G_{\rm N}$	...	$-0.009^{+0.003}_{-0.009}$	> -0.027 (95% CL)	> -0.027 (95% CL)
$10^{13}\,\dot{G}_{\rm N}(z=0)/G_{\rm N}$ [yr^{-1}]	...	-0.37^{+34}_{-12}	> -1.4 (95% CL)	> -0.97 (95% CL)

Table 4.1: Constraints on main and derived parameters for P15 + BAO11 (at 68% CL if not otherwise stated). In the first column I report the results obtained for the branch with $\xi > 0$ and in the second the branch for $\xi < 0$. In the first column I report the results obtained for the ΛCDM model with the same dataset [252] and in the second column IG case, i.e. $N_{pl} = 0$, for comparison [222].

	P15 + BAO11	P15 + BAO11 + R18
$\omega_{\rm b}$	0.02223 ± 0.00021	0.02228 ± 0.00021
$\omega_{\rm c}$	$0.1188^{+0.0014}_{-0.0015}$	0.1187 ± 0.0015
H_0 [km s^{-1} Mpc^{-1}]	$69.19^{+0.77}_{-0.93}$	70.20 ± 0.83
$\tau_{\rm re}$	$0.068^{+0.012}_{-0.014}$	$0.070^{+0.013}_{-0.015}$
$\ln\left(10^{10}A_{\rm s}\right)$	3.070 ± 0.024	3.074 ± 0.024
$n_{\rm s}$	0.9699 ± 0.0045	0.9728 ± 0.0043
N_{pl} [M$_{pl}$]	< 1.000038 (95% CL)	$1.000028^{+0.000012}_{-0.000014}$
$\gamma_{\rm PN}$	> 0.99996 (95% CL)	1.00003 ± 0.00001
$\beta_{\rm PN}$	< 1.000003 (95% CL)	0.999998 ± 0.000001

Table 4.2: Constraints on main and derived parameters for *Planck* TT + lowP + lensing + BAO in the case of the CC model (at 68% CL if not otherwise stated).

where $\tilde{N}_{pl}$ can take only values larger than one in this case.

All these models provide a fit to *Planck* 2015 and BAO data very similar to ΛCDM with an improvement of $\Delta\chi^2 \sim -2.6$ for all the models considered above. Due to the limited improvement in $\Delta\chi^2$ at the expense of additional parameters, none of these models is preferred at a statistically significant level with respect to ΛCDM.

H_0 tension. As explained above, the model mimics a dark radiation contribution at early times so it may help alleviate the H_0 tension. Indeed, although constraints compatible with the ΛCDM values for the standard cosmological parameters are found, the shifts in H_0 deserve a particular mention and the mean values for H_0 are larger for all the models studied here. Fig. 4.9 shows how the 2D marginalized contours for (H_0, N_{pl}) have a degeneracy. I find:

$$H_0 = 69.19^{+0.77}_{-0.93}\ [\text{km/s/Mpc}], \tag{4.2.15}$$

This value is larger, but compatible at 2σ level with the ΛCDM value ($H_0 = 67.78 \pm 0.57$ [km/s/Mpc]). However, it is still lower than the local measurement of the Hubble constant [253] ($H_0 = 73.52 \pm 1.62$ [km/s/Mpc]) obtained by including the MW parallaxes from R18 and Gaia to the rest of the data from [254]. Therefore the tension between the model dependent estimate of the Hubble parameter from P15 plus BAO11 data and the local measurement from [253] decreases to 2.3σ from the 3.3σ of the ΛCDM model. For comparison, by varying the number degree of relativistic species $N_{\rm eff}$ in Einstein gravity, a lower value for the Hubble parameter, i.e. $H_0 = 68.00 \pm 1.5$ [km/s/Mpc] (with $N_{\rm eff} = 3.08^{+0.22}_{-0.24}$) for *Planck* TT + lowP + lensing + BAO at 68% CL, is obtained compared to the CC case reported in Eq. (4.2.15). When the local measurement of the Hubble constant [253] is included in the fit the constraint is instead:

$$H_0 = 70.20 \pm 0.83 \text{ [km/s/Mpc]}, \tag{4.2.16}$$

$$N_{pl} = 1.000028^{+0.000012}_{-0.000014} \text{ [M}_{pl}\text{]}\,. \tag{4.2.17}$$

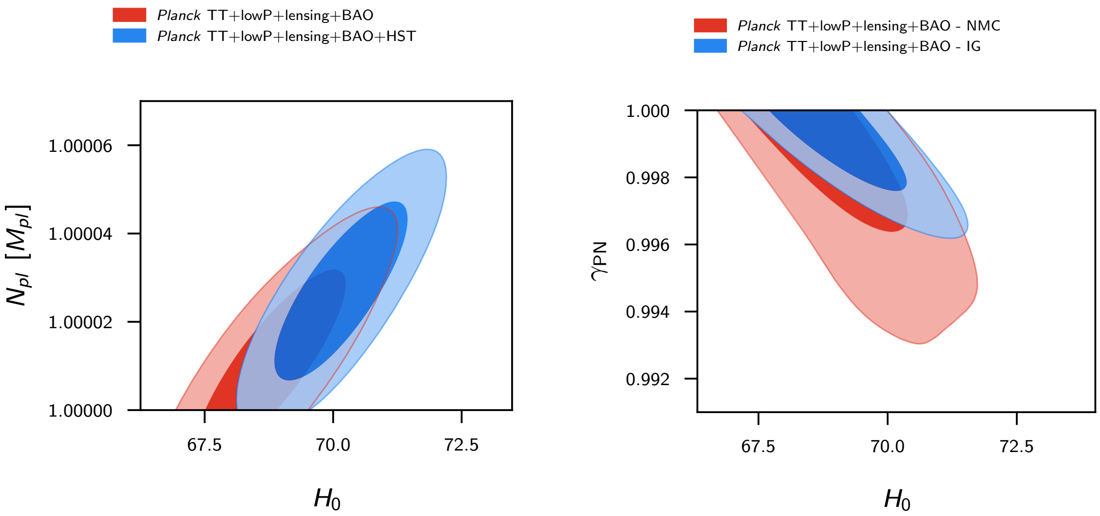

Figure 4.9: [Left] 2D marginalized confidence levels at 68% and 95% for (H_0, N_{pl}) for conformal coupling with P15 + BAO11 + R18. [Right] 2D marginalized confidence levels at 68% and 95% for (H_0, $\gamma_{\rm PN}$) for NMC $\xi > 0$ (red) and IG (blue) with P15 + BAO11. Figure taken from Ref. [2].

Constraints on the post-Newtonian parameters. Finally, I quote the derived constraints on the post-Newtonian parameters. In this class of models $\gamma_{\rm PN}$, $\beta_{\rm PN} \neq 1$

according to Eqs. (2.2.21)-(2.2.22) at 95% CL:

$$0.995 < \gamma_{\rm PN} < 1, \ \ (\xi > 0) \tag{4.2.18}$$

$$0.99987 < \beta_{\rm PN} < 1, \tag{4.2.19}$$

$$0.997 < \gamma_{\rm PN} < 1, \ \ (\xi < 0) \tag{4.2.20}$$

$$1 < \beta_{\rm PN} < 1.00001. \tag{4.2.21}$$

See Fig. 23 for the 2D marginalized constraints in the $(\gamma_{\rm PN}, \beta_{\rm PN})$ plane. See Fig. 24 for the 2D marginalized constraints in the $(H_0, \gamma_{\rm PN})$ plane for $\xi > 0$ compared to the IG case studied in [222].

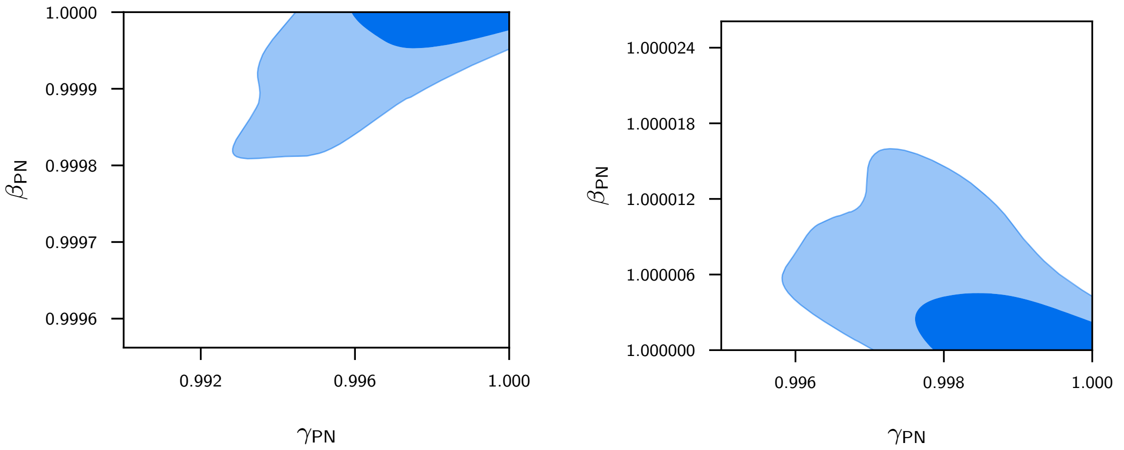

Figure 4.10: 2D marginalized confidence levels at 68% and 95% for ($\gamma_{\rm PN}$, $\beta_{\rm PN}$) for NMC $\xi > 0$ [left] and $\xi < 0$ [right] with P15 + BAO11. Figure taken from Ref. [2].

The tight constraint on N_{pl} for the CC case correspond at 95% CL to:

$$0 < 1 - \gamma_{\rm PN} < 4 \times 10^{-5}, \tag{4.2.22}$$

$$0 < \beta_{\rm PN} - 1 < 3 \times 10^{-6}, \tag{4.2.23}$$

for *Planck* TT + lowP + lensing + BAO, where the latter is tighter than the constraint from the perihelion shift $\beta_{\rm PN} - 1 = (4.1 \pm 7.8) \times 10^{-5}$ [85] and the former is twice the uncertainty of the Shapiro time delay constraint $\gamma_{\rm PN} - 1 = (2.1 \pm 2.3) \times 10^{-5}$ [134].

4.2.3 Updated cosmological constraints from Planck DR3

I now update the constraints to the most recent Planck DR3 and complementary data sets. The constraints are summarized in Table 4.3.

	P18	P18 + BAO	P18 + BAO + R19
$\omega_{\rm b}$	0.02244 ± 0.00015	0.02241 ± 0.00013	0.0250 ± 0.0013
$\omega_{\rm c}$	0.1197 ± 0.0012	0.11990 ± 0.00094	0.1195 ± 0.0010
H_0 [km s^{-1}Mpc^{-1}]	$69.0^{+0.7}_{-1.2}$ (3.2σ)	$68.62^{+0.47}_{-0.66}$ (3.6σ)	$69.64^{+0.65}_{-0.73}$ (2.8σ)
τ	$0.0554^{+0.0064}_{-0.0081}$	$0.0551^{+0.0058}_{-0.0076}$	$0.0562^{+0.0066}_{-0.0077}$
$\ln\left(10^{10}A_{\rm s}\right)$	$3.048^{+0.013}_{-0.016}$	$3.047^{+0.011}_{-0.015}$	$3.050^{+0.013}_{-0.015}$
$n_{\rm s}$	0.9684 ± 0.0047	0.9668 ± 0.0039	0.9707 ± 0.0040
$N_{\rm pl}$ [M$_{\rm pl}$]	< 1.000028 (95% CL)	< 1.000018 (95% CL)	< 1.000031 (95% CL)
γ_{PN}	> 0.999972 (95% CL)	> 0.999982 (95% CL)	> 0.999969 (95% CL)
β_{PN}	< 1.0000023 (95% CL)	< 1.0000015 (95% CL)	< 1.0000025 (95% CL)
$\delta G_{\rm N}/G_{\rm N}$	> -0.026 (95% CL)	> -0.017 (95% CL)	> -0.029 (95% CL)
$10^{13}\dot{G}_{\rm N}/G_{\rm N}$ [yr^{-1}]	$> -3.8 \times 10^{-9}$ (95% CL)	$> -2.5 \times 10^{-9}$ (95% CL)	$> -4.2 \times 10^{-9}$ (95% CL)
$G_{\rm N}/G$	> 0.999986 (95% CL)	> 0.999991 (95% CL)	> 0.999985 (95% CL)
$\Omega_{\rm m}$	$0.299^{+0.011}_{-0.009}$	0.3023 ± 0.0061	0.2928 ± 0.0064
σ_8	$0.832^{+0.011}_{-0.007}$	$0.8299^{+0.0060}_{-0.0088}$	$0.8364^{+0.0089}_{-0.011}$
r_s [Mpc]	$146.71^{+0.46}_{-0.33}$	$146.82^{+0.37}_{-0.28}$	$146.53^{+0.51}_{-0.42}$
$\Delta\chi^2$	2.2	0.8	−1.7

Table 4.3: Updated constraints on main and derived parameters (at 68% CL if not otherwise stated) considering P18 in combination with BAO and BAO + R19 for the CC model. Figure taken from Ref. [4].

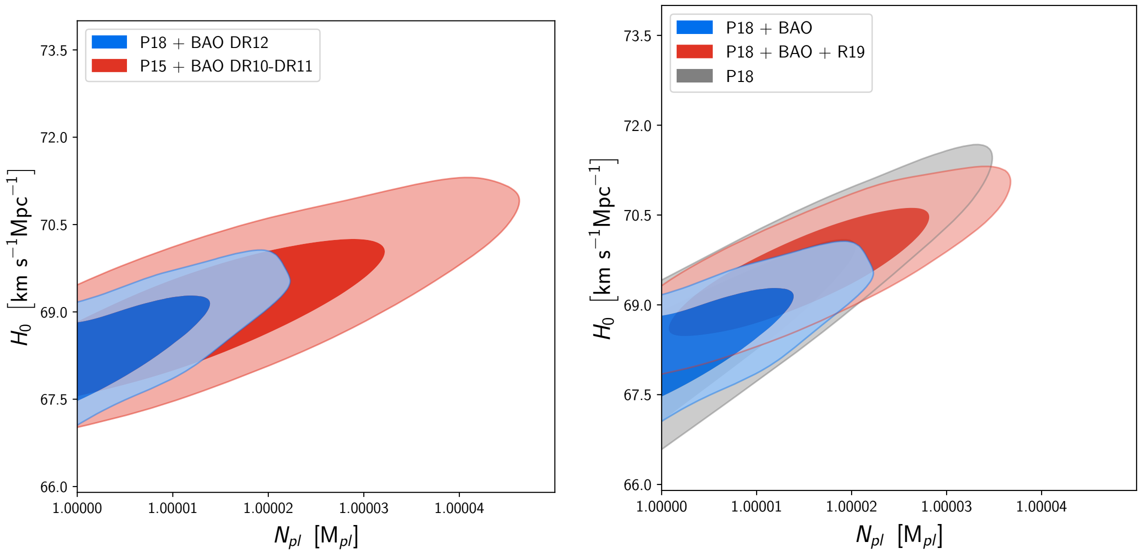

Figure 4.11: [Left] Marginalized joint 68% and 95% CL regions 2D parameter space using P18 (P15) data in combination BAO in blue (red). [Right] Marginalized joint 68% and 95% CL regions 2D parameter space using P18 (gray) in combination with BAO (blue) and BAO + R19 (red) for the CC model. Figure taken from Ref. [4].

The coupling to gravity is constrained to $N_{pl} < 1.000028\ \mathrm{M}_{pl}$ at 95% CL for P18 and $N_{pl} < 1.000018\ \mathrm{M}_{pl}$ at 95% CL in combination with BAO data. These constraints update the ones obtained with P15 in combination with D10-DR11 BAO $N_{pl} < 1.000038\ \mathrm{M}_{pl}$ at 95% CL in Ref. [2], presented in the previous Section. Again, there is a clear degeneracy between H_0 and the coupling to gravity N_{pl} as visible from Fig. 4.11. The results do not vary much for NMC, for which the same cosmological parameters and uncertainties are obtained if ξ is allowed to vary, with prior range $[0, 0.1]$ and $[-0.1, 0]$, together with N_{pl}. In particular, for the positive branch ($N_{pl} < M_{pl}$, $\xi > 0$) of the coupling I obtain:

$$N_{pl} > 0.64\ \mathrm{M}_{pl}\ (> 0.60\ \mathrm{M}_{pl})\,, \qquad \xi < 0.046\ (< 0.055) \tag{4.2.24}$$

both at 95% CL and $H_0 = \left(68.78^{+0.56}_{-0.84}\right)$ km s^{-1}Mpc^{-1} ($70.14^{+0.86}_{-0.72}$ km s^{-1}Mpc^{-1}) with P18+BAO (P18+BAO+R19). The constraints for the negative branch ($N_{pl} > M_{pl}$, $\xi < 0$) are:

$$N_{pl} < 1.05\ \mathrm{M}_{pl}\ (< 1.04\ \mathrm{M}_{pl})\,, \qquad \xi > -0.042\ (> -0.051) \tag{4.2.25}$$

both at 95% CL and $H_0 = \left(68.76^{+0.54}_{-0.78}\right)$ km s^{-1}Mpc^{-1} (69.74 ± 0.75 km s^{-1}Mpc^{-1}) with P18+BAO (P18+BAO+R19).

Consistently with the constraints on the coupling parameters ξ and N_{pl}, I find also tighter limits on the variation of the Newton's gravitational constant and its derivative at present time. The following 95% CL bounds for P18 + BAO are obtained:

$$\frac{\delta G_{\mathrm{N}}}{G_{\mathrm{N}}}(z=0) > -0.017\,, \qquad \frac{\dot{G}_{\mathrm{N}}}{G_{\mathrm{N}}}(z=0) > -0.25 \times 10^{-23}\ \mathrm{yr}^{-1}\,. \tag{4.2.26}$$

Note that whereas the constraints on $\delta G_{\mathrm{N}}/G_{\mathrm{N}}(z=0)$ hardly change for different coupling $F(\sigma)$, the limits on $\dot{G}_{\mathrm{N}}/G_{\mathrm{N}}(z=0)$ strongly depend on the details of the model, but are anyway much tighter than those obtained by the Lunar Laser Ranging experiment, see Chapter 2. It is interesting to note from Table 4.3 that the bounds on $\gamma_{\mathrm{PN}}\,, \beta_{\mathrm{PN}}$ are now tighter than those in the Solar System. Furthermore, note that although the results of this Section are obtained using $V(\sigma) \propto F^2(\sigma)$, they are stable with respect to considering $V(\sigma) = \Lambda$, since the potential is very flat around the origin. This is shown in Fig. 4.12.

H_0 tension. Concerning consequences on the H_0 tension, the inferred value of the Hubble constant is $H_0 = \left(69.0^{+0.7}_{-1.2}\right)$ km s^{-1}Mpc^{-1}, compared to the ΛCDM case, i.e. $H_0 = (67.36 \pm 0.54)$ km s^{-1}Mpc^{-1}, for P18.

The addition of BAO drives the value for H_0 to lower values, for CC to $H_0 =$

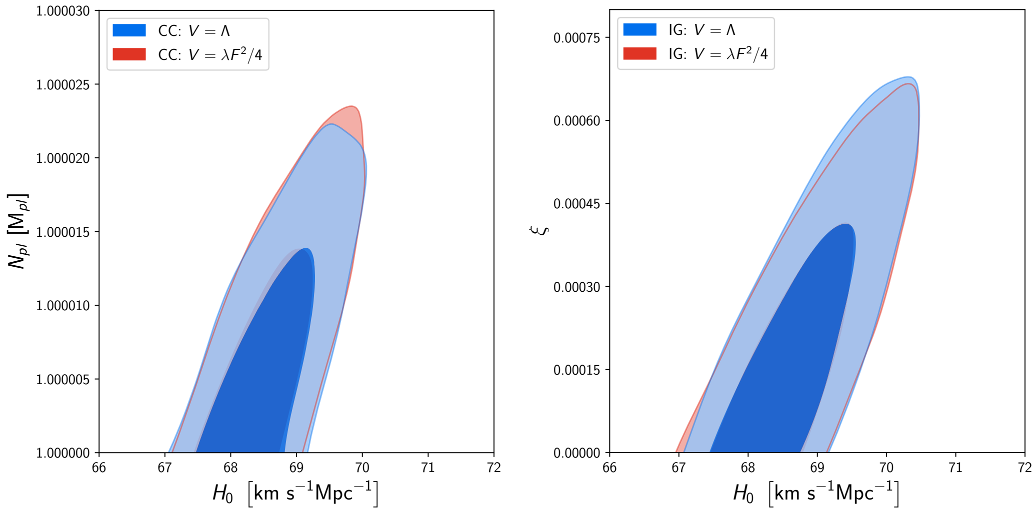

Figure 4.12: Marginalized joint 68% and 95% CL regions 2D parameter space $H_0 - N_{pl}$ using P18 + BAO data for CC [left] and IG [right] (see Sections 3.5 and 4.4) with $V(\sigma) = \lambda F(\sigma)^2/4$ (red) and $V(\sigma) = \Lambda$ (blue). Figure taken from Ref. [4].

$\left(68.62^{+0.47}_{-0.66}\right)$ km s^{-1}Mpc^{-1}. Note however that these values are larger than the corresponding ΛCDM value, i.e. $H_0 = (67.66 \pm 0.42)$ km s^{-1}Mpc^{-1}. Again, this is very important as it shows that the H_0 is generically higher in these models, even if R19 is not included.

Once R19 is included, the constraint change to $H_0 = \left(69.64^{+0.65}_{-0.73}\right)$ km s^{-1}Mpc^{-1} at 68% CL, $N_{pl} < 1.000031$ M$_{pl}$ at 95% CL for CC. Fig. 4.11 shows how the degeneracy between H_0 and ξ can easily accommodate for larger H_0 value with respect to the ΛCDM concordance model reducing the H_0 *tension* from 4.4σ to 3.2σ for P18 and 3.6σ including BAO for CC. The reduction of the tension is due to the combination of having an higher mean and larger uncertainties on H_0 compared to the ΛCDM model. Note that, although the tension with R19 is not solved, the CC model considered here can produce values of H_0 in complete agreement with the local value of H_0 measured using red giants [255].

4.3 Initial conditions on the scalar field σ_i

As mentioned in Section 4.1, fixing the boundary conditions on the scalar field so to recover consistency with laboratory experiments is not the only possibility. Indeed, as shown in Section 4.2, when the coupling is negative the scalar field decreases and the non-minimal coupling tends to $F(\sigma) \to F(\sigma_0) \sim N_{\rm pl}^2$. In the simplest case $N_{\rm pl} = M_{\rm pl}$, this suggests that consistency with laboratory and Solar System tests might be recovered even without imposing any boundary condition on σ in some regions of the parameter space. This approach was explored in Ref. [3], where the

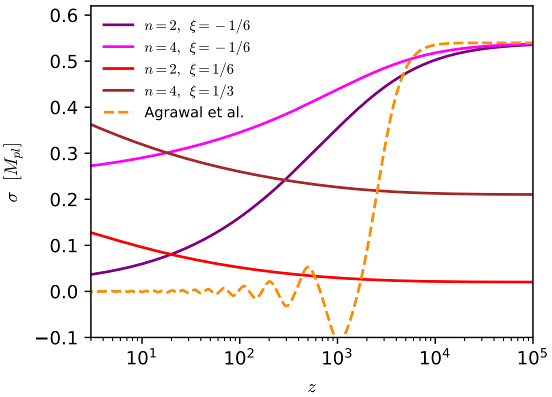

Figure 4.13: Evolution of the scalar field σ for the models with $n = 2$, $\xi < 0$ (purple lines), $n = 4$, $\xi < 0$ (magenta lines), $n = 2$, $\xi > 0$ (red lines) and $n = 4$, $\xi > 0$ (brown lines), together with the EDE model of Ref. [199] (orange lines) and the ΛCDM+$N_{\rm eff}$ model (cyan lines). In order to compare the evolution of our model to the aforementioned ones, I set the cosmological parameters to the bestfit values in Table 3 of Ref. [199] and set $\xi = -1/6$. In the cases with $\xi > 0$, I change the values of the initial conditions on the scalar field and the coupling ξ as in the plot legends. Figure taken from Ref. [3].

analysis was carried out for $F(\sigma) = M_{\rm pl}^2 + \xi\sigma^n$ and $V(\sigma) = \Lambda$, for both $n = 2$ and $n = 4$.

I plot the evolution of the scalar field σ is shown in Fig. 4.13 and other relevant background quantities is shown in Fig. 4.14 for the case of $n = 2$ and $n = 4$ (see caption for the parameters used in the plots). As can be seen from the central panel in Fig. 4.14, the scalar field is nearly frozen deep in the radiation era, and is driven by the coupling to non-relativistic matter around the radiation-matter equality era $z \sim \mathcal{O}(10^3 - 10^4)$, as evident from the Klein-Gordon equation (2.2.14), decreasing (growing) for $\xi < 0$ ($\xi > 0$).

In order to confront with other attempts at solving the H_0 tension, I also plot the relevant quantities for two other reference models, i.e. the $\Delta N_{\rm eff}$ model and the EDE Rock'n Roll model introduced Ref. [199]. Let me stress again the important differences between the model studied here, and the two other reference cases. By considering our model as Einstein gravity analogues [110, 111], the resulting effective DE has an equation of state $w_{\rm DE} \equiv p_{\rm DE}/\rho_{\rm DE} \sim 1/3$ during radiation era (see e.g. Fig. 4.1) and the contribution of the scalar field to the total expansion rate $H(z)$ thus resembles the one from an extra *dark* radiation component. This is confirmed by the top panel in Fig. 4.14, where I plot the energy fraction of the scalar field, parameterized by $\Omega_\sigma = \rho_{\rm DE}/3H^2F_0$ - where the subscript 0 denotes quantities evaluated at $z = 0$ - and compare it to the ΛCDM+$N_{\rm eff}$ model. As can be seen, when $\xi < 0$, the scalar field contributes to the total energy density in a way that is very similar to the ΛCDM

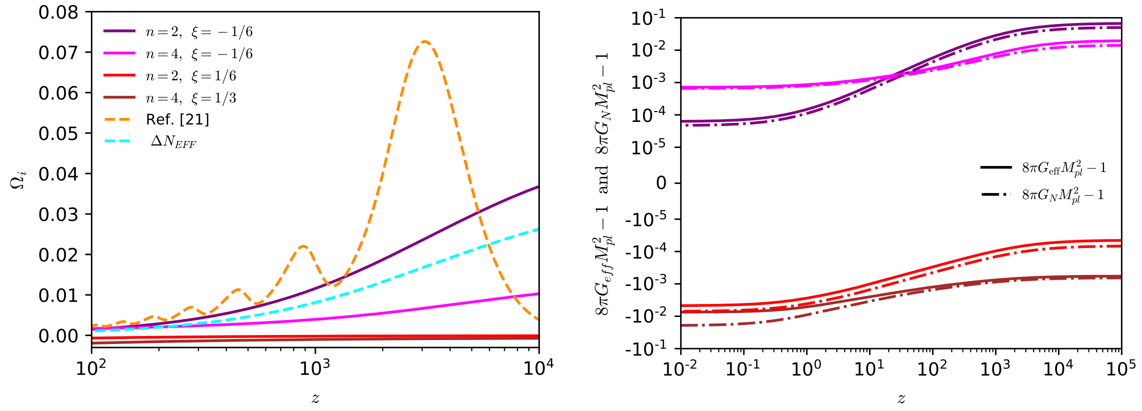

Figure 4.14: [Left] Evolution of the energy injection $\Omega_i := \rho_i/\rho_c$ and [right] the deviation from 1 of the effective (solid lines) and cosmological (dot-dashed lines) Newton constant. See Fig. 4.13 for the parameters used. Figure taken from Ref. [3].

$+N_{\rm eff}$ model. Having started with the same $\xi < 0$ and initial condition $\sigma_i/M_{\rm pl} < 1$ in both the $n = 2$ and $n = 4$ case, the term multiplying the square bracket in Eq. (2.2.14) is smaller in the latter case and the rolling of the scalar field towards smaller values is less efficient. The equation of state $w_{\rm DE}$ is not 1/3 anymore in general when the scalar field is subsequently driven by matter.

The model, as already mentioned in Chapter 3, is therefore different from EDE models recently proposed in the literature (see e.g. Refs. [189, 198, 199, 201, 202]) for which the equation of state is close to -1 at early times. Again, it is important to stress that the scalar field moves in a natural way without the need of any fine tuning after radiation-matter equality, being driven by non-relativistic matter, and is not important just around recombination.

It is also instructive to see the effects of removing the boundary conditions on the scalar field. For $\xi < 0$, being the scalar field contribution negligible at late times, both G_N and $G_{\rm eff}$ are very close to G today and the model is consistent with laboratory and Solar System experiments for a large volume of the parameter space. However, for a positive coupling ξ, σ grows and $G_{\rm eff}$, which is very close to G at high redshifts, deviates substantially from it at late times, as can be seen from the right panel in Fig. 4.14.

4.3.1 Constraints from cosmological observations

Since the boundary condition on the scalar field is now removed, a prior on its initial value deep in the radiation era has to be chosen. In Ref. [3] flat priors consistent with the stability conditions in Sec. 4.1 on the extra parameters were considered, i.e. $\xi \in [-0.9,\ 0.9]$ and $\sigma_i/M_{\rm pl} \in [0,\ 0.9]$, for $n = 2$ case with free ξ and $\sigma_i/M_{\rm pl} \in [0,\ 0.9]$

in the CC case. The analysis has been also carried out for the case with $n = 4$, in which the prior on ξ had to be restricted to $\xi \in [-0.9, 0.2]$ as larger positive values for the coupling ξ lead to a deviation of order 10^{-1} from GR as can be seen from Fig. 4.14.

Note that the analysis differs from the one of Refs. [2] presented in Section 4.2.2 not only in the updated data, but also in theoretical priors: now flat priors are set on (ξ, σ_i), whereas in [2] flat priors were assumed on $(\xi,\, \Delta\tilde{N}_{\rm pl})$, with $\xi > 0$ and $\xi < 0$ considered separately, and $\Delta\tilde{N}_{\rm pl}$ was also allowed to vary, with a boundary condition on σ_0 (the value of the scalar field today) to fix consistency between $G_{\rm eff}$ and G.

The results of our cosmological analysis for the CC ($n = 2$ with free ξ) model are summarized in Fig. 4.15 (Fig. 4.16), where I show the reconstructed two-dimensional posterior distributions of main and derived parameters, and in Table 4.4 (Table 4.5), where I report the reconstructed mean values and the 68% and 95% CL. I also report the results for the $n = 4$ case in Table 4.6

H_0 **tension.** The plots show that all the models, regardless of the dataset considered, lead to a larger H_0 than in ΛCDM. I find $H_0 = 68.47^{+0.58}_{-0.86}$ ($H_0 = 68.40^{+0.59}_{-0.80}$) km s^{-1}Mpc^{-1} at 68% CL for CC (for free ξ) with P18 data only. As in other similar models, as also mentioned in Chapter 4, there is a shift in $n_s\,, \omega_c\,, \sigma_8$ toward larger values and smaller values for ω_b compared to the baseline ΛCDM model. When BAO and SH0ES data are combined, i.e. P18+BAO+R19, I obtain $H_0 = 69.29^{+0.59}_{-0.72}$ ($H_0 = 69.10^{+0.49}_{-0.66}$) km s^{-1}Mpc^{-1} for CC (for free ξ). Higher values for H_0 can be obtained by substituting the combination of measurements V19[1] to R19, as can be seen from Tables 4.4 and 4.5. Note that similar results are also obtained in the $n = 4$ case, for which the value of $H_0 = 68.05 \pm 0.56$ ($H_0 = 69.09^{+0.52}_{-0.69}$) km s^{-1}Mpc^{-1} with P18 (P18+BAO+R19) data slightly smaller than th $n = 2$ case. For this reason, I focus the discussion on the $n = 2$ case in the following, commenting only when results for $n = 4$ substantially differ.

In Tables 4.5, 4.4 and 4.6, I also report the difference in the best-fit of the model with respect to ΛCDM, i.e. $\Delta\chi^2 = \chi^2 - \chi^2(\Lambda\text{CDM})$, where negative values indicate an improvement in the fit of the given model with respect to the ΛCDM for the same dataset [2]. Although the models studied here provide a similar or slightly worst fit

---

[1] With V19, I denote a tight Gaussian likelihood, i.e. $H_0 = 73.3 \pm 0.8$ km s^{-1}Mpc^{-1} [146], obtained from a combination of H_0 measurements from R19 [145], MIRAS [150], CCHP [255], H0LiCOW [159], MCP [256] and SBF. The reader should be warned that the V19 value is obtained by neglecting covariances between the aforementioned observations, as stressed in Ref. [146]. Nevertheless, V19 can give an idea of how the model can respond to a possible future worsening of the H_0 tension.

[2] Note that the ΛCDM reference cosmology in our case has massless neutrinos, differently from the assumption adopted by the Planck collaboration of one massive neutrino with $m_\nu = 0.06$ eV consistent with a normal hierarchy with minimum mass allowed by particle physics. The differences

to P18 data compared to ΛCDM, the fit gets better $\Delta\chi^2 \sim -5$ (-6.8) for CC (free ξ) when BAO+R19 are combined. Higher values of $\Delta\chi^2$ are obviously obtained by substituting V19 to R19. In order to give an idea of whether the improvement in the fit actually leads to a statistical preference for the model, I compute values of the Aikike (Bayes) information criteria ΔAIC (ΔBIC) defined as $\Delta\mathrm{AIC} = \Delta\chi^2 + 2\Delta p$ ($\Delta\mathrm{BIC} = \Delta\chi^2 + \Delta p \ln N$), where Δp is the number of extra parameters with respect to ΛCDM model and N is the number of data points considered in the MCMC analysis [1] [257]. According to both criteria, all the models are penalized compared to ΛCDM for P18 data only due to the addition of parameters. Only for AIC the model with $n = 2$ is favoured for (CC) free ξ compared to ΛCDM when BAO and R19 are combined. Substituting V19 to R19 makes the statistical preference of the model stronger in general.

Constraints on modified gravity parameters: The constraints on the modified gravity parameter are very different in the CC and $n = 2$ case, which are a one- and two-parameter extension of the ΛCDM model. Although the mean values are very similar, constraints are very much looser in the latter case. This is because, when ξ is large and negative, the decreasing of the scalar field is very efficient and thus its effect redshifts away even before matter-radiation equality, leaving smaller imprints on the CMB. Note that positive values of ξ, for which the scalar field increases after matter-radiation equality contributing to the late-time background evolution, seem disfavoured by the data for our priors. In particular for P18, I find an upper bound $\xi < 0.052$ ($\xi < 0.02$) at the 2σ level for $n = 2$ ($n = 4$). The upper bound is even more stringent when BAO + R19 data are added to the analysis, for which $\xi < 0.047$ ($\xi < -0.026$) at the 2σ level for $n = 2$ ($n = 4$).

Comparison with BBN constraints: With the choice of the priors as above, the departure of $\sqrt{F}$ from $M_{\rm pl}$ can also be constrained by BBN, as explained in Chapter 2 Section [128–130, 258]. Since the scalar field is frozen at very early times, the BBN constraints reported in [128, 129] would imply $\xi\sigma_i^n = 0.01^{+0.20}_{-0.16}$ at 68% CL, which are consistent, but less stringent, than the constraints reported in Tables 4.4, 4.5 and 4.6, as already mentioned in previous works on scalar-tensor [222]. The constraints from the MCMC analysis are $-0.014^{+0.026}_{-0.052}$ (> -0.0150) for the $n = 2$ (CC[2]) and $-0.0010^{+0.0029}_{-0.0076}$ for the $n = 4$ case at 95% CL using P18 data only. When adding BAO+R19 a higher $\xi\sigma_i^n$ is obtained and the constraints change to $-0.025^{+0.037}_{-0.070}$

---

with respect to the baseline *Planck* results in the estimate of the cosmological parameters due the choice $N_{\rm eff} = 3.046$ and $m_\nu = 0$ is small, except for a shift towards higher values for H_0, as $H_0 = 67.98 \pm 0.54$ ($H_0 = 68.60 \pm 0.43$) km s^{-1}Mpc^{-1} for P18 (P18+BAO+R19).

[1] I consider 2352 points for P18, 8 for BAO and 1 (6) for R19 (V19).

[2] Note that, in the CC case, $\xi\sigma_i^2 < 0$ by construction.

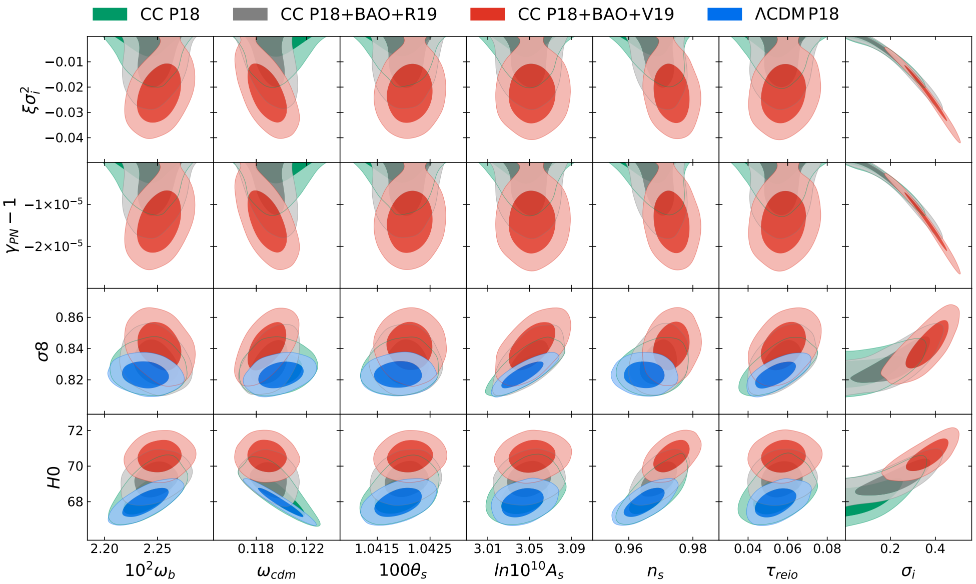

Figure 4.15: Constraints on main and derived parameters of the CC model with $n = 2$ and $\xi = -1/6$ from Planck 2018 data (P18), P18 in combination with BAO and SH0ES measurements and P18 in combination with BAO and a combined prior which takes into account all the late time measurements. Parameters on the bottom axis are sampled MCMC parameters with flat priors, and parameters on the left axis are derived parameters (with H_0 in [km s^{-1}Mpc^{-1}]). Constraints for the ΛCDM model obtained with P18 data are also shown for a comparison. Contours contain 68% and 95% of the probability. Figure taken from Ref. [3].

(> -0.0234) for the $n = 2$ (CC) and $-0.013^{+0.021}_{-0.038}$ for the $n = 4$ case at 95% CL. Note that $\xi\sigma_i^n$ is more constrained in the CC case compared to $n = 2$ and $n = 4$, as the coupling is fixed to $\xi = -1/6$.

Comparison with PN: The derived cosmological PN parameters are well consistent with GR and their uncertainties are comparable with bounds from Solar System experiments [85, 134]. Again, because of the large errors on ξ, the bounds in the $n = 2$ model are somewhat looser than in the CC model. Therefore, the CC ($n = 2$) model potentially offers a simple one (two) modified gravity parameter extension to the baseline ΛCDM that naturally eases the H_0 tension and can be consistent at 2σ with Solar System constraints on the deviation from GR. I have checked that the inclusion of Solar System constraints in the analysis by means of a Gaussian prior based on the Cassini constraint $\gamma_{\rm PN} - 1 = 2.1 \pm 2.3 \times 10^{-5}$ [134] has a very small impact in our constraints on the six standard cosmological parameters.

For the representative example of $n = 2$ with free ξ the constraint on H_0 obtained from P18+BAO+R19 changes to $H_0 = 69.00^{+0.47}_{-0.57}$ km s^{-1}Mpc^{-1}. The constraints on the modified gravity parameters instead change substantially. Thanks to the constraining power of the prior I find $\sigma_i = 0.19^{+0.13}_{-0.08}\, M_{\rm pl}$ at 68% CL and

$\gamma_{\rm PN} - 1 > -2.2 \cdot 10^{-6}$ and a bound on $\xi < -0.15$ at 95% CL. Although ξ remains unconstrained, note that the upper limit is tighter than the the one obtained without the prior information on $\gamma_{\rm PN}$. Negative values of ξ are more favored as they lead to a more efficient rolling of the scalar field toward smaller values, and therefore a smaller $\gamma_{\rm PN} - 1$.

Robustness and caveats of the inclusion of SNe data: So far I did not use the SNe Ia luminosity distance because the time evolution of gravitational constant changes the peak luminosity of SNe and this needs to be properly accounted in the analysis [235–238]. However, for the bestfit value obtained from P18 + BAO + R19 with the priors on $\gamma_{\rm PN}$, the relative change of $G_{\rm eff}$ from G today is at most 10^{-5} in the relevant range of redshifts for SNe Ia. Under the assumption that the effect of time evolution of $G_{\rm eff}$ on the magnitude-redshift relation of SNe Ia can be ignored, the Pantheon Sample of SNe can be used to check the robustness of our constraint on H_0 [84]. I obtain $H_0 = 69.28^{+0.58}_{-0.74}$ ($H_0 = 68.98^{+0.46}_{-0.54}$) km s^{-1}Mpc^{-1} for CC (for free ξ) using P18+BAO+R19+Pantheon with the prior on $\gamma_{\rm PN}$. This shows that the inclusion of SNe Ia data does not change the constraint on H_0. Note also that the modification of the gravitational constant can also change the low-redshift distance ladder measurements of the Hubble constant [233, 234]. However, again due to the smallness of the relative change of $G_{\rm eff}$ from G today, this effect can be ignored safely in our models.

Comparison with other EDE models: Models based on a sharp energy injection around the time of matter-radiation equality lead to a value of H_0 which can be higher than the ones found within our model for any choice of n and ξ although this is model dependent (see e.g. Refs. [189, 198, 199, 201, 202]). However, the radiation-like behavior of the scalar field in theories described by the action (2.2.3), is completely generic and, provided that the coupling ξ is negative, the scalar field contribution quickly becomes negligible thanks to the coupling to non-relativistic matter and modifies essentially only the early time dynamics. For this reason, a higher H_0 than in ΛCDM is a natural outcome of the NMC for a large portion of the parameter space compared to EDE models, which have more extra parameters to tune.

4.4 Cosmological constraints on the Induced Gravity model

Before ending this Chapter, I present the constraints on the IG model, introduced in Section 3.5. Like Section, I consider here a very flat potential of the form $V(\sigma) =$

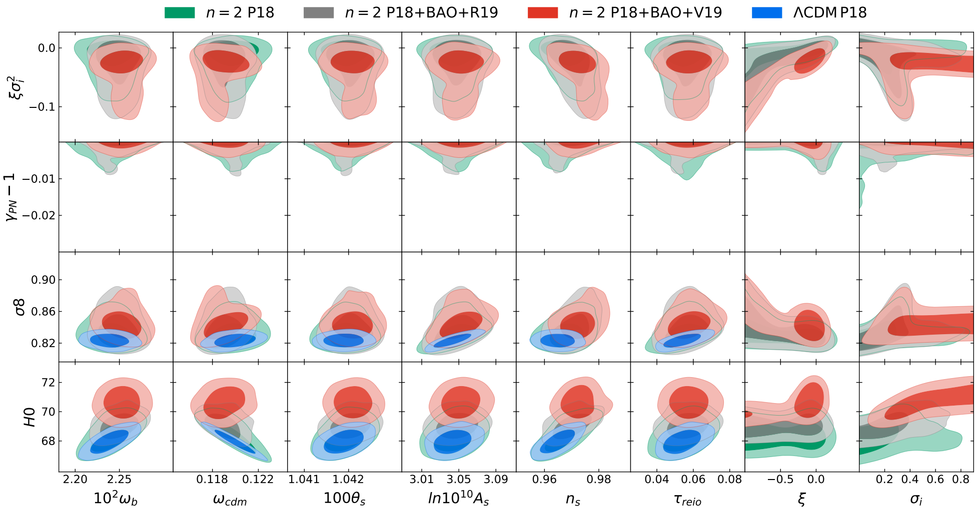

Figure 4.16: Constraints on main and derived parameters of the model with $n = 2$ and ξ as a main parameter from *Planck* 2018 data (P18), P18 in combination with BAO and SH0ES measurements and P18 in combination with BAO and a combined prior which takes into account all the late time measurements. Parameters on the bottom axis are our sampled MCMC parameters with flat priors, and parameters on the left axis are derived parameters (with H_0 in [km s^{-1}Mpc^{-1}]). Constraints for the ΛCDM model obtained with P18 data are also shown for a comparison. Contours contain 68% and 95% of the probability. Figure taken from Ref. [3].

CC	P18	P18 + BAO + R19	P18 + BAO + V19
$10^2\omega_{\rm b}$	2.242 ± 0.015	2.248 ± 0.014	2.252 ± 0.013
$\omega_{\rm c}$	0.1197 ± 0.0012	0.11910 ± 0.00099	0.1188 ± 0.0010
$100 * \theta_s$	1.04194 ± 0.00030	1.04205 ± 0.00028	1.042 ± 0.00028
$\tau_{\rm reio}$	0.0547 ± 0.0077	0.0570 ± 0.0071	0.05803 ± 0.0075
$\ln\left(10^{10} A_{\rm s}\right)$	3.046 ± 0.015	3.049 ± 0.014	3.053 ± 0.015
$n_{\rm s}$	0.9675 ± 0.0046	0.9695 ± 0.0038	0.9734 ± 0.0037
σ_i [M$_{\rm pl}$]	$0.1312^{+0.039}_{-0.13}$	$0.224^{+0.13}_{-0.081}$	$0.3585^{+0.078}_{-0.047}$
H_0 [km s^{-1}Mpc^{-1}]	$68.47^{+0.58}_{-0.86}$	$69.29^{+0.59}_{-0.72}$	70.56 ± 0.6
σ_8	$0.8272^{+0.0063}_{-0.0081}$	$0.8313^{+0.0079}_{-0.011}$	0.841 ± 0.010
r_s [Mpc]	$146.97^{+0.33}_{-0.29}$	$146.83^{+0.48}_{-0.34}$	146.4 ± 0.45
$\xi\sigma_i^2$ [$M_{\rm pl}^2$]	> -0.0150	> -0.0234	$-0.022^{+0.016}_{-0.015}$
σ_0 [M$_{\rm pl}$]	$0.004017^{+0.0012}_{-0.004}$	$0.006841^{+0.004}_{-0.0025}$	$0.01102^{+0.0024}_{-0.0015}$
$\gamma_{\rm PN} - 1$	$> -0.95 \cdot 10^{-5}$	$> -1.5 \cdot 10^{-5}$	$\left(-1.4^{+1.0}_{-0.9}\right) \cdot 10^{-5}$
$\beta_{\rm PN} - 1$	$\left(0.23^{+0.61}_{-0.34}\right) \cdot 10^{-6}$	$\left(0.53^{+0.75}_{-0.61}\right) \cdot 10^{-6}$	$\left(1.16^{+0.78}_{-0.84}\right) \cdot 10^{-6}$
$\Delta\chi^2$	$+0.42$	-5.0	-13.64

Table 4.4: Constraints on main and derived parameters considering P18, P18 in combination with BAO and SH0ES measurements and P18 in combination with BAO and a combined prior which takes into account all the late time measurements for the CC model $n = 2$ and $\xi = -1/6$. I report mean values and the 68% CL, except for the modified gravity derived parameters in the third block, for which I report the 95% CL.

$n=2$	P18	P18 + BAO + R19	P18 + BAO + V19
$10^2\omega_{\rm b}$	2.241 ± 0.015	2.249 ± 0.014	2.253 ± 0.014
$\omega_{\rm c}$	0.1198 ± 0.0012	$0.11903^{+0.00095}_{-0.0011}$	0.1190 ± 0.0012
$100 * \theta_s$	1.04193 ± 0.00030	1.04205 ± 0.00031	1.04210 ± 0.00029
$\tau_{\rm reio}$	0.0544 ± 0.0076	0.0564 ± 0.0076	0.0578 ± 0.0072
$\ln\left(10^{10} A_{\rm s}\right)$	3.045 ± 0.0014	3.048 ± 0.015	3.052 ± 0.014
$n_{\rm s}$	0.9673 ± 0.0046	0.9699 ± 0.0046	0.9724 ± 0.0041
σ_i [M$_{\rm pl}$]	< 0.224	$0.260^{+0.088}_{-0.19}$	> 0.46
ξ	< 0.052 (95% CL)	< 0.047 (95% CL)	< -0.0283(95% CL)
H_0 [km s^{-1}Mpc^{-1}]	$68.40^{+0.59}_{-0.80}$	$69.10^{+0.49}_{-0.66}$	70.64 ± 0.71
σ_8	$0.8456^{+0.013}_{-0.018}$	$0.8370^{+0.0072}_{-0.020}$	$0.8450^{+0.0088}_{-0.014}$
r_s [Mpc]	147.01 ± 0.36	$146.95^{+0.48}_{-0.30}$	$146.08^{+0.77}_{-0.89}$
$\xi\sigma_i^2$ $[M_{\rm pl}^2]$	$-0.014^{+0.026}_{-0.052}$	$-0.025^{+0.037}_{-0.070}$	$-0.030^{+0.030}_{-0.074}$
σ_0 [M$_{\rm pl}$]	$0.1046^{+0.40}_{-0.18}$	$0.09^{+0.46}_{-0.19}$	$0.20^{+0.33}_{-0.26}$
$\gamma_{\rm PN} - 1$	$> -1.73 \cdot 10^{-3}$	$> -1.56 \cdot 10^{-3}$	$> -1.26 \cdot 10^{-3}$
$\beta_{\rm PN} - 1$	$-\left(3.0^{+1.8}_{-1.6}\right) \cdot 10^{-5}$	$-\left(3.0^{+1.7}_{-1.4}\right) \cdot 10^{-5}$	$-\left(1.5^{+2.9}_{-2.5}\right) \cdot 10^{-5}$
$\Delta\chi^2$	$+0.52$	-6.8	-18.44

Table 4.5: Constraints on main and derived parameters considering P18, P18 in combination with BAO and SH0ES measurements and P18 in combination with BAO and a combined prior which takes into account all the late time measurements for $n = 2$. I report mean values and the 68% CL, except for the modified gravity derived parameters in the third block, for which I report the 95% CL.

$n=4$	P18	P18 + BAO + R19	P18 + BAO + V19
$10^2\omega_{\rm b}$	2.240 ± 0.015	2.250 ± 0.013	2.258 ± 0.013
$\omega_{\rm c}$	0.1198 ± 0.0012	0.11892 ± 0.00093	0.11830 ± 0.00097
$100 * \theta_s$	1.04190 ± 0.00028	1.04205 ± 0.00028	1.04217 ± 0.00028
$\tau_{\rm reio}$	0.0545 ± 0.0074	0.0564 ± 0.0076	$0.0596^{+0.0070}_{-0.0078}$
$\ln\left(10^{10} A_{\rm s}\right)$	3.045 ± 0.014	3.049 ± 0.015	3.055 ± 0.015
$n_{\rm s}$	0.9662 ± 0.0043	$0.9706^{+0.0037}_{-0.0042}$	$0.9757^{+0.0039}_{-0.0044}$
σ_i [M$_{\rm pl}$]	< 0.257	$0.37^{+0.20}_{-0.17}$	$0.55^{+0.13}_{-0.11}$
ξ	< 0.02 (95% CL)	< -0.026 (95% CL)	< -0.031(95% CL)
H_0 [km s^{-1}Mpc^{-1}]	68.05 ± 0.56	$69.09^{+0.52}_{-0.69}$	70.23 ± 0.54
σ_8	0.8247 ± 0.0061	$0.8370^{+0.0072}_{-0.020}$	$0.845^{+0.010}_{-0.018}$
r_s [Mpc]	147.06 ± 0.28	$146.96^{+0.39}_{-0.33}$	$146.69^{+0.38}_{-0.43}$
$\xi\sigma_i^4$ $[M_{\rm pl}^4]$	$-0.0010^{+0.0029}_{-0.0076}$	$-0.013^{+0.021}_{-0.038}$	$-0.035^{+0.038}_{-0.057}$
σ_0 [M$_{\rm pl}$]	$0.18^{+0.39}_{-0.22}$	$0.18^{+0.25}_{-0.17}$	$0.20^{+0.21}_{-0.13}$
$\gamma_{\rm PN} - 1$	$> -1.72 \cdot 10^{-4}$	$> -1.65 \cdot 10^{-4}$	$> -2.34 \cdot 10^{-4}$
$\beta_{\rm PN} - 1$	$\left(-0.8^{+11.0}_{-9.4}\right) \cdot 10^{-6}$	$\left(0.4^{+6.1}_{-3.8}\right) \cdot 10^{-6}$	$\left(2.5^{+7.4}_{-6.6}\right) \cdot 10^{-6}$
$\Delta\chi^2$	-0.58	-1.14	-9.42

Table 4.6: Constraints on main and derived parameters considering P18, P18 in combination with BAO and SH0ES measurements and P18 in combination with BAO and a combined prior which takes into account all the late time measurements for $n = 4$. I report mean values and the 68% CL, except for the modified gravity derived parameters in the third block, for which I report the 95% CL.

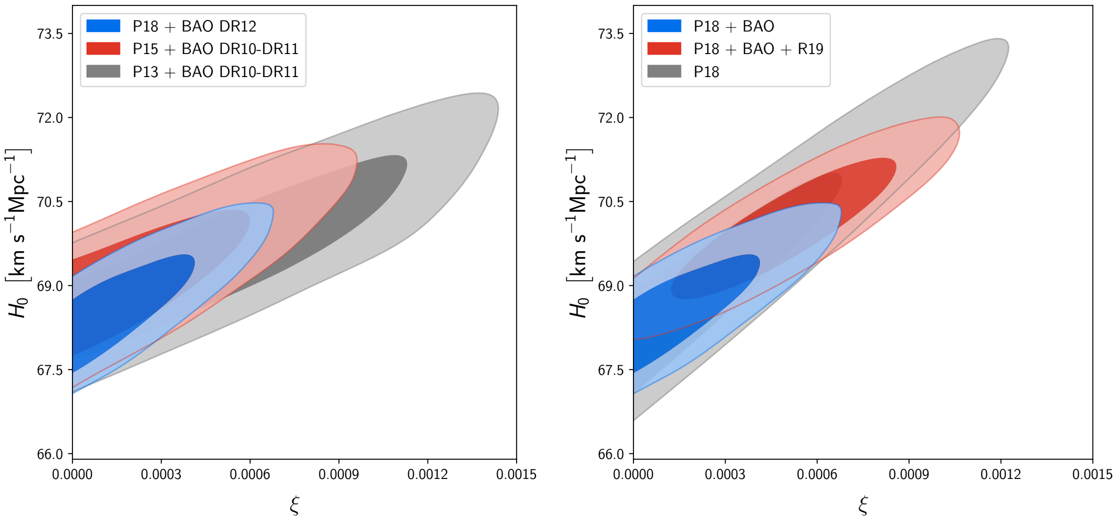

Figure 4.17: [Left] Marginalized joint 68% and 95% CL regions 2D parameter space using current versus previous releases of P18 data and BOSS BAO data from [221,222]. [Right] Marginalized joint 68% and 95% CL regions 2D parameter space using P18 (gray) in combination with BAO (blue) and BAO + R19 (red) for the IG model. Figure taken from Ref. [4].

$\lambda F(\sigma)^2/4$ so that the theory is effectively massless and the motion of the scalar field is entirely driven by the coupling to pressureless matter. Again, the results are stable when switching to an exactly flat potential $V(\sigma) = \Lambda$, see Fig. 4.12.

Unlike the NMC model, here the scalar field undergoes a super-Planckian motion so that it is never convenient to set initial conditions on σ_i like in Section 4.3 and one is forced to use the procedure described in Section 4.2 and set the boundary condition in Eq. (4.2.1) on the value of the scalar field today σ_0. I now discuss the cosmological constraints on the IG model obtained in Ref. [4] using such a procedure.

The constraint on the coupling parameter ξ obtained from the CMB alone is almost half of the bound obtained with P15 which was $\xi < 0.0017$ at 95% CL. With the full high-ℓ polarization information and the new determination of τ I obtain $\xi < 0.00098$ at 95% CL. Adding the BAO data, I obtain $\xi < 0.00055$ at 95% CL, which is 25% tighter compared to the limit obtained with P15 in combination with BAO DR10-11, i.e. $\xi < 0.00075$ and half of the one obtained with P13 in combination with BAO DR10-11, i.e. $\xi < 0.0012$, see the left panel of Fig. 4.17. As can be seen from Tab. 4.7, BAO data strongly constrain the model and are useful to break the degeneracy in the $H_0 - \xi$ parameter space.

Concerning the H_0 tension, I find a higher value for the Hubble parameter, i.e. $H_0 = \left(69.6^{+0.8}_{-1.7}\right)$ km s^{-1}Mpc^{-1} compared to the ΛCDM case, i.e. $H_0 = (67.36 \pm 0.54)$ km s^{-1}Mpc^{-1}, for P18. The addition of BAO drives the value for H_0 to a lower $H_0 = \left(68.78^{+0.53}_{-0.78}\right)$ km s^{-1}Mpc^{-1}, but again larger than the corresponding ΛCDM

	P18	P18 + BAO	P18 + BAO + R19
$\omega_{\rm b}$	$0.02244^{+0.00014}_{-0.00016}$	0.02239 ± 0.00013	0.02246 ± 0.00013
$\omega_{\rm c}$	0.1198 ± 0.0012	0.1201 ± 0.0011	0.1200 ± 0.0011
H_0 [km s^{-1}Mpc^{-1}]	$69.6^{+0.8}_{-1.7}$ (2.7σ)	$68.78^{+0.53}_{-0.78}$ (3.5σ)	70.06 ± 0.81 (2.4σ)
τ	$0.0551^{+0.0065}_{-0.0078}$	$0.0545^{+0.0063}_{-0.0071}$	$0.0554^{+0.0064}_{-0.0073}$
$\ln\left(10^{10} A_{\rm s}\right)$	$3.047^{+0.014}_{-0.015}$	3.046 ± 0.013	3.049 ± 0.013
$n_{\rm s}$	$0.9680^{+0.0044}_{-0.0052}$	0.9662 ± 0.0038	0.9688 ± 0.0037
$\zeta_{\rm IG}$	< 0.0039 (95% CL)	< 0.0022 (95% CL)	$0.00202^{+0.00090}_{-0.00100}$
ξ	< 0.00098 (95% CL)	< 0.00055 (95% CL)	$0.00051^{+0.00043}_{-0.00046}$ (95% CL)
γ_{PN}	> 0.9961 (95% CL)	> 0.9978 (95% CL)	$0.9980^{+0.0010}_{-0.0009}$
$\delta G_{\rm N}/G_{\rm N}$ (z=0)	> -0.029 (95% CL)	> -0.016 (95% CL)	-0.0149 ± 0.0068
$10^{13}\dot{G}_{\rm N}/G_{\rm N}$ (z=0) [yr^{-1}]	> -1.16 (95% CL)	> -0.66 (95% CL)	-0.61 ± 0.28
$G_{\rm N}/G$ (z=0)	> 0.9981 (95% CL)	> 0.9989 (95% CL)	$0.99899^{+0.00050}_{-0.00045}$
$\Omega_{\rm m}$	$0.2940^{+0.0150}_{-0.0095}$	$0.3013^{+0.0072}_{-0.0062}$	0.2903 ± 0.0068
σ_8	$0.8347^{+0.0074}_{-0.0130}$	$0.8308^{+0.0067}_{-0.0096}$	0.840 ± 0.010
r_s [Mpc]	$146.37^{+0.79}_{-0.40}$	$146.63^{+0.55}_{-0.34}$	$146.03^{+0.67}_{-0.59}$
$\Delta\chi^2$	0.2	0.2	-3.1

Table 4.7: Constraints on main and derived parameters (at 68% CL if not otherwise stated) considering P18 in combination with BAO and BAO + R19 for the IG model.

value, i.e. $H_0 = (67.66 \pm 0.42)$ km s^{-1}Mpc^{-1}.

Once R19 is included, I obtain $H_0 = (70.1 \pm 0.8)$ km s^{-1}Mpc^{-1} at 68% CL and a constraint on the coupling of $\xi = 0.00051^{+0.00043}_{-0.00046}$ at 95% CL for IG. Fig. 4.17 shows how the degeneracy between H_0 and ξ can easily accommodate for larger H_0 value with respect to the ΛCDM concordance model reducing the H_0 *tension* from 4.4σ to 2.7σ for P18 and 3.5σ including BAO. Again, as for the NMC model, the reduction of the tension is due to the combination of having an higher mean and larger uncertainties on H_0 compared to the ΛCDM model. Note that H_0 is about ~ 0.5 km s^{-1}Mpc^{-1} higher in the IG compared to the CC case for every choice of datasets combination, see Section 4.2.

4.5 Summary of the results

In this Chapter, I have studied the evolution of NMC models described by the Lagrangian Eq. (2.2.3) with $F(\sigma) = N_{\rm pl}^2 + \xi\sigma^2$ and a potential of the form $V(\sigma) = \lambda F(\sigma)^2/4$ or $V(\sigma) = \Lambda$ and constrained them with cosmological data. I explored two possibilities to set the boundary conditions on the free parameters of the theory. The first one, adopted in Refs. [2, 4], is to set the Newton constant G to be consistent with laboratory measurements and the second one, adopted in Ref. [3], is instead to leave the initial condition on σ deep in the radiation as a free input parameter with $N_{\rm pl} = M_{\rm pl}$. A particularly interesting case is the CC one, i.e. $\xi = -1/6$, justified by theoretical arguments, therefore reducing to 1 the number of extra parameters with respect to the baseline ΛCDM model.

The results of this Chapter show that NMC models generically lead to a larger H_0, with interesting consequences on the H_0 tension which is always alleviated within these models, no matter what combination of data sets is considered. Although the reduction in the tension is not as effective as in EDE models (see Chapter 4), the bright side is the degree of fine tuning, which is considerably reduced within NMC since the requirement of σ moving around recombination is naturally embedded in this framework as triggered by its coupling to pressureless matter fields, unlike EDE models, where the potential has to be finely tuned.

In the particular case of a negative coupling, for which σ decreases, the consistency with both laboratory and Solar System experiments is recovered without the need of any screening mechanism. It is very interesting to see that in this case, there is no need to impose specific boundary conditions on the scalar field and cosmological data alone seem to favour the negative branch of the coupling. Note that the results obtained here for the CC case have recently been confirmed in Ref. [259], where also weak lensing data and the full shape of the power spectrum have been used.

A relevant limit of the NMC model, i.e. the IG or eJBD model, which is the archetypal example of ST theory, has also been discussed in Chapters 2 and 3. In this model I consider only a positive coupling and therefore the analysis is limited to the case in which the consistency of the Newton constant with laboratory experiments is set. However, even imposing such a condition, Solar System constraints are tighter than those from cosmology. Concerning the H_0 tension, the value of H_0 is always ~ 0.5 km s^{-1} Mpc^{-1} larger than in NMC models. I end on noting that future galaxy surveys in combination with CMB will further constrain the IG model [260,261], with a precision comparable to Solar System tests.

Chapter 5

Cosmological constraints on Non-Minimally Coupled theories with a small effective mass and consequences on the H_0 tension

5.1 Introducing a small effective mass

All the models studied in the previous Chapter had in common the feature of being nearly massless, since the scalar field σ had a either a flat potential or $V(\sigma) \propto F(\sigma)^2$, also very close to flat. In this Chapter, I explore the possibility that the scalar field is endowed with a small effective mass, that I constrain with cosmological data.

A minimal realization of this model can be obtained by extending the model of Section 4.3, by providing it with a small effective mass, which for the sake of simplicity I consider as induced by a quartic potential. In this model, the scalar field starts to move around the redshift of matter-radiation equality driven by the coupling to non-relativistic matter, and then rolls faster when the effective mass become larger than the Hubble parameter and ends in a regime of coherent oscillations around the minimum of the potential. The choice of a quartic potential is dictated by the fact that coherent oscillations of σ are in conformal time and therefore tractable by an Einstein-Boltzmann code, without ad-hoc modifications, see e.g. Ref. [262]. Note also that with this choice the model is described only by dimensionless couplings, i.e. ξ and λ.

A peculiarity of the model is that, thanks to the fast rolling of σ towards the bottom of the potential, the tight constraints on G_{eff} from laboratory experiments and Solar System measurements on post-Newtonian parameters are automatically satisfied by the small cosmological values of σ within the EMG model, as it happens in the range of $\xi < 0$ in the massless case where σ is decreased just by coupling to non-relativistic matter (see previous Chapter). The small effective mass and the consequent naturally achieved consistency of cosmology with laboratory and Solar System constraints are particularly important for positive values of the coupling, since σ would grow for $\xi > 0$ for $\lambda = 0$, and therefore I mainly focus on this range.

Because of its similarity to EDE models (see Section 3.4), I denote this model as Early Modified Gravity (EMG). Note, however, that the model differs from previously introduced ones also named Early Modified Gravity [263–265].

Another interesting feature of this EMG is that the effective Newtonian constant $G_{\rm eff}$ grows with time, as opposed to nearly massless models (see e.g. Fig. 4.3), implying a weaker gravity at early times. This effect, as shown below, implies different predictions on Large Scale Structure (LSS) observables that can help disentangle EMG and EDE. This is crucial, since, as mentioned in Section 3.4, EDE models have been recently claimed not to be able to solve the H_0 tension when LSS data are included in the analysis [216–218].

This Chapter is based on the research work in Ref. [266] and the plots are produced using a modified version of `hiCLASS` [246, 247] which allows to study consistently oscillating scalar fields.

5.2 Background evolution

As mentioned above, the model is described by Eq. (2.2.3) with $F(\sigma) = M_{\rm pl}^2 + \xi\sigma^2$ and $V(\sigma) = \Lambda + \lambda\,\sigma^4/4$, where Λ is a cosmological constant. Note that, with this choice, the model reduces to the one studied in Section 4.3 for $\lambda = 0$ and to the Rock'n'Roll EDE model of Ref. [199] for $\xi = 0$. For later convenience, it is useful to define $\lambda \equiv 10^{2V_0}/(3.516 \times 10^{109})$[1].

The evolution of relevant background quantities is shown in Fig. 5.1. For a comparison, I consider the bestfit cosmological parameters given in Table 3 of Ref. [199], that is

$$\begin{aligned}&\theta_s = 1.0417, \quad 100\,\omega_b = 2.264, \quad \omega_c = 0.1267, \quad \tau_{\rm reio} = 0.081, \quad \ln 10^{10} A_s = 3.105,\\ &n_s = 0.981, \quad \sigma_i[M_{\rm pl}] = 0.54, \quad V_0 = 2 \end{aligned} \tag{5.2.1}$$

for EMG, for which I vary the non-minimal coupling ξ according to the legend in the figures, and

$$\begin{aligned}&\theta_s = 1.0422, \quad 100\,\omega_b = 2.236, \quad \omega_c = 0.1177, \quad \tau_{\rm reio} = 0.077, \quad \ln 10^{10} A_s = 3.080,\\ &\quad n_s = 0.969 \end{aligned} \tag{5.2.2}$$

---

[1] 3.516×10^{109} is the *numerical* value of $M_{\rm pl}^4$ in eV^4

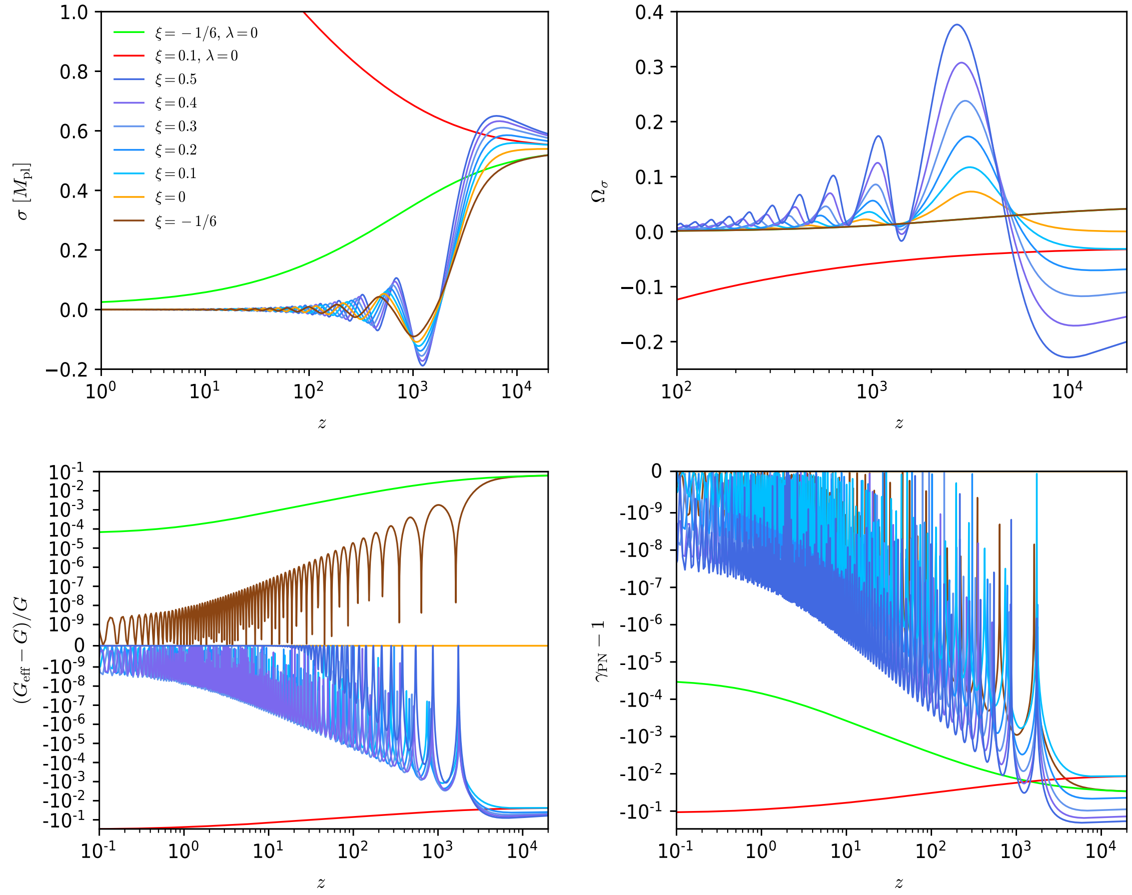

Figure 5.1: [Top] Evolution of the scalar field (left) and the energy injection Ω_σ defined in the main text. [Bottom] Evolution of the variation of the effective Newton constant $(G_{\rm eff} - G)/G$ (left) and of the post-Newtonian parameter $\gamma_{\rm PN} - 1$ (right). The model parameters used in the plot are $\sigma_i = 0.54\, M_{\rm pl}$ and $V_0 = 2$ and the value of the non-minimal coupling ξ is varied according to the legend in the top-left panel. Figure taken from Ref. [266].

for the ΛCDM model to which I compare the results. These values are only used to build intuition and will be superseded the cosmological parameter estimation presented in the next Section. As can be seen from the top-left panel, the addition of the effective mass makes EMG more similar to EDE models (see Fig. 3.6) with respect to nearly massless NMC models [2, 3, 228]. Indeed, σ starts frozen deep in the radiation era and, when its effective mass becomes larger than the Hubble flow, eventually rolls down the potential and starts oscillating around its effective minimum located at $\sigma = 0$. It is clear from Fig. 5.1, that the corrections to the effective mass of the scalar field induced by the non-minimal coupling $F(\sigma)$ modify the dynamics of σ, which, for $\xi \geq 0$, experiences a temporary growth before falling down the potential. Because of this initial growth, the oscillations around $\sigma = 0$ have a visibly larger amplitude and their phase is slightly shifted compared to the case with $\xi = 0$.

The importance of such a modification to the dynamics for $\xi = 0$ can be understood by looking at the shape of Ω_σ in the top-right panel of Fig. 5.1. For the same values of $\{\sigma_i, V_0\}$, a larger ξ sizeably increases the energy that the scalar field injects into the cosmic fluid once it starts to roll down its potential, an effect which, at a fixed value of ξ, can also be obtained by increasing the initial value of the scalar field σ_i. On the other hand, for larger values of ξ, Ω_σ becomes gradually more negative, therefore suppressing $H(z)$, with respect to the $\xi = 0$ case, before σ starts to thaw, reducing the degeneracy of the non-minimal coupling ξ with the initial condition σ_i (see also next Section). Therefore the EMG model offers a broader phenomenology than EDE ones, which is interesting since the exact shape in redshift of the energy injection plays a crucial role in physical models that aim at solving the H_0 tension, as stressed in Section 3.4.

Although the main focus of the following analysis will be on the $\xi \geq 0$ regime, it is also instructive to show the behavior of Ω_σ when the coupling is negative. I take the conformal coupling $\xi = -1/6$ as an example. For such a large and negative ξ, the profile of the energy injection is continuous and resembles the one in models with extra dark radiation, exactly as the massless case with $\lambda = 0$ in Section 4.3.

By the addition of the effective mass, consistency of $G_{\rm eff}$ and PN parameters with Cavendish-type measurements and Solar System constraints, respectively, can be obtained without any fine tuning for $\xi > 0$, as can be seen from the bottom panels of Fig. 5.1. Note also that, thanks to the potential $V(\sigma)$, $G_{\rm eff}$ now grows with time, which is not possible in standard scalar-tensor models involving only the coupling $F(\sigma)$, for which $G_{\rm eff}$ decreases with time regardless of the sign of the non-minimal coupling, see Fig. 4.3. However, in the conformally coupled case, $G_{\rm eff}$ decreases as in the massless case [3].

5.3 Imprints of the Non-Minimal coupling on CMB and LSS

I now show the imprints of EMG on CMB and LSS observables. The temperature and E-mode polarization CMB angular power spectra are shown in the top panels of Fig. 5.2, from which it can be seen that the coupling sizeably affects the acoustic peaks structure of the CMB spectra, as a consequence of the modification to gravity around recombination. However, note that thanks to the potential $V(\sigma)$ and the different cosmological evolution of σ, the imprint of ξ is drastically reduced with respect to the massless case with $\lambda = 0$. Indeed, in the latter case, relative changes in $\Delta C_\ell / C_\ell$ of the same magnitude of the ones shown in the top panels of Fig. 5.2 can be obtained with much smaller values of ξ, see e.g. Fig. 9 of Ref. [2]. It is also instructive to see that the modifications to acoustic peaks for $\xi = -1/6$ are out of phase with respect to the case of a positive coupling.

As discussed in the previous Subsection, the non-minimal coupling ξ enhances the energy injection of the scalar field into the cosmic fluid, similarly to what can be obtained with a larger σ_i. In order to compare the two effects, in the bottom panels of Fig. 5.2, I fix $\xi = 0$ and plot the residual CMB spectra for a set of initial conditions σ_i that give the same maximum energy injection of the curves presented in the top panel. Although both parameters modify the acoustic structure of the CMB, the pattern of the CMB residuals is different. In particular, given the same energy injection obtained by varying ξ or σ_i with $\xi = 0$ respectively, the former has a stronger impact on the CMB since, thanks to the non-minimal coupling, the scalar field modifies the expansion history already while it is frozen, slightly decreasing $H(z)$ since its effective energy density is negative (see Fig. 5.1).

In the perspective of future experiments dedicated to CMB polarization, it is also instructive to show the imprints of EMG on primordial B-mode polarization. These are shown in Fig. 5.3, where I vary ξ in the left panel and fix $\xi = 0$ and vary σ_i in the right one. As explained in Section 2.3.1, the non-minimal coupling modifies the propagation equation for the two polarization states of the gravitational waves $h_{+,\times}$. In the language of Eq. (2.3.2), in this model the non-minimal coupling contributes to an additional friction term $\alpha_M = \dot{F}/HF$.

As shown in Refs. [265, 267, 268], such an additional friction term induced by the non-minimal coupling may leave interesting observational signatures. In the case of $V(\sigma) = 0$, the impact on B-mode polarization was analyzed in Ref. [2], where it was found the effects increase with $|\xi|$. In the EMG model, where the potential $V(\sigma)$

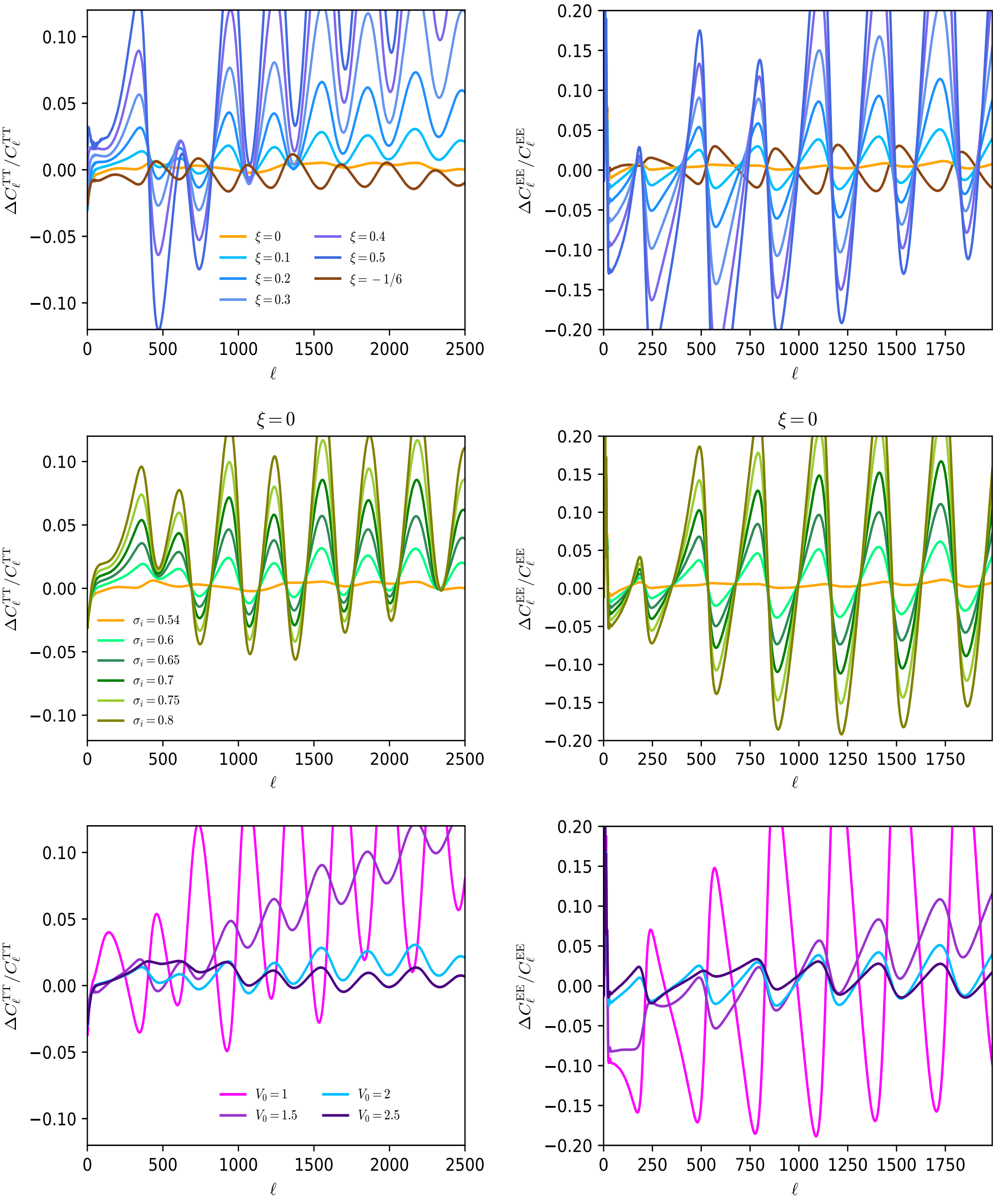

Figure 5.2: [Top] Lensed CMB TT (left) and EE (right) angular power spectrum as a function of the non-minimal coupling ξ. [Center] Lensed CMB TT (left) and EE (right) angular power spectrum as a function of the initial condition on the scalar field σ_i with $\xi = 0$. [Bottom] Lensed CMB TT (left) and EE (right) angular power spectrum as a function of the potential parameter V_0 keeping the non-minimal coupling fixed to $\xi = 0.1$. I utilize the set of parameters used to produce Fig. 5.1.

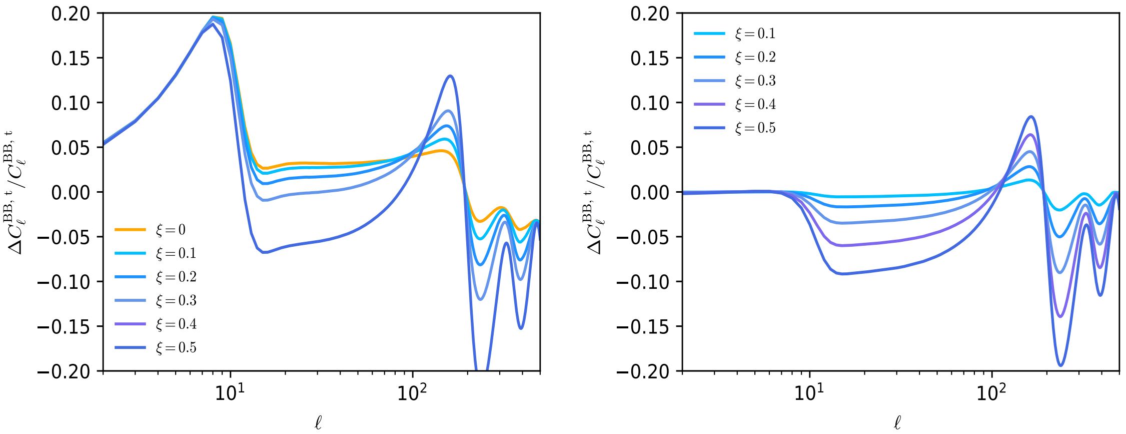

Figure 5.3: CMB BB angular power spectrum due to tensor perturbations. In order to clarify the distinction between effects due to the shift in cosmological parameters and the genuine effects of the non-minimal coupling, I plot both the relative differences between the EDE and ΛCDM baselines in Eq. (5.2.1) and (5.2.2) (left) and the ones obtained by fixing the EDE parameters in Eq. (5.2.1) and varying ξ (right). I set the tensor-to-scalar ratio to $r_{0.05} = 0.05$. The lensing spectra are almost unaffected by the variation of these parameters, so the relative differences for the total spectra do not change from the ones in the plots. Figure taken from Ref. [266].

enlarge the range of ξ which is compatible with the data (see next Section), the effects can indeed be larger, as can be seen from the left panel of Fig. 5.3. The effect of an increasing ξ is twofold. First it changes the acoustic structure of the C_ℓ's for $\ell \gtrsim 100$, with a pattern which cannot be mimicked by a change in σ_i, similarly to what happens with the other CMB spectra, as can be appreciated by looking at the right panel of Fig. 5.3. Second, it also decreases the power in the range $10 \lesssim \ell \lesssim 100$ compared to the ΛCDM model. The plots also show a bump at very large scales. This, however, is a feature which is not directly ascribed to the EMG model or the EDE one. In fact, such a peak comes from the interplay of the different cosmological parameters in Eqs. (5.2.1) and (5.2.2). Nevertheless, such a bump also occurs when considering the relative differences between the bestfit values for ΛCDM and EMG/EDE cosmologies shown in the next Section, and thus it may constitute an indirect signature of EMG and EDE models that can be tested with future CMB B modes experiments.

Since EDE scenarios have been recently shown to be constrained by the matter power spectrum at low redshift [216–218, 269, 270], it is important to investigate the imprints of our model also on LSS and compare them to the ones of NMC and EDE models. I plot the ratio between the linear matter power spectra for our EMG model and the ΛCDM one in the left panel of Fig. 5.4. As previously studied in [2, 221–224], the matter power spectrum is enhanced at small scales in effectively massless

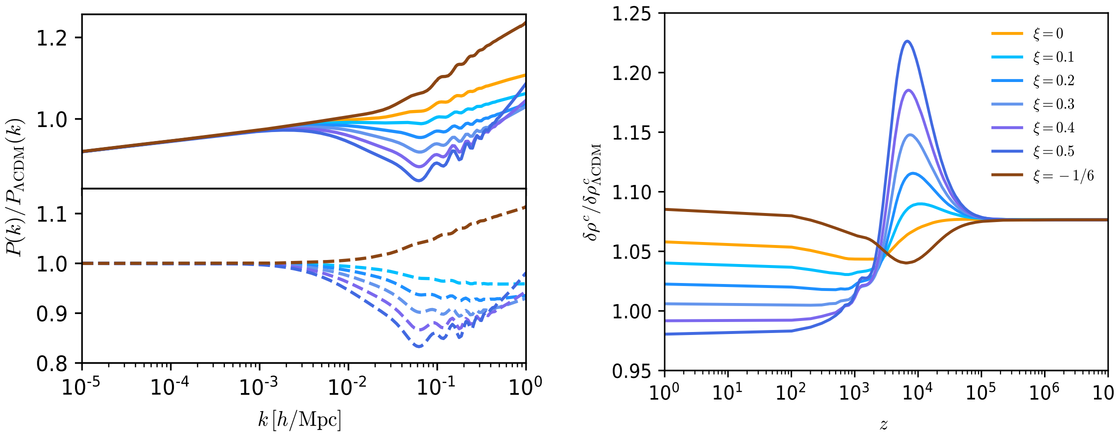

Figure 5.4: Ratio of the EMG and ΛCDM linear matter power spectra at $z = 0$ (left) and evolution of the dark matter perturbation $\delta\rho_c$ for $k = 0.1\ h/\mathrm{Mpc}$ divided by the one for the ΛCDM model (right) as a function of the non-minimal coupling ξ. As in the previous plot, for solid lines, I utilize the set of parameters used to produce Fig. 5.1 and I compute relative differences between the EDE and ΛCDM baselines in Eq. (5.2.1) and (5.2.2). To make clear which are the effects due only to the variation of ξ, I also plot in dashed lines $P(k)$ by keeping fixed the EDE baseline parameters in Eq. (5.2.1) and varying ξ in dashed lines. Figure taken from Ref. [266].

scalar-tensor models aiming at alleviating the H_0 problem since gravity was relatively stronger at early times. Analogously, EDE models also enhance the matter power spectrum at small scales compared to the ΛCDM one, as can be seen from the orange line in the plot. It is however important to understand that this effect is not due to the EDE component itself, but rather by the shift towards a larger ω_c that is needed to maintain the fit to the CMB data, see Eqs. (5.2.1) and (5.2.2). In fact, the larger is the fraction of EDE the greater is the suppression of the growth of the perturbations within the horizon during the epoch when EDE is not negligible. From the right panel of Fig. 5.4, it can be seen that, fixing all the other parameters, the non-minimal coupling ξ goes instead in the direction of suppressing the power at small scales, as it weakens the strength of gravity during the EMG epoch, see Fig. 5.1. This is not true anymore for the $\xi = -1/6$ case in which a stronger gravity ($G_{\mathrm{eff}}/G > 1$) at early times leads to an enhancement of the power at smaller scales. Again, the results are completely different from the case with $\lambda = 0$, for which the G_{eff} always decreases with time, leading to a stronger gravity at early times and a consequent larger power in $P(k)$ at small scales [2].

The results in Fig. 5.4 can be better understood by looking at the evolution of dark matter perturbations. For this purpose, the evolution of the ratio of the dark matter perturbation $\delta\rho_c$ for the EMG and the ΛCDM model for the mode $k = 0.1$

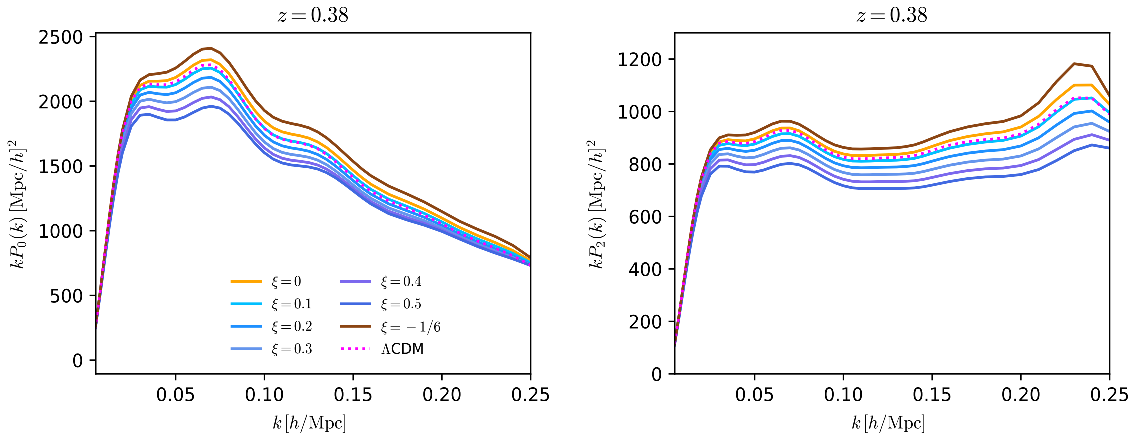

Figure 5.5: 1 loop $\ell = 0$ (left) and $\ell = 2$ (right) multipole moments of the galaxy power spectrum as a function of the non-minimal coupling ξ. I utilize the set of parameters used to produce Fig. 5.1. I also plot the ΛCDM results in magenta dotted lines for a comparison. Figure taken from Ref. [266].

h/Mpc is plotted in the right panel of Fig. 5.4. As can be seen, for a positive ξ, initially scalar field perturbations enhance the growth of dark matter perturbations with respect to the ΛCDM case, overcoming the suppression factor due to having $G_{\rm eff}/G < 1$. The opposite occurs for a negative value, as can be seen from the brown line. On even smaller scales (larger k), there is also a fifth force (scale dependent) contribution from the scalar field perturbations that further enhances the growth of dark matter perturbations at very early times with respect to the ΛCDM case, which explains the raise in the $P(k)$ at small scales for $\xi = 0.5$ in the left panel of Fig. 5.4.

Once the scalar field starts to roll down the potential, however, the scalar field perturbations become negligible and the only effect of the modification to gravity is to suppress (enhance) the gravitational potentials by a factor of $F(\sigma) < 1$ (> 1) depending on the sign of ξ, leading to the observed suppression (enhancement) in the left panel of Fig. 5.4.

Furthermore, it is instructive to show the effects on the observed redshift-space galaxy-spectrum. I plot the multipole moments in Fig. 5.5 where also the monopole $\ell = 0$ (left panel) and the quadrupole $\ell = 2$ (right panel) resummed at 1 loop order in perturbation theory are shown. These spectra are produced with the publicly available code PyBird[1] [71]. Although PyBird works in the framework of a ΛCDM effective field theory of LSS, the deviations from General Relativity at the relevant redshift considered by PyBird are so small that its use in this context is safe (see Fig. 5.1). As an example, I have considered the multipole moments at $z = 0.38$,

---

[1] https://github.com/pierrexyz/pybird

which corresponds to the redshift of the low-z NGC BOSS data (see next Section). Note that the effect of ξ is to reduce the amplitude of both $P_0(k)$ and $P_2(k)$. It is very interesting to note that, starting from the parameters in Eqs. (5.2.1) and (5.2.2), similar spectra for ΛCDM and the EMG model with $\xi = 0.1$ are recovered, suggesting that the non-minimal coupling can help reconcile EDE models with LSS observations.

5.4 Constraints from cosmological data

In this Section, I report the constraints obtained from the the MCMC exploration of the EMG model, see Ref. [266]. In this MCMC massless neutrinos ($N_{\text{eff}} = 3.046$) are assumed the I set the initial velocity of the scalar field to zero and adiabatic initial conditions on the scalar field perturbations [2, 5].

For the extra parameters I consider flat priors $\xi \in [0, 1]$, $\sigma_i/M_{\text{pl}} \in [0, 0.9]$ and $V_0 \in [0.6,\ 3.5]$. Note that EDE models are usually parameterized with two parameters describing the redshift at which the scalar field starts to roll down the potential, usually denoted as critical redshift z_c, and the maximum energy injection f_{scf} [189, 199, 200]. For the particular case of the RnR model, the correspondence between $\{V_0,\ \sigma_i\}$ and $\{z_c,\ f_{\text{scf}}\}$ is unique under the assumption of the same initial velocity of the scalar field. However, as explained in Section 5.2, this one to one correspondence is not possible in our model, where also ξ contributes to the energy injection into the cosmic fluid. For this reason, it is better to use the physical parameters describing the EMG model as in Chapter 4. Nevertheless, I quote $\log_{10} z_c$ and $f_{\text{scf}} \equiv \Omega_{\text{scf}}$ as derived parameters. The non-linear power spectra is modelled using HALOFIT [271, 272]. In this respect, see also Ref. [215] for a comparison between of HALOFIT and HMcode [273] in the context of EDE.

Differently from the previous Chapters, I also compute the best-fit values extracted using the MINUIT algorithm [274] implemented in the IMINUIT python package[1] and quote the difference in the model χ^2 with respect to ΛCDM one, i.e. $\Delta\chi^2 = \chi^2 - \chi^2(\Lambda\text{CDM})$, where negative values indicate an improvement in the fit of the given model with respect to the ΛCDM for the same dataset.

In addition, in order to quantify to what extent the improvement in the fit to the data warrants the increase in the model complexity compared to the baseline ΛCDM model, I compute the Bayes factor defined as the ratio of the evidences for the extended model $\mathcal{M}_{\text{E}}$ with respect to the baseline $\mathcal{M}_{\text{L}}$ as [275]:

---

[1] https://iminuit.readthedocs.io/en/stable/

$$B_{EL} \equiv \frac{\int d\boldsymbol{\theta}_E \, \pi(\boldsymbol{\theta}_E|\mathcal{M}_E)\mathcal{L}(\mathbf{x}|\boldsymbol{\theta}_E, \mathcal{M}_E)\,,}{\int d\boldsymbol{\theta}_L \, \pi(\boldsymbol{\theta}_L|\mathcal{M}_L)\mathcal{L}(\mathbf{x}|\boldsymbol{\theta}_L, \mathcal{M}_L)\,,}\,, \tag{5.4.1}$$

where $\pi(\boldsymbol{\theta}_{\mathrm{E,\,L}})$ is the prior for the parameters $\theta_{\mathrm{E,\,L}}$ and $\mathcal{L}(\mathbf{x}|\boldsymbol{\theta}_{\mathrm{E,\,L}})$ the likelihood of the data given the model $\mathcal{M}_{\mathrm{E,\,L}}$. The extent to what the extended model $\mathcal{M}_{\mathrm{E}}$ is preferred over the baseline $\mathcal{M}_{\mathrm{L}}$ can be qualitatively assessed using the Jeffreys scale reported in Table 5.1 [276]. I compute the evidence directly from our MCMC using the method introduced in Ref. [277] implemented in the MCEvidence code[1].

$\ln B \equiv \ln B_{\mathrm{EL}}$	Strength of preference for model $\mathcal{M}_i$
$0 \leq \ln B < 1$	Weak
$1 \leq \ln B < 3$	Definite
$3 \leq \ln B < 5$	Strong
$\ln B \geq 5$	Very strong

Table 5.1: Revised Jeffreys scale used to interpret the values of $\ln B$ obtained when comparing two competing models through their Bayesian evidence [276]. A value of $\ln B > 0$ indicates that the extended model is favoured with respect to the ΛCDM baseline model.

I now present the results of our MCMC analysis performed using several combinations of the data sets introduced in Chapter 1 and comment on each combination in turn. For convenience, I collect in Section 5.8 all the Tables containing the mean values and error on the cosmological parameters and their best-fit values, as well as the χ^2 for each data set and the Bayes factors.

I start by discussing the results obtained using the data set **P18 + BAO + FS + SN +** H_0, which are presented in Fig. 5.6 and Table 5.2. They clearly show that in the EMG model a large value of $H_0 = 71.00^{+0.87}_{-0.79}$ km s^{-1}Mpc^{-1} at 68% CL is obtained, reducing the tension with SH0ES + H0LiCOW at 1.7σ, better than the 2.1 (4) σ reduction for the EDE (ΛCDM) obtained for $H_0 = 70.57^{+0.77}_{-0.98}$ (68.82 ± 0.39) km s^{-1}Mpc^{-1} at 68% CL. This reduction comes both from the larger mean value of H_0 and the larger errors compared to ΛCDM. As for other models aiming at solving the H_0, I obtain a larger ω_c and n_s compared to the ΛCDM model.

It is interesting to note that EMG helps fitting CMB data better with respect to EDE (and also to the ΛCDM). This is reflected in our 68 % CL estimate for $\xi = 0.15^{+0.06}_{-0.07}$, its 95 % CL upper limit $\xi < 0.42$, and a best-fit value of $\xi = 0.178$. I

---

[1] https://github.com/yabebalFantaye/MCEvidence

also get $\sigma_i = 0.49^{+0.11}_{-0.06}$ at 68%CL, or equivalently $f_{\rm scf} = 0.084^{+0.030}_{-0.021}$. Note however the remarks in Section 5.2 about the meaning of $f_{\rm scf}$ in the context of EMG.

Compared to ΛCDM, both the EMG and the EDE model exacerbate the tension with measurements of σ_8 and S_8. I get consistent results in terms of σ_8 for EMG and EDE, i.e. $\sigma_8 = 0.830 \pm 0.008$ at 68%CL for EMG and $\sigma_8 = 0.832^{+0.009}_{-0.011}$ at 68%CL for EDE. However, the larger ω_c and H_0 leads to essentially the same $S_8 = 0.829 \pm 0.011(\pm 0.13)$ at 68%CL for EMG (EDE).

Overall, the EMG models fits the data much better than the ΛCDM model with an improvement of $\Delta\chi^2 = -16.0$. Such an improvement (better than $\Delta\chi^2 = -9.3$ for the EDE model) is largely due to the better fit to the H_0 prior, but there is also some improvement in the fit to CMB data, in particular to high-ℓ TTTEEE data. As for LSS data, there is only a very small degradation compared to ΛCDM due to the $\Delta\chi^2 = +2.5$ in the fit to BAO DR12 FS + BAO, high-z NGC. The suppression of the matter power spectrum given by the large positive coupling ξ helps fitting FS + BAO data keeping the value of H_0 large at the same time. This large improvement in the fit corresponds to a Bayes factor of $\ln B_{ij} = +1.0$ for EMG. The EDE model, which leads to a smaller improvement in the fit , i.e. $\Delta\chi^2 = -9.3$, has nevertheless a slightly larger Bayes factor of $\ln B_{ij} = +1.5$ due to the smaller number of extra parameters compared to EMG. Note that, from its definition in Eq. (5.4.1), the Bayes factor depends on the prior range of the extra parameter ξ and as such has to be interpreted with some caution. In fact, especially if a parameter is not well constrained (as for the case of some the EMG parameters as V_0 and ξ, see next Section) one could enhance the evidence for the EMG model by reducing the prior range and therefore the sampling volume. For attempts towards model selection techniques which are less dependent on the specific choice of the prior see e.g. Ref. [278].

With the choice of V_0 prior as above, however, it is not possible to recover the model studied in Ref. [3] as the particular $\lambda \to 0$ limit. The reason of this choice is to make sure that for every possible combination of parameters the scalar field always decreases toward $\sigma = 0$, so to be able to safely use the FS data. Indeed, for $\lambda = 0$, the deviation from GR grows at late times, invalidating the use of the FS likelihood and PyBird for a large portion of the parameter space.

On the other hand, it is instructive to study the effects of widening the V_0 prior to see if the data constrain the model with $\lambda = 0$. For this purpose I perform an MCMC analysis with the data set **P18 + BAO + SN +** H_0 that does not suffer from the issue raised above and I set the prior range $V_0 \in [-4, 3.5]$. I have checked that for $V_0 \leq -3$, the potential is essentially negligible.

The posteriors obtained for this MCMCs analysis are shown as red contours in

Fig. 5.6 and they show that data do not prefer the small V_0 region for which the scalar field grows. The results also show another interesting feature of the EMG model, i.e. there is only a small difference in constraints on the EMG model when using BAO in place of the more complete BAO + FS data. As can be seen, the only effect of using BAO is have slightly larger posteriors, but with the same mean as those obtained with BAO + FS data. Note that this is in agreement for the findings of Ref. [210] in the context of the New Early Dark Energy model.

In order to further assess the role of BAO + FS data, I also perform an MCMC analysis without considering them, and use the data set **P18 + SN +** H_0. The results are presented in Fig. 5.7 and Table 5.3. As can be seen, removing BAO and FS data leads to a somewhat larger value of $H_0 = 70.85 \pm 0.92$ km $\mathrm{s}^{-1}\mathrm{Mpc}^{-1}$ for the EDE (and a much larger bestfit of $H_0 = 71.38$ km $\mathrm{s}^{-1}\mathrm{Mpc}^{-1}$), confirming that BAO + FS have the power to constrain these models, as shown in Refs. [216–218]. On the other hand, H_0 for the EMG model increases only a bit to $H_0 = 71.21 \pm 0.93$ km $\mathrm{s}^{-1}\mathrm{Mpc}^{-1}$, since BAO + FS data constrain it less than they constrain EDE models. It is very interesting to note that the best-fit value for the coupling $\xi = 0.17$ is very close to the one found including BAO + FS data. The EMG model fits most of the data, with the exception of CMB lensing, better than both the EDE and the ΛCDM model, leading to a $\Delta\chi^2 = -17.1$. This time, however, the improvement in the fit does not warrant the increase in the model complexity compared to ΛCDM and I obtain a Bayes factor of $\ln B_{ij} = -0.2$.

I have shown that the EMG model leads to a larger value of S_8 compared to the ΛCDM one. Therefore, it would be interesting to test it against weak lensing data. Strictly speaking, this would require using data from e.g. the KiDS-VIKING galaxy shear measurements. However, it was claimed in Refs. [216, 217] that the same results can be obtained by implementing weak lensing data through a Gaussian prior on the parameter $S_8 = 0.770 \pm 0.017$ (see also Ref. [215] for a thorough comparison of this method to the correct use of cosmic shear measurements). With these caveats, I follow Refs. [216, 217] and present in Fig. 5.8 and Table 5.4 the results for the data set **P18 + BAO + FS + SN +** S_8 **+** H_0. Note, despite being far from a resolution to the S_8 tension, the EMG model shows now a much smaller $S_8 = 0.809 \pm 0.009$ and a bestfit value of $S_8 = 0.807$, lower than the one obtained for ΛCDM i.e. $S_8 = 0.811$. This confirms the conclusion of Ref. [215] for EDE models that, even though it is true that the S_8 tension is not resolved within this model, the same holds for the ΛCDM model which, however, is not able to address the H_0 tension, as opposed to the EMG model, for which I obtain a mean $H_0 = 70.63^{+0.80}_{-1.00}$ and a best fit of $H_0 = 71.59$ km $\mathrm{s}^{-1}\mathrm{Mpc}^{-1}$.

Even in this case, however, I note that the large improvement in the fit (not followed by a preference from the model-selection point of view) is coming mainly from the substantial improvement in the fit to H_0. It is therefore natural to ask what happens when the prior on H_0 is removed from the data set.

I present the results obtained without the combined SHOES-Holicow determination of H_0 in Fig. 5.9 and Table 5.5 for the data set **P18 + BAO + FS + SN**. The results show that the mean value for H_0 in the EMG model (and in the EDE one) is only slightly larger then the one in ΛCDM, as also found in previous studies of effectively massless models of scalar-tensor theories [221, 222] . This can be appreciated by looking at the larger posterior distributions of H_0 and ω_c for the EMG and EDE models in Figs. 5.9. The incapability of EDE to solve the H_0 tension when prior information on H_0 is not included, has been recently discussed in the literature [216]. A similar result holds for EMG. [1]

Although the best-fit parameters shown in the third column of Table 5.5 do not lead to a very large H_0, I confirm the results of Refs. [215, 279] for EMG and find some set of parameters exist that lead to a large H_0 without a significant change in $\Delta\chi^2$. For example, I find that $100\,\omega_b = 2.285$, $\omega_c = 0.1308$, $100 * \theta_s = 1.04089$, $\tau_{\rm reio} = 0.057$, $\ln 10^{10} A_s = 3.066$ $n_s = 0.9840$, $\xi = 0.151$, $V_0 = 2.19$, and $\sigma_i = 0.57$ leads to $\Delta\chi^2 = 0.7$, fitting the data very similarly to ΛCDM, with an improvement in the fit to CMB data and a slight worsening to the fit to BAO DR12 FS + BAO, high-z NGC data. Such a parameter set, leads to a large $f_{\rm scf} = 0.081$ and and a large $H_0 = 70.15$ km s^{-1}Mpc^{-1}.

5.5 Analysis of the 1 parameter extension

The ΛCDM model predictions can be recovered in both the EDE and the EMG models when σ_i, or equivalently the energy injection of the scalar field into the cosmic fluid, goes to zero. In this regime, both V_0 and the coupling ξ essentially play no role. When using the Metropolis-Hasting algorithm, as in this case, this can give rise to a large portion of the parameter space that can artificially enhance the statistical weight of ΛCDM models. This issue has been recently addressed, within EDE models, in Refs. [198, 202, 203, 208, 218].

Here, I take a similar, but somewhat alternative approach, and follow the lines of

---

[1] However, it has also been proposed in Refs. [215, 279] (see also next Section), that a distinction should be made between looking at the posterior distributions and the fact that there are some parameters that fit the data in a way that is statistically indistinguishable from ΛCDM and still lead to a large H_0.

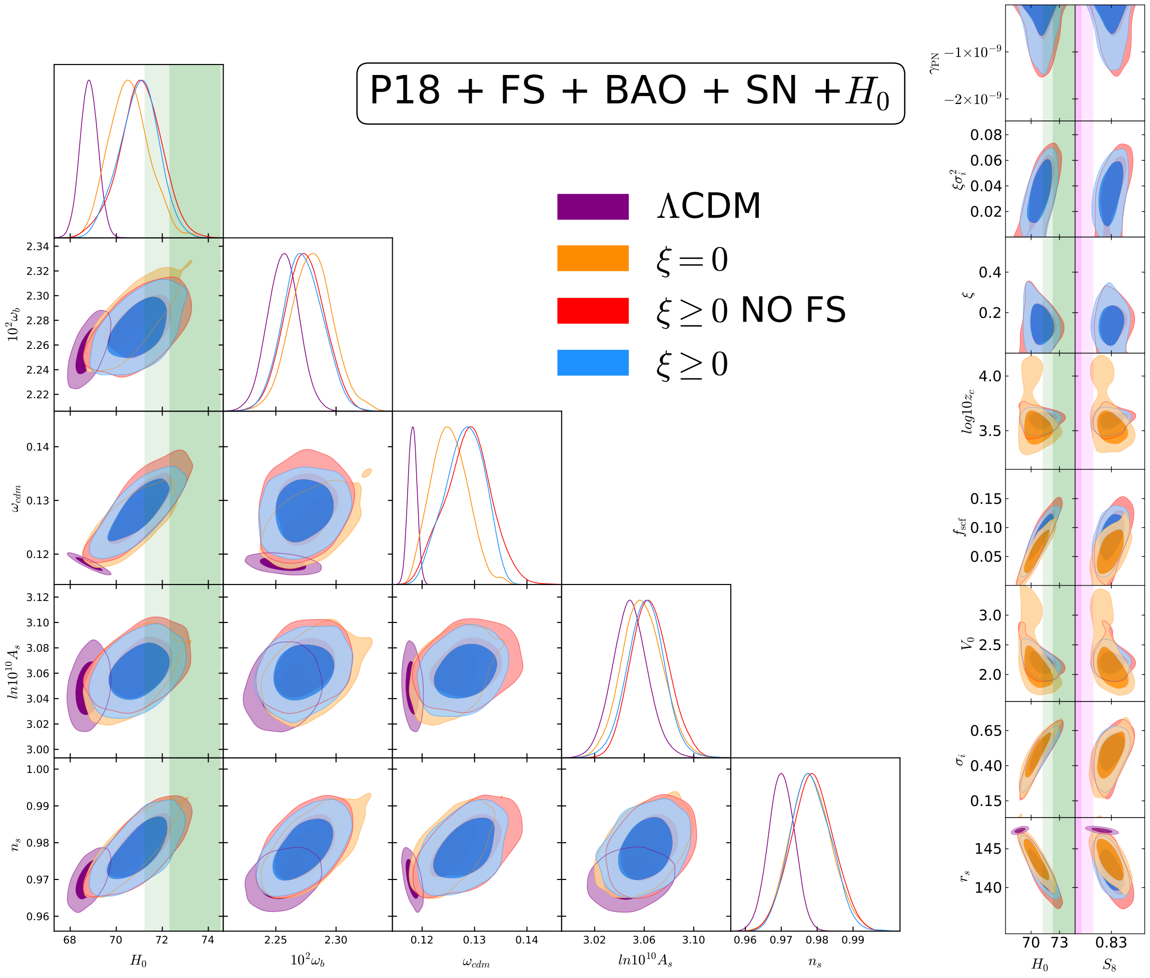

Figure 5.6: 1D and 2D posterior distributions of a subset of parameters for ΛCDM, EDE and EMG obtained using the data set **P18 + BAO + FS + SN +** H_0. Red contours show the results obtained for EMG with a larger prior on V_0 (see main text), for which I use the data set **P18 + BAO + SN +** H_0. 2D contours contain 68% and 95% of the probability. I also plot the 68% and 95% CL for the priors on H_0 and S_8 described in the main text. Figure taken from Ref. [266].

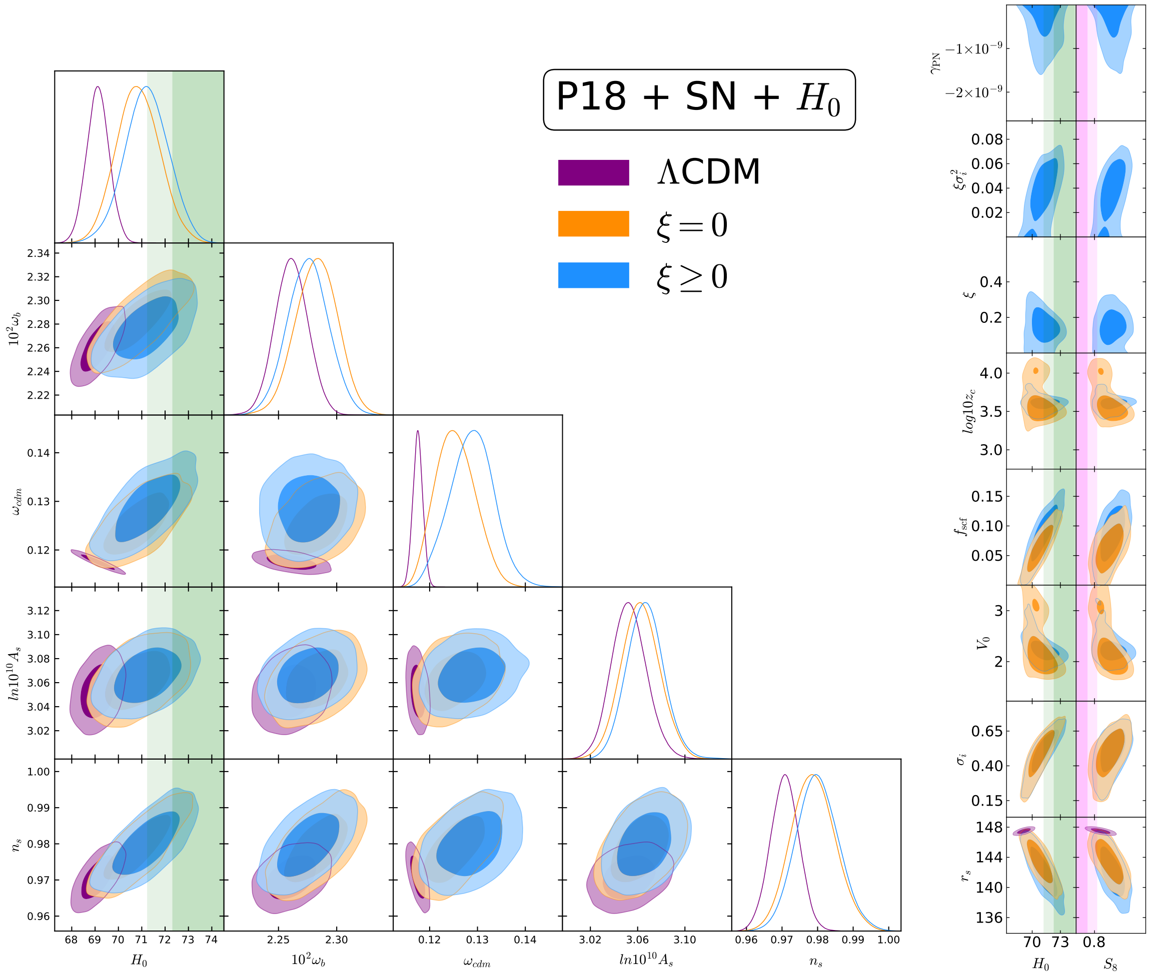

Figure 5.7: 1D and 2D posterior distributions of a subset of parameters for ΛCDM, EDE and EMG obtained using the data set **P18 + SN +** H_0 . 2D contours contain 68% and 95% of the probability. I also plot the 68% and 95% CL for the priors on H_0 and S_8 described in the main text. Figure taken from Ref. [266].

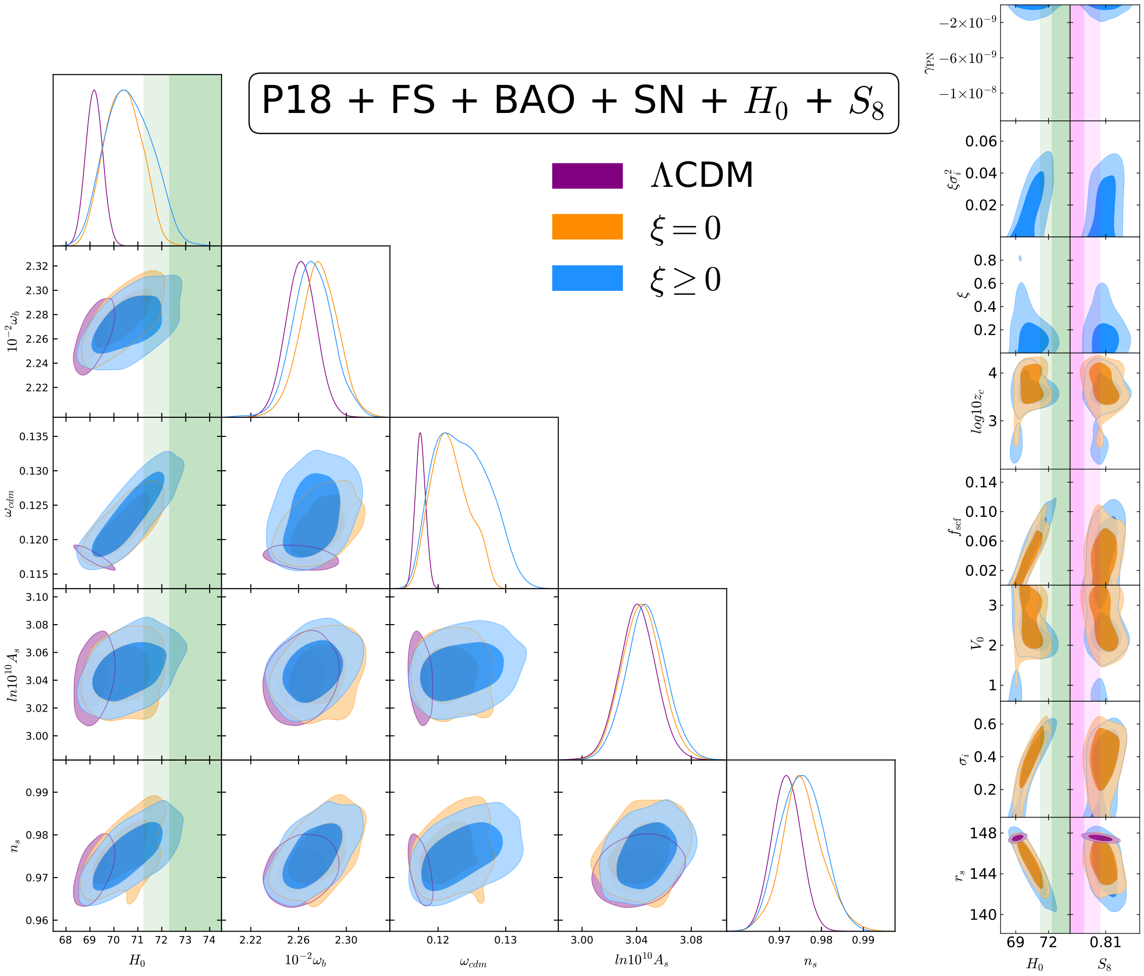

Figure 5.8: 1D and 2D posterior distributions of a subset of parameters for ΛCDM, EDE and EMG obtained using the data set **P18 + BAO + FS + SN +** H_0 **+** S_8. 2D contours contain 68% and 95% of the probability. I also plot the 68% and 95% CL for the priors on H_0 and S_8 described in the main text. Figure taken from Ref. [266].

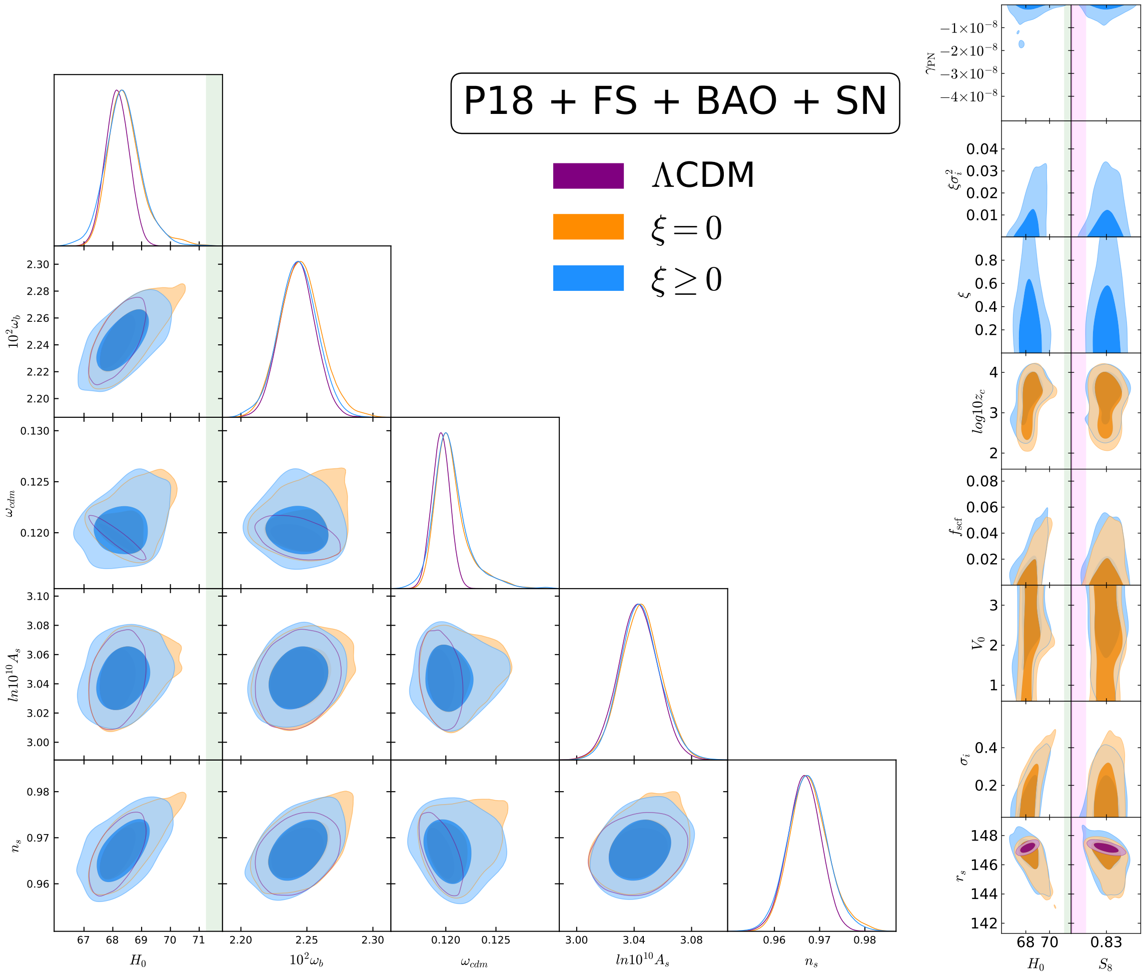

Figure 5.9: 1D and 2D posterior distributions of a subset of parameters for ΛCDM, EDE and EMG obtained using the data set **P18 + BAO + FS + SN** . 2D contours contain 68% and 95% of the probability. I also plot the 68% and 95% CL for the priors on H_0 and S_8 described in the main text. Figure taken from Ref. [266].

Refs. [215, 279], where it was shown that by fixing[1] $\log_{10} z_c$ (or V_0 in our language) it is possible to extend the $f_{\rm scf} - H_0$ degeneracy even for a choice of datasets without prior information on H_0, avoiding problems related to the volume sampling and to the choice of a prior that allows for a ΛCDM limit. Such a degeneracy is clearly disrupted (see Fig. 5.9) when a prior on H_0 is not included in the data set and a tight upper bound on $f_{\rm scf}$ is obtained.

Note, however, that in absence of theoretical motivations, this must be seen only as a purely phenomenological approach, which is rather unorthodox from the standard Bayesian point of view, for which all the parameters has to be varied altogether. Nevertheless, in the class of MG considered here, there is however the possibility to reduce the number of parameters by restricting to $\xi = -1/6$, which corresponds to the theoretical value for conformal coupling [2] (see more in the following Section).

Based on the former argument, I perform an analysis similar to the one of Ref. [208, 215] for the EMG model, for which I fix V_0 and ξ to their best-fit values in the third column of Table 5.2 and leave σ_i free to vary. I do not include H_0 data and I use the **P18 + BAO + FS + SN** data set. The results are presented in Fig. 5.10, where I confront our results to ones for EMG obtained in the previous section considering the data sets **P18 + BAO + FS + SN** and **P18 + BAO + FS + SN +** H_0.

From the plot, it is easy to see that the degeneracy between σ_i and H_0 is now more visible leading to a larger of $H_0 = 69.18^{+0.79}_{-1.00}$ km s^{-1}Mpc^{-1} at 68% CL and slightly reducing the tension with SH0ES+H0LiCOW (3.2σ vs 4.2σ in the 3 parameter case using the same data set). However, the value of σ_i remains consistent with $\sigma_i = 0$ and most of the improvement in reducing the tension is ascribed to a larger error on H_0 compared to the 3 parameters case. In fact, the best-fit value for H_0 that I obtain is $H_0 = 68.79$ km s^{-1}Mpc^{-1}, corresponding to $\sigma_i = 0.30\, M_{\rm pl}$. The best-fit cosmology for the 1 parameter EMG leads to a total χ^2 of 4001.5, i.e. $\Delta\chi^2 = 1.8$, nearly indistinguishable from the 3 parameters one. Compared to the 3 parameters models I have a $\Delta\chi^2 \sim -1.3$ and a $\Delta\chi^2 \sim -0.9$ gain in the fitting Planck high-ℓ TTTEEE data and BAO DR12 FS + BAO, low-z NGC and high-z SGC respectively, whereas the fit to BAO DR12 FS + BAO, high-z NGC is worsen by a factor of $\sim +1.6$, all the other partial χ^2s being essentially the same.

It is interesting to note that now there is only 1 extra parameter and the model is not as penalized as for the case with 3 parameters. In fact, the Bayes factor is now $\ln B = 1.4$ and for the data set **P18 + BAO + FS + SN**, the model results slightly preferred over ΛCDM according to the Jeffreys scale in Table 5.1.

---

[1] In the EDE model of Refs. [215,279] also a second parameter related to the axion decay constant f, namely Θ_i, has to be fixed.

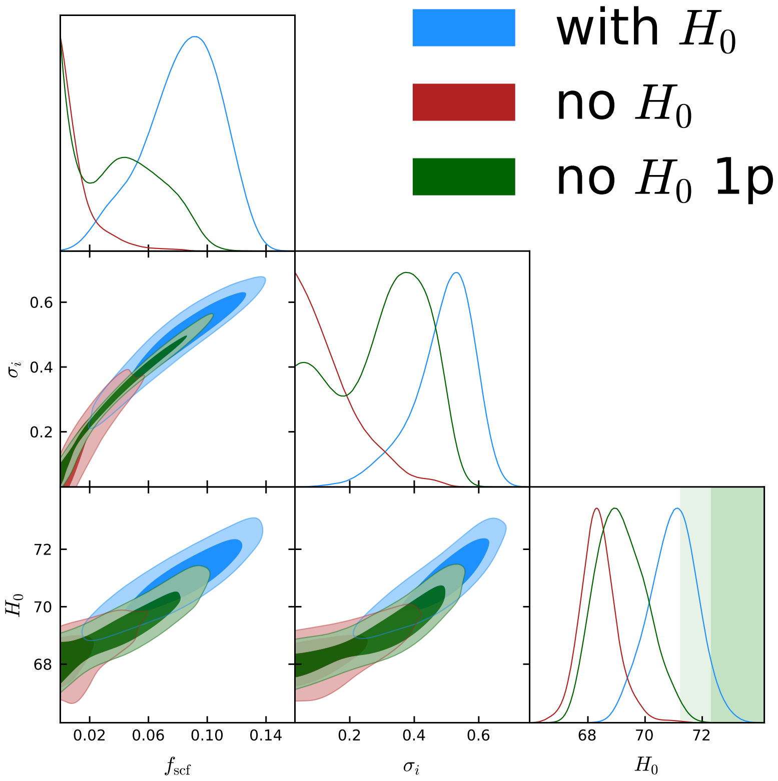

Figure 5.10: 1D and 2D posterior distributions of a subset of parameters for the EMG model. Blue and dark red contours are drawn from the samples in Fig. 5.6 and 5.9 respectively, while the green ones are drawn from the sample obtained by using the data set **P18 + BAO + FS + SN** and fixing V_0 and ξ to their best-fit values in the third column of Table 5.2. 2D contours contain 68% and 95% of the probability. I also plot the 68% and 95% CL for the prior on H_0 described in the main text. Figure taken from Ref. [266].

The conclusion is therefore that by fixing two parameters does not help much alleviate the H_0 tension, which is only addressed when additional prior information from local measurements of the Hubble constant is added, as shown in the previous Section. As in Section 5.4, though, I do find some choices of parameters for which the fit to the data is not substantially different from the one in the ΛCDM model, but lead to a larger H_0, as in Refs. [215, 279], with which I qualitatively agree. A fully quantitative comparison with Refs. [215, 279] is however not possible because of the presence of the non-minimal coupling and the different potential considered. Indeed, potentials with a different curvature such as those with flattened wings and power-law minima are well known to lead to a larger value of H_0 compared to the simpler quartic potential [1, 189, 198, 202].

5.6 The $\xi = -1/6$ case

So far, I have focused on the case of a positive coupling $\xi \geq 0$ and only touched upon negative couplings. As a representative example of the parameter space with $\xi < 0$, I also show the results obtained by fixing $\xi = -1/6$ (see also Chapter 4.

From Fig. 5.1 in Section 5.2, it can be seen that the energy injection is not sharp in redshift anymore, but rather a continuous energy injection in the early Universe is observed, until the scalar field contribution redshits away. The similarity between the background dynamics of this model and the one of a model with extra dark-radiation parameterized by $N_{\rm eff}$ and the consequent difficulty in constraining the coupling ξ has been studied in Chapter 4. Here, the contribution of the scalar field to the total energy budget is similar so significant differences between the results here and the ones found in Chapter 4 are not expected. However, note that thanks to the small effective mass, the scalar field decreases more rapidly compared to the massless case with $\lambda = 0$, see e.g. Fig. 4.14.

For the MCMC analysis I use the data set **P18 + BAO + FS + SN +** H_0 and I fix $\xi = -1/6$. The results are shown in Fig. 5.11, where I compare to results of the previous section and show also the results for the case with $\xi = -1/6$ and $\lambda = 0$ obtained with the same prior on σ_i for a comparison (for simplicity I refer to it as CC). Note that, for the $\lambda = 0$, I have used the data set **P18 + BAO + SN +** H_0, since for a large portion of the σ_i prior I have $G_{\rm eff}/G - 1 \sim 10^{-3}$ and the use of the FS likelihood might be less accurate.

Fig. 5.11 shows that the EMG case with $\xi = -1/6$ leads to $H_0 = 70.11 \pm 0.79$ km s^{-1}Mpc^{-1} at 68% CL a value smaller than the one obtained in the EDE and EMG model with $\xi \geq 0$. This is expected, as the ability of the EDE and EMG model with $\xi \geq 0$ to alleviate the H_0 tension relies on an energy injection very localized in redshift, a feature that is not shared by the EMG model with $\xi = -1/6$. The bestfit value of $\sigma_i = 0.46\, M_{\rm pl}$ leads to $H_0 = 70.30$ km s^{-1}Mpc^{-1}, again smaller than the $\xi = 0$ and $\xi \leq 0$ case. The improvement in the fit is $\Delta\chi^2 = -9.0$ accompanied by a Bayes factor of $\ln B_{ij} = -1.4$, as in the EDE case, which has the same number of parameters. The main improvement in the $\Delta\chi^2$ comes from a better fit to Planck high-ℓ data compared to the other EMG and EDE models, but it is compensated by a degradation in the fit to LSS and H_0 data.

On the other hand, in the latter model, the energy density of the scalar field redshifts away much faster than for $\lambda = 0$, since the scalar field is driven towards $\sigma \simeq 0$ by the quartic potential. This is the reason why the H_0 in this model is larger than $H_0 = 69.78 \pm 0.66$ km s^{-1}Mpc^{-1} at 68% CL, obtained for $\lambda = 0$, for which the scalar field contribution is not completely negligible after recombination. For the very same argument, note that a larger $|\xi\sigma_i^2|$, which is a measure of the scalar field contribution to the fractional $\Delta H(z)/H(z)$ before recombination when $\xi < 0$, is allowed in the EMG model compared to the CC one. Also, the value of $\gamma_{\rm PN}$ is orders of magnitude larger in the CC model, i.e. $\gamma_{\rm PN} > -2.1 \cdot 10^{-5}$ at 95%CL, compared to the EMG case with $\xi = -1/6$ in which $\gamma_{\rm PN} > -3.5 \cdot 10^{-9}$ at 95%CL. If the former is comparable to Solar System experiments, the latter is much smaller.

Furthermore, as expected from the discussion in Section 5.2 and Fig. 5.4, the negative coupling leads to larger σ_8. I get $\sigma_8 = 0.837^{+0.013}_{-0.021}$ and $\sigma_8 = 0.835 \pm 0.010$ for $\lambda \neq 0$ and $\lambda = 0$, respectively, larger than the EDE or EMG model with a positive coupling (see Table 5.2). However, this is accompanied by a comparable $S_8 = 0.833^{+0.016}_{-0.022}$ for EMG with $\xi = -1/6$ and a smaller $S_8 = 0.822 \pm 0.011$ for $\xi = -1/6\,, \lambda = 0$, since H_0 is smaller and therefore the shift in the value of ω_c necessary to restore the fit with CMB data is slightly smaller as well. This is again in line with the observation that models that lead to a larger H_0 modifying the sound horizon inevitably lead to a larger ω_c and therefore S_8 [280].

5.7 Summary of the results

In this Chapter, I have presented a model of Early Modified Gravity (EMG) where a scalar field with a non-minimal coupling to the Ricci scalar of the type $M_{\rm pl}^2 + \xi\sigma^2$ has a self-interacting potential. In this model, which extends the massless one of Section 4.3 and reduces to the Rock'n'Roll Early Dark Energy (EDE) model of Ref. [199] for $\xi = 0$, the scalar field σ, which is frozen during radiation era, grows around the time of recombination driven by the coupling to pressureless matter and is subsequently driven into damped oscillations around its minimum at $\sigma = 0$ by the small effective mass induced by the quartic potential. The rolling of the field towards $\sigma = 0$ suppresses the modification to gravity at late times, recovering an excellent agreement of the laboratory experiments and Solar System tests with General Relativity. The addition of the effective potential has the virtue of reconciling the $\xi > 0$ branch of the model studied in Section 4.3 with GR without any fine tuning.

The modification to gravity at early times, however, has the important consequence of alleviating the H_0 tension as it modifies the redshift profile of the energy injected into the cosmic fluid when the scalar field thaws. The MCMC analysis, performed with a variety of cosmological data, shows that the tension can be reduced substantially and at the same time a positive coupling $\xi > 0$ suppresses the small scale matter power spectrum and thus helps fit the full Shape of the matter power spectrum

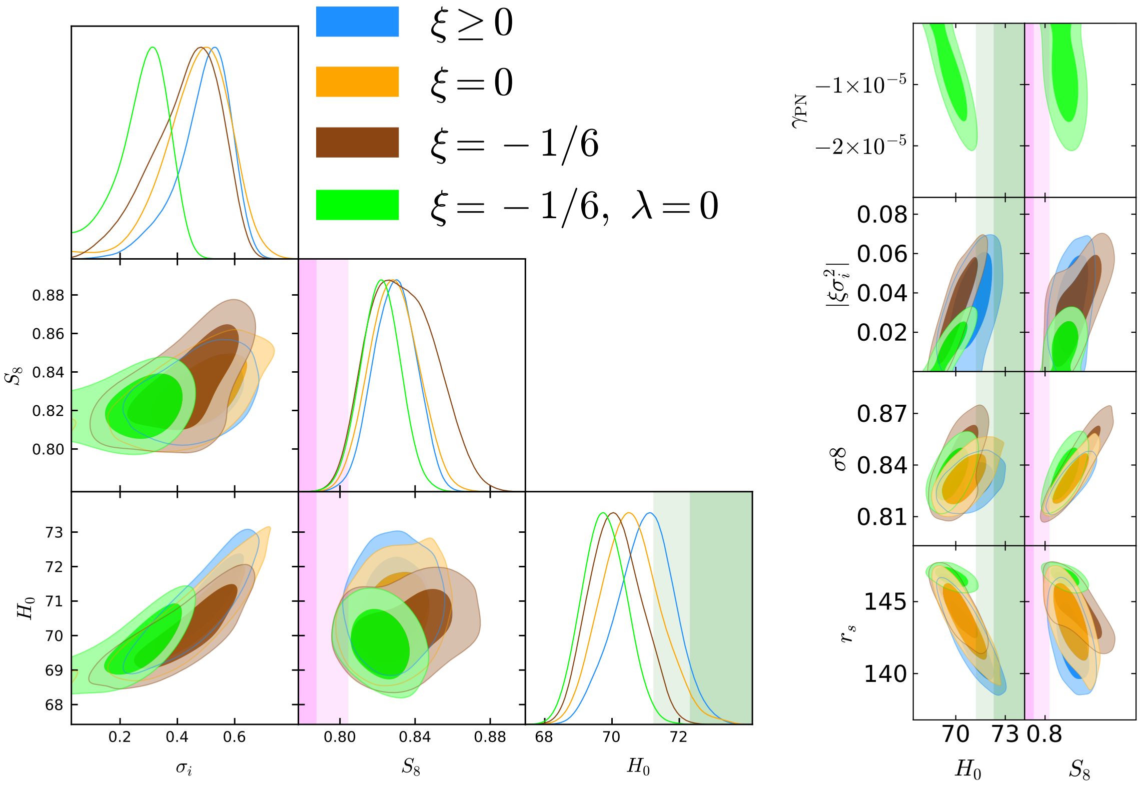

Figure 5.11: 1D and 2D posterior distributions of a subset of parameters for the EDE (orange), EMG (blue) and conformally coupled EMG (brown) using the data set **P18 + BAO + FS + SN +** H_0. I also show in green the results for the case with $\xi = -1/6$ and $\lambda = 0$ for a comparison. Note that for the latter case the data set **P18 + BAO + SN +** H_0 is instead used. 2D contours contain 68% and 95% of the probability. I also plot the 68% and 95% CL for the priors on H_0 and S_8 described in the main text. Figure taken from Ref. [266].

data, that has recently claimed to constrain the EDE resolution of the H_0 tension. In particular, the tension with the combination of recent SH0ES and H0LiCOW measurements, i.e. $H_0 = 73.4 \pm 1.1$ km s^{-1}Mpc^{-1}, is reduced at the 1.7σ level when this is added to Cosmic Microwave Background, SNe, Baryonic Acoustic Oscillations and the Full Shape of the matter power spectrum data. For this data set, I obtain $H_0 = 71.00^{+0.87}_{-0.79}$ km s^{-1}Mpc^{-1} at 68 % CL which is larger than, but consistent with, the one I get for EDE for $\xi = 0$ i.e. $H_0 = 70.57^{+0.77}_{-0.98}$ km s^{-1}Mpc^{-1}.

Performing the MCMC analysis with different combinations of the data mentioned above helps trace the origin of the larger H_0 back to the suppression of the power spectrum caused by the non minimal coupling ξ, for which I get $\xi = 0.15^{+0.06}_{-0.07}$ at 68% CL ($\xi < 0.39$ at 95%CL). In fact, for all the data set that are used, a similar constrain on the parameter ξ is recovered. Although the fit to data is always improved the Bayesian model selection for EMG depends on the data set considered, and is penalized by the larger number (3) of extra parameters compared to ΛCDM, therefore never resulting in a strong preference.

In order to confirm the argument above I have performed the same analysis fixing ξ to the conformal coupling $\xi = -1/6$. In this case rather than a suppression there is an enhancement of the matter power spectrum and the capability of the model to ease the tension is therefore reduced, with $H_0 = 70.11 \pm 0.79$ km s^{-1}Mpc^{-1}, smaller than the the $\xi = 0$ case, showing a clear hierarchy for negative, null and positive couplings. Note, however, that the addition of the small effective mass to the $\xi = -1/6$ case leads to larger H_0 than the one for the conformally coupled massless case of Ref. [3] for which $H_0 = 69.78 \pm 0.66$ km s^{-1}Mpc^{-1} (see Section 5.6).

As a last comment, in this Chapter I have considered two dimensionless couplings for a cosmological scalar field, which rule the coupling to the Ricci scalar (ξ) and its self-interaction (λ). A quartic potential for the scalar field σ, implies that the RnR model [199] is recovered for $\xi = 0$. However, it is known that potentials with flattened wings that have a different curvature around the minimum at $\sigma = 0$, such as those in the original EDE proposal of Ref. [189] or in the α-attractor EDE model of Section 3.4, provide a better fit to Planck polarization data and lead to an even larger H_0. An exploration of different choices of the potential in the EMG framework is currently ongoing.

5.8 Tables

Here I collect the Tables containing the constraints from the MCMC analysis in Section 5.4. Note that H_0, σ_i, r_s and $\xi\sigma_i^2$ are given in units of [km s^{-1}Mpc^{-1}], $M_{\rm pl}$, Mpc and $M_{\rm pl}^2$ respectively.

	ΛCDM	EDE	EMG
$10^2\omega_{\rm b}$	2.256 ± 0.013 (2.255)	2.280 ± 0.018 (2.286)	2.273 ± 0.017 (2.281)
$\omega_{\rm c}$	0.1182 ± 0.0009 (0.1184)	$0.1253^{+0.0033}_{-0.0038}$ (0.1242)	$0.1282^{+0.0042}_{-0.0033}$ (0.1302)
$100 * \theta_s$	1.04209 ± 0.00028 (1.04216)	1.04152 ± 0.00036, (1.04170)	$1.04118^{+0.00040}_{-0.00046}$ (1.04120)
$\tau_{\rm reio}$	0.058 ± 0.007 (0.052)	$0.058^{+0.007}_{-0.008}$ (0.059)	0.056 ± 0.007 (0.057)
$\ln\left(10^{10} A_{\rm s}\right)$	3.049 ± 0.014 (3.038)	3.059 ± 0.016 (3.059)	3.061 ± 0.015 (3.067)
$n_{\rm s}$	0.9701 ± 0.0036 (0.9710)	$0.9783^{+0.0054}_{-0.0061}$ (0.9813)	0.9782 ± 0.0055 (0.9849)
σ_i	–	< 0.70 (0.48)	$0.49^{+0.11}_{-0.06}$ (0.53)
V_0	–	$2.21^{+0.07}_{-0.38}$ (2.09)	$2.21^{+0.10}_{-0.15}$ (2.25)
ξ	–	–	< 0.42 (0.18)
H_0	68.82 ± 0.39 (68.74)	$70.57^{+0.77}_{-0.98}$ (70.90)	$71.00^{+0.87}_{-0.79}$ (71.59)
r_s	147.37 ± 0.22 (147.33)	143.5 ± 1.8 (143.78)	$142.2^{+1.5}_{-2.0}$ (141.21)
σ_8	0.821 ± 0.006 (0.818)	$0.832^{+0.009}_{-0.011}$ (0.831)	0.830 ± 0.008 (0.850)
S_8	0.817 ± 0.010 (0.815)	0.829 ± 0.013 (0.820)	0.829 ± 0.011 (0.847)
$\log_{10}\, z_c$	–	$3.58^{+0.04}_{-0.16}$ (3.53)	$3.60^{+0.06}_{-0.05}$ (3.63)
$f_{\rm scf}$	–	< 0.119 (0.057)	$0.084^{+0.030}_{-0.021}$ (0.099)
$\xi\sigma_i^2$	–	–	< 0.067 (0.050)
$\gamma_{\rm PN} - 1$	–	–	$> -1.7 \cdot 10^{-9}$ $(-8.9 \cdot 10^{-9})$
$\Delta\chi^2$	–	-9.3	-16.0
$\ln B_{ij}$	–	+1.5	+1.0

P18 + BAO + FS + SN + H_0	ΛCDM	EDE	EMG
Planck high-ℓ TTTEEE	2350.07	2352.08	2347.75
Planck low-ℓ EE	395.70	396.69	396.37
Planck low-ℓ TT	22.32	21.51	21.52
Planck lensing	9.37	9.36	9.17
BAO BOSS low-z	2.21	2.74	2.06
BAO DR12 FS + BAO, high-z NGC	65.13	65.15	67.64
BAO DR12 FS + BAO, high-z SGC	62.63	63.29	62.83
BAO DR12 FS + BAO, low-z NGC	70.06	70.53	69.89
Pantheon	1026.86	1026.93	1026.88
H_0	18.57	5.35	2.81
Total	4022.94	4013.64	4006.92

Table 5.2: [Upper table] Constraints on main and derived parameters considering the data set **P18 + BAO + FS + SN +** H_0 for ΛCDM, $\xi = 0$ and $\xi \geq 0$. I report mean values and the 68% CL, except for the case of upper or lower limits, for which I report the 95% CL. I also report the best-fit values in round brackets. [Lower table] Best-fit χ^2 per experiment for the data set **P18 + BAO + FS + SN +** H_0 for ΛCDM, EDE and EMG model.

	ΛCDM	EDE	EMG
$10^2\omega_{\rm b}$	2.261 ± 0.014 (2.263)	2.283 ± 0.018 (2.292)	2.275 ± 0.018 (2.284)
$\omega_{\rm c}$	0.1175 ± 0.0011 (0.1170)	$0.1253^{+0.0036}_{-0.0044}$ (0.1285)	0.1288 ± 0.0046 (0.131)
$100 * \theta_s$	1.04216 ± 0.00029 (1.04200)	1.04153 ± 0.00038 (1.04135)	1.04114 ± 0.00048 (1.04107)
$\tau_{\rm reio}$	$0.061^{+0.007}_{-0.008}$ (0.060)	$0.060^{+0.007}_{-0.008}$ (0.061)	$0.058^{+0.007}_{-0.008}$ (0.056)
$\ln\left(10^{10}A_{\rm s}\right)$	$3.053^{+0.014}_{-0.016}$ (3.050)	3.062 ± 0.016 (3.072)	3.067 ± 0.016 (3.067)
$n_{\rm s}$	0.9707 ± 0.0040 (0.9733)	0.9788 ± 0.0061 (0.9849)	0.9800 ± 0.0059 (0.9870)
σ_i	–	$0.48^{+0.14}_{-0.09}$ (0.58)	$0.50^{+0.12}_{-0.07}$ (0.56)
V_0	–	$2.23^{+0.10}_{-0.45}$ (1.97)	$2.22^{+0.11}_{-0.13}$ (2.24)
ξ	–	–	< 0.39 (0.17)
H_0	69.13 ± 0.49 (69.25)	70.85 ± 0.92 (71.38)	71.21 ± 0.93 (71.87)
r_s	147.49 ± 0.25 (147.61)	143.4 ± 1.9 (141.83)	$141.9^{+1.9}_{-2.2}$ (140.70)
σ_8	0.820 ± 0.006 (0.818)	0.833 ± 0.011 (0.842)	0.833 ± 0.008 (0.836)
S_8	0.811 ± 0.011 (0.806)	0.827 ± 0.016 (0.838)	0.831 ± 0.014 (0.833)
$\log_{10} z_c$	–	$3.59^{+0.06}_{-0.19}$ (3.50)	$3.60^{+0.06}_{-0.04}$ (3.64)
$f_{\rm scf}$	–	< 0.134 (0.083)	$0.088^{+0.033}_{-0.025}$ (0.107)
$\xi\sigma_i^2$	–	–	< 0.072 (0.053)
$\gamma_{\rm PN} - 1$	–	–	$> -1.7 \cdot 10^{-9}$ $(-1.8 \cdot 10^{-9})$
$\Delta\chi^2$	–	-11.5	-17.1
$\ln B_{ij}$	–	$+1.8$	-0.2

P18 + SN + H_0	ΛCDM	EDE	EMG
Planck high-ℓ TTTEEE	2351.75	2352.22	2349.25
Planck low-ℓ EE	396.94	397.51	396.23
Planck low-ℓ TT	22.08	21.41	21.29
Planck lensing	9.59	9.07	9.32
Pantheon	1026.96	1026.87	1026.86
H_0	14.76	3.50	2.00
Total	3822.08	3810.58	3804.97

Table 5.3: [Upper table] Constraints on main and derived parameters considering the data set **P18 + SN +** H_0 for ΛCDM, $\xi = 0$ and $\xi \geq 0$. I report mean values and the 68% CL, except for the case of upper or lower limits, for which I report the 95% CL. I also report the best-fit values in round brackets. [Lower table] Best-fit χ^2 per experiment for the data set **P18 + SN +** H_0 for ΛCDM, EDE and EMG model.

	ΛCDM	EDE	EMG
$10^2\omega_\mathrm{b}$	2.262 ± 0.013 (2.265)	2.277 ± 0.016 (2.276)	2.272 ± 0.016 (2.275)
ω_c	0.1174 ± 0.0008 (0.1178)	$0.1218^{+0.0022}_{-0.0034}$ (0.1228)	$0.1234^{+0.0028}_{-0.0047}$ (0.1262)
$100 * \theta_s$	1.04213 ± 0.00029 (1.04229)	$1.04160^{+0.00052}_{-0.00034}$ ()	1.04154 ± 0.00043 (1.04148)
τ_reio	0.055 ± 0.007 (0.057)	0.055 ± 0.007 (0.058)	0.054 ± 0.007 (0.057)
$\ln\left(10^{10}A_\mathrm{s}\right)$	3.041 ± 0.014 (3.047)	3.044 ± 0.015 (3.042)	3.047 ± 0.015 (3.058)
n_s	0.9716 ± 0.0035 (0.9719)	$0.9756^{+0.0043}_{-0.0053}$ (0.9752)	$0.9755^{+0.0046}_{-0.0054}$ (0.9791)
σ_i	–	< 0.60 (0.47)	$0.39^{+0.15}_{-0.10}$ (0.50)
V_0	–	$2.59^{+0.72}_{-0.64}$ (3.21)	$2.44^{+0.76}_{-0.50}$ (2.05)
ξ	–	–	< 0.63 (0.14)
H_0	69.17 ± 0.35 (69.09)	70.40 ± 0.76 (70.75)	$70.63^{+0.80}_{-1.0}$ (71.59)
r_s	147.51 ± 0.21 (147.38)	$145.0^{+1.7}_{-1.3}$ (144.43)	$144.3^{+2.3}_{-1.5}$ (142.75)
σ_8	0.815 ± 0.005 (0.819)	$0.819^{+0.006}_{-0.008}$ (0.81682)	$0.819^{+0.006}_{-0.007}$ (0.820)
S_8	0.805 ± 0.008 (0.811)	0.808 ± 0.010 (0.804)	0.809 ± 0.009 (0.807)
$\log_{10}\, z_c$	–	$3.72^{+0.37}_{-0.26}$ (4.12)	$3.66^{+0.04}_{-0.20}$ (3.52)
f_scf	–	< 0.101 (0.064)	< 0.121 (0.085)
$\xi\sigma_i^2$	–	–	< 0.054 (0.030)
$\gamma_\mathrm{PN} - 1$	–	–	$> -1.8 \cdot 10^{-9}$ $(-8.0 \cdot 10^{-10})$
$\Delta\chi^2$	–	-11.0	-11.5
$\ln B_{ij}$	–	-0.4	-0.12

P18 + BAO + FS + SN + H_0 + S_8	ΛCDM	EDE	EMG
Planck high-ℓ TTTEEE	2351.17	2351.13	2351.51
Planck low-ℓ EE	396.43	396.47	396.48
Planck low-ℓ TT	22.36	21.70	22.19
Planck lensing	9.32	10.09	10.46
BAO BOSS low-z	2.65	2.96	2.91
BAO DR12 FS + BAO, high-z NGC	64.76	64.08	65.53
BAO DR12 FS + BAO, high-z SGC	63.11	63.23	63.00
BAO DR12 FS + BAO, low-z NGC	70.57	71.14	70.54
Pantheon	1026.89	1026.97	1026.98
H_0	15.88	6.00	2.90
S_8	5.66	4.02	4.82
Total	4028.81	4017.81	4017.35

Table 5.4: [Upper table] Constraints on main and derived parameters considering the data set **P18 + BAO + FS + SN +** H_0 **+** S_8 for ΛCDM, $\xi = 0$ and $\xi \geq 0$. I report mean values and the 68% CL, except for the case of upper or lower limits, for which I report the 95% CL. I also report the best-fit values in round brackets. [Lower table] Best-fit χ^2 per experiment for the data set **P18 + BAO + FS + SN +** H_0 **+** S_8 for ΛCDM, EDE and EMG model.

	ΛCDM	EDE	EMG
$10^2\omega_{\rm b}$	2.243 ± 0.013 (2.251)	$2.245^{+0.015}_{-0.016}$ (2.240)	2.244 ± 0.015 (2.247)
$\omega_{\rm c}$	0.1195 ± 0.0009 (0.1186)	$0.1206^{+0.0008}_{-0.0019}$ (0.1200)	$0.1206^{+0.0011}_{-0.0019}$ (0.1234)
$100 * \theta_s$	1.04193 ± 0.00029 (1.04199)	1.04182 ± 0.00032, (1.04181)	$1.04181^{+0.00033}_{-0.00029}$ (1.04168)
$\tau_{\rm reio}$	0.054 ± 0.007 (0.059)	0.054 ± 0.007, (0.054)	0.054 ± 0.007 (0.54)
$\ln\left(10^{10}A_{\rm s}\right)$	3.043 ± 0.014 (3.050)	3.045 ± 0.014 (3.044)	3.045 ± 0.014 (3.0491)
$n_{\rm s}$	0.9666 ± 0.0037 (0.9699)	$0.9678^{+0.0037}_{-0.0047}$ (0.9663)	0.9673 ± 0.0044 (0.9686)
σ_i	$-$	< 0.50 (0.05)	< 0.45 (0.31)
V_0	$-$	2.14 ± 0.78 (0.69)	$2.47^{+0.86}_{-0.39}$ (2.28)
ξ	$-$	$-$	< 0.81 (0.18)
H_0	68.16 ± 0.41 (68.55)	$68.46^{+0.42}_{-0.68}$ (67.90)	$68.39^{+0.50}_{-0.67}$ (68.94)
r_s	147.16 ± 0.22 (147.32)	$146.53^{+0.94}_{-0.23}$ (147.08)	$146.59^{+0.90}_{-0.38}$ (145.17)
σ_8	0.822 ± 0.0058 (0.823)	$0.823^{+0.006}_{-0.007}$ (0.824)	0.822 ± 0.007 (0.824)
S_8	0.830 ± 0.010 (0.823)	0.831 ± 0.011 (0.836)	0.830 ± 0.011 (0.834)
$\log_{10}\, z_c$	$-$	$3.26^{+0.65}_{-0.72}$ (2.07)	$3.44^{+0.52}_{-0.17}$ (3.54)
$f_{\rm scf}$	$-$	< 0.0617 (0.0004)	< 0.0726 (0.037)
$\xi\sigma_i^2$	$-$	$-$	< 0.0381 (0.0172)
$\gamma_{\rm PN} - 1$	$-$	$-$	$> -1.7 \cdot 10^{-8}$ $(-5.0 \cdot 10^{-10})$
$\Delta\chi^2$	$-$	-1.2	-2.6
$\ln B_{ij}$	$-$	-1.3	-2.7

P18 + BAO + FS+ SN	ΛCDM	EDE	EMG
Planck high-ℓ TTTEEE	2347.99	2346.77	2345.32
Planck low-ℓ EE	396.89	396.00	396.04
Planck low-ℓ TT	22.69	23.23	23.34
Planck lensing	8.82	8.86	8.80
BAO BOSS low-z	2.00	1.33	1.44
BAO DR12 FS + BAO, high-z NGC	65.78	67.86	67.91
BAO DR12 FS + BAO, high-z SGC	62.42	61.76	61.69
BAO DR12 FS + BAO, low-z NGC	69.82	69.25	69.17
Pantheon	1026.89	1027.09	1027.02
Total	4003.30	4002.15	4000.74

Table 5.5: [Upper table] Constraints on main and derived parameters considering the data set **P18 + BAO + FS + SN** for ΛCDM, $\xi = 0$ and $\xi \geq 0$. I report mean values and the 68% CL, except for the case of upper or lower limits, for which I report the 95% CL. I also report the best-fit values in round brackets. [Lower table] Best-fit χ^2 per experiment for the data set **P18 + BAO + FS + SN** for ΛCDM, EDE and EMG model.

Chapter 6

Scalar-tensor theories and neutrino physics

In the previous Chapters, I have studied the dynamics of several models belonging to the class of ST theories and constrained them with cosmological data. Except for the introduction of a new degree of freedom, identified with the scalar field of ST theories, I have not modified any of the other ΛCDM assumptions. In particular, I have always assumed a standard neutrino physics[1] and fixed all the parameters describing the number of effective relativistic species and the neutrino masses. With these assumptions, I have shown that a generic outcome of these ST theories is a larger value of the Hubble constant compared to the one derived within the ΛCDM model.

In the specific case of the models studied in Chapter 4, however, the mechanism that drives a higher inferred H_0 relies on a behavior of the scalar field contribution the the expansion history at early times which resembles the one of relativistic species. Therefore, it is interesting to investigate to what extent these simple scalar-tensor theories are degenerate with effective number neutrinos and to any additional massless particles produced well before recombination $N_{\rm eff}$. The current tight constraints from the latest *Planck* 2018 data $N_{\rm eff} = 2.89 \pm 0.19$ ($N_{\rm eff} = 2.99 \pm 0.17$ including BAO) at 68% CL [21] can indeed be changed in modified gravity theories as previously shown in the context of $f(R)$ gravity in [281, 282] for Planck DR1.

While changing $N_{\rm eff}$ can lead to a higher value for H_0 compared with the value inferred in the ΛCDM model from CMB anisotropies measurements, in its extension model with non-zero neutrino mass m_ν, the two parameters are instead anti-correlated so lower values of H_0 correspond to higher values of m_ν and viceversa. For instance, the constraint from *Planck* 2018 data in combination with BAO data is $m_\nu < 0.12$ eV at 95% CL [21, 283] and combining with the measurement from the SH0ES team the limit further tightens to $m_\nu < 0.076$ eV [284]. On the other hand in ST theories

---

[1] Note that I have always considered massless neutrinos with $N_{\rm eff} = 3.046$ in comparing the models of Chapters 4 and 5 with cosmological data, whereas oftentimes the choice of one massive neutrino with $m_\nu = 0.06$ eV is adopted in the literature [21] (see discussions in Chapters 4 and 5 and in the following).

of gravity, it is possible to keep fixed the angular diameter distance at decoupling or even increase it in order to recover a higher H_0 while increasing the total neutrino mass [285]. Given that neutrino oscillations are the only evidence of physics beyond the Standard Model of Particle Physics [286], a natural question is to explore how the constraints on neutrino physics can be relaxed or tightened if the underlying cosmological model is one of those analyzed in the previous Chapters, rather than the ΛCDM one.

I also note that future CMB experiments, such as the Simons Observatory[1] [287], CMB-S4[2] [288], and future LSS surveys from DESI[3] [289], Euclid[4] [290, 291], LSST[5] [292], SKA[6] [293, 294] will help improve the constraints on these extended cosmologies [260, 261, 295] and limit the degeneracy of neutrino parameters $N_{\rm eff}$ and m_ν with scalar-tensor theories [296].

This Chapter is based on the research work in Ref. [4], in particular, I will focus on the models studied in Chapter 4 and set boundary conditions on σ so that laboratory experiments on the variation of G are automatically satisfied, as explained in Sec. 4.2. All the results and plots are produced using the `CLASSig` code [2, 221].

6.1 Degeneracy with the number of effective relativistic degrees of freedom

As explained in Sec. 6.1, in the context of the ΛCDM model, the presence of extra relativistic degrees of freedom in the Universe increases the expansion rate during the radiation-dominated era and shifts the epoch of matter-radiation equality, the shape of the matter power spectrum, and the history of recombination (see Refs. [182, 297] for a review). The extra radiation is usually parameterized by $\Delta N_{\rm eff} \equiv N_{\rm eff} - 3.046$ [298–301]. By reducing the size of the comoving sound horizon at baryon drag, a larger value of $N_{\rm eff}$ can ease the tension on H_0, at the price of worsening the fit to CMB polarization and BAO data [21, 178], see Sec. 6.1.

In the context of modified gravity theories, however, there is an interplay (negative correlation) between the contribution of extra radiation $\Delta N_{\rm eff}$ and the scalar field coupling[7] which acts as an additional source of radiation in the analogue Einstein system at the background level. By decreasing the effective number of extra relativistic

---

[1] https://simonsobservatory.org/

[2] https://cmb-s4.org/

[3] http://desi.lbl.gov/

[4] http://sci.esa.int/euclid/

[5] http://www.lsst.org/

[6] http://www.skatelescope.org/

[7] See Refs. [281, 282] for an application in the context of $f(R)$ gravity.

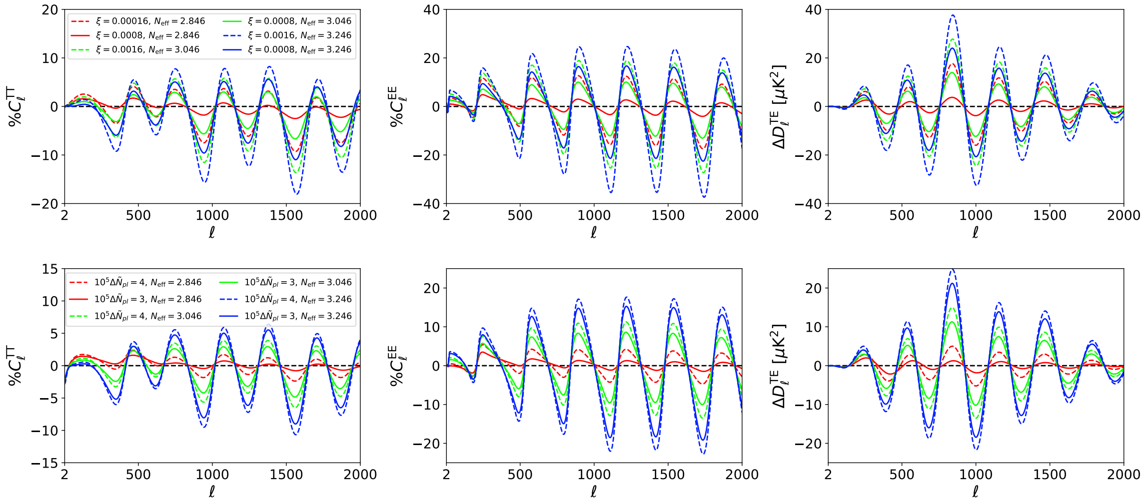

Figure 6.1: Differences with respect to the ΛCDM with ($N_{\rm eff} = 3.046$) with IG (top panels) for $\xi = 0.0008, 0.0016$ (solid, dashed) and $N_{\rm eff} = 2.846, 3.046, 3.246$ (red, green, blue), and CC (bottom panels) for $N_{pl} = 1.00003, 1.00004$ M$_{pl}$ (solid, dashed) and $N_{\rm eff} = 2.846, 3.046, 3.246$ (red, green, blue). $D_\ell \equiv \ell(\ell+1)C_\ell/(2\pi)$ are the band-power angular power spectra. Figure taken from Ref. [4].

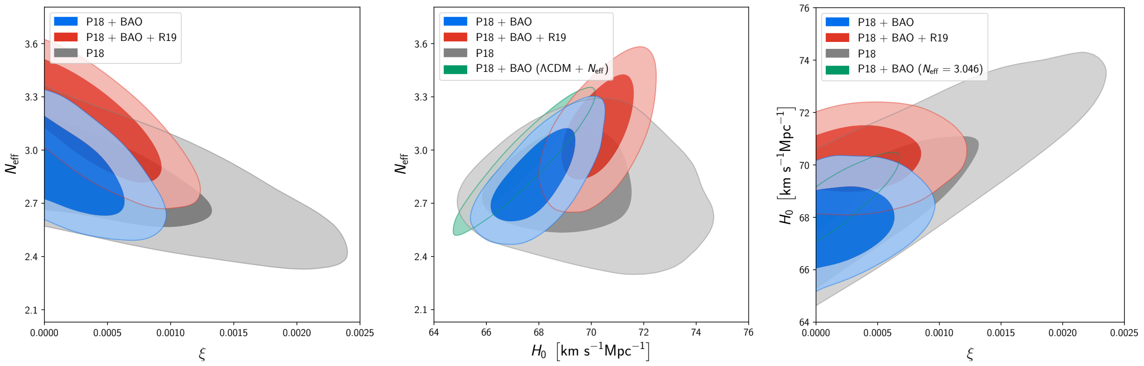

Figure 6.2: Marginalized joint 68% and 95% CL regions 2D parameter space using the P18 (gray) in combination with BAO (blue) and BAO + R19 (red) for the IG+$N_{\rm eff}$ model. In the central panel, I include the $H_0 - N_{\rm eff}$ contours for the ΛCDM in green. In the right panel, I include the $H_0 - \xi$ contours for the IG with $N_{\rm eff} = 3.046$ in green. Figure taken from Ref. [4].

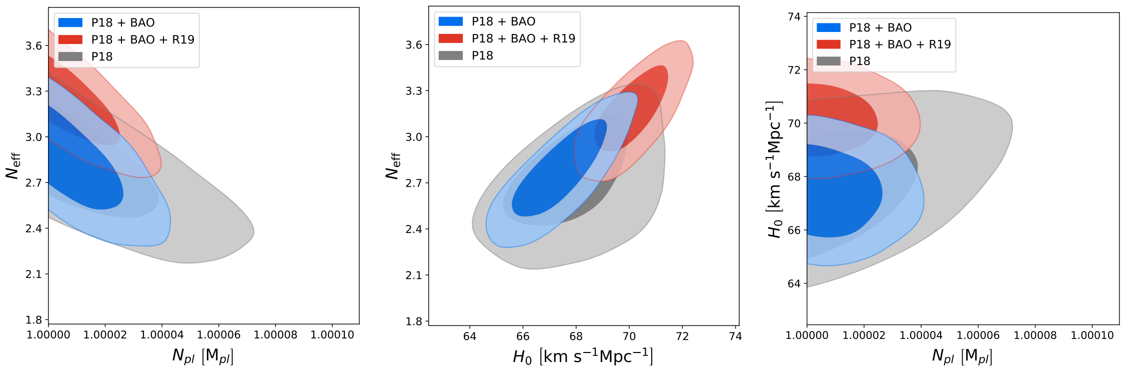

Figure 6.3: Marginalized joint 68% and 95% CL regions 2D parameter space using the *Planck* legacy data (gray) in combination with DR12 (blue) and DR12 + R19 (red) for the CC+$N_{\rm eff}$ model. Figure taken from Ref. [4].

species to $N_{\rm eff} = 2.846$ it is possible to obtain deviations of the CMB anisotropies angular power spectra to the ΛCDM model of the same order of the ones obtained with ξ halved and $N_{\rm eff} = 3.046$, see Fig. 6.1.

Therefore, preferring lower values of $N_{\rm eff}$, the datasets allow for larger values for ξ compared to the case with $N_{\rm eff} = 3.046$ fixed. The constraints on the coupling change from $\xi < 0.00098$ to $\xi < 0.0019$ at 95% CL with P18 alone (and from $\xi < 0.00055$ to $\xi < 0.00078$ once BAO are included), see Tab. 6.1 and Tables in Chapter 4.

The mean of $N_{\rm eff}$ moves around 1σ towards lower values with respect to the ΛCDM case with a similar error. For IG, I get at 68% CL $N_{\rm eff} = 2.79 \pm 0.20$ for P18 compared to $N_{\rm eff} = 2.89 \pm 0.19$ in ΛCDM and $N_{\rm eff} = 2.85 \pm 0.17$ in combination with BAO compared to $N_{\rm eff} = 2.99 \pm 0.17$ in ΛCDM. In Fig. 6.2 (central panel), I show the enlarged $H_0 - N_{\rm eff}$ parameter space in IG compared to the ΛCDM concordance model (green contours) where it is possible to reach higher value of H_0 without increasing $N_{\rm eff}$ in presence of a modification of gravity.

In the CC model, an analogous correlation in the $N_{\rm eff} - N_{pl}$ parameter space is found, see Fig. 6.3. The constraints on N_{pl} are larger, from $N_{pl} < 1.000028$ M$_{pl}$ (see Chapter 4) to $N_{pl} < 1.000057$ M$_{pl}$ at 95% CL with P18 alone and from $N_{pl} < 1.000018$ M$_{pl}$ to $N_{pl} < 1.000019$ M$_{pl}$ at 95% CL once BAO are included, see Tab. 6.2.

While the Hubble constant is larger than in ΛCDM for the combination P18 + BAO H_0, i.e. $H_0 = \left(68.78^{+0.53}_{-0.78}\right)$ km s^{-1}Mpc^{-1} and $H_0 = \left(68.62^{+0.47}_{-0.66}\right)$ km s^{-1}Mpc^{-1}, for the IG and CC models respectively, the addition of R19 data leads to a closer posterior distribution for H_0 among the three cases, i.e. (70.1 ± 0.8) km s^{-1}Mpc^{-1} for IG, (69.6 ± 0.7) km s^{-1}Mpc^{-1} for CC, and $H_0 = (70.0 \pm 0.9)$ km s^{-1}Mpc^{-1} for ΛCDM+$N_{\rm eff}$. I find a similar posterior distribution also for IG+$N_{\rm eff}$ (CC+$N_{\rm eff}$), i.e. (70.3 ± 0.9) km s^{-1}Mpc^{-1} ((70.1 ± 0.9) km s^{-1}Mpc^{-1}), see Fig. 6.2.

The addition of BAO data reduces the degeneracy $H_0 - \xi$ $(-N_{pl})$ increasing the one between $N_{\rm eff} - \xi$ $(-N_{pl})$ and $H_0 - N_{\rm eff}$. In order to reduce the comoving sound horizon and therefore accommodate a larger value of H_0, in this case $N_{\rm eff}$ is moved towards larger values, i.e. 3.11 ± 0.19 for IG and 3.16 ± 0.19 for CC, see Tab. 6.1.

6.2 Degeneracy with Neutrino masses

As opposed to $N_{\rm eff}$, which mainly changes the early expansion of the Universe, the changes in the background evolution caused by neutrino masses, under standard assumptions and for a fixed set of standard cosmological parameters, are confined to late times. In particular, the neutrino mass impact the angular diameter distance and z_Λ (the redshift of matter-to-cosmological-constant equality) (see Refs. [182,297,302–306] for a review on neutrino mass in cosmology).

In the standard ΛCDM scenario, a larger value of m_ν results in a lower Hubble rate inferred from the CMB, exacerbating the H_0 *tension*. However, there is partial correlation between the equation of state of dark energy (DE) w and the total neutrino mass m_ν, as first noticed by [303]. When m_ν is increased (or more generally Ω_ν), Ω_m can be kept unchanged by simultaneously decreasing w in order to keep the angular diameter distance at decoupling fixed. In this case, the impact of neutrino mass on the background is confined to variations of z_Λ and of the late-time ISW effect.

Cosmological bounds on the neutrino masses can therefore be relaxed if a DE component with $w_{\rm DE} \neq -1$ is used instead of a cosmological constant. Vice versa, cosmological constraints on the DE parameters become larger in comparison to cosmologies with massless neutrinos or with the standard minimal assumption of $m_\nu = 0.06$ eV. Analogous conclusions were obtained in the context of Galileon gravity [285].

In Fig. 6.4, I show the combined effect on the CMB anisotropies of varying both ξ and m_ν in the IG model. Note that my assumption, which is the one I adopt throughout this Section is to have one massive and two massless neutrinos. For a fixed value of the coupling parameter $\xi = 0.0008$, the differences with respect to the ΛCDM concordance model are reduced by increasing the value of the neutrino mass m_ν from 0.1 eV to 0.3 eV. On the late-time observables, i.e. the weak lensing CMB anisotropies and the linear matter power spectrum, the partial degeneracy between modified gravity and the neutrino mass is still present but with differences concentrated on small scales, see Fig. 6.5.

In this case the constraints on the coupling parameter ξ become tighter compared to the case with $m_\nu = 0$, i.e. from $\xi < 0.00098$ to $\xi < 0.00094$ at 95% CL for P18. The CMB anisotropies data prefer to relax the upper bound on the neutrino mass which becomes $m_\nu < 0.31$ eV at 95% CL for P18 29% larger to the ΛCDM case $m_\nu < 0.24$

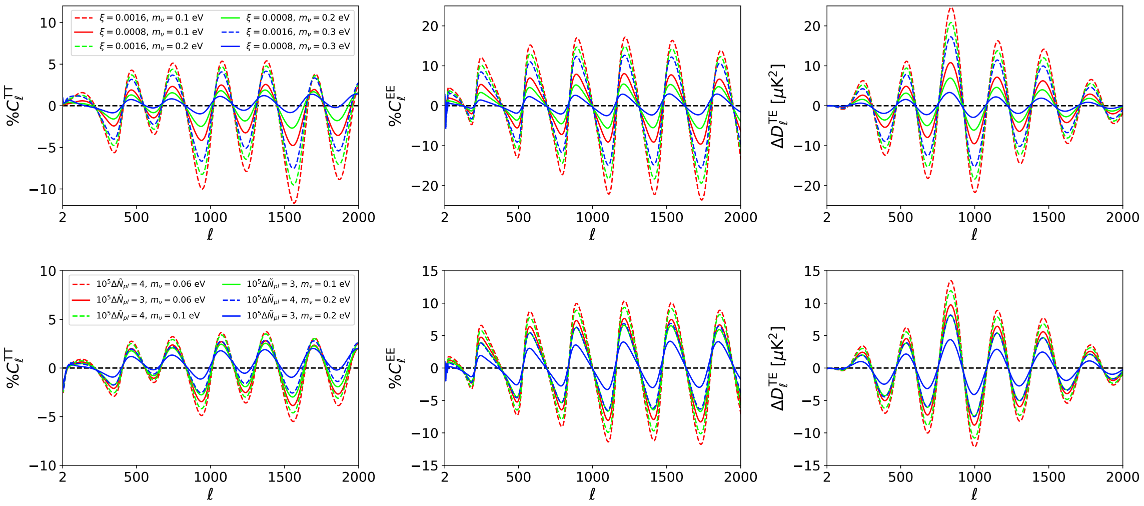

Figure 6.4: Differences with respect to the ΛCDM with $m_\nu = 0$ eV with IG (top panels) for $\xi = 0.0008, 0.0016$ (solid, dashed) and $m_\nu = 0.1, 0.2, 0.3$ eV (red, green, blue), and CC (bottom panels) for $N_{pl} = 1.00003, 1.00004$ M$_{pl}$ (solid, dashed) and $m_\nu = 0.06, 0.1, 0.2$ eV (red, green, blue). Figure taken from Ref. [4].

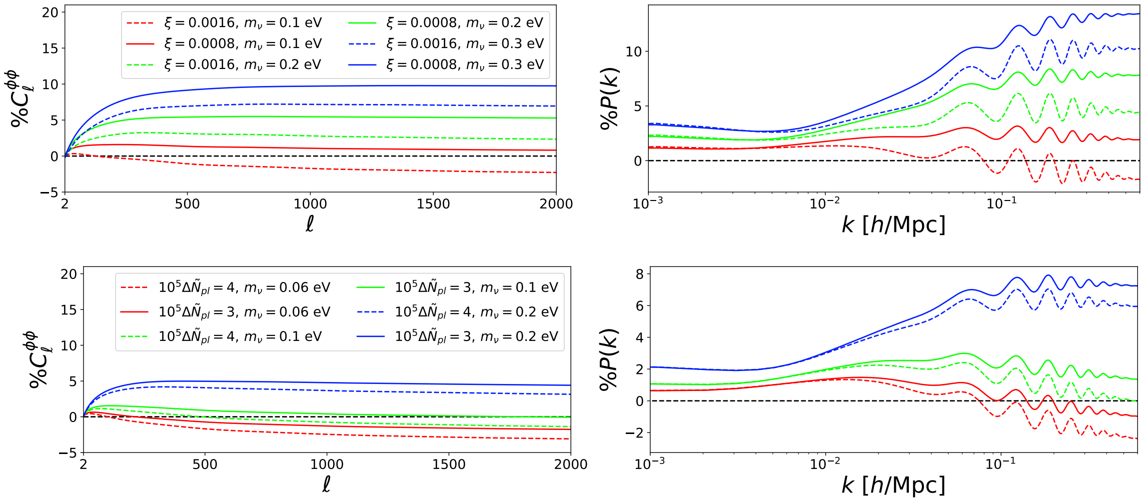

Figure 6.5: Differences with respect to the ΛCDM with $m_\nu = 0$ eV with IG (top panels) for $\xi = 0.0008, 0.0016$ (solid, dashed) and $m_\nu = 0.1, 0.2, 0.3$ eV (red, green, blue), and CC (bottom panels) for $N_{pl} = 1.00003, 1.00004$ M$_{pl}$ (solid, dashed) and $m_\nu = 0.06, 0.1, 0.2$ eV (red, green, blue). Figure taken from Ref. [4].

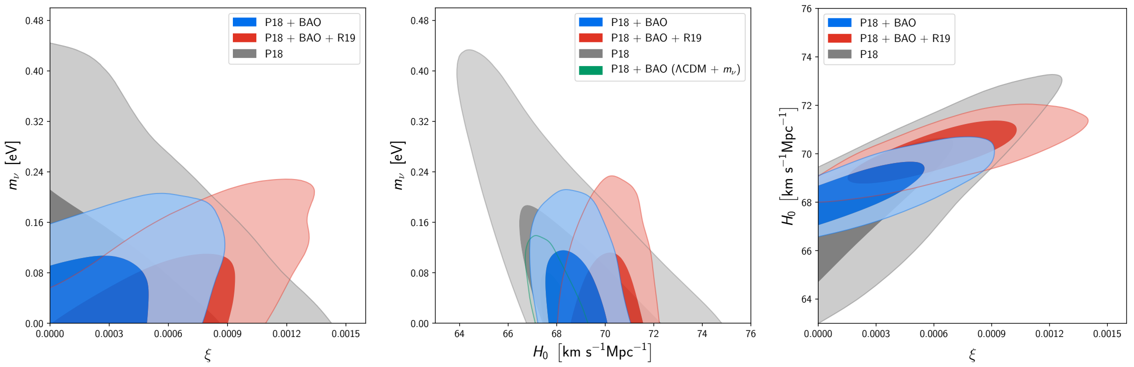

Figure 6.6: Marginalized joint 68% and 95% CL regions 2D parameter space using P18 (gray) in combination with BAO (blue) and BAO + R19 (red) for the IG+m_ν model. In the central panel, I include the $H_0 - N_{\rm eff}$ contours for the ΛCDM in green. Figure taken from Ref. [4].

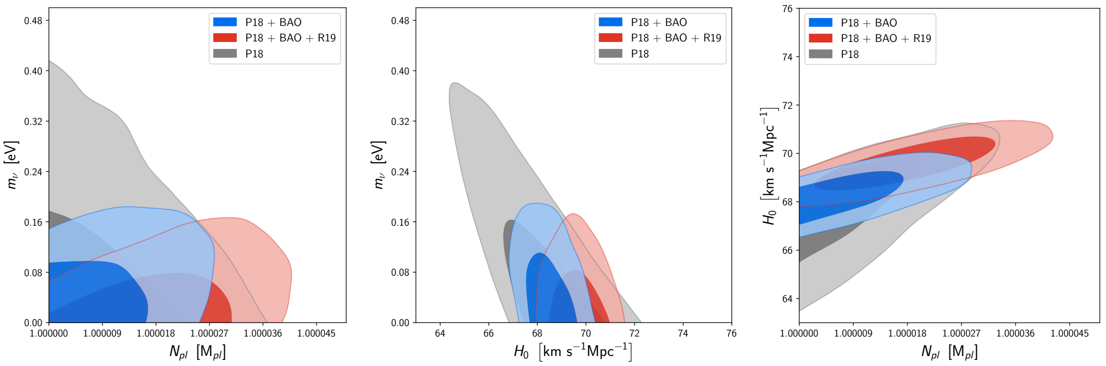

Figure 6.7: Marginalized joint 68% and 95% CL regions 2D parameter space using P18 (gray) in combination with BAO (blue) and BAO + R19 (red) for the CC+m_ν model. Figure taken from Ref. [4].

eV. Including the BAO data, the total neutrino mass is constrained to $m_\nu < 0.17$ eV at 95% CL, 42% larger to the ΛCDM case $m_\nu < 0.12$ eV, and I find $\xi < 0.00076$ at 95% CL, see Tab. 6.3. The addition of R19 data leads to $H_0 = (70.1 \pm 0.8)$ km s^{-1}Mpc^{-1} with an upper bound on the total neutrino mass $m_\nu < 0.19$ eV at 95% CL, 2.5 times larger than the limit based on the ΛCDM model, with a 2σ detection of the coupling parameter $\xi = 0.00065 \pm 0.00057$ at 95% CL, see Fig. 6.6.

Analogously, for CC the constraint on N_{pl} becomes tighter compared to the case with $m_\nu = 0$, i.e. $N_{pl} < 1.000026$ M$_{pl}$ for P18 and $N_{pl} < 1.000024$ M$_{pl}$ for P18 + BAO at 95% CL, see Fig. 6.7. Also, for this model, the upper bound on the neutrino mass becomes 30% larger compared to the ΛCDM case, see Tab. 6.4.

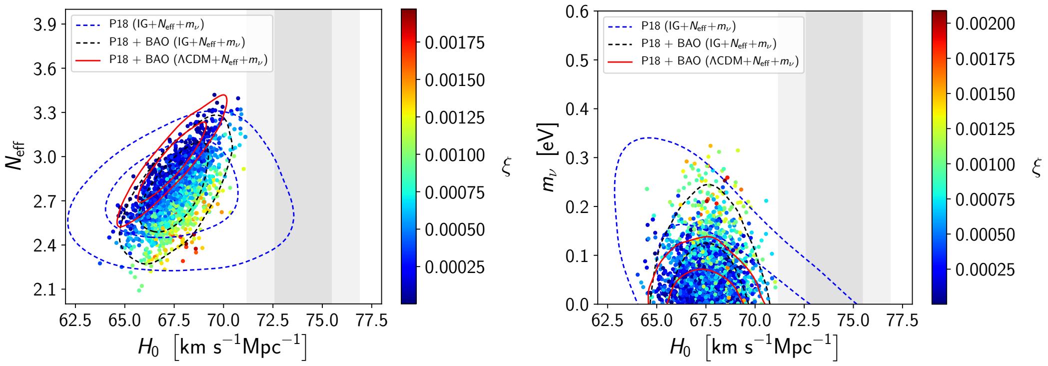

Figure 6.8: Samples of the P18 + BAO chains in the $H_0 - N_{\rm eff}$ ($H_0 - m_\nu$) plane, colour-coded by ξ for the IG+$N_{\rm eff}$+m_ν model. Dashed blue contours show the constraints for IG+$N_{\rm eff}$+m_ν with P18 alone. Solid red contours show the constraints for the ΛCDM+$N_{\rm eff}$+m_ν model. The gray bands denote the local Hubble parameter measurement from R19 [145]. Figure taken from Ref. [4].

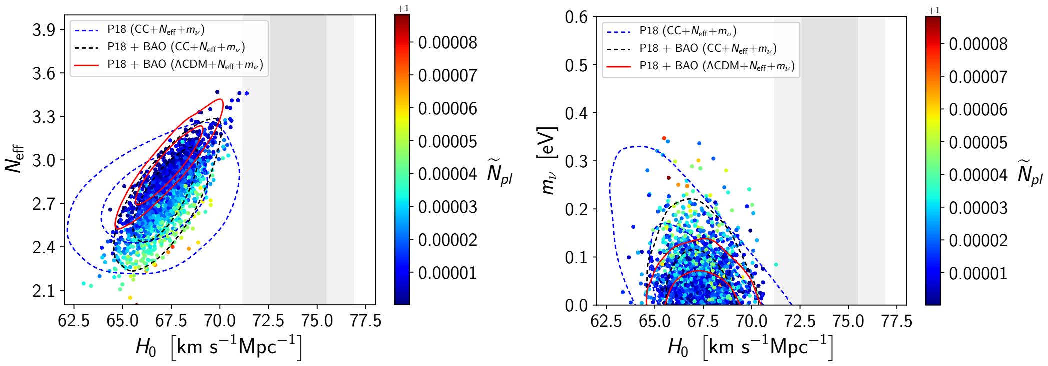

Figure 6.9: Samples of the P18 + BAO chains in the $H_0 - N_{\rm eff}$ ($H_0 - m_\nu$) plane, colour-coded by N_{pl} for the CC+$N_{\rm eff}$+m_ν model. Dashed blue contours show the constraints for CC+$N_{\rm eff}$+m_ν with P18 alone. Solid red contours show the constraints for the ΛCDM+$N_{\rm eff}$+m_ν model. The gray bands denote the local Hubble parameter measurement from R19 [145]. Figure taken from Ref. [4].

6.3 Joint constraints on $N_{\rm eff}$ and neutrino mass

Finally, it is interesting to consider also the case where both $N_{\rm eff}$ and m_ν are allowed to vary. Despite the larger parameter space and the larger limits on the parameters, the models do not accommodate higher values of the Hubble parameter compared to the 7- and 8-parameters case analysed before, see Figs. 6.8-6.9. Moreover, contrary to the case where $N_{\rm eff}$ was fixed, the total neutrino mass is now almost uncorrelated with the Hubble parameter. In this case, the modified gravity parameters ξ and N_{pl} are always compatible at 2σ with the GR limit due to the larger parameter space and are given by (see Tabs. 6.5-6.6):

$$\xi < 0.0018 \text{ (95\% CL)}\,, \qquad N_{\rm eff} = 2.74 \pm 0.22\,, \qquad m_\nu < 0.26 \text{ eV (95\% CL)}$$

for IG and

$$N_{pl} < 1.000050 \text{ M}_{pl} \text{ (95\% CL)}\,, \qquad N_{\rm eff} = 2.73 \pm 0.21\,, \qquad m_\nu < 0.26 \text{ eV (95\% CL)}$$

for the CC case. When BAO data are included, the constraints change to

$$\xi < 0.0012 \text{ (95\% CL)}\,, \qquad N_{\rm eff} = 2.77 \pm 0.20\,, \qquad m_\nu < 0.19 \text{ eV (95\% CL)}$$

for IG and

$$N_{pl} < 1.000042 \text{ M}_{pl} \text{ (95\% CL)}\,, \qquad N_{\rm eff} = 2.75 \pm 0.21\,, \qquad m_\nu < 0.17 \text{ eV (95\% CL)}$$

for the CC case. Further adding R19, I get

$$\xi < 0.0013 \text{ (95\% CL)}\,, \qquad N_{\rm eff} = 3.08 \pm 0.20\,, \qquad m_\nu < 0.19 \text{ eV (95\% CL)}$$

for IG and

$$N_{pl} < 1.000040 \text{ M}_{pl} \text{ (95\% CL)}\,, \qquad N_{\rm eff} = 3.14 \pm 0.20\,, \qquad m_\nu < 0.14 \text{ eV (95\% CL)}$$

for the CC case.

6.4 Summary of the results

In this Chapter, I have investigated the degeneracy of the ST theories studied in Chapter 4 with the the physics of neutrinos [4]. To do so, I have extended the analysis for the IG and CC models in Sections 4.2 and 4.4 respectively, to a general neutrino sector by allowing the effective number of relativistic species $N_{\rm eff}$ and the neutrino mass m_ν to vary. Both $N_{\rm eff}$ and m_ν are partially degenerate with the deviations from GR, as happens in other modified gravity models [281,282,285]. Whereas $N_{\rm eff}$ and the scalar field act as an additional source of radiation in the early Universe, at late times the background contribution to Ω_m due to m_ν can be compensated from the scalar field in order to keep the angular diameter distance at decoupling fixed, see Figs. 6.1-6.4-6.5. However, I have shown that these are only partial degeneracies which could be broken by combination of observations at different redshifts.

In the case where $N_{\rm eff}$ is left free to vary (Sec. 6.1) the limit on ξ becomes $\sim 94\%$ ($\sim 42\%$) larger with P18 (P18+BAO) while the mean on the number of neutrinos moves around 1σ towards lower values compared to the ΛCDM case without significantly degrading its uncertainty, i.e. $N_{\rm eff} = 2.79 \pm 0.20$ ($N_{\rm eff} = 2.85 \pm 0.17$). For CC the limit on N_{pl} becomes $\sim 104\%$ ($\sim 6\%$) larger with P18 (P18+BAO) and analogously to IG I find $N_{\rm eff} = 2.73^{+0.25}_{-0.22}$ ($N_{\rm eff} = 2.81 \pm 0.19$).

The upper bound on the neutrino mass (Sec. 6.2) is $\sim 29\%$ ($\sim 42\%$) is also degraded with P18 (P18+BAO) compared to the ΛCDM case, i.e. $m_\nu < 0.31$ eV ($m_\nu < 0.17$ eV), whereas the constraint on ξ is slightly tighter with CMB data alone in order to relax the constraint on m_ν. Analogously, for CC the limit on the neutrino mass is $\sim 17\%$ ($\sim 33\%$) larger with P18 (P18+BAO) compared to the ΛCDM case. When both $N_{\rm eff}$ and m_ν are allowed to vary, the constraints on ξ and $N_{\rm pl}$ degrade by a factor two compared to the case with $N_{\rm eff} = 3.046$ and $m_\nu = 0$ eV also in presence of BAO data, i.e. $\xi < 0.0012$ and $N_{pl} < 1.000042$ M_{pl} at 95% CL. For the data used, the combination of the modification to gravity in our models to non-standard neutrino physics does not lead to higher values of H_0 compared to the case with standard assumptions in the neutrino sector.

6.5 Tables

Here I collect the Tables containing the constraints from the MCMC analysis considered in this Chapter.

	P18	P18 + BAO	P18 + BAO + R19
$\omega_{\rm b}$	$0.02227^{+0.00018}_{-0.00021}$	0.02225 ± 0.00019	0.02250 ± 0.00019
$\omega_{\rm c}$	0.1161 ± 0.0031	0.1172 ± 0.0030	0.1210 ± 0.0029
H_0 [km s^{-1}Mpc^{-1}]	$69.2^{+1.5}_{-2.4}$ (2.3σ)	$67.9^{+1.0}_{-1.2}$ (3.5σ)	70.28 ± 0.92 (2.2σ)
τ	0.0547 ± 0.0078	0.0526 ± 0.0069	0.0549 ± 0.0072
$\ln\left(10^{10} A_{\rm s}\right)$	3.038 ± 0.016	3.035 ± 0.015	3.050 ± 0.016
$n_{\rm s}$	$0.9617^{+0.0049}_{-0.0088}$	$0.9600^{+0.0045}_{-0.0079}$	0.9707 ± 0.0069
$\zeta_{\rm IG}$	< 0.0076 (95% CL)	< 0.0031 (95% CL)	< 0.0040 (95% CL)
$N_{\rm eff}$	2.79 ± 0.20	2.85 ± 0.17	3.11 ± 0.19
ξ	< 0.0019 (95% CL)	< 0.00078 (95% CL)	< 0.0010 (95% CL)
γ_{PN}	> 0.9925 (95% CL)	> 0.9969 (95% CL)	> 0.9960 (95% CL)
$\delta G_{\rm N}/G_{\rm N}$ (z=0)	> -0.055 (95% CL)	> -0.023 (95% CL)	> -0.029 (95% CL)
$10^{13}\dot{G}_{\rm N}/G_{\rm N}$ (z=0) [yr^{-1}]	> -2.2 (95% CL)	> -0.93 (95% CL)	> -1.2 (95% CL)
$\delta G_{\rm N}/G$ (z=0)	> 0.9962 (95% CL)	> 0.9985 (95% CL)	> -0.9980 (95% CL)
$\Omega_{\rm m}$	$0.290^{+0.022}_{-0.012}$	0.3022 ± 0.0074	0.2906 ± 0.0067
σ_8	$0.834^{+0.012}_{-0.018}$	0.825 ± 0.010	0.841 ± 0.010
r_s [Mpc]	$148.2^{+1.8}_{-1.5}$	148.4 ± 1.7	145.5 ± 1.5
$\Delta\chi^2$	1.7	-1.8	-3.0

Table 6.1: Constraints on main and derived parameters (at 68% CL if not otherwise stated) considering P18 in combination with BAO and BAO + R19 for the IG+$N_{\rm eff}$ model.

	P18	P18 + BAO	P18 + BAO + R19
$\omega_{\rm b}$	0.02223 ± 0.00022	0.02215 ± 0.00022	0.02257 ± 0.00018
$\omega_{\rm c}$	0.1151 ± 0.0033	0.1162 ± 0.0031	0.1213 ± 0.0030
H_0 [km s^{-1}Mpc^{-1}]	67.9 ± 1.4 (3.1σ)	67.1 ± 1.2 (3.7σ)	70.10 ± 0.92 (2.0σ)
τ	$0.0539^{+0.0060}_{-0.0074}$	$0.0544^{+0.0061}_{-0.0074}$	$0.0561^{+0.0063}_{-0.0075}$
$\ln\left(10^{10} A_{\rm s}\right)$	3.034 ± 0.017	3.035 ± 0.016	$3.053^{+0.014}_{-0.016}$
$n_{\rm s}$	0.9598 ± 0.0084	0.9606 ± 0.0071	0.9736 ± 0.0062
$N_{\rm pl}$ [M$_{\rm pl}$]	< 1.000057 (95% CL)	< 1.000019 (95% CL)	< 1.000032 (95% CL)
$N_{\rm eff}$	$2.73^{+0.25}_{-0.22}$	2.81 ± 0.19	3.16 ± 0.19
γ_{PN}	> 0.999943 (95% CL)	> 0.999981 (95% CL)	> 0.999968 (95% CL)
β_{PN}	< 1.0000048 (95% CL)	< 1.0000015 (95% CL)	< 1.0000027 (95% CL)
$\delta G_{\rm N}/G_{\rm N}$ (z=0)	> -0.052 (95% CL)	> -0.018 (95% CL)	> -0.030 (95% CL)
$10^{13}\dot{G}_{\rm N}/G_{\rm N}$ (z=0) [yr^{-1}]	$> -7.5 \times 10^{-9}$ (95% CL)	$> -2.5 \times 10^{-9}$ (95% CL)	$> -4.3 \times 10^{-9}$ (95% CL)
$G_{\rm N}/G$ (z=0)	> 0.999975 (95% CL)	> 0.999991 (95% CL)	> 0.999984 (95% CL)
$\Omega_{\rm m}$	$0.299^{+0.014}_{-0.011}$	0.3070 ± 0.0066	0.2929 ± 0.0062
σ_8	$0.827^{+0.011}_{-0.013}$	0.8204 ± 0.0099	0.8391 ± 0.0095
r_s [Mpc]	149.5 ± 2.0	149.3 ± 2.0	145.5 ± 1.6
$\Delta\chi^2$	1.4	-0.2	-3.8

Table 6.2: Constraints on main and derived parameters (at 68% CL if not otherwise stated) considering P18 in combination with BAO and BAO + R19 for the CC+$N_{\rm eff}$ model.

	P18	P18 + BAO	P18 + BAO + R19
$\omega_{\rm b}$	0.02239 ± 0.00017	0.02241 ± 0.00014	0.02247 ± 0.00013
$\omega_{\rm c}$	0.1205 ± 0.0013	0.1203 ± 0.0011	0.1203 ± 0.0012
H_0 [km s^{-1}Mpc^{-1}]	68.5 ± 1.8 (2.4σ)	$68.66^{+0.69}_{-0.87}$ (3.4σ)	70.12 ± 0.81 (2.4σ)
τ	$0.0567^{+0.0065}_{-0.0082}$	$0.0564^{+0.0066}_{-0.0080}$	$0.0572^{+0.0063}_{-0.0080}$
$\ln\left(10^{10}A_{\rm s}\right)$	$3.052^{-0.016}_{+0.013}$	$3.051^{-0.016}_{+0.013}$	$3.054^{+0.013}_{-0.016}$
$n_{\rm s}$	0.9668 ± 0.0053	0.9672 ± 0.0038	0.9700 ± 0.0038
$\zeta_{\rm IG}$	< 0.0037 (95% CL)	< 0.0030 (95% CL)	$0.0026^{+0.0010}_{-0.0013}$
m_ν [eV]	< 0.31 (95% CL)	< 0.17 (95% CL)	< 0.19 (95% CL)
ξ	< 0.00094 (95% CL)	< 0.00076 (95% CL)	0.00065 ± 0.00057 (95% CL)
γ_{PN}	> 0.9963 (95% CL)	> 0.9970 (95% CL)	$0.9974^{+0.0013}_{-0.0010}$
$\delta G_{\rm N}/G_{\rm N}$ (z=0)	> -0.027 (95% CL)	> -0.022 (95% CL)	$-0.0190^{+0.0093}_{-0.0075}$
$10^{13}\dot{G}_{\rm N}/G_{\rm N}$ (z=0) [yr^{-1}]	> -1.1 (95% CL)	> -0.93 (95% CL)	$-0.78^{+0.39}_{-0.31}$
$G_{\rm N}/G$ (z=0)	> 0.9981 (95% CL)	> 0.9985 (95% CL)	$0.9987^{+0.00064}_{-0.00051}$
$\Omega_{\rm m}$	$0.306^{+0.015}_{-0.018}$	0.3029 ± 0.0076	0.2905 ± 0.0068
σ_8	$0.815^{+0.025}_{-0.014}$	$0.821^{+0.014}_{-0.010}$	0.832 ± 0.013
r_s [Mpc]	$146.18^{+0.78}_{-0.38}$	$146.31^{+0.71}_{-0.37}$	$145.56^{+0.78}_{-0.69}$
$\Delta\chi^2$	3.0	0.2	-3.3

Table 6.3: Constraints on main and derived parameters (at 68% CL if not otherwise stated) considering P18 in combination with BAO and BAO + R19 for the IG+m_ν model.

	P18	P18 + BAO	P18 + BAO + R19
$\omega_{\rm b}$	0.02240 ± 0.00016	0.02242 ± 0.00013	0.02252 ± 0.00013
$\omega_{\rm c}$	0.1203 ± 0.0013	0.12011 ± 0.00097	0.1197 ± 0.0010
H_0 [km s^{-1}Mpc^{-1}]	68.0 ± 1.4 (3.0σ)	$68.31^{+0.62}_{-0.69}$ (3.7σ)	$69.62\ 0.71$ (2.8σ)
τ	$0.0563^{+0.0063}_{-0.0080}$	$0.0564^{+0.0065}_{-0.0077}$	$0.0576^{+0.0067}_{-0.0077}$
$\ln\left(10^{10}A_{\rm s}\right)$	$3.051^{+0.013}_{-0.016}$	$3.047^{+0.013}_{-0.015}$	$3.054^{+0.013}_{-0.016}$
$n_{\rm s}$	0.9674 ± 0.0053	0.9681 ± 0.0043	0.9720 ± 0.0041
$N_{\rm pl}$ [M$_{\rm pl}$]	< 1.000026 (95% CL)	< 1.000024 (95% CL)	$1.000019^{+0.000017}_{-0.000018}$ (95% CL)
m_ν [eV]	< 0.28 (95% CL)	< 0.16 (95% CL)	< 0.13 (95% CL)
γ_{PN}	> 0.999926 (95% CL)	> 0.999924 (95% CL)	$0.9999192^{+0.000009}_{-0.000011}$ (95% CL)
β_{PN}	< 1.0000021 (95% CL)	< 1.0000020 (95% CL)	< 1.0000030 (95% CL)
$\delta G_{\rm N}/G_{\rm N}$	> -0.024 (95% CL)	> -0.023 (95% CL)	$-0.0181^{+0.0099}_{-0.0082}$
$10^{13}\dot{G}_{\rm N}/G_{\rm N}$ (z=0) [yr^{-1}]	$> -3.6 \times 10^{-9}$ (95% CL)	$> -3.3 \times 10^{-9}$ (95% CL)	$(-2.7^{+1.5}_{-1.2}) \times 10^{-9}$
$G_{\rm N}/G$ (z=0)	> 0.999987 (95% CL)	> 0.9999988 (95% CL)	$0.9999904^{+0.0000054}_{-0.0000043}$
$\Omega_{\rm m}$	$0.309^{+0.011}_{-0.015}$	0.3047 ± 0.0067	0.2935 ± 0.0064
σ_8	0.814 ± 0.010	$0.820^{+0.013}_{-0.010}$	0.831 ± 0.012
r_s [Mpc]	$146.52^{+0.47}_{-0.34}$	$146.58^{+0.47}_{-0.31}$	$146.26^{+0.55}_{-0.48}$
$\Delta\chi^2$	3.0	0.0	-1.5

Table 6.4: Constraints on main and derived parameters (at 68% CL if not otherwise stated) considering P18 in combination with BAO and BAO + R19 for the CC+m_ν model.

	P18	P18 + BAO	P18 + BAO + R19
$\omega_{\rm b}$	0.02218 ± 0.00022	$0.02220^{+0.00022}_{-0.00019}$	0.02250 ± 0.00020
$\omega_{\rm c}$	0.1162 ± 0.0034	0.1164 ± 0.0031	0.1208 ± 0.0030
H_0 [km s^{-1}Mpc^{-1}]	$67.7^{+2.0}_{-2.4}$ (2.6σ)	$67.6 \pm 1.2 (3.5\sigma)$	70.25 ± 0.92 (2.2σ)
τ	$0.0556^{+0.0065}_{-0.0083}$	$0.0554^{+0.0065}_{-0.0073}$	$0.0576^{+0.0063}_{-0.0081}$
$\ln\left(10^{10}A_{\rm s}\right)$	$3.039^{-0.018}_{+0.016}$	3.039 ± 0.016	3.056 ± 0.016
$n_{\rm s}$	0.9577 ± 0.0086	0.9582 ± 0.0076	0.9710 ± 0.0071
$\zeta_{\rm IG}$	< 0.0070 (95% CL)	< 0.0047 (95% CL)	< 0.0053 (95% CL)
m_ν [eV]	< 0.26 (95% CL)	< 0.19 (95% CL)	< 0.19 (95% CL)
$N_{\rm eff}$	2.74 ± 0.22	2.77 ± 0.20	3.08 ± 0.20
ξ	< 0.0018 (95% CL)	< 0.0012 (95% CL)	< 0.0013 (95% CL)
γ_{PN}	> 0.9931 (95% CL)	> 0.9954 (95% CL)	> 0.9948 (95% CL)
$\delta G_{\rm N}/G_{\rm N}$ (z=0)	> -0.050 (95% CL)	> -0.034 (95% CL)	> -0.038 (95% CL)
$10^{13}\dot{G}_{\rm N}/G_{\rm N}$ (z=0) [yr^{-1}]	> -2.0 (95% CL)	> -1.4 (95% CL)	> 1.6 (95% CL)
$G_{\rm N}/G$ (z=0)	> 0.9966 (95% CL)	> 0.9977 (95% CL)	> 0.9974 (95% CL)
$\Omega_{\rm m}$	$0.303^{+0.022}_{-0.019}$	0.3035 ± 0.0081	0.2904 ± 0.0069
σ_8	$0.814^{+0.025}_{-0.019}$	$0.815^{+0.015}_{-0.012}$	$0.833^{+0.013}_{-0.011}$
r_s [Mpc]	148.6 ± 1.9	148.6 ± 1.8	145.3 ± 1.6
$\Delta\chi^2$	1.1	0.5	-2.5

Table 6.5: Constraints on main and derived parameters (at 68% CL if not otherwise stated) considering P18 in combination with BAO and BAO + R19 for the IG+$N_{\rm eff}$+m_ν model.

	P18	P18 + BAO	P18 + BAO + R19
$\omega_{\rm b}$	0.02217 ± 0.00022	0.02222 ± 0.00020	0.02257 ± 0.00018
$\omega_{\rm c}$	0.1158 ± 0.0034	0.1158 ± 0.0032	0.1212 ± 0.0031
H_0 [km s^{-1}Mpc^{-1}]	66.7 ± 1.8 (3.2σ)	$67.2 \pm 1.1 (3.8\sigma)$	69.96 ± 0.93 (2.1σ)
τ	$0.0554^{+0.0064}_{-0.0076}$	$0.0556^{+0.0063}_{-0.0075}$	$0.0577^{+0.0069}_{-0.0082}$
$\ln\left(10^{10}A_{\rm s}\right)$	3.039 ± 0.017	3.039 ± 0.016	3.057 ± 0.016
$n_{\rm s}$	0.9582 ± 0.0084	0.9596 ± 0.0074	0.9745 ± 0.0064
N_{pl} [M$_{\rm pl}$]	< 1.000050 (95% CL)	< 1.000042 (95% CL)	< 1.000040 (95% CL)
m_ν [eV]	< 0.26 (95% CL)	< 0.17 (95% CL)	< 0.14 (95% CL)
$N_{\rm eff}$	2.73 ± 0.21	2.75 ± 0.21	3.14 ± 0.20
γ_{PN}	> 0.999950 (95% CL)	> 0.9958 (95% CL)	> 0.9960 (95% CL)
β_{PN}	< 1.0000041 (95% CL)	< 1.0000035 (95% CL)	< 1.0000033 (95% CL)
$\delta G_{\rm N}/G_{\rm N}$ (z=0)	> -0.046 (95% CL)	> -0.040 (95% CL)	> -0.037 (95% CL)
$10^{13}\dot{G}_{\rm N}/G_{\rm N}$ (z=0) [yr^{-1}]	$> -6.7 \times 10^{-9}$ (95% CL)	$> -5.7 \times 10^{-9}$ (95% CL)	$> -5.5 \times 10^{-9}$ (95% CL)
$G_{\rm N}/G$ (z=0)	> 0.999975 (95% CL)	> 0.999979 (95% CL)	> 0.999980 (95% CL)
$\Omega_{\rm m}$	$0.310^{+0.016}_{-0.018}$	0.3056 ± 0.0074	0.2939 ± 0.0064
σ_8	$0.808^{+0.024}_{-0.015}$	$0.814^{+0.015}_{-0.011}$	0.833 ± 0.012
r_s [Mpc]	$149.3^{+1.8}_{-2.1}$	149.2 ± 1.9	145.4 ± 1.7
$\Delta\chi^2$	3.0	0.4	-0.6

Table 6.6: Constraints on main and derived parameters (at 68% CL if not otherwise stated) considering P18 in combination with BAO and BAO + R19 for the CC+$N_{\rm eff}$+m_ν model.

Chapter 7

Isocurvature initial conditions in scalar-tensor theories

7.1 Introduction

In the previous Chapters I have always assumed adiabatic initial conditions on the cosmological perturbations, following the discussion in Section 1.8. In the same Section, though, I also discussed that the current constraints do not rule out completely isocurvature perturbations, but leave open the possibility of a small fraction of isocurvature modes that can arise because of the multi-component nature of the cosmic fluid. In the context of ST tensor theories, the scalar field σ is yet another component which is active during the expansion of the Universe, and therefore additional isocurvature modes can arise.

This fact is very well known in the case of quintessence models with $F(\sigma) = 1$, for which it was found that fluctuations are very close to be adiabatic during a tracking regime in which the parameter of state of quintessence mimics the one of the component dominating the total energy density of the Universe [307]. In the case of thawing quintessence models, in which a tracking regime is absent, isocurvature quintessence fluctuations are instead allowed [307, 308]. From the phenomenological point of view, a mixture of curvature and quintessence isocurvature perturbations is an interesting explanation of the low amplitude of the quadrupole and more in general of the low-ℓ anomaly of the CMB anisotropies pattern [308, 309].

In this Chapter, I study the most general set of set of cosmological perturbations produced in ST theories with the Lagrangian of the form (2.2.3), focusing in particular on a new isocurvature mode exclusively due to the presence of σ and absent in Einstein Gravity. I analytically derive the initial conditions for Einstein-Boltzmann codes and analyze its imprints on the CMB spectra. I conclude by constraining the allowed isocurvature fraction using the recent CMB data from the last Planck release to constrain their allowed fraction.

This Chapter is based on the research work in Ref. [5] and on the preliminary results that will be soon published in Ref. [6], where the phenomenology of isocurvature modes is studied in the context of the IG. For this reason, in this Chapter, I focus on the latter model, leaving the detailed analysis of isocurvature perturbations in ST models described by the action in Eq. (2.2.3) for future studies.

7.2 Initial Conditions in Scalar-Tensor Theories

The initial conditions on the cosmological perturbations are usually expressed as a series in power of $k\tau$, where τ is the conformal time [37, 40]. To derive them, the set of the perturbed Einstein-Boltzmann equations described in Chapters 1 and 3 has therefore to be expanded in powers of $k\tau \to 0$ and solved at every order in $k\tau$. This amounts to considering perturbations deep in the radiation era and in the super-horizon limit.

In order to solve the perturbed equations, expressions for the background quantities, such as the scale factor a and the Hubble parameter $\mathcal{H} = a'/a$, need to be derived in the $\tau \to 0$ limit too. In ST theories, also the scalar field σ is needed. By expanding the background equations in Section 2.2.1 in powers of the conformal time τ, the following solutions at the leading order in τ the are easily obtained:

$$a(\tau) = \sqrt{\frac{\rho_{r0}}{3F_i}}\tau \left[1 + \frac{\omega}{4}\tau - \frac{5}{16}\frac{\xi^2\sigma_i^2(1+6\xi)}{F_i + 6\xi^2\sigma_i^2}\omega^2\tau^2\right], \tag{7.2.1}$$

$$\mathcal{H}(\tau) = \frac{1}{\tau}\left[1 + \frac{\omega}{4}\tau - \frac{1}{16}\frac{F_i + 4\xi^2\sigma_i^2(4+15\xi)}{F_i + 6\xi^2\sigma_i^2}\omega^2\tau^2\right], \tag{7.2.2}$$

$$\sigma(\tau) = \sigma_i\left[1 + \frac{3}{2}\xi\omega\tau - \frac{2F_i(1-3\xi) + 27\xi^2\sigma_i^2(1+2\xi)}{8(F_i + 6\xi^2\sigma_i^2)}\omega^2\tau^2\right], \tag{7.2.3}$$

where I define ω as

$$\omega = \frac{\rho_{m0}}{\sqrt{3\rho_{r0}}}\frac{\sqrt{F_i}}{F_i + 6\xi^2\sigma_i^2} \tag{7.2.4}$$

and $F_i = N_{\rm pl}^2 + \xi\sigma_i^2$. As can be seen from the solution above, the scalar field σ is initially frozen and starts to thaw because of its coupling to non-relativistic matter, as discussed in the previous Chapters.

Inserting these solutions in the perturbed Einstein-Boltzmann equations, it is possible to derive the most general set of initial conditions. As mentioned above, this consists in the usual adiabatic and isocurvature modes discussed in Section 1.8 supplemented with a new isocurvature mode caused by the presence of the field σ. The results presented here are specific of the choice $F(\sigma) = N_{\rm pl}^2 + \xi\sigma_2$, but can easily generalized to every functional form of $F(\sigma)$.

I closely follow Ref. [40] in presenting the initial conditions, for which I explicitly report the leading order in the $k\tau$ series expansion. To complete the characterization of the initial conditions, I also report the leading order of the Newtonian potentials and the curvature perturbation $\mathcal{R}$. The latter is very important since, as discussed in Section 1.8, adiabatic and isocurvature initial conditions are classified according to their contribution to the comoving gauge curvature perturbation [35]. In particular, the adiabatic mode leads $\mathcal{R} \simeq C$ at leading order in the $k\tau$ expansion, where C is a normalization related to the primordial spectrum produced by inflation, whereas at leading order $\mathcal{R} \simeq 0$ for isocurvature modes.

I closely follow Ref. [40] in presenting the initial conditions, for which I explicitly report the leading orders in a double expansion in $k\tau$ and $\omega\tau$. To complete the characterization of the initial conditions, I also report the leading order of the Newtonian potentials Φ and Ψ and the curvature perturbation $\mathcal{R}_{\rm rad} = \Phi + (\Phi'/\mathcal{H} + \Psi)/2$ [1].

For later convenience I define the quantities:

$$R_\nu \equiv \frac{\rho_{\nu 0}}{\rho_{\rm r0}}, \qquad R_b \equiv \frac{\rho_{b0}}{\rho_{\rm m0}}, \qquad R_\gamma \equiv 1 - R_\nu \qquad R_c \equiv 1 - R_b. \tag{7.2.5}$$

Adiabatic mode (ADI) The adiabatic mode in Einstein Gravity is slightly modified by the presence of the scalar field and becomes [2]:

$$\begin{aligned}
&\delta_\gamma = \delta_\nu = \frac{4}{3}\delta_b = \frac{4}{3}\delta_c = -\frac{2C}{3}k^2\tau^2\left[1 - \frac{\omega\tau}{5}\right],\\
&\theta_\gamma = -\frac{Ck^4\tau^3}{36}\left[1 - \frac{3\omega\tau}{20}\frac{(5R_b + R_\gamma)F_i + 30\xi^2\sigma_i^2}{R_\gamma F_i}\right],\\
&\theta_\nu = -\frac{C}{18}k^4\tau^3\left[\frac{4R_\nu + 23}{4R_\nu + 15} - \frac{3\omega\tau\left((8R_\nu^2 + 50R_\nu + 275)F_i + 60(5 - 4R_\nu)\xi^2\sigma_i^2\right)}{20(2R_\nu + 15)(4R_\nu + 15)F_i}\right],\\
&\sigma_\nu = \frac{4Ck^2\tau^2}{3(4R_\nu + 15)}\left[1 + \frac{(4R_\nu - 5)(F_i + 6\xi^2\sigma_i^2)}{4(4R_\nu + 15)(2R_\nu + 15)}\omega\tau\right],\\
&h = Ck^2\tau^2\left[1 - \frac{\omega\tau}{5}\right],\\
&\eta = 2C - \frac{Ck^2\tau^2}{6}\left[\frac{(4R_\nu + 5)}{(4R_\nu + 15)} - \omega\tau\frac{150(4R_\nu - 5)\xi^2\sigma_i^2 + (16R_\nu^2 + 280R_\nu + 325)F_i}{10(2R_\nu + 15)(4R_\nu + 15)F_i}\right],\\
&\frac{\delta\sigma}{\sigma_i} = -\frac{C\xi\omega k^2\tau^3}{4} + \frac{C\xi\omega^2k^2\tau^4}{40}\frac{\left[2\xi^2\sigma_i^2(24 + 45\xi) + (4 - 9\xi)F_i\right]}{(F_i + 6\xi^2\sigma_i^2)}.
\end{aligned} \tag{7.2.6}$$

The Newtonian potentials are given by $\Psi = \frac{4C(2R_\nu+5)}{(4R_\nu+15)}$ and $\Phi = \frac{20}{(4R_\nu+15)}$ at leading order and the curvature perturbation is equal to $\mathcal{R} \simeq C$.

---

[1] Note that $\mathcal{R}_{\rm rad}$ coincides with the right hand side of Eq. (1.8.18) for $w_{\rm tot} = 1/3$

Baryon Isocurvature mode (BI)

$$\delta_\gamma = -\frac{2R_b\omega\tau}{3}\left[1 - \frac{6N_{\rm pl}^2}{16(F_i+6\xi^2\sigma_i^2)}\omega\tau - \frac{3\xi(1+6\xi)(15\xi+2)\sigma_i^2}{16(F_i+6\xi^2\sigma_i^2)}\omega\tau\right],$$

$$\delta_\nu = \delta_\gamma,$$

$$\theta_\gamma = -\frac{\omega R_b}{12}k^2\tau^2 + \frac{{R_b}^2\omega^2(F_i+6\xi^2\sigma_i^2)}{16R_\gamma F_i}k^2\tau^3 + \frac{R_b\omega^2\left(\xi(1+6\xi)(15\xi+2)\sigma_i^2+2N_{\rm pl}^2\right)}{96(F_i+6\xi^2\sigma_i^2)}k^2\tau^3,$$

$$\delta_c = -\frac{R_b\omega}{2}\tau + \frac{3R_b\omega^2\tau^2}{32(F_i+6\xi^2\sigma_i^2)}\left[\xi(1+6\xi)(15\xi+2)\sigma_i^2 + 2N_{\rm pl}^2\right],$$

$$\delta_b = 1 + \delta_c,$$

$$\theta_\nu = \theta_\gamma - \frac{{R_b}^2\omega^2(F_i+6\xi^2\sigma_i^2)}{16R_\gamma F_i}k^2\tau^3,$$

$$\sigma_\nu = -\frac{R_b\omega(F_i+6\xi^2\sigma_i^2)}{6(2R_\nu+15)F_i}k^2\tau^3,$$

$$h = R_b\omega\tau\left[1 - \frac{6N_{\rm pl}^2}{16(F_i+6\xi^2\sigma_i^2)}\omega\tau - \frac{3\xi(1+6\xi)(15\xi+2)\sigma_i^2}{16(F_i+6\xi^2\sigma_i^2)}\omega\tau\right],$$

$$\eta = -\frac{h}{6},$$

$$\frac{\delta\sigma}{\sigma_i} = \frac{3\xi R_b\omega\tau}{2}\left[1 - \frac{(5-12\xi)N_{\rm pl}^2}{12(F_i+6\xi^2\sigma_i^2)}\omega\tau - \frac{\xi(1+6\xi)(18\xi+5)\sigma_i^2}{12(F_i+6\xi^2\sigma_i^2)}\omega\tau\right].$$

The Newtonian potentials are given by

$$\Psi = -\frac{R_b\omega(15\xi\sigma_i^2(1-6\xi)+15N_{\rm pl}^2+4R_\nu F_i)}{8(2R_\nu+15)F_i}\tau,$$

$$\Phi = -\frac{R_b\omega\left(15\xi\sigma_i^2(1+8\xi)+15N_{\rm pl}^2-4R_\nu F_i\right)}{8(2R_\nu+15)F_i}\tau$$

at leading order and $\mathcal{R} \simeq 0$.

CDM Isocurvature mode (CDI)

$$\delta_\gamma = -\frac{2R_c\omega\tau}{3}\left[1 - \frac{6N_{\rm pl}^2}{16(F_i+6\xi^2\sigma_i^2)}\omega\tau - \frac{3\xi(1+6\xi)(15\xi+2)\sigma_i^2}{16(F_i+6\xi^2\sigma_i^2)}\omega\tau\right],$$

$$\delta_\nu = \delta_\gamma,$$

$$\theta_\gamma = -\frac{\omega R_c}{12}k^2\tau^2 + \frac{{R_c}^2\omega^2(F_i+6\xi^2\sigma_i^2)}{16R_\gamma F_i}k^2\tau^3 + \frac{R_c\omega^2\left(\xi(1+6\xi)(15\xi+2)\sigma_i^2+2N_{\rm pl}^2\right)}{96(F_i+6\xi^2\sigma_i^2)}k^2\tau^3,$$

$$
\begin{aligned}
\delta_b &= -\frac{R_c\omega}{2}\tau + \frac{3R_c\omega^2\tau^2}{32(F_i+6\xi^2\sigma_i^2)}\left[\xi(1+6\xi)(15\xi+2)\sigma_i^2 + 2N_{\rm pl}^2\right],\\
\delta_c &= 1+\delta_b,\\
\theta_\nu &= \theta_\gamma - \frac{{R_c}^2\omega^2(F_i+6\xi^2\sigma_i^2)}{16R_\gamma F_i}k^2\tau^3,\\
\sigma_\nu &= -\frac{R_c\omega(F_i+6\xi^2\sigma_i^2)}{6(2R_\nu+15)F_i}k^2\tau^3,\\
h &= R_c\omega\tau\left[1 - \frac{6N_{\rm pl}^2}{16(F_i+6\xi^2\sigma_i^2)}\omega\tau - \frac{3\xi(1+6\xi)(15\xi+2)\sigma_i^2}{16(F_i+6\xi^2\sigma_i^2)}\omega\tau\right],\\
\eta &= -\frac{h}{6},\\
\frac{\delta\sigma}{\sigma_i} &= \frac{3\xi R_c\omega\tau}{2}\left[1 - \frac{(5-12\xi)N_{\rm pl}^2}{12(F_i+6\xi^2\sigma_i^2)}\omega\tau - \frac{\xi(1+6\xi)(18\xi+5)\sigma_i^2}{12(F_i+6\xi^2\sigma_i^2)}\omega\tau\right]. \qquad (7.2.7)
\end{aligned}
$$

The Newtonian potentials are given by

$$
\begin{aligned}
\Psi &= -\frac{R_c\omega(15\xi\sigma_i^2(1-6\xi)+15N_{\rm pl}^2+4R_\nu F_i)}{8(2R_\nu+15)F_i}\tau,\\
\Phi &= -\frac{R_c\omega\left(15\xi\sigma_i^2(1+8\xi)+15N_{\rm pl}^2-4R_\nu F_i\right)}{8(2R_\nu+15)F_i}\tau
\end{aligned}
$$

at leading order and, again, $\mathcal{R} \simeq 0$.

Neutrino Density Isocurvature mode (NDI)

$$
\begin{aligned}
\delta_\gamma &= -\frac{R_\nu}{R_\gamma}\,\delta_\nu = -\frac{R_\nu}{R_\gamma} + \frac{k^2R_\nu\tau^2}{6R_\gamma},\\
\theta_\gamma &= -\frac{k^2R_\nu\tau}{4R_\gamma} + \frac{3(F_i+6\xi^2\sigma_i^2)k^2R_bR_\nu\omega\tau^2}{16R_\gamma^2F_i},\\
\delta_b &= \frac{k^2R_\nu\tau^2}{8R_\gamma}, \quad \delta_c = -\frac{k^2R_bR_\nu\tau^3\omega}{80R_\gamma} + k^4\tau^4\frac{R_\nu}{72(4R_\nu+15)},\\
\theta_\nu &= \frac{k^2\tau}{4}, \quad \text{and} \quad \sigma_\nu = \frac{k^2\tau^2}{2(4R_\nu+15)},\\
h &= \frac{k^2R_bR_\nu\tau^3\omega}{40R_\gamma}, \quad \eta = -\frac{R_\nu k^2\tau^2}{6(4R_\nu+15)},\\
\frac{\delta\sigma}{\sigma_i} &= \frac{\xi k^2R_bR_\nu\tau^3\omega}{32R_\gamma}. \qquad (7.2.8)
\end{aligned}
$$

The Newtonian potentials are given by

$$
\Psi = \frac{R_\nu}{4R_\nu+15} \quad \text{and} \quad \Phi = -\frac{2R_\nu}{4R_\nu+15}
$$

at leading order and, again, $\mathcal{R} \simeq 0$.

Neutrino Velocity Isocurvature mode (NIV)

$$\begin{aligned}
\delta_\gamma =& \frac{4R_\nu}{3R_\gamma}k\tau - \frac{R_b R_\nu \omega F_i(R_\gamma + 2) + 12\xi^2\sigma_i^2}{4R_\gamma^2 F_i}k\tau^2, \\
\theta_\gamma =& -\frac{kR_\nu}{R_\gamma} + \frac{3R_b R_\nu \omega(F_i + 6\xi^2\sigma_i^2)}{4R_\gamma^2 F_i}k\tau + \left[\frac{k^3\tau^2 R_\nu}{6R_\gamma} - \frac{27(R_b\omega\xi\sigma_i)^2 R_\nu(F_i + 6\xi^2\sigma_i^2)}{8R_\gamma^3 F_i^2}k\tau^2 \right. \\
&\left. - \frac{3R_b R_\nu \omega^2(F_i + 6\xi^2\sigma_i^2)(3R_b - R_\gamma)}{16R_\gamma^3 F_i}k\tau^2\right], \\
\delta_b =& \frac{R_\nu}{R_\gamma}k\tau - \frac{3R_b R_\nu \omega(F_i(R_\gamma + 2) + 12\xi^2\sigma_i^2}{16R_\gamma^2 F_i}k\tau^2, \\
\delta_c =& -\frac{3R_b R_\nu \omega}{16R_\gamma}k\tau^2, \\
\delta_\nu =& -\frac{4}{3}k\tau - \frac{R_b R_\nu \omega}{4R_\gamma}k\tau^2, \\
\theta_\nu =& k - \frac{(4R_\nu + 9)}{6(4R_\nu + 5)}k^3\tau^2, \\
\sigma_\nu =& \frac{4}{3(4R_\nu + 5)}k\tau + \frac{4R_\nu \omega(F_i + 6\xi^2\sigma_i^2)}{(4R_\nu + 5)(4R_\nu + 15)F_i}k\tau^2, \\
h =& \frac{3R_b R_\nu \omega}{8R_\gamma}k\tau^2, \\
\eta =& -\frac{4R_\nu}{3(4R_\nu + 5)}k\tau - \frac{R_b R_\nu \omega}{16R_\gamma}\tau^2 + \frac{5R_\nu \omega(F_i + 6\xi^2\sigma_i^2)}{(4R_\nu + 5)(4R_\nu + 15)F_i}k\tau^2, \\
\frac{\delta\sigma}{\sigma_i} =& \frac{\xi R_b R_\nu \omega}{2R_\gamma}k\tau^2
\end{aligned} \tag{7.2.9}$$

The Newtonian potentials are given by

$$\Psi = -\Phi = \frac{4R_\nu}{k(4R_\nu + 5)\tau}$$

at leading order and, again, $\mathcal{R} \simeq 0$.

New Isocurvature mode (ISONMC) The initial conditions for the new isocurvature mode, which unlike the previous ones is peculiar of ST theories, are the following:

$$
\begin{aligned}
\delta_\gamma =&\delta_\nu = -\frac{\xi\sigma_i^2}{F_i} - \frac{2\omega\tau}{3}\frac{\xi(1+6\xi)\sigma_i^2}{F_i+6\xi^2\sigma_i^2} + \frac{k^2\tau^2}{6}\frac{\xi\sigma_i^2}{F_i} - \frac{\omega^2\tau^2}{16}\frac{\xi(1+6\xi)\sigma_i^2}{(F_i+6\xi^2\sigma_i^2)^2}\Bigg[(15\xi-4)N_{\rm pl}^2 \\
&- 2\xi(1+6\xi)(15\xi+2)\sigma_i^2\Bigg], \\
\theta_\gamma =& -\frac{\xi\sigma_i^2}{4F_i}k^2\tau - \frac{\omega k^2\tau^2}{12}\frac{\xi(1+6\xi)\sigma_i^2}{F_i+6\xi^2\sigma_i^2} + \frac{3R_b(F_i+6\xi^2\sigma_i^2)\xi\sigma_i^2}{R_\gamma F_i^2}\frac{\omega k^2\tau^2}{16}, \\
\delta_c =& -\frac{\omega\tau}{2}\frac{\xi(1+6\xi)\sigma_i^2}{F_i+6\xi^2\sigma_i^2} + \frac{3\omega^2\tau^2\xi(1+6\xi)\sigma_i^2}{32(F_i+6\xi^2\sigma_i^2)^2}\left[\xi(1+6\xi)(15\xi+2)\sigma_i^2 - \frac{(15\xi-4)N_{\rm pl}^2}{2}\right], \\
\delta_b =&\delta_c + \frac{k^2\tau^2}{8}\frac{\xi\sigma_i^2}{F_i}, \\
\theta_\nu =& -\frac{\xi\sigma_i^2}{4F_i}k^2\tau - \frac{\omega k^2\tau^2}{12}\frac{\xi(1+6\xi)\sigma_i^2}{F_i+6\xi^2\sigma_i^2}, \\
\sigma_\nu =&\frac{\xi\sigma_i^2}{6(4R_\nu+15)F_i}k^2\tau^2, \\
h =&\omega\tau\frac{\xi(1+6\xi)\sigma_i^2}{F_i+6\xi^2\sigma_i^2} + 3\omega^2\tau^2\frac{\xi(1+6\xi)\sigma_i^2}{32(F_i+6\xi^2\sigma_i^2)^2}\left[(15\xi-4)N_{\rm pl}^2 - 2\xi(1+6\xi)(15\xi+2)\sigma_i^2\right], \\
\eta =& -\frac{\omega\tau}{6}\frac{\xi(1+6\xi)\sigma_i^2}{F_i+6\xi^2\sigma_i^2} + \frac{(R_\nu+5)\xi\sigma_i^2}{6(4R_\nu+15)F_i}k^2\tau^2 + \frac{\xi(1+6\xi)\sigma_i^2\omega^2\tau^2}{64(F_i+6\xi^2\sigma_i^2)^2}\Bigg[(4-15\xi)N_{\rm pl}^2 \\
&+ 2\xi(1+6\xi)(15\xi+2)\sigma_i^2\Bigg] \\
\frac{\delta\sigma}{\sigma_i} =& -\frac{1}{2} + \frac{3\xi\omega\tau[\xi(1+6\xi)\sigma_i^2 - N_{\rm pl}^2]}{4(F_i+6\xi^2\sigma_i^2)} + \frac{k^2\tau^2}{12} - \frac{\omega^2\tau^2\xi^3(1+6\xi)^2(27\xi+8)\sigma_i^4}{16(F_i+6\xi^2\sigma_i^2)^2} \\
&- \frac{\xi(\omega\tau N_{\rm pl})^2}{16(F_i+6\xi^2\sigma_i^2)}\left[(6\xi-2)N_{\rm pl}^2 - 3\xi(6\xi+1)(19\xi-2)\sigma_i^2\right].
\end{aligned}
\tag{7.2.10}
$$

The Newtonian potentials are given by

$$
\begin{aligned}
\Psi =& -\frac{(R_\nu+5)}{(4R_\nu+15)}\frac{\xi\sigma_i^2}{F_i}, \\
\Phi =&\frac{2(R_\nu+5)}{(4R_\nu+15)}\frac{\xi\sigma_i^2}{F_i}
\end{aligned}
$$

at leading order and $\mathcal{R} \simeq 0$.

Note that in all the isocurvature modes above, for simplicity, I omitted an overall multiplying constant $D \equiv f_{\rm ISO}C$ which represents the isocurvature power spectrum.

The new mode (7.2.10) has no analogue in Einstein Gravity. Crucial for the existence and linear independence of this mode is the fact that the background scalar field is almost frozen deep in the radiation era, leading to a constant synchronous gauge perturbation $\delta\sigma$. On the other hand, if the background scalar field is described by a running or scaling solution, such a mode is negligible [310] and the set of initial conditions is completely described by the ADI, CDI, BI, NDI and NIV modes [40].

Another feature of this new mode is that it is independent on the scalar field potential, as can be read off from Eqs. (7.2.10), and is completely characterized by the non-minimal coupling with the Ricci scalar. The choice of the potential affects only higher orders in the $k\tau$ expansion which are negligible. Eqs. (7.2.10) show that, in the limit $\xi \to 0$, all the leading orders in the perturbations vanish except for the constant and second order perturbations in the scalar field. Going to higher orders in the expansion, it can be seen that the first non-vanishing ones are those dependent on the potential of the scalar field would become only source term for the scalar field perturbations. This confirms results in the literature, where it was proved that isocurvature perturbations due to σ have only a small effect in minimally-coupled quintessence models [307–309, 311].

As discussed above, the new mode gives a vanishing contribution to the gauge-invariant curvature perturbation in the comoving gauge $\mathcal{R}$ [312] and therefore can be accounted as an isocurvature. As a cautionary remark, however, note that the definition of the curvature perturbation $\mathcal{R}$ and its interpretation in the Jordan frame are not obvious [313]. Independently on the interpretation, though, the mode in Eqs. (7.2.10) is a growing one and regular and independent on the other modes and as such can have interesting physical implications that I discuss in the following.

As discussed above, the new mode gives a vanishing contribution to $\mathcal{R}_{\rm rad}$ and therefore can be accounted as an isocurvature mode. The variable $\mathcal{R}_{\rm rad}$ should be the leading order contribution of a gauge-invariant curvature perturbation in the comoving gauge in the Jordan frame. The search and the full definition of gauge-invariant curvature perturbation in a multi-fluid system in the Jordan frame is in progress, but beyond the scope of this thesis.

7.3 Correlated Isocurvature and Adiabatic Perturbations

As already stressed, CMB measurements tightly constrain the nature of the initial conditions and only allow for a small fraction of isocurvature ones. Moreover, constraints change depending on the correlation between adiabatic and isocurvature initial conditions, which ultimately depends on the specific inflationary mechanism that generated the primordial fluctuations [314,315]. Before discussing the imprints of the new mode on the CMB spectra, it is therefore necessary to discuss the formalism to deal with such a correlation [316,317].

Defining the transfer functions for the pure adiabatic and isocurvature modes as $\Theta_l^{\rm ad}(k)$ and $\Theta_l^{\rm iso}(k)$ respectively, it is useful to define the following quantities:

$$
\begin{aligned}
C_l^{\rm ad} &= \int \frac{dk}{k}\left(\frac{k}{k_0}\right)^{n_{\rm ad}-1}[\Theta_l^{\rm ad}(k)]^2, &(7.3.1)\\
C_l^{\rm iso} &= \int \frac{dk}{k}\left(\frac{k}{k_0}\right)^{n_{\rm iso}-1}[\Theta_l^{\rm iso}(k)]^2, &(7.3.2)\\
C_l^{\rm corr} &= \int \frac{dk}{k}\left(\frac{k}{k_0}\right)^{(n_{\rm ad}+n_{\rm iso})/2-1}\Theta_l^{\rm ad}(k)\Theta_l^{\rm iso}(k), &(7.3.3)
\end{aligned}
$$

which contribute to the total angular power spectrum as follows

$$C_l^{\rm tot} = A^2 C_l^{\rm ad} + B^2 C_l^{\rm iso} + 2AB\cos\theta C_l^{\rm corr}. \tag{7.3.4}$$

The equation above can be conveniently expressed as

$$C_l^{\rm tot} = A^2[C_l^{\rm ad} + f_{\rm iso}^2 C_l^{\rm iso} + 2f_{\rm iso}\cos\theta C_l^{\rm corr}]. \tag{7.3.5}$$

Therefore the correlation is parameterized by the two parameters $f_{\rm iso}$ and $\cos\theta$. Another possibility which is commonly used in the literature, see e.g. Refs. [317,318], is to identify $\alpha \equiv B^2/(A^2+B^2)$ and $\beta \equiv \cos\theta$, so that in order to α can run from a purely adiabatic mode ($\alpha = 0$) to a purely isocurvature one ($\alpha = 1$). The two parameterizations are related by $\alpha = f_{\rm iso}^2/(1+f_{\rm iso}^2)$ so that Eq. (7.3.5) now reads:

$$C_l^{\rm tot} = (A^2+B^2)[(1-\alpha)C_l^{\rm ad} + \alpha C_l^{\rm iso} + 2\beta\sqrt{\alpha(1-\alpha)}C_l^{\rm corr}]. \tag{7.3.6}$$

Note that, since the isocurvature fraction allowed by data is usually very small, i.e. $f_{\rm iso} \ll 1$, the dominant isocurvature contribution comes from the cross-correlation with the adiabatic mode, which is in turn why the largest fraction of isocurvature modes is allowed for uncorrelated modes with $\cos\theta = 0$ [54]. In the following I will consider $n_{ISO} = n_s$ for simplicity.

7.4 Impact on CMB anisotropies

Armed with the formalism of Section 7.3, I now go on to analyze the imprints of the new mode in Eq. (7.2.10) on the CMB power spectra, focusing on the IG model [5,6].

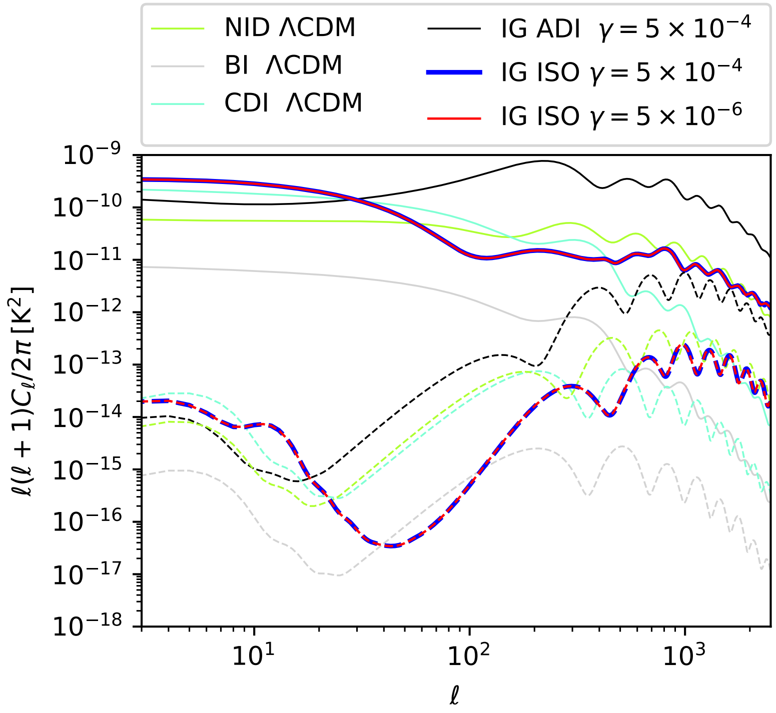

Figure 7.1: CMB anisotropy angular power spectra in temperature, solid lines, and E-mode polarization, dashed lines. The black curve is the adiabatic case, thin curves represent the three standard ΛCDM isocurvature modes and the thick curve represent the new isocurvature mode. In order to compare the spectrum shapes I have assumed equal amplitude between isocurvatures and adiabatic mode, i.e. $f_{\rm ISO} = 1$. Note that blue and red lines are superimposed. Figure taken from Ref. [5].

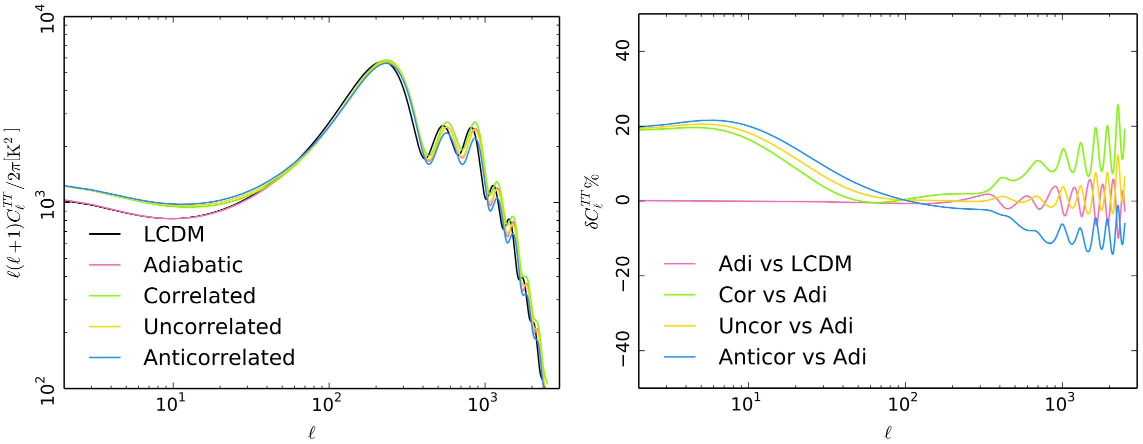

Figure 7.2: [Left] Temperature angular power spectrum of adiabatic+isocurvature modes for the different correlation extrema. [Right] Relative differences to show the impact of isocurvatures in IG. The difference between IG and the standard LCDM corresponding model and the isocurvature contributions are plotted in pink and green, gold and blue lines respectively. In particular I plot the change with respect to the adiabatic case with the same coupling. Figure taken from Ref. [6].

In Fig. 7.1, I show the comparison of the new mode with the adiabatic and standard isocurvature modes in the ΛCDM model within Einstein gravity. Fig. 7.1 also shows the weak dependence of the new isocurvature mode on ξ (γ in the Figure) at least for the small values consistent with the cosmological 95%CL upper bound $\xi \lesssim 0.75 \times 10^{-3}$ [222] (updated to the time Ref. [5] was published) and for Solar System constraints $\gamma \lesssim 0.6 \times 10^{-5}$ [134].

I show the total angular power spectra in temperature and polarization given by the mixture of adiabatic and isocurvature, considering an isocurvature $f_{\mathrm{ISO}} = 0.5$ in the left panels of Figs. 7.2 and 7.3, and their relative differences in the right ones. In order to isolate the effect of isocurvature perturbations, I show in pink the effect of the adiabatic ST case with respect to the one in LCDM and in colored curves the relative difference with respect to the IG adiabatic case with the same coupling. The presence of the isocurvature perturbations has an impact on both intermediate and small angular scales affecting also the acoustic peak region. In polarization, there is also an evident effect on the reionization bump which represents an interesting target for future CMB experiments dedicated to the large scale polarization measurements.

7.5 Constraints with Planck data

In this Section, I present Planck constraints on the new isocurvature mode.

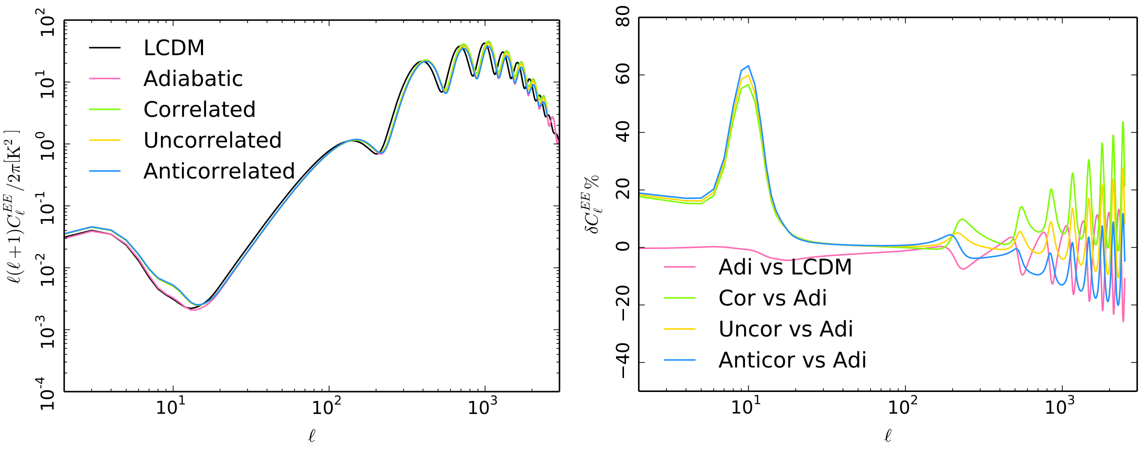

Figure 7.3: [Left] E-mode polarization angular power spectrum of adiabatic+isocurvature modes for the different correlation extrema. [Right] Relative differences to show the impact of isocurvatures in IG. The difference between IG and the standard LCDM corresponding model and the isocurvature contributions are plotted in pink and green, gold and blue lines respectively. Figure taken from Ref. [6].

Planck 2015. Constraints on this isocurvature mode were first obtained in Ref. [5] and I start by discussing the results obtained therein. At the time of preparation of Refs. [5] and [2], a serious bottleneck was a problem in the memory allocation of the ClassIG code, which was responsible for a very limited capability to explore cosmological models by MCMC. For this analysis the value of the non-minimal coupling is fixed to $\gamma = 5 \times 10^{-4}$ to contain the computational cost of the MCMC investigation. The only extra parameter with respect to the baseline adiabatic ΛCDM is therefore the isocurvature fraction $f_{\rm ISO}$, with a flat prior $f_{\rm ISO} \in [0, 0.8]$, but a smooth ΛCDM limit cannot be recovered since the non-minimal coupling is not allowed to vanish by construction. The three cases of correlation between adiabatic and isocurvature perturbations $\cos\theta = -1, 0, 1$ are considered separately as in Ref. [318]. Since at the time of the publication of Ref. [5] P18 data were not public yet, the results discussed here are obtained using P15 data, like in Section 4.2.2. In order to speed up the MCMC exploration, the foreground marginalized PlikLite likelihood at high ℓ is used instead of the full binned Plik one: the use of PlikLite should be a good approximation for one parameter extensions of ΛCDM such as the model including a fraction of isocurvature perturbations with fixed correlation and spectral index [319].

The results of Ref. [5] show no evidence at a statistical significant level for the new isocurvature mode Eq. (7.2.10). The 95% CL bounds from the MCMC exploration are $f_{\rm ISO} < 0.07$ for the fully anti-correlated case $\cos\theta = -1$, $f_{\rm ISO} < 0.12$ for the fully correlated case $\cos\theta = 1$ and $f_{\rm ISO} < 0.31$ for the uncorrelated case $\theta = \pi/2$. These allowed abundances are slightly larger than those of the known isocurvature modes in Einstein gravity, although scale similarly with the degree of correlation [318].

Planck 2018. As of the time I am writing this thesis, an update of the results presented above is in preparation and I will now present some preliminar results. The problem of memory allocation of the ClassIG code reported in the analysis with Planck 2015 data has now been resolved by a significant update of the ClassIG code which allowed an efficient MCMC exploration of cosmological models beyond ΛCDM as in [4].

Differently from the previous analysis, now the coupling γ is varied together with the six ΛCDM parameters and the isocurvature fraction $f_{\rm ISO}$ and now the Planck 2018 baseline likelihood, denoted as P18 in the previous Chapters, is used. Also here, for simplicity, the relation $n_{\rm ISO} = n_s$ is assumed and the extrema of the possible correlations $\cos\theta = -1, 1$ are considered separately[1], as in [54].

The results for the isocurvature fraction and the coupling γ are presented in Table 7.1. In Figure 7.4, I show the triangle plot representing the posterior distribution of the relevant parameters together with their correlation, and compare them to the pure adiabatic case with $f_{\rm ISO} = 0$.

	Correlated	Anti-Correlated
γ_{IG}	< 0.00090	< 0.00105
$f_{\rm ISO}$	< 0.08	< 0.20 (=$0.10^{+0.05}_{-0.07}$at 68% CL)

Table 7.1: Constraints on the amplitude of the isocurvature allowed and the non-minimal coupling γ.

Note that the presence of isocurvature perturbations has an almost negligible impact on the constraints on the coupling γ. Nonetheless, introducing isocurvatures changes the distribution of standard cosmological parameters, most notably the scalar spectral index, as for other isocurvature modes [54].

In Table 7.2, I present the constraints on the cosmological parameters the standard cosmological parameters compared with the adiabatic case. Note that almost all cosmological parameters are perfectly recovered in presence of isocurvature. The shift in the amplitude of scalar primordial fluctuations is within at 1-σ as the differences in the scalar spectral index. The only exception, although always compatible with adiabatic initial conditions at one σ, is the anticorrelated case that shows a slight degeneracy of both isocurvature and coupling parameters with the normalization power spectrum of scalar fluctuations A_s.

---

[1] Note that here I am not presenting results for the uncorrelated case, as they are not ready yet. I expect the results to be ready for the revised version of this thesis.

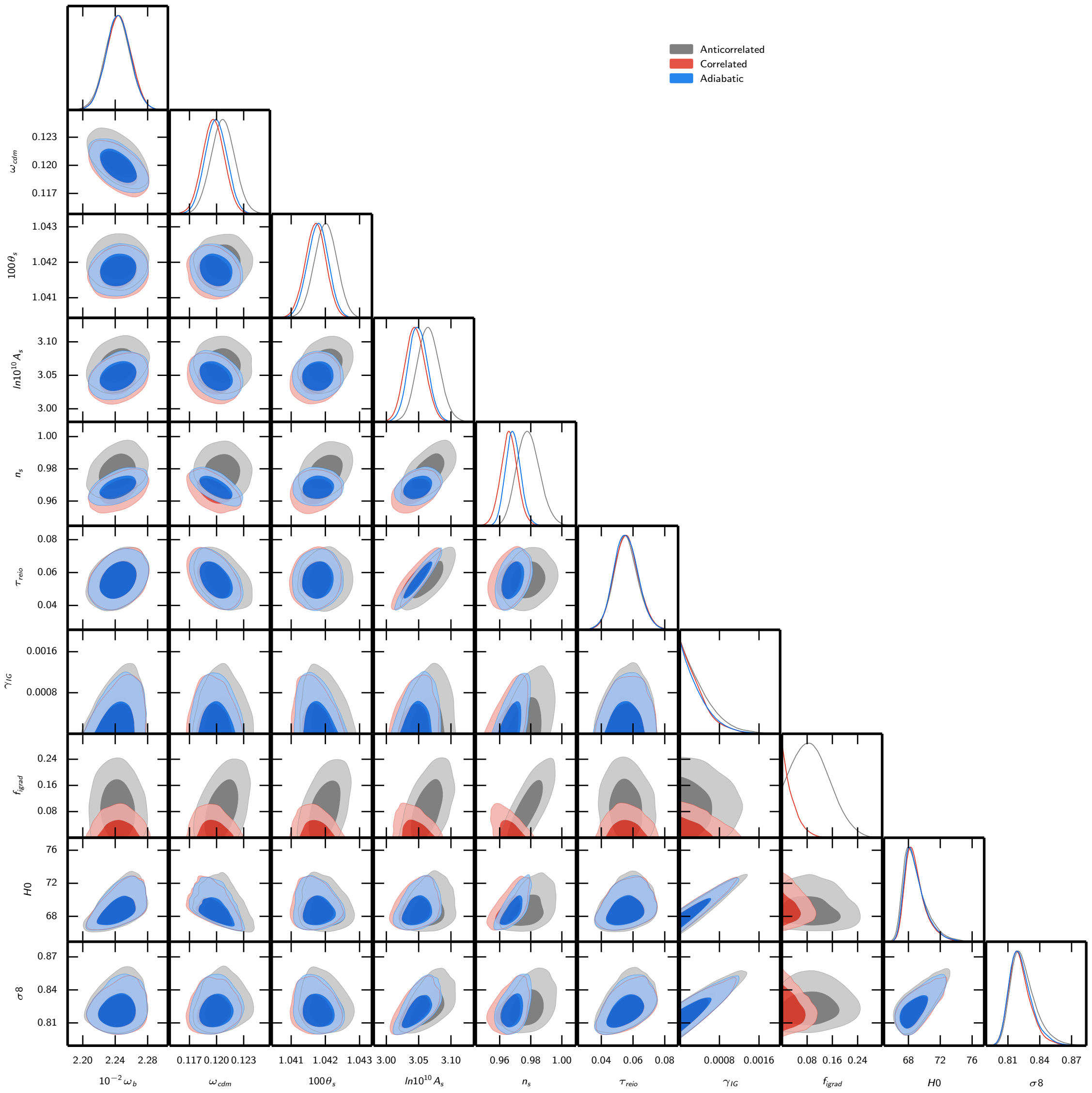

Figure 7.4: Posterior distribution of cosmological+isocurvature parameters compared with the adiabatic case. Preliminary results from Ref. [6].

	Correlated	Anti-Correlated	Adiabatic
$10^{-2}\omega_b$	2.244 ± 0.015	2.242 ± 0.015	2.244 ± 0.015
ω_{cdm}	0.120 ± 0.001	0.121 ± 0.001	0.120 ± 0.001
$100\theta_s$	1.0417 ± 0.0003	1.0420 ± 0.0003	1.0418 ± 0.0003
$\ln(10^{10}A_s)$	3.044 ± 0.015	3.065 ± 0.017	$3.050^{+0.014}_{-0.015}$
n_s	0.9660 ± 0.0053	$0.9784^{+0.0067}_{-0.0080}$	$0.9687^{+0.0045}_{-0.0051}$
τ_{reio}	$0.0557^{+0.0074}_{-0.0075}$	$0.0555^{+0.0073}_{-0.0075}$	$0.0555^{+0.0072}_{-0.0078}$
γ_{IG}	< 0.00090	< 0.00105	< 0.00094

Table 7.2: Comparison of cosmological parameters with the adiabatic case. I report 68% CL constraints except for upper limits, for which I report 95% CL limits.

7.6 Summary of the results

In this Chapter, I have studied in details the most general set of initial conditions for the cosmological perturbations in ST theories. In particular, I have derived a new regular and growing isocurvature mode which is due to the presence of the nearly frozen non-minimally coupled scalar field during the radiation era. The mode, which is absent in GR, is characterized by constant perturbations to the density contrast of photons and neutrinos and to the perturbation to the scalar field $\delta\sigma$.

Its imprints on the CMB spectra are much stronger than the ones of the corresponding mode in minimally-coupled quintessence models and are enhanced by the non-minimal coupling $F(\sigma)$, at least in the IG model studied in this Chapter. Furthermore, the CMB spectra for this new mode are completely different from the ones derived assuming other known isocurvature initial conditions.

Assuming the three benchmark cases of fully correlated, fully anti-correlation and uncorrelated adiabatic and isocurvature initial conditions, I have shown how current Planck data constrain the contribution of this isocurvature mode to be significantly subdominant with respect to the adiabatic one. This is in line with results in the literature, although the bounds I find are slightly less tight then the ones derived for other Einstein Gravity isocurvature modes.

Chapter 8

Discussion and Outlook

During my PhD, the field of observational cosmology has seen important developments. The last release by the Planck team in 2018 has provided a map of the Cosmic Microwave Background (CMB) anisotropies of a quality never reached before, the BOSS team released extraordinary constraints on the matter power spectrum and on the Baryon Acoustic Oscillations (BAO) and the list is still very long. Furthermore, a special mention goes to nascent field of Gravitational Waves astronomy which is already revolutionizing our understanding of the Universe. One one hand, this lead to improved constraints on the cosmological parameters describing the standard ΛCDM cosmological model. On the other, the unprecedented precision (and the growing number) of cosmological and astrophysical measurements have increased considerably some of the already existing tensions between datasets, such as the tensions on $S_8 = \sigma_8\sqrt{\Omega_m/0.3}$ and H_0. The latter is a tension between the model dependent inference of the H_0 parameter from early Universe data such as the CMB and other cosmological observations and its model independent local measurements. Given the constraining power of cosmological data and the number of unanswered questions, this is a great time to explore new physics beyond the ΛCDM model.

The aim of my thesis work is to use data to constrain cosmological models of Scalar-Tensor (ST) theories where a scalar field σ is coupled to the Ricci scalar through a function of the form $F(\sigma) = N_{\rm pl}^2 + \xi\sigma^2$. In these models, also named Non-Minimally Coupled (NMC) model, the modification to gravity manifests itself in a time-variation of the Newton constant $G_N(\sigma) = 1/8\pi F(\sigma)$ and its derivatives, the so called Post Newtonian (PN) parameters, with respect to General Relativity (GR). Despite these theories are very simple and only constitute a small corner in the more complex space of theoretically and observationally viable ST theories, the functional form of $F(\sigma)$ introduced above, together with the freedom of choosing the potential $V(\sigma)$, lead to a vast phenomenology. I focus on those models in which the scalar field is frozen deep in the radiation era and starts to move around the time of matter-radiation equality and its energy density eventually redshifts away, leading to a late time evolution of the Universe very close to ΛCDM. These peculiarities make these modified gravity models candidates for early solutions to H_0 tension. The latter has become more and more pressing over the past few years and a series of recent works has shown that the solutions which are most likely to work are 'early' Universe ones that lower the comoving sound horizon r_s compared to ΛCDM. For this reason, throughout this thesis, particular attention is given to the consequences of ST theories on the Hubble tension.

The simplest scenario studied in this thesis is the one of a (nearly) massless scalar field. This is implemented by choosing a potential of the form $V(\sigma) \propto F(\sigma)^2$ or simply by setting it to a cosmological constant $V(\sigma) = \Lambda$, though cosmological data are not able to tell the two choices apart, so they are effectively equivalent. When dealing with these models, a strategy commonly used to deal with the tight constraints on the Newton constant from laboratory experiments is to fix it to its measured value using a shooting algorithm on one of the ST parameters. With this method I have contributed to derive constraints the model parameters using a variety of cosmological data such as Planck 2015 (P15) and 2018 (P18) measurements of the CMB anisotropies, BAO and SH0ES measurements of H_0 (R19). Although in the most general NMC models, cosmological constraints on the PN parameters are in agreement with Solar System ones, in the Induced Gravity (IG) model, which is a redefinition of the Jordan-Brans-Dicke (JBD) one, Solar System constraints are much tighter than cosmological ones. Within NMC, we can alternatively set $N_{\rm pl} = M_{\rm pl}$, sample on the initial value of the field σ_i and abandon the prior on the Newton constant. With these priors, the region with $\xi < 0$, where the scalar field decreases in the matter dominated era, covers most of the parameter space allowed by the data. As expected, all these possibilities lead to an H_0 significantly larger than the obtained in ΛCDM, regardless of particular choice of dataset, although the Hubble tension is only alleviated.

A more complex situation is obtained when a small effective mass for the scalar field σ is induced by a a quartic potential $V(\sigma) = \lambda\sigma^4/4$. In this case, dubbed Early Modified Gravity (EMG) model, the scalar field eventually becomes massive compared to the Hubble flow, rolls down its potential and undergoes damped oscillations around its minimum in turn injecting a sharp amount of energy into the cosmic fluid, similarly to what happens in Early Dark Energy models. Specializing again to $N_{\rm pl} = M_{\rm pl}$ the model is naturally in agreement with all the tests of gravity. An interesting consequences of adding the potential is that the positive branch of the coupling $\xi \geq 0$, which is not allowed in the massless case, is now consistent with cosmological data and actually helps fit Large Scale Structure (LSS) data such as measurements of the full shape of the matter power spectrum. Furthermore, compared to the massless models, the H_0 tension is significantly reduced, although the price to pay is a higher degree of fine tuning in λ.

A common consequence of many modified gravity theories is a radical change in the cosmological constraints on neutrino masses m_ν and on the number of active relativistic species $N_{\rm eff}$. This, together with the fact that a large $N_{\rm eff}$ is very well known to significantly ease the tension, as our models, naively suggests a degeneracy between the physics of Neutrinos and the one of ST theories. To this purpose, I have used several combinations of cosmological datasets in the context of NMC and IG to analyze their interplay with Neutrino physics, by opening the Monte-Carlo-Markov-Chain (MCMC) exploration to the parameters m_ν and $N_{\rm eff}$. I discuss that only small degeneracies are left by current data and the tension on H_0 is only mildly affected and constraints on m_ν and $N_{\rm eff}$ are relaxed with respect to the ones in the ΛCDM context.

Finally, the presence of a nearly frozen scalar field deep in the radiation era could justify a new isocurvature mode in the set of initial conditions for the linear cosmological perturbations. For this new growing and regular mode the imprints on cosmological observables are boosted by the non-minimal coupling compared to its counterpart in minimally-coupled quintessence models. As for other isocurvature modes it leads to a vanishing contribution to the curvature perturbations at leading order in expansion in powers of $k\tau$. An MCMC analysis with CMB P15 and P18 data shows that only a small fraction of this new isocurvature mode (but slightly larger than other known isocurvature modes in GR) is allowed in combination with the adiabatic one. The latter fraction, quantified by the parameter $f_{\rm ISO}$, depends on the specific correlation between curvature and isocurvature modes and is found to be maximum when the modes are uncorrelated, consistently with bounds on other isocurvature modes in the literature.

The results of this thesis show that non-minimally coupled scalar field have a wide range of implications for cosmology and are a very good candidate to address the H_0 tension. These are the simplest ST tensor theories that can be extended in several ways from the model building point of view. It is therefore natural to expect an even richer phenomenology by exploring, e.g. different shapes for the scalar field potential, an issue that I am currently exploring, and/or non-trivial kinetic terms or self-interactions in the Horndeski framework. In particular, these terms can induce a scale dependent modification to the growth of structure that can help solve the S_8 tension, which is instead exacerbated in our models. This is also suggested by the results for the EMG model, which show that the non-minimal coupling help improve the fit to LSS data compared to minimally-coupled EDE ones. A necessary step in this direction is also to analyze the models proposed in this thesis, and eventually their extensions, in light of weak-lensing full likelihoods from collaborations such as DES and KiDS.

Bibliography

[1] Matteo Braglia, William T. Emond, Fabio Finelli, A. Emir Gumrukcuoglu, and Kazuya Koyama. Unified framework for Early Dark Energy from α-attractors. 2020.

[2] Massimo Rossi, Mario Ballardini, Matteo Braglia, Fabio Finelli, Daniela Paoletti, Alexei A. Starobinsky, and Caterina Umiltà. Cosmological constraints on post-Newtonian parameters in effectively massless scalar-tensor theories of gravity. *Phys. Rev.*, D100(10):103524, 2019.

[3] Matteo Braglia, Mario Ballardini, William T. Emond, Fabio Finelli, A. Emir Gumrukcuoglu, Kazuya Koyama, and Daniela Paoletti. Larger value for H_0 by an evolving gravitational constant. *Phys. Rev.*, D102(2):023529, 2020.

[4] Mario Ballardini, Matteo Braglia, Fabio Finelli, Daniela Paoletti, Alexei A. Starobinsky, and Caterina Umiltà. Scalar-tensor theories of gravity, neutrino physics, and the H_0 tension. 2020.

[5] D. Paoletti, M. Braglia, F. Finelli, M. Ballardini, and C. Umiltà. Isocurvature fluctuations in the effective Newton's constant. *Phys. Dark Univ.*, 25:100307, 2019.

[6] D. Paoletti, M. Braglia, F. Finelli, M. Ballardini, and C. Umiltà. Planck 2018 constraints on isocurvature fluctuations in extended Jordan-Brans-Dicke gravity. In preparation (2021).

[7] Adam G. Riess et al. Observational evidence from supernovae for an accelerating universe and a cosmological constant. *Astron. J.*, 116:1009–1038, 1998.

[8] G. Hinshaw et al. Nine-Year Wilkinson Microwave Anisotropy Probe (WMAP) Observations: Cosmological Parameter Results. *Astrophys. J. Suppl.*, 208:19, 2013.

[9] N. Aghanim et al. Planck 2018 results. I. Overview and the cosmological legacy of Planck. *Astron. Astrophys.*, 641:A1, 2020.

[10] Steven Weinberg. *Gravitation and Cosmology: Principles and Applications of the General Theory of Relativity.* John Wiley and Sons, New York, 1972.

[11] Charles W. Misner, K.S. Thorne, and J.A. Wheeler. *Gravitation.* W. H. Freeman, San Francisco, 1973.

[12] Robert M. Wald. *General Relativity.* Chicago Univ. Pr., Chicago, USA, 1984.

[13] Bernard F. Schutz. *A FIRST COURSE IN GENERAL RELATIVITY.* Cambridge Univ. Pr., Cambridge, UK, 1985.

[14] Scott Dodelson. *Modern Cosmology.* Academic Press, Amsterdam, 2003.

[15] Sean M. Carroll. *Spacetime and Geometry.* Cambridge University Press, 7 2019.

[16] V. Mukhanov. *Physical Foundations of Cosmology.* Cambridge University Press, Oxford, 2005.

[17] Viatcheslav Mukhanov and Sergei Winitzki. *Introduction to quantum effects in gravity.* Cambridge University Press, 6 2007.

[18] Steven Weinberg. *Cosmology.* 9 2008.

[19] Ruth Durrer. *The Cosmic Microwave Background.* Cambridge University Press, Cambridge, 2008.

[20] David H. Lyth and Andrew R. Liddle. *The primordial density perturbation: Cosmology, inflation and the origin of structure.* 2009.

[21] N. Aghanim et al. Planck 2018 results. VI. Cosmological parameters. *Astron. Astrophys.*, 641:A6, 2020.

[22] George Efstathiou and Steven Gratton. The evidence for a spatially flat Universe. *Mon. Not. Roy. Astron. Soc.*, 496(1):L91–L95, 2020.

[23] Sunny Vagnozzi, Abraham Loeb, and Michele Moresco. Eppur \‘e piatto? The cosmic chronometer take on spatial curvature and cosmic concordance. 11 2020.

[24] Will Handley. Curvature tension: evidence for a closed universe. 8 2019.

[25] Eleonora Di Valentino, Alessandro Melchiorri, and Joseph Silk. Planck evidence for a closed Universe and a possible crisis for cosmology. *Nature Astron.*, 4(2):196–203, 2019.

[26] Eleonora Di Valentino, Alessandro Melchiorri, and Joseph Silk. Cosmic Discordance: Planck and luminosity distance data exclude LCDM. 3 2020.

[27] E. Hubble. *A Relation Between Distance and Radial Velocity Among Extra-Galactic Nebulae*, page 9. 1988.

[28] G. Gamow. Expanding universe and the origin of elements. *Phys. Rev.*, 70:572–573, 1946.

[29] Ann Merchant Boesgaard and Gary Steigman. Big Bang Nucleosynthesis: Theories and Observations. *Ann. Rev. Astron. Astrophys.*, 23:319–378, 1985.

[30] R.H. Dicke, P.J.E. Peebles, P.G. Roll, and D.T. Wilkinson. Cosmic Black-Body Radiation. *Astrophys. J.*, 142:414–419, 1965.

[31] Daniel Baumann. Inflation. In *Theoretical Advanced Study Institute in Elementary Particle Physics: Physics of the Large and the Small*, pages 523–686, 2011.

[32] D.J. Fixsen. The Temperature of the Cosmic Microwave Background. *Astrophys. J.*, 707:916–920, 2009.

[33] Viatcheslav F. Mukhanov, H.A. Feldman, and Robert H. Brandenberger. Theory of cosmological perturbations. Part 1. Classical perturbations. Part 2. Quantum theory of perturbations. Part 3. Extensions. *Phys. Rept.*, 215:203–333, 1992.

[34] Julien Lesgourgues. Cosmological Perturbations. In *Theoretical Advanced Study Institute in Elementary Particle Physics: Searching for New Physics at Small and Large Scales*, pages 29–97, 2013.

[35] Chung-Pei Ma and Edmund Bertschinger. Cosmological perturbation theory in the synchronous and conformal Newtonian gauges. *Astrophys. J.*, 455:7–25, 1995.

[36] James M. Bardeen. Gauge Invariant Cosmological Perturbations. *Phys. Rev. D*, 22:1882–1905, 1980.

[37] Massimo Giovannini. Theoretical tools for the physics of CMB anisotropies. *Int. J. Mod. Phys. D*, 14:363–510, 2005.

[38] J.R. Bond and A.S. Szalay. The Collisionless Damping of Density Fluctuations in an Expanding Universe. *Astrophys. J.*, 274:443–468, 1983.

[39] Arthur Kosowsky. Cosmic microwave background polarization. *Annals Phys.*, 246:49–85, 1996.

[40] Martin Bucher, Kavilan Moodley, and Neil Turok. The General primordial cosmic perturbation. *Phys. Rev. D*, 62:083508, 2000.

[41] Julien Lesgourgues. The Cosmic Linear Anisotropy Solving System (CLASS) I: Overview. 2011.

[42] Diego Blas, Julien Lesgourgues, and Thomas Tram. The Cosmic Linear Anisotropy Solving System (CLASS) II: Approximation schemes. *JCAP*, 1107:034, 2011.

[43] D. Langlois. Isocurvature cosmological perturbations and the CMB. *Comptes Rendus Physique*, 4:953–959, 2003.

[44] Steven Weinberg. Adiabatic modes in cosmology. *Phys. Rev. D*, 67:123504, 2003.

[45] John C. Mather et al. Measurement of the Cosmic Microwave Background spectrum by the COBE FIRAS instrument. *Astrophys. J.*, 420:439–444, 1994.

[46] D.J. Fixsen, E.S. Cheng, J.M. Gales, John C. Mather, R.A. Shafer, and E.L. Wright. The Cosmic Microwave Background spectrum from the full COBE FIRAS data set. *Astrophys. J.*, 473:576, 1996.

[47] P.J.E. Peebles and J.T. Yu. Primeval adiabatic perturbation in an expanding universe. *Astrophys. J.*, 162:815–836, 1970.

[48] C.L. Bennett et al. Nine-Year Wilkinson Microwave Anisotropy Probe (WMAP) Observations: Final Maps and Results. *Astrophys. J. Suppl.*, 208:20, 2013.

[49] Marc Kamionkowski, Arthur Kosowsky, and Albert Stebbins. Statistics of cosmic microwave background polarization. *Phys. Rev. D*, 55:7368–7388, 1997.

[50] Uros Seljak and Matias Zaldarriaga. A Line of sight integration approach to cosmic microwave background anisotropies. *Astrophys. J.*, 469:437–444, 1996.

[51] Yuto Minami and Eiichiro Komatsu. New Extraction of the Cosmic Birefringence from the Planck 2018 Polarization Data. *Phys. Rev. Lett.*, 125(22):221301, 2020.

[52] Wayne Hu and Martin J. White. The Damping tail of CMB anisotropies. *Astrophys. J.*, 479:568, 1997.

[53] Antony Lewis and Anthony Challinor. Weak gravitational lensing of the CMB. *Phys. Rept.*, 429:1–65, 2006.

[54] Y. Akrami et al. Planck 2018 results. X. Constraints on inflation. *Astron. Astrophys.*, 641:A10, 2020.

[55] Nabila Aghanim, Subhabrata Majumdar, and Joseph Silk. Secondary anisotropies of the CMB. *Rept. Prog. Phys.*, 71:066902, 2008.

[56] R.K. Sachs and A.M. Wolfe. Perturbations of a cosmological model and angular variations of the microwave background. *Astrophys. J.*, 147:73–90, 1967.

[57] Scott Dodelson. Coherent phase argument for inflation. *AIP Conf. Proc.*, 689(1):184–196, 2003.

[58] Daniel J. Eisenstein et al. Detection of the Baryon Acoustic Peak in the Large-Scale Correlation Function of SDSS Luminous Red Galaxies. *Astrophys. J.*, 633:560–574, 2005.

[59] Joseph Silk. Cosmic black body radiation and galaxy formation. *Astrophys. J.*, 151:459–471, 1968.

[60] R.A. Sunyaev and Ya.B. Zeldovich. Small scale fluctuations of relic radiation. *Astrophys. Space Sci.*, 7:3–19, 1970.

[61] R.A. Sunyaev and Ya.B. Zeldovich. Microwave background radiation as a probe of the contemporary structure and history of the universe. *Ann. Rev. Astron. Astrophys.*, 18:537–560, 1980.

[62] M.J. Rees and D.W. Sciama. Large scale Density Inhomogeneities in the Universe. *Nature*, 217:511–516, 1968.

[63] Robert G. Crittenden and Neil Turok. Looking for Lambda with the Rees-Sciama effect. *Phys. Rev. Lett.*, 76:575, 1996.

[64] Pablo Fosalba, Enrique Gaztanaga, and Francisco Castander. Detection of the ISW and SZ effects from the CMB-galaxy correlation. *Astrophys. J. Lett.*, 597:L89–92, 2003.

[65] P.A.R. Ade et al. Planck 2013 results. XXII. Constraints on inflation. *Astron. Astrophys.*, 571:A22, 2014.

[66] N. Aghanim et al. Planck 2018 results. V. CMB power spectra and likelihoods. *Astron. Astrophys.*, 641:A5, 2020.

[67] N. Aghanim et al. Planck 2018 results. VIII. Gravitational lensing. *Astron. Astrophys.*, 641:A8, 2020.

[68] Héctor Gil-Marín et al. The clustering of galaxies in the SDSS-III Baryon Oscillation Spectroscopic Survey: RSD measurement from the LOS-dependent power spectrum of DR12 BOSS galaxies. *Mon. Not. Roy. Astron. Soc.*, 460(4):4188–4209, 2016.

[69] Guido D'Amico, Jérôme Gleyzes, Nickolas Kokron, Katarina Markovic, Leonardo Senatore, Pierre Zhang, Florian Beutler, and Héctor Gil-Marín. The Cosmological Analysis of the SDSS/BOSS data from the Effective Field Theory of Large-Scale Structure. *JCAP*, 05:005, 2020.

[70] Thomas Colas, Guido D'amico, Leonardo Senatore, Pierre Zhang, and Florian Beutler. Efficient Cosmological Analysis of the SDSS/BOSS data from the Effective Field Theory of Large-Scale Structure. *JCAP*, 06:001, 2020.

[71] Guido D'Amico, Leonardo Senatore, and Pierre Zhang. Limits on wCDM from the EFTofLSS with the PyBird code. 2020.

[72] Daniel J. Eisenstein and Wayne Hu. Baryonic features in the matter transfer function. *Astrophys. J.*, 496:605, 1998.

[73] Daniel J. Eisenstein and Martin J. White. Theoretical uncertainty in baryon oscillations. *Phys. Rev. D*, 70:103523, 2004.

[74] Daniel J. Eisenstein, Hee-jong Seo, and Martin J. White. On the Robustness of the Acoustic Scale in the Low-Redshift Clustering of Matter. *Astrophys. J.*, 664:660–674, 2007.

[75] Bruce A. Bassett and Renee Hlozek. Baryon Acoustic Oscillations. 10 2009.

[76] David H. Weinberg, Michael J. Mortonson, Daniel J. Eisenstein, Christopher Hirata, Adam G. Riess, and Eduardo Rozo. Observational Probes of Cosmic Acceleration. *Phys. Rept.*, 530:87–255, 2013.

[77] Shaun Cole et al. The 2dF Galaxy Redshift Survey: Power-spectrum analysis of the final dataset and cosmological implications. *Mon. Not. Roy. Astron. Soc.*, 362:505–534, 2005.

[78] Shadab Alam et al. The clustering of galaxies in the completed SDSS-III Baryon Oscillation Spectroscopic Survey: cosmological analysis of the DR12 galaxy sample. *Mon. Not. Roy. Astron. Soc.*, 470(3):2617–2652, 2017.

[79] Ashley J. Ross et al. The clustering of galaxies in the completed SDSS-III Baryon Oscillation Spectroscopic Survey: Observational systematics and baryon

acoustic oscillations in the correlation function. *Mon. Not. Roy. Astron. Soc.*, 464(1):1168–1191, 2017.

[80] Mariana Vargas-Magaña et al. The clustering of galaxies in the completed SDSS-III Baryon Oscillation Spectroscopic Survey: theoretical systematics and Baryon Acoustic Oscillations in the galaxy correlation function. *Mon. Not. Roy. Astron. Soc.*, 477(1):1153–1188, 2018.

[81] Florian Beutler et al. The clustering of galaxies in the completed SDSS-III Baryon Oscillation Spectroscopic Survey: baryon acoustic oscillations in the Fourier space. *Mon. Not. Roy. Astron. Soc.*, 464(3):3409–3430, 2017.

[82] Florian Beutler, Chris Blake, Matthew Colless, D. Heath Jones, Lister Staveley-Smith, Lachlan Campbell, Quentin Parker, Will Saunders, and Fred Watson. The 6dF Galaxy Survey: Baryon Acoustic Oscillations and the Local Hubble Constant. *Mon. Not. Roy. Astron. Soc.*, 416:3017–3032, 2011.

[83] Ashley J. Ross, Lado Samushia, Cullan Howlett, Will J. Percival, Angela Burden, and Marc Manera. The clustering of the SDSS DR7 main Galaxy sample – I. A 4 per cent distance measure at $z = 0.15$. *Mon. Not. Roy. Astron. Soc.*, 449(1):835–847, 2015.

[84] D. M. Scolnic et al. The Complete Light-curve Sample of Spectroscopically Confirmed SNe Ia from Pan-STARRS1 and Cosmological Constraints from the Combined Pantheon Sample. *Astrophys. J.*, 859(2):101, 2018.

[85] Clifford M. Will. The Confrontation between General Relativity and Experiment. *Living Rev. Rel.*, 17:4, 2014.

[86] Kazuya Koyama. Cosmological Tests of Modified Gravity. *Rept. Prog. Phys.*, 79(4):046902, 2016.

[87] Pascual Jordan. Formation of the Stars and Development of the Universe. *Nature*, 164:637–640, 1949.

[88] C. Brans and R.H. Dicke. Mach's principle and a relativistic theory of gravitation. *Phys. Rev.*, 124:925–935, 1961.

[89] Y. Fujii and K. Maeda. *The scalar-tensor theory of gravitation*. Cambridge Monographs on Mathematical Physics. Cambridge University Press, 2007.

[90] Jose María Ezquiaga and Miguel Zumalacárregui. Dark Energy in light of Multi-Messenger Gravitational-Wave astronomy. *Front. Astron. Space Sci.*, 5:44, 2018.

[91] Israel Quiros. Selected topics in scalar–tensor theories and beyond. *Int. J. Mod. Phys. D*, 28(07):1930012, 2019.

[92] Richard P. Woodard. Ostrogradsky's theorem on Hamiltonian instability. *Scholarpedia*, 10(8):32243, 2015.

[93] Gregory Walter Horndeski. Second-order scalar-tensor field equations in a four-dimensional space. *Int. J. Theor. Phys.*, 10:363–384, 1974.

[94] Tsutomu Kobayashi. Horndeski theory and beyond: a review. *Rept. Prog. Phys.*, 82(8):086901, 2019.

[95] Alberto Nicolis, Riccardo Rattazzi, and Enrico Trincherini. The Galileon as a local modification of gravity. *Phys. Rev. D*, 79:064036, 2009.

[96] C. Deffayet, S. Deser, and G. Esposito-Farese. Generalized Galileons: All scalar models whose curved background extensions maintain second-order field equations and stress-tensors. *Phys. Rev. D*, 80:064015, 2009.

[97] C. Deffayet, Xian Gao, D.A. Steer, and G. Zahariade. From k-essence to generalised Galileons. *Phys. Rev. D*, 84:064039, 2011.

[98] Tsutomu Kobayashi, Masahide Yamaguchi, and Jun'ichi Yokoyama. Generalized G-inflation: Inflation with the most general second-order field equations. *Prog. Theor. Phys.*, 126:511–529, 2011.

[99] Miguel Zumalacárregui and Juan García-Bellido. Transforming gravity: from derivative couplings to matter to second-order scalar-tensor theories beyond the Horndeski Lagrangian. *Phys. Rev. D*, 89:064046, 2014.

[100] Guillem Domènech, Shinji Mukohyama, Ryo Namba, Atsushi Naruko, Rio Saitou, and Yota Watanabe. Derivative-dependent metric transformation and physical degrees of freedom. *Phys. Rev. D*, 92(8):084027, 2015.

[101] Jérôme Gleyzes, David Langlois, Federico Piazza, and Filippo Vernizzi. Healthy theories beyond Horndeski. *Phys. Rev. Lett.*, 114(21):211101, 2015.

[102] Jérôme Gleyzes, David Langlois, Federico Piazza, and Filippo Vernizzi. Exploring gravitational theories beyond Horndeski. *JCAP*, 02:018, 2015.

[103] David Langlois and Karim Noui. Degenerate higher derivative theories beyond Horndeski: evading the Ostrogradski instability. *JCAP*, 02:034, 2016.

[104] Jibril Ben Achour, David Langlois, and Karim Noui. Degenerate higher order scalar-tensor theories beyond Horndeski and disformal transformations. *Phys. Rev. D*, 93(12):124005, 2016.

[105] Marco Crisostomi, Kazuya Koyama, and Gianmassimo Tasinato. Extended Scalar-Tensor Theories of Gravity. *JCAP*, 04:044, 2016.

[106] Claudia de Rham and Andrew Matas. Ostrogradsky in Theories with Multiple Fields. *JCAP*, 06:041, 2016.

[107] Jibril Ben Achour, Marco Crisostomi, Kazuya Koyama, David Langlois, Karim Noui, and Gianmassimo Tasinato. Degenerate higher order scalar-tensor theories beyond Horndeski up to cubic order. *JHEP*, 12:100, 2016.

[108] David Langlois. Dark energy and modified gravity in degenerate higher-order scalar–tensor (DHOST) theories: A review. *Int. J. Mod. Phys. D*, 28(05):1942006, 2019.

[109] David I. Kaiser. Conformal Transformations with Multiple Scalar Fields. *Phys. Rev. D*, 81:084044, 2010.

[110] Radouane Gannouji, David Polarski, Andre Ranquet, and Alexei A. Starobinsky. Scalar-Tensor Models of Normal and Phantom Dark Energy. *JCAP*, 0609:016, 2006.

[111] B. Boisseau, Gilles Esposito-Farese, D. Polarski, and Alexei A. Starobinsky. Reconstruction of a scalar tensor theory of gravity in an accelerating universe. *Phys. Rev. Lett.*, 85:2236, 2000.

[112] Tessa Baker, Dimitrios Psaltis, and Constantinos Skordis. Linking Tests of Gravity On All Scales: from the Strong-Field Regime to Cosmology. *Astrophys. J.*, 802:63, 2015.

[113] A.I. Vainshtein. To the problem of nonvanishing gravitation mass. *Phys. Lett. B*, 39:393–394, 1972.

[114] Justin Khoury and Amanda Weltman. Chameleon fields: Awaiting surprises for tests of gravity in space. *Phys. Rev. Lett.*, 93:171104, 2004.

[115] Justin Khoury and Amanda Weltman. Chameleon cosmology. *Phys. Rev. D*, 69:044026, 2004.

[116] Kurt Hinterbichler and Justin Khoury. Symmetron Fields: Screening Long-Range Forces Through Local Symmetry Restoration. *Phys. Rev. Lett.*, 104:231301, 2010.

[117] Austin Joyce, Bhuvnesh Jain, Justin Khoury, and Mark Trodden. Beyond the Cosmological Standard Model. *Phys. Rept.*, 568:1–98, 2015.

[118] B.P. Abbott et al. Observation of Gravitational Waves from a Binary Black Hole Merger. *Phys. Rev. Lett.*, 116(6):061102, 2016.

[119] B.P. Abbott et al. GW170817: Observation of Gravitational Waves from a Binary Neutron Star Inspiral. *Phys. Rev. Lett.*, 119(16):161101, 2017.

[120] B.P. Abbott et al. Gravitational Waves and Gamma-rays from a Binary Neutron Star Merger: GW170817 and GRB 170817A. *Astrophys. J. Lett.*, 848(2):L13, 2017.

[121] B.P. Abbott et al. Multi-messenger Observations of a Binary Neutron Star Merger. *Astrophys. J. Lett.*, 848(2):L12, 2017.

[122] Jose María Ezquiaga and Miguel Zumalacárregui. Dark Energy After GW170817: Dead Ends and the Road Ahead. *Phys. Rev. Lett.*, 119(25):251304, 2017.

[123] Emilio Bellini and Ignacy Sawicki. Maximal freedom at minimum cost: linear large-scale structure in general modifications of gravity. *JCAP*, 07:050, 2014.

[124] Paolo Creminelli and Filippo Vernizzi. Dark Energy after GW170817 and GRB170817A. *Phys. Rev. Lett.*, 119(25):251302, 2017.

[125] T. Baker, E. Bellini, P.G. Ferreira, M. Lagos, J. Noller, and I. Sawicki. Strong constraints on cosmological gravity from GW170817 and GRB 170817A. *Phys. Rev. Lett.*, 119(25):251301, 2017.

[126] Jeremy Sakstein and Bhuvnesh Jain. Implications of the Neutron Star Merger GW170817 for Cosmological Scalar-Tensor Theories. *Phys. Rev. Lett.*, 119(25):251303, 2017.

[127] Claudia de Rham and Scott Melville. Gravitational Rainbows: LIGO and Dark Energy at its Cutoff. *Phys. Rev. Lett.*, 121(22):221101, 2018.

[128] Craig J. Copi, Adam N. Davis, and Lawrence M. Krauss. A New nucleosynthesis constraint on the variation of G. *Phys. Rev. Lett.*, 92:171301, 2004.

[129] Cosimo Bambi, Maurizio Giannotti, and F.L. Villante. The Response of primordial abundances to a general modification of G(N) and/or of the early Universe expansion rate. *Phys. Rev. D*, 71:123524, 2005.

[130] James Alvey, Nashwan Sabti, Miguel Escudero, and Malcolm Fairbairn. Improved BBN Constraints on the Variation of the Gravitational Constant. *Eur. Phys. J. C*, 80(2):148, 2020.

[131] S. B. Lambert and C. Le Poncin-Lafitte. Improved determination of γ by VLBI. 529:A70, May 2011.

[132] S.B. Lambert and C. Le Poncin-Lafitte. Determination of the relativistic parameter gamma using very long baseline interferometry. *Astron. Astrophys.*, 499:331, 2009.

[133] S.S. Shapiro, J.L. Davis, D.E. Lebach, and J.S. Gregory. Measurement of the Solar Gravitational Deflection of Radio Waves using Geodetic Very-Long-Baseline Interferometry Data, 1979-1999. *Phys. Rev. Lett.*, 92:121101, 2004.

[134] B. Bertotti, L. Iess, and P. Tortora. A test of general relativity using radio links with the Cassini spacecraft. *Nature*, 425:374–376, 2003.

[135] Slava G. Turyshev, Michael Shao, and Kenneth L. Nordtvedt. Science, technology and mission design for the laser astrometric test of relativity. *Astrophys. Space Sci. Libr.*, 349:473–543, 2008.

[136] R. Mecheri, T. Abdelatif, A. Irbah, J. Provost, and G. Berthomieu. New values of gravitational moments J_2 and J_4 deduced from helioseismology. 222(2):191–197, August 2004.

[137] H.M. Antia, S.M. Chitre, and D.O. Gough. Temporal Variations in the Sun's Rotational Kinetic Energy. *Astron. Astrophys.*, 477:657, 2008.

[138] Philippe Brax, Clare Burrage, and Anne-Christine Davis. Laboratory constraints. *Int. J. Mod. Phys. D*, 27(15):1848009, 2018.

[139] Simone Aiola et al. The Atacama Cosmology Telescope: DR4 Maps and Cosmological Parameters. 7 2020.

[140] T.M.C. Abbott et al. Dark Energy Survey Year 1 Results: A Precise H0 Estimate from DES Y1, BAO, and D/H Data. *Mon. Not. Roy. Astron. Soc.*, 480(3):3879–3888, 2018.

[141] S. Birrer et al. TDCOSMO IV: Hierarchical time-delay cosmography – joint inference of the Hubble constant and galaxy density profiles. 7 2020.

[142] A.J. Shajib et al. STRIDES: a 3.9 per cent measurement of the Hubble constant from the strong lens system DES J0408−5354. *Mon. Not. Roy. Astron. Soc.*, 494(4):6072–6102, 2020.

[143] T. de Jaeger, B.E. Stahl, W. Zheng, A.V. Filippenko, A.G. Riess, and L. Galbany. A measurement of the Hubble constant from Type II supernovae. *Mon. Not. Roy. Astron. Soc.*, 496(3):3402–3411, 2020.

[144] N. Khetan et al. A new measurement of the Hubble constant using Type Ia supernovae calibrated with surface brightness fluctuations. 8 2020.

[145] Adam G. Riess, Stefano Casertano, Wenlong Yuan, Lucas M. Macri, and Dan Scolnic. Large Magellanic Cloud Cepheid Standards Provide a 1% Foundation for the Determination of the Hubble Constant and Stronger Evidence for Physics beyond ΛCDM. *Astrophys. J.*, 876(1):85, 2019.

[146] L. Verde, T. Treu, and A.G. Riess. Tensions between the Early and the Late Universe. 7 2019.

[147] James Schombert, Stacy McGaugh, and Federico Lelli. Using the Baryonic Tully–Fisher Relation to Measure H o. *Astron. J.*, 160(2):71, 2020.

[148] Ehsan Kourkchi, R. Brent Tully, Gagandeep S. Anand, Helene M. Courtois, Alexandra Dupuy, James D. Neill, Luca Rizzi, and Mark Seibert. Cosmicflows-4: The Calibration of Optical and Infrared Tully–Fisher Relations. *Astrophys. J.*, 896(1):3, 2020.

[149] D.W. Pesce et al. The Megamaser Cosmology Project. XIII. Combined Hubble constant constraints. *Astrophys. J. Lett.*, 891(1):L1, 2020.

[150] Caroline D. Huang, Adam G. Riess, Wenlong Yuan, Lucas M. Macri, Nadia L. Zakamska, Stefano Casertano, Patricia A. Whitelock, Samantha L. Hoffmann, Alexei V. Filippenko, and Daniel Scolnic. Hubble Space Telescope Observations of Mira Variables in the Type Ia Supernova Host NGC 1559: An Alternative Candle to Measure the Hubble Constant. 8 2019.

[151] In Sung Jang and Myung Gyoon Lee. The Tip of the Red Giant Branch Distances to Typa Ia Supernova Host Galaxies. V. NGC 3021, NGC 3370, and NGC 1309 and the Value of the Hubble Constant. *Astrophys. J.*, 836(1):74, 2017.

[152] Wenlong Yuan, Adam G. Riess, Lucas M. Macri, Stefano Casertano, and Dan Scolnic. Consistent Calibration of the Tip of the Red Giant Branch in the Large Magellanic Cloud on the Hubble Space Telescope Photometric System and a Re-determination of the Hubble Constant. *Astrophys. J.*, 886:61, 2019.

[153] Wendy L. Freedman, Barry F. Madore, Taylor Hoyt, In Sung Jang, Rachael Beaton, Myung Gyoon Lee, Andrew Monson, Jill Neeley, and Jeffrey Rich. Calibration of the Tip of the Red Giant Branch (TRGB). 2 2020.

[154] Wendy L. Freedman, Barry F. Madore, Victoria Scowcroft, Chris Burns, Andy Monson, S.Eric Persson, Mark Seibert, and Jane Rigby. Carnegie Hubble Program: A Mid-Infrared Calibration of the Hubble Constant. *Astrophys. J.*, 758:24, 2012.

[155] Christopher R. Burns et al. The Carnegie Supernova Project: Absolute Calibration and the Hubble Constant. *Astrophys. J.*, 869(1):56, 2018.

[156] Louise Breuval et al. The Milky Way Cepheid Leavitt law based on Gaia DR2 parallaxes of companion stars and host open cluster populations. 6 2020.

[157] Oliver H.E. Philcox, Mikhail M. Ivanov, Marko Simonović, and Matias Zaldarriaga. Combining Full-Shape and BAO Analyses of Galaxy Power Spectra: A 1.6% CMB-independent constraint on H0. *JCAP*, 05:032, 2020.

[158] G.E. Addison, D.J. Watts, C.L. Bennett, M. Halpern, G. Hinshaw, and J.L. Weiland. Elucidating ΛCDM: Impact of Baryon Acoustic Oscillation Measurements on the Hubble Constant Discrepancy. *Astrophys. J.*, 853(2):119, 2018.

[159] Kenneth C. Wong et al. H0LiCOW XIII. A 2.4% measurement of H_0 from lensed quasars: 5.3σ tension between early and late-Universe probes. 2019.

[160] M. J. Reid, D. W. Pesce, and A. G. Riess. An Improved Distance to NGC 4258 and its Implications for the Hubble Constant. *Astrophys. J. Lett.*, 886(2):L27, 2019.

[161] Adam G. Riess, Lucas Macri, Stefano Casertano, Hubert Lampeitl, Henry C. Ferguson, Alexei V. Filippenko, Saurabh W. Jha, Weidong Li, and Ryan Chornock. A 3% Solution: Determination of the Hubble Constant with the Hubble Space Telescope and Wide Field Camera 3. *Astrophys. J.*, 730:119, 2011. [Erratum: Astrophys.J. 732, 129 (2011)].

[162] P.A.R. Ade et al. Planck 2013 results. XVI. Cosmological parameters. *Astron. Astrophys.*, 571:A16, 2014.

[163] George Efstathiou. H0 Revisited. *Mon. Not. Roy. Astron. Soc.*, 440(2):1138–1152, 2014.

[164] M. Rigault et al. Confirmation of a Star Formation Bias in Type Ia Supernova Distances and its Effect on Measurement of the Hubble Constant. *Astrophys. J.*, 802(1):20, 2015.

[165] M. Rigault et al. Strong Dependence of Type Ia Supernova Standardization on the Local Specific Star Formation Rate. 6 2018.

[166] Pablo Lemos, Elizabeth Lee, George Efstathiou, and Steven Gratton. Model independent $H(z)$ reconstruction using the cosmic inverse distance ladder. *Mon. Not. Roy. Astron. Soc.*, 483(4):4803–4810, 2019.

[167] Eleonora Di Valentino, Alessandro Melchiorri, and Joseph Silk. Reconciling Planck with the local value of H_0 in extended parameter space. *Phys. Lett.*, B761:242–246, 2016.

[168] Ryan E. Keeley, Shahab Joudaki, Manoj Kaplinghat, and David Kirkby. Implications of a transition in the dark energy equation of state for the H_0 and σ_8 tensions. *JCAP*, 1912:035, 2019.

[169] Sunny Vagnozzi. New physics in light of the H_0 tension: An alternative view. *Phys. Rev.*, D102(2):023518, 2020.

[170] Marco Raveri. Reconstructing Gravity on Cosmological Scales. *Phys. Rev. D*, 101(8):083524, 2020.

[171] Eleonora Di Valentino, Alessandro Melchiorri, Olga Mena, and Sunny Vagnozzi. Interacting dark energy in the early 2020s: A promising solution to the H_0 and cosmic shear tensions. *Phys. Dark Univ.*, 30:100666, 2020.

[172] Giampaolo Benevento, Wayne Hu, and Marco Raveri. Can Late Dark Energy Transitions Raise the Hubble constant? *Phys. Rev.*, D101(10):103517, 2020.

[173] G. Alestas, L. Kazantzidis, and L. Perivolaropoulos. H_0 tension, phantom dark energy, and cosmological parameter degeneracies. *Phys. Rev.*, D101(12):123516, 2020.

[174] Eleonora Di Valentino, Eric V. Linder, and Alessandro Melchiorri. H_0 Ex Machina: Vacuum Metamorphosis and Beyond H_0. 2020.

[175] Rodrigo Calderón, Radouane Gannouji, Benjamin L'Huillier, and David Polarski. A negative cosmological constant in the dark sector? 2020.

[176] Abdolali Banihashemi, Nima Khosravi, and Arman Shafieloo. Dark Energy as a Critical Phenomenon: a Resolution for Hubble Tension. 12 2020.

[177] Kevin Aylor, MacKenzie Joy, Lloyd Knox, Marius Millea, Srinivasan Raghunathan, and W. L. Kimmy Wu. Sounds Discordant: Classical Distance Ladder & ΛCDM -based Determinations of the Cosmological Sound Horizon. *Astrophys. J.*, 874(1):4, 2019.

[178] Jose Luis Bernal, Licia Verde, and Adam G. Riess. The trouble with H_0. *JCAP*, 1610:019, 2016.

[179] Alan Heavens, Raul Jimenez, and Licia Verde. Standard rulers, candles, and clocks from the low-redshift Universe. *Phys. Rev. Lett.*, 113(24):241302, 2014.

[180] Lloyd Knox and Marius Millea. Hubble constant hunter's guide. *Phys. Rev.*, D101(4):043533, 2020.

[181] E.L. Wright et al. Interpretation of the COBE FIRAS spectrum. *Astrophys. J.*, 420:450, 1994.

[182] Julien Lesgourgues, Gianpiero Mangano, Gennaro Miele, and Sergio Pastor. *Neutrino Cosmology.* Cambridge University Press, 2013.

[183] Francesco D'Eramo, Ricardo Z. Ferreira, Alessio Notari, and José Luis Bernal. Hot Axions and the H_0 tension. *JCAP*, 1811:014, 2018.

[184] Mark Wyman, Douglas H. Rudd, R.Ali Vanderveld, and Wayne Hu. Neutrinos Help Reconcile Planck Measurements with the Local Universe. *Phys. Rev. Lett.*, 112(5):051302, 2014.

[185] Francis-Yan Cyr-Racine and Kris Sigurdson. Limits on Neutrino-Neutrino Scattering in the Early Universe. *Phys. Rev. D*, 90(12):123533, 2014.

[186] Lachlan Lancaster, Francis-Yan Cyr-Racine, Lloyd Knox, and Zhen Pan. A tale of two modes: Neutrino free-streaming in the early universe. *JCAP*, 07:033, 2017.

[187] Manuel A. Buen-Abad, Martin Schmaltz, Julien Lesgourgues, and Thejs Brinckmann. Interacting Dark Sector and Precision Cosmology. *JCAP*, 01:008, 2018.

[188] Christina D. Kreisch, Francis-Yan Cyr-Racine, and Olivier Doré. Neutrino puzzle: Anomalies, interactions, and cosmological tensions. *Phys. Rev.*, D101(12):123505, 2020.

[189] Vivian Poulin, Tristan L. Smith, Tanvi Karwal, and Marc Kamionkowski. Early Dark Energy Can Resolve The Hubble Tension. *Phys. Rev. Lett.*, 122(22):221301, 2019.

[190] David J.E. Marsh. The Axiverse Extended: Vacuum Destabilisation, Early Dark Energy and Cosmological Collapse. *Phys. Rev. D*, 83:123526, 2011.

[191] Marc Kamionkowski, Josef Pradler, and Devin G. E. Walker. Dark energy from the string axiverse. *Phys. Rev. Lett.*, 113(25):251302, 2014.

[192] Tanvi Karwal and Marc Kamionkowski. Dark energy at early times, the Hubble parameter, and the string axiverse. *Phys. Rev. D*, 94(10):103523, 2016.

[193] Joshua A. Frieman, Christopher T. Hill, Albert Stebbins, and Ioav Waga. Cosmology with ultralight pseudo Nambu-Goldstone bosons. *Phys. Rev. Lett.*, 75:2077–2080, 1995.

[194] Miguel Montero, Angel M. Uranga, and Irene Valenzuela. Transplanckian axions!? *JHEP*, 08:032, 2015.

[195] Tom Banks, Michael Dine, Patrick J. Fox, and Elie Gorbatov. On the possibility of large axion decay constants. *JCAP*, 06:001, 2003.

[196] Tom Rudelius. On the Possibility of Large Axion Moduli Spaces. *JCAP*, 04:049, 2015.

[197] Michael S. Turner. Coherent Scalar Field Oscillations in an Expanding Universe. *Phys. Rev. D*, 28:1243, 1983.

[198] Tristan L. Smith, Vivian Poulin, and Mustafa A. Amin. Oscillating scalar fields and the Hubble tension: a resolution with novel signatures. *Phys. Rev.*, D101(6):063523, 2020.

[199] Prateek Agrawal, Francis-Yan Cyr-Racine, David Pinner, and Lisa Randall. Rock 'n' Roll Solutions to the Hubble Tension. 2019.

[200] Vivian Poulin, Tristan L. Smith, Daniel Grin, Tanvi Karwal, and Marc Kamionkowski. Cosmological implications of ultralight axionlike fields. *Phys. Rev. D*, 98(8):083525, 2018.

[201] Stephon Alexander and Evan McDonough. Axion-Dilaton Destabilization and the Hubble Tension. *Phys. Lett.*, B797:134830, 2019.

[202] Meng-Xiang Lin, Giampaolo Benevento, Wayne Hu, and Marco Raveri. Acoustic Dark Energy: Potential Conversion of the Hubble Tension. *Phys. Rev.*, D100(6):063542, 2019.

[203] Florian Niedermann and Martin S. Sloth. New Early Dark Energy. 2019.

[204] Kim V. Berghaus and Tanvi Karwal. Thermal Friction as a Solution to the Hubble Tension. *Phys. Rev.*, D101(8):083537, 2020.

[205] Jeremy Sakstein and Mark Trodden. Early Dark Energy from Massive Neutrinos as a Natural Resolution of the Hubble Tension. *Phys. Rev. Lett.*, 124(16):161301, 2020.

[206] Nemanja Kaloper. Dark energy, H_0 and weak gravity conjecture. *Int. J. Mod. Phys.*, D28(14):1944017, 2019.

[207] Mark Gonzalez, Mark P. Hertzberg, and Fabrizio Rompineve. Ultralight Scalar Decay and the Hubble Tension. 2020.

[208] Florian Niedermann and Martin S. Sloth. Resolving the Hubble tension with new early dark energy. *Phys. Rev.*, D102(6):063527, 2020.

[209] Gen Ye and Yun-Song Piao. Is the Hubble tension a hint of AdS phase around recombination? *Phys. Rev.*, D101(8):083507, 2020.

[210] Florian Niedermann and Martin S. Sloth. New Early Dark Energy is compatible with current LSS data. 2020.

[211] Meng-Xiang Lin, Wayne Hu, and Marco Raveri. Testing H_0 in Acoustic Dark Energy with Planck and ACT Polarization. 2020.

[212] Eric V. Linder. Dark Energy from α-Attractors. *Phys. Rev. D*, 91(12):123012, 2015.

[213] Carlos García-García, Eric V. Linder, Pilar Ruíz-Lapuente, and Miguel Zumalacárregui. Dark energy from α-attractors: phenomenology and observational constraints. *JCAP*, 08:022, 2018.

[214] David J. E. Marsh. Axion Cosmology. *Phys. Rept.*, 643:1–79, 2016.

[215] Riccardo Murgia, Guillermo F. Abellán, and Vivian Poulin. The early dark energy resolution to the Hubble tension in light of weak lensing surveys and lensing anomalies. 2020.

[216] J. Colin Hill, Evan McDonough, Michael W. Toomey, and Stephon Alexander. Early dark energy does not restore cosmological concordance. *Phys. Rev.*, D102(4):043507, 2020.

[217] Mikhail M. Ivanov, Evan McDonough, J. Colin Hill, Marko Simonović, Michael W. Toomey, Stephon Alexander, and Matias Zaldarriaga. Constraining Early Dark Energy with Large-Scale Structure. 2020.

[218] Guido D'Amico, Leonardo Senatore, Pierre Zhang, and Henry Zheng. The Hubble Tension in Light of the Full-Shape Analysis of Large-Scale Structure Data. 2020.

[219] Anton Chudaykin, Dmitry Gorbunov, and Nikita Nedelko. Combined analysis of Planck and SPTPol data favors the early dark energy models. *JCAP*, 08:013, 2020.

[220] Zachary J. Weiner, Peter Adshead, and John T. Giblin. Constraining early dark energy with gravitational waves before recombination. 8 2020.

[221] C. Umiltà, M. Ballardini, F. Finelli, and D. Paoletti. CMB and BAO constraints for an induced gravity dark energy model with a quartic potential. *JCAP*, 1508:017, 2015.

[222] Mario Ballardini, Fabio Finelli, Caterina Umiltà, and Daniela Paoletti. Cosmological constraints on induced gravity dark energy models. *JCAP*, 1605:067, 2016.

[223] Rafael C. Nunes. Structure formation in $f(T)$ gravity and a solution for H_0 tension. *JCAP*, 1805:052, 2018.

[224] Meng-Xiang Lin, Marco Raveri, and Wayne Hu. Phenomenology of Modified Gravity at Recombination. *Phys. Rev.*, D99(4):043514, 2019.

[225] Joan Solà Peracaula, Adria Gomez-Valent, Javier de Cruz Pérez, and Cristian Moreno-Pulido. Brans–Dicke Gravity with a Cosmological Constant Smoothes Out ΛCDM Tensions. *Astrophys. J. Lett.*, 886(1):L6, 2019.

[226] Miguel Zumalacarregui. Gravity in the Era of Equality: Towards solutions to the Hubble problem without fine-tuned initial conditions. *Phys. Rev.*, D102(2):023523, 2020.

[227] Deng Wang and David Mota. Can $f(T)$ gravity resolve the H_0 tension? *Phys. Rev.*, D102(6):063530, 2020.

[228] Guillermo Ballesteros, Alessio Notari, and Fabrizio Rompineve. The H_0 tension: ΔG_N vs. $\Delta N_{\rm eff}$. 2020.

[229] Joan Sola, Adria Gomez-Valent, Javier de Cruz Perez, and Cristian Moreno-Pulido. Brans-Dicke cosmology with a Λ- term: a possible solution to ΛCDM tensions. 2020.

[230] Deng Wang. Can $f(R)$ gravity relieve H_0 and σ_8 tensions? 8 2020.

[231] Shahab Joudaki, Pedro G. Ferreira, Nelson A. Lima, and Hans A. Winther. Testing Gravity on Cosmic Scales: A Case Study of Jordan-Brans-Dicke Theory. 10 2020.

[232] F. Finelli, A. Tronconi, and Giovanni Venturi. Dark Energy, Induced Gravity and Broken Scale Invariance. *Phys. Lett. B*, 659:466–470, 2008.

[233] Harry Desmond, Bhuvnesh Jain, and Jeremy Sakstein. Local resolution of the Hubble tension: The impact of screened fifth forces on the cosmic distance ladder. *Phys. Rev. D*, 100(4):043537, 2019. [Erratum: Phys.Rev.D 101, 069904 (2020), Erratum: Phys.Rev.D 101, 129901 (2020)].

[234] Harry Desmond and Jeremy Sakstein. Screened fifth forces lower the TRGB-calibrated Hubble constant too. *Phys. Rev. D*, 102(2):023007, 2020.

[235] E. Garcia-Berro, E. Gaztanaga, J. Isern, O. Benvenuto, and L. Althaus. On the evolution of cosmological type ia supernovae and the gravitational constant. 7 1999.

[236] Alain Riazuelo and Jean-Philippe Uzan. Cosmological observations in scalar - tensor quintessence. *Phys. Rev. D*, 66:023525, 2002.

[237] S. Nesseris and Leandros Perivolaropoulos. Evolving newton's constant, extended gravity theories and snia data analysis. *Phys. Rev. D*, 73:103511, 2006.

[238] Bill S. Wright and Baojiu Li. Type Ia supernovae, standardizable candles, and gravity. *Phys. Rev. D*, 97(8):083505, 2018.

[239] A. Avilez and C. Skordis. Cosmological constraints on Brans-Dicke theory. *Phys. Rev. Lett.*, 113(1):011101, 2014.

[240] Nicola Bartolo and Massimo Pietroni. Scalar tensor gravity and quintessence. *Phys. Rev. D*, 61:023518, 2000.

[241] Luca Amendola. Scaling solutions in general nonminimal coupling theories. *Phys. Rev. D*, 60:043501, 1999.

[242] Jean-Philippe Uzan. Cosmological scaling solutions of nonminimally coupled scalar fields. *Phys. Rev. D*, 59:123510, 1999.

[243] Francesca Perrotta, Carlo Baccigalupi, and Sabino Matarrese. Extended quintessence. *Phys. Rev. D*, 61:023507, 1999.

[244] Takeshi Chiba. Quintessence, the gravitational constant, and gravity. *Phys. Rev. D*, 60:083508, 1999.

[245] Carlo Baccigalupi, Sabino Matarrese, and Francesca Perrotta. Tracking extended quintessence. *Phys. Rev. D*, 62:123510, 2000.

[246] Miguel Zumalacárregui, Emilio Bellini, Ignacy Sawicki, Julien Lesgourgues, and Pedro G. Ferreira. hi_class: Horndeski in the Cosmic Linear Anisotropy Solving System. *JCAP*, 1708:019, 2017.

[247] Emilio Bellini, Ignacy Sawicki, and Miguel Zumalacárregui. hi class: Background Evolution, Initial Conditions and Approximation Schemes. *JCAP*, 2002:008, 2020.

[248] E. Bellini et al. Comparison of Einstein-Boltzmann solvers for testing general relativity. *Phys. Rev. D*, 97(2):023520, 2018.

[249] C. Wetterich. Cosmology and the Fate of Dilatation Symmetry. *Nucl. Phys. B*, 302:668–696, 1988.

[250] Fred Cooper and Giovanni Venturi. Cosmology and Broken Scale Invariance. *Phys. Rev. D*, 24:3338, 1981.

[251] Fedor L. Bezrukov and Mikhail Shaposhnikov. The Standard Model Higgs boson as the inflaton. *Phys. Lett. B*, 659:703–706, 2008.

[252] P.A.R. Ade et al. Planck 2015 results. XIII. Cosmological parameters. *Astron. Astrophys.*, 594:A13, 2016.

[253] Adam G. Riess et al. Milky Way Cepheid Standards for Measuring Cosmic Distances and Application to Gaia DR2: Implications for the Hubble Constant. *Astrophys. J.*, 861(2):126, 2018.

[254] Adam G. Riess et al. A 2.4% Determination of the Local Value of the Hubble Constant. *Astrophys. J.*, 826(1):56, 2016.

[255] Wendy L. Freedman et al. The Carnegie-Chicago Hubble Program. VIII. An Independent Determination of the Hubble Constant Based on the Tip of the Red Giant Branch. 7 2019.

[256] M.J. Reid, J.A. Braatz, J.J. Condon, L.J. Greenhill, C. Henkel, and K.Y. Lo. The Megamaser Cosmology Project: I. VLBI observations of UGC 3789. *Astrophys. J.*, 695:287–291, 2009.

[257] Andrew R Liddle. Information criteria for astrophysical model selection. *Mon. Not. Roy. Astron. Soc.*, 377:L74–L78, 2007.

[258] Alain Coc, Keith A. Olive, Jean-Philippe Uzan, and Elisabeth Vangioni. Big bang nucleosynthesis constraints on scalar-tensor theories of gravity. *Phys. Rev. D*, 73:083525, 2006.

[259] Tal Abadi and Ely D. Kovetz. Can Conformally Invariant Modified Gravity Solve The Hubble Tension? 11 2020.

[260] David Alonso, Emilio Bellini, Pedro G. Ferreira, and Miguel Zumalacárregui. Observational future of cosmological scalar-tensor theories. *Phys. Rev. D*, 95(6):063502, 2017.

[261] M. Ballardini, D. Sapone, C. Umiltà, F. Finelli, and D. Paoletti. Testing extended Jordan-Brans-Dicke theories with future cosmological observations. *JCAP*, 05:049, 2019.

[262] Renée Hložek, David J. E. Marsh, Daniel Grin, Rupert Allison, Jo Dunkley, and Erminia Calabrese. Future CMB tests of dark matter: Ultralight axions and massive neutrinos. *Phys. Rev. D*, 95(12):123511, 2017.

[263] Philippe Brax, Carsten van de Bruck, Sebastien Clesse, Anne-Christine Davis, and Gregory Sculthorpe. Early Modified Gravity: Implications for Cosmology. *Phys. Rev. D*, 89(12):123507, 2014.

[264] Nelson A. Lima, Vanessa Smer-Barreto, and Lucas Lombriser. Constraints on decaying early modified gravity from cosmological observations. *Phys. Rev. D*, 94(8):083507, 2016.

[265] Valeria Pettorino and Luca Amendola. Friction in Gravitational Waves: a test for early-time modified gravity. *Phys. Lett. B*, 742:353–357, 2015.

[266] Matteo Braglia, Mario Ballardini, Fabio Finelli, and Kazuya Koyama. Early modified gravity in light of the H_0 tension and LSS data. *Phys. Rev. D*, 103:043528, 2021.

[267] Alain Riazuelo and Jean-Philippe Uzan. Quintessence and gravitational waves. *Phys. Rev. D*, 62:083506, 2000.

[268] Luca Amendola, Guillermo Ballesteros, and Valeria Pettorino. Effects of modified gravity on B-mode polarization. *Phys. Rev. D*, 90:043009, 2014.

[269] Philip Bull, Martin White, and Anže Slosar. Searching for dark energy in the matter-dominated era. 2020.

[270] Anatoly Klypin, Vivian Poulin, Francisco Prada, Joel Primack, Marc Kamionkowski, Vladimir Avila-Reese, Aldo Rodriguez-Puebla, Peter Behroozi, Doug Hellinger, and Tristan L. Smith. Clustering and Halo Abundances in Early Dark Energy Cosmological Models. 2020.

[271] R.E. Smith, J.A. Peacock, A. Jenkins, S.D.M. White, C.S. Frenk, F.R. Pearce, P.A. Thomas, G. Efstathiou, and H.M.P. Couchmann. Stable clustering, the halo model and nonlinear cosmological power spectra. *Mon. Not. Roy. Astron. Soc.*, 341:1311, 2003.

[272] Ryuichi Takahashi, Masanori Sato, Takahiro Nishimichi, Atsushi Taruya, and Masamune Oguri. Revising the Halofit Model for the Nonlinear Matter Power Spectrum. *Astrophys. J.*, 761:152, 2012.

[273] Alexander Mead, John Peacock, Catherine Heymans, Shahab Joudaki, and Alan Heavens. An accurate halo model for fitting non-linear cosmological power spectra and baryonic feedback models. *Mon. Not. Roy. Astron. Soc.*, 454(2):1958–1975, 2015.

[274] F. James and M. Roos. Minuit: A System for Function Minimization and Analysis of the Parameter Errors and Correlations. *Comput. Phys. Commun.*, 10:343–367, 1975.

[275] Harold Jeffreys. *The Theory of Probability*. Oxford Classic Texts in the Physical Sciences. 1939.

[276] Robert E. Kass and Adrian E. Raftery. Bayes Factors. *J. Am. Statist. Assoc.*, 90(430):773–795, 1995.

[277] Alan Heavens, Yabebal Fantaye, Arrykrishna Mootoovaloo, Hans Eggers, Zafiirah Hosenie, Steve Kroon, and Elena Sellentin. Marginal Likelihoods from Monte Carlo Markov Chains. 4 2017.

[278] S. Gariazzo. Constraining power of open likelihoods, made prior-independent. *Eur. Phys. J. C*, 80(6):552, 2020.

[279] Tristan L. Smith, Vivian Poulin, José Luis Bernal, Kimberly K. Boddy, Marc Kamionkowski, and Riccardo Murgia. Early dark energy is not excluded by current large-scale structure data. 9 2020.

[280] Karsten Jedamzik, Levon Pogosian, and Gong-Bo Zhao. Why reducing the cosmic sound horizon can not fully resolve the Hubble tension. 10 2020.

[281] Hayato Motohashi, Alexei A. Starobinsky, and Jun'ichi Yokoyama. Cosmology Based on f(R) Gravity Admits 1 eV Sterile Neutrinos. *Phys. Rev. Lett.*, 110(12):121302, 2013.

[282] A.S. Chudaykin, D.S. Gorbunov, A.A. Starobinsky, and R.A. Burenin. Cosmology based on f(R) gravity with Script O(1) eV sterile neutrino. *JCAP*, 05:004, 2015.

[283] Sunny Vagnozzi, Elena Giusarma, Olga Mena, Katherine Freese, Martina Gerbino, Shirley Ho, and Massimiliano Lattanzi. Unveiling ν secrets with cosmological data: neutrino masses and mass hierarchy. *Phys. Rev. D*, 96(12):123503, 2017.

[284] Shouvik Roy Choudhury and Steen Hannestad. Updated results on neutrino mass and mass hierarchy from cosmology with Planck 2018 likelihoods. *JCAP*, 07:037, 2020.

[285] Alexandre Barreira, Baojiu Li, Carlton Baugh, and Silvia Pascoli. Modified gravity with massive neutrinos as a testable alternative cosmological model. *Phys. Rev. D*, 90(2):023528, 2014.

[286] M. Tanabashi et al. Review of Particle Physics. *Phys. Rev. D*, 98(3):030001, 2018.

[287] Peter Ade et al. The Simons Observatory: Science goals and forecasts. *JCAP*, 02:056, 2019.

[288] Kevork N. Abazajian et al. CMB-S4 Science Book, First Edition. 10 2016.

[289] Michael Levi et al. The DESI Experiment, a whitepaper for Snowmass 2013. 8 2013.

[290] R. Laureijs et al. Euclid Definition Study Report. 10 2011.

[291] Luca Amendola et al. Cosmology and fundamental physics with the Euclid satellite. *Living Rev. Rel.*, 16:6, 2013.

[292] Paul A. Abell et al. LSST Science Book, Version 2.0. 12 2009.

[293] Roy Maartens, Filipe B. Abdalla, Matt Jarvis, and Mario G. Santos. Overview of Cosmology with the SKA. *PoS*, AASKA14:016, 2015.

[294] David J. Bacon et al. Cosmology with Phase 1 of the Square Kilometre Array: Red Book 2018: Technical specifications and performance forecasts. *Publ. Astron. Soc. Austral.*, 37:e007, 2020.

[295] Thejs Brinckmann, Deanna C. Hooper, Maria Archidiacono, Julien Lesgourgues, and Tim Sprenger. The promising future of a robust cosmological neutrino mass measurement. *JCAP*, 01:059, 2019.

[296] Nicola Bellomo, Emilio Bellini, Bin Hu, Raul Jimenez, Carlos Pena-Garay, and Licia Verde. Hiding neutrino mass in modified gravity cosmologies. *JCAP*, 02:043, 2017.

[297] Steen Hannestad. Primordial neutrinos. *Ann. Rev. Nucl. Part. Sci.*, 56:137–161, 2006.

[298] Scott Dodelson and Michael S. Turner. Nonequilibrium neutrino statistical mechanics in the expanding universe. *Phys. Rev. D*, 46:3372–3387, 1992.

[299] Brian D. Fields, Scott Dodelson, and Michael S. Turner. Effect of neutrino heating on primordial nucleosynthesis. *Phys. Rev. D*, 47:4309–4314, 1993.

[300] A.D. Dolgov and M. Fukugita. Nonequilibrium effect of the neutrino distribution on primordial helium synthesis. *Phys. Rev. D*, 46:5378–5382, 1992.

[301] Gianpiero Mangano, Gennaro Miele, Sergio Pastor, Teguayco Pinto, Ofelia Pisanti, and Pasquale D. Serpico. Relic neutrino decoupling including flavor oscillations. *Nucl. Phys. B*, 729:221–234, 2005.

[302] Sergei Bashinsky and Uros Seljak. Neutrino perturbations in CMB anisotropy and matter clustering. *Phys. Rev. D*, 69:083002, 2004.

[303] Steen Hannestad. Neutrino masses and the dark energy equation of state - Relaxing the cosmological neutrino mass bound. *Phys. Rev. Lett.*, 95:221301, 2005.

[304] Julien Lesgourgues and Sergio Pastor. Massive neutrinos and cosmology. *Phys. Rept.*, 429:307–379, 2006.

[305] Yvonne Y.Y. Wong. Neutrino mass in cosmology: status and prospects. *Ann. Rev. Nucl. Part. Sci.*, 61:69–98, 2011.

[306] Maria Archidiacono, Thejs Brinckmann, Julien Lesgourgues, and Vivian Poulin. Physical effects involved in the measurements of neutrino masses with future cosmological data. *JCAP*, 02:052, 2017.

[307] L.R.W. Abramo and F. Finelli. Attractors and isocurvature perturbations in quintessence models. *Phys. Rev. D*, 64:083513, 2001.

[308] Takeo Moroi and Tomo Takahashi. Correlated isocurvature fluctuation in quintessence and suppressed CMB anisotropies at low multipoles. *Phys. Rev. Lett.*, 92:091301, 2004.

[309] Christopher Gordon and Wayne Hu. A Low CMB quadrupole from dark energy isocurvature perturbations. *Phys. Rev. D*, 70:083003, 2004.

[310] Michael Doran, Christian M. Muller, Gregor Schafer, and Christof Wetterich. Gauge-invariant initial conditions and early time perturbations in quintessence universes. *Phys. Rev. D*, 68:063505, 2003.

[311] Rahul Dave, R.R. Caldwell, and Paul J. Steinhardt. Sensitivity of the cosmic microwave background anisotropy to initial conditions in quintessence cosmology. *Phys. Rev. D*, 66:023516, 2002.

[312] D.H. Lyth. Large Scale Energy Density Perturbations and Inflation. *Phys. Rev. D*, 31:1792–1798, 1985.

[313] Jonathan White, Masato Minamitsuji, and Misao Sasaki. Curvature perturbation in multi-field inflation with non-minimal coupling. *JCAP*, 07:039, 2012.

[314] David Langlois. Correlated adiabatic and isocurvature perturbations from double inflation. *Phys. Rev. D*, 59:123512, 1999.

[315] David Langlois and Alain Riazuelo. Correlated mixtures of adiabatic and isocurvature cosmological perturbations. *Phys. Rev. D*, 62:043504, 2000.

[316] Luca Amendola, Christopher Gordon, David Wands, and Misao Sasaki. Correlated perturbations from inflation and the cosmic microwave background. *Phys. Rev. Lett.*, 88:211302, 2002.

[317] Maria Beltran, Juan Garcia-Bellido, Julien Lesgourgues, and Matteo Viel. Squeezing the window on isocurvature modes with the lyman-alpha forest. *Phys. Rev. D*, 72:103515, 2005.

[318] P.A.R. Ade et al. Planck 2015 results. XX. Constraints on inflation. *Astron. Astrophys.*, 594:A20, 2016.

[319] N. Aghanim et al. Planck 2015 results. XI. CMB power spectra, likelihoods, and robustness of parameters. *Astron. Astrophys.*, 594:A11, 2016.